National Library of Canada
Bibliothèque nationale du Canada

Canadian Theses Service
Service des thèses canadiennes

Ottawa, Canada
K1A 0N4

NOTICE

The quality of this microform is heavily dependent upon the quality of the original thesis submitted for microfilming. Every effort has been made to ensure the highest quality of reproduction possible.

If pages are missing, contact the university which granted the degree.

Some pages may have indistinct print especially if the original pages were typed with a poor typewriter ribbon or if the university sent us an inferior photocopy.

Reproduction in full or in part of this microform is governed by the Canadian Copyright Act, R.S.C. 1970, c. C-30, and subsequent amendments.

AVIS

La qualité de cette microforme dépend grandement de la qualité de la thèse soumise au microfilmage. Nous avons tout fait pour assurer une qualité supérieure de reproduction.

S'il manque des pages, veuillez communiquer avec l'université qui a conféré le grade.

La qualité d'impression de certaines pages peut laisser à désirer, surtout si les pages originales ont été dactylographiées à l'aide d'un ruban usé ou si l'université nous a fait parvenir une photocopie de qualité inférieure.

La reproduction, même partielle, de cette microforme est soumise à la Loi canadienne sur le droit d'auteur, SRC 1970, c. C-30, et ses amendements subséquents.

NL-339 (r. 88/04) c

Canada

UNIVERSITY OF ALBERTA

High accuracy modeling of the effect of interface recombination on the quantum efficiency of silicon photodiodes

BY

Jon Geist

A thesis submitted to the Faculty of Graduate Studies and Research in partial fulfillment of the requirements for the degree of Doctor of Philosophy

Department of Electrical Engineering

Edmonton, Alberta

Spring 1992

National Library of Canada
Bibliothèque nationale du Canada

Canadian Theses Service
Service des thèses canadiennes

Ottawa, Canada
K1A 0N4

The author has granted an irrevocable non-exclusive licence allowing the National Library of Canada to reproduce, loan, distribute or sell copies of his/her thesis by any means and in any form or format, making this thesis available to interested persons.

L'auteur a accordé une licence irrévocable et non exclusive permettant à la Bibliothèque nationale du Canada de reproduire, prêter, distribuer ou vendre des copies de sa thèse de quelque manière et sous quelque forme que ce soit pour mettre des exemplaires de cette thèse à la disposition des personnes intéressées.

The author retains ownership of the copyright in his/her thesis. Neither the thesis nor substantial extracts from it may be printed or otherwise reproduced without his/her permission.

L'auteur conserve la propriété du droit d'auteur qui protège sa thèse. Ni la thèse ni des extraits substantiels de celle-ci ne doivent être imprimés ou autrement reproduits sans son autorisation.

ISBN 0-315-73102-8

Canada

UNIVERSITY OF ALBERTA

RELEASE FORM

NAME OF AUTHOR: Jon Geist

TITLE OF THESIS: High accuracy modeling of the effect of interface recombination on the quantum efficiency of silicon photodiodes

DEGREE: Doctor of Philosophy

YEAR THIS DEGREE GRANTED: 1992

Permission is hereby granted to the University of Alberta Library to reproduce single copies of this thesis and to lend or sell such copies for private, scholarly or scientific research purposes only.

The author reserves all other publication and other rights in association with the copyright in the thesis, and except as hereinbefore provided neither the thesis nor any substantial portion thereof may be printed or otherwise reproduced in any material form whatever without the author's prior written permission.

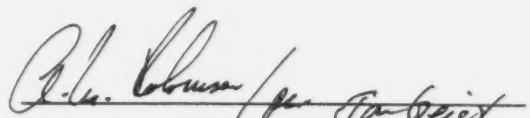

4008 Fulford Street

Olney, MD 20832

USA

Date: 92/03/25

UNIVERSITY OF ALBERTA

FACULTY OF GRADUATE STUDIES AND RESEARCH

The undersigned certify that they have read, and recommend to the Faculty of Graduate Studies and Research for acceptance, a thesis entitled HIGH ACCURACY MODELING OF THE EFFECT OF INTERFACE RECOMBINATION ON THE QUANTUM EFFICIENCY OF SILICON PHOTODIODES submitted by Jon Geist in partial fulfillment of the requirements for the degree of Doctor of Philosophy.

Dr. C.R. James (Co-supervisor)

Dr. A.M. Robinson (Co-supervisor)

Dr. M. J. Brett

Dr. R. P. W. Lawson

Dr. F. L. Weichman

Dr. R. W. Boyd

Date: 4 March, 1992

This Thesis is dedicated to Cathie Quinn Geist.

ABSTRACT

The importance of high accuracy modeling of silicon photodiodes for applications in radiometry is discussed as the motivation for the work reported in this thesis. Deficiencies in the existing absorption coefficient data, and the ability to test the accuracy of numerical simulations of photodiode quantum efficiency are identified. These deficiencies are overcome as follows:

High-resolution, high precision absorption coefficient measurements are carried out over a limited spectral region with dye-laser radiation to demonstrate that the absorption coefficient is locally smooth. A high accuracy absorption coefficient measurement is carried out with 633 nm HeNe radiation to verify the accuracy of Weakliem and Redfield's absorption coefficient data. An integral transform of the photodiode front-region majority carrier concentration is derived to test the consistency of the former quantity with the internal quantum efficiency when both of these quantities are calculated by a numerical solution of the carrier transport equations for a semiconductor. A high-accuracy analytic approximation to the charge accumulation of the equilibrium majority carrier concentration is derived to test the accuracy of this quantity when calculated by a numerical solution of the carrier transport equations.

A suite of programs is developed to support the use of a commercial semiconductor-device modeling program, which is optimized for modeling solar cells, for high-accuracy modeling of photodiodes. These are used to simulate oxide-bias self-calibration experiments of interest to radiometry, and uncertainties in the results of the simulations are derived using the work carried out on the absorption coefficient of silicon and on testing the accuracy of numerical solutions of the carrier transport equations for semiconductors. The results of the simulations are compared with experimental measurements and found to agree within the combined uncertainty of the experiments and the simulations.

A new, more accurate data reduction technique for oxide-bias self-calibration experiments is an important result of the work reported here. Another is a calculation that shows that the internal quantum efficiency of one type of silicon photodiode is equal to 0.9997 ± 0.0003 between 440 and 460 nm. A third consists of two formulae that can be used to interpolate the internal quantum efficiency spectra of another type of silicon photodiode over the 440 nm to 860 nm spectral region from one measurement at each end of the region without loss of accuracy.

ACKNOWLEDGMENTS

The author wishes to thank 1) his thesis advisors, Drs. A. M. Robinson and C. R. James, for support and guidance during this work, and for being flexible enough to provide this support and guidance while the author was carrying out the majority of his research at the National Institute of Standards and Technology (NIST) in Gaithersburg, MD, USA, 2) the Faculty of Graduate Studies and Research for approving this alternate plan for meeting the residency requirements of the University of Alberta that allowed him to carry out his research at NIST, since this research would not have been possible under any other arrangement, and 3) Dr. D. L. Seiler and Mr. F. F. Oettinger, the Group Leader and Division Chief, respectively, during the major part of the research period, for allowing him to carry out this research as part of his official duties and for providing other forms of support. Special thanks also go to Drs. Henry Baltes and H. L. Bennett, the thesis advisor and Group Leader, respectively, during the planning and early stages of the research, for making the arrangements that allowed the research to be carried out at NIST.

The author also wishes to thank the various colleagues who helped him with the different aspects of the research reported in the different chapters of this thesis. Some are acknowledged on the first page of each chapter, where the publication resulting from our collaboration is mentioned. The rest are acknowledged below in an excerpt from one or more of those publications, keyed to the appropriate chapter of this thesis. Special thanks also go to Drs. M. I. Bell and J. R. Lowney for constantly stimulating discussions on various aspects of the thesis topic.

With respect to Chapter 3, the author wishes to thank Mr. J. M. Thomas for preparing the silicon wafer, Mr. D. H. Monk for machining the mounting jig and box, Dr. A. R. Schaefer for instructions in how to use the dye-laser based characterization facility, Dr. M. C. Croarkin for calculating and interpreting the F statistics, Dr. R. S. Turgel for suggesting that Dr. Croarkin could assist in the data analysis, and Dr. C. L. Cromer for suggesting the form of Fig. 3.3.

With respect to Chapter 4, the author would like to acknowledge the careful skill and craftsmanship of Mr. Robert Larsen of SAIC in production of the etched sample.

With respect to Chapter 6, the author wishes to acknowledge the contribution of Mr. Eli Liang to the early work on this topic.

TABLE OF CONTENTS

CHAPTER	PAGE
1. INTRODUCTION	1
1.1 SILICON PHOTODIODE SELF-CALIBRATION	3
1.2 PHOTODIODE MODELS	6
1.3 ORGANIZATION OF THESIS	11
REFERENCES	14
2. SILICON PHOTODIODE SELF-CALIBRATION	18
2.1 THE CLASSICAL SELF-CALIBRATION PROCEDURE	18
2.2 APPLICATION AND VALIDATION	25
2.3 THE QUEST FOR HIGHER ACCURACY	26
REFERENCES	35
3. SHAPE OF THE SILICON ABSORPTION COEFFICIENT SPECTRUM	39
3.1 PHYSICAL BASIS	40
3.2 EXPERIMENTAL PROCEDURE	42
3.3 RESULTS	45
3.4 CONCLUSION	51
REFERENCES	61
4. ACCURATE VALUE FOR THE 633 nm ABSORPTION COEFFICIENT	62
4.1 SILICON SAMPLE	65
4.2 EXPERIMENTAL MEASUREMENTS	65
4.3 DATA REDUCTION AND UNCERTAINTY ANALYSIS	75
REFERENCES	95
5. ANALYTIC REPRESENTATION OF THE ABSORPTION COEFFICIENT	97
5.1 PREVIOUS WORK	97
5.2 NEW EQUATION	98
5.3 QUALITY OF FIT TO WR DATA	99
5.4 COMPARISON WITH OTHER DATA	100

5.5 CONCLUSION 102

REFERENCES 108

6. TESTING THE ACCURACY OF QUANTUM EFFICIENCY CALCULATIONS 109

6.1 ITERATIVE NUMERICAL SOLUTIONS WITH PC-1D 113

6.2 NEW EXPRESSION FOR PHOTOCURRENT 116

6.3 ACCURACY OF THE APPROXIMATION 130

6.4 CONCLUSION 137

REFERENCES 145

7. TESTING THE ACCURACY OF EQUILIBRIUM CARRIER CONCENTRATIONS 147

7.1 DIFFERENTIAL EQUATIONS FOR CARRIER CONCENTRATIONS 149

7.2 SOLUTIONS 151

7.3 BOUNDARY VALUES 155

7.4 APPLICATIONS 157

7.5 CONCLUSION 159

REFERENCES 168

8. HIGH-ACCURACY MODELING OF SILICON PHOTODIODES WITH PC-1D 170

8.1 DESCRIPTION OF PC-1D 171

8.2 THE PHOTODIODE MODELING SHELL PROGRAMS 178

8.3 CONCLUSION 183

REFERENCES 191

9. MODELING OXIDE BIAS SELF-CALIBRATION EXPERIMENTS 193

9.1 EG&G UV444B PHOTODIODE 195

9.2 HAMAMATSU 1337 PHOTODIODE 198

9.3 UDT UV100 PHOTODIODE 201

9.4 CONCLUSION 205

REFERENCES 220

10. INTERPOLATION OF QUANTUM EFFICIENCY CALIBRATIONS 222

10.1 ERRORS ASSOCIATED WITH THE QUANTUM-DEFICIENCY APPROXIMATIONS 223

10.2 ERRORS ASSOCIATED WITH THE QUANTUM-DEFICIENCY CALCULATIONS 229

10.3 COMPARISON WITH EXPERIMENT 236

10.4 CONCLUSIONS 240

REFERENCES 261

11. CONCLUSIONS 263

11.1 SILICON ABSORPTION COEFFICIENT 263

11.2 FORMULAE FOR UNCERTAINTY ANALYSES 264

11.3 HIGH ACCURACY PHOTODIODE SIMULATIONS 265

11.5 SUMMARY OF CONTRIBUTION 267

REFERENCES 268

APPENDIX I. A listing of the program MAKE_PRM.PAS 269

APPENDIX II. A listing of the program READ_PDF.PAS 279

LIST OF TABLES

TABLE

2.1 Summary of intralaboratory comparisons of self-calibration 30

3.1 Non-linear, least squares parameters for different models of the shape of silicon absorption coefficient near 1.6 eV 55

3.2 F statistics for the different models 56

4.1 Transmittance measured at 9 points on silicon sample at 633 nm 81

4.2 Sample thickness measured at 64 points on same sample 82

4.3 Weights used to average thickness data 83

4.4 Average thickness at 9 points on silicon sample 84

4.5 Absorption coefficient calculated at 9 points on silicon sample 85

4.6 Sources of error and associated uncertainty estimates 86

5.1 Parameters used to represent absorption coefficient in visible 103

6.1 Nominal front-region parameters for Hamamatsu 1337 photodiode 139

7.1 Parameters for modeling equilibrium carrier concentration 161

7.2 Comparison of calculated electron concentrations 162

9.1 Comparison of simulated and experimental oxide bias results 207

10.1 Recombination related parameters for 1337 photodiode 241

10.2 Parameters for extrapolating 1337 quantum deficiency 242

10.3 Measured 1337 quantum deficiencies at 441 and 633 nm 243

10.4 Measured 1337 oxide and quantum deficiency data 244

10.5 Comparison of predicted and measured quantum deficiencies 245

10.6 Comparison of predicted and measured quantum deficiencies 246

10.7 Comparison of predicted and measured quantum deficiencies 247

LIST OF FIGURES

FIGURE

2.1 Schematic cross section of oxide and reverse bias experiments 31

2.2 Typical result of oxide bias at short wavelengths 32

2.3 Typical result of reverse bias at long wavelengths 33

2.4 Summary of 1985 interlaboratory comparisons of self-calibration 34

3.1 Apparatus used to measure absorption coefficient near 1.6 eV 57

3.2 Housing for sample and photodiode 58

3.3 High-resolution silicon absorption coefficient data at 1.6 eV 59

3.4 Residuals between models and experimental data 60

4.1 Apparatus for measuring transmittance and reflectance at 633 nm 87

4.2 Scattermeter used in reflectance and transmittance measurements 88

4.3 Illustration of use of scattermeter 89

4.4 Location of roughness measurements on sample 90

4.5 Location of thickness and transmittance measurements on sample 91

4.6 Relation between true and measured thickness due to compression 92

4.7 Illustration of weighting of thickness data 93

4.8 Comparison of measured absorption coefficient with earlier data 94

5.1 Comparison of fit with WR data from 1.05 to 2.7 eV 104

5.2 Residuals of fits to WR data 105

5.3 Comparison of experimental data near silicon band edge 106

5.4 Comparison of fit with Philipp's data 107

6.1 Equilibrium electron and hole concentrations in photodiode 140

6.2 Carrier mobilities as a function of depth in photodiode 141

6.3 Comparison of surface and Auger recombination 142

6.4 Partition of photodiode into regions 143

6.5 Comparison of calculated quantum-deficiency spectra 144

7.1 Comparison of calculated electron and hole concentrations 163

7.2 Function used in analytic description of carrier accumulation 164
7.3 Relative errors associated with use of previous function 165
7.4 Function used in analytic description of carrier depletion 166
7.5 Differences between calculated carrier concentrations 167
8.1 Opening menu of PC-1D 184
8.2 Ratio of different absorption coefficient data 185
8.3 Experimental and calculated reverse-bias self-calibration data 186
8.4 Experimental and calculated reverse-bias self-calibration data 187
8.5 Listing of MSDOS batch file RUN-PC1D.BAT 188
8.6 A sample screen produced by the program MAKE-PRM.EXE 189
8.7 Total calculated photocurrent as a function of position 207
9.1 Front region doping concentration in a UV444B photodiode 208
9.2 Measured and simulated oxide bias data for a UV444B photodiode 209
9.3 Residuals of fit to oxide bias data 210
9.4 Residuals of fit to oxide bias data 211
9.5 Residuals of fit to oxide bias data 212
9.6 Front region doping concentrations in 1337 photodiodes 213
9.7 Measured and simulated oxide bias data for 1337 photodiodes 214
9.8 Simulated quantum-deficiency spectra for 1337 photodiodes 215
9.9 Measured and simulated oxide bias data for a UV100 photodiode 216
9.10 Simulated quantum-deficiency spectra for UV100 photodiodes 217
9.11 Simulated quantum-deficiency spectra for UV100 photodiodes 218
9.12 Simulated quantum-deficiency spectra for UV100 photodiodes 219
10.1 Front- and rear-region quantum-deficiency spectra 248
10.2 Comparison of front-region quantum-deficiency spectra 249
10.3 Limiting cases of 1337 front-region doping profiles 250
10.4 Differences between quantum deficiency spectra 251
10.5 Band-to-band recombination lifetime calculated by PC-1D 252
10.6 Comparison of rear-region quantum-deficiency spectra 253

10.7 Differences between quantum deficiency spectra 254

10.8 Comparison $\hat{M}_0(x)$, $n_{ie}(x)$, $\hat{\mu}(x)$, and $\exp(-\alpha(400nm)\ x)$ 255

10.9 Differences between quantum deficiency spectra 256

10.10 Differences between quantum deficiency spectra 257

10.11 Quadrature sum of differences between quantum deficiencies 258

10.12 Quadrature sum of differences between quantum deficiencies 259

10.13 Comparison of predicted and measured quantum deficiencies 260

1. INTRODUCTION

Since its invention in 1954, the planar silicon photodiode[1] has become the most widely used device for solar energy conversion in both terrestrial and space applications, and the most widely used device for the detection and measurement of optical radiation in the visible and near visible spectral regions. The fabrication of photodiodes is the largest application of planar silicon technology other than the fabrication of integrated circuits.

The planar silicon photodiode is also worthy of consideration in connection with the recent growth of interest in integrated sensors, since silicon photodiodes are the prototypical integrated sensor. Silicon photodiodes were the first sensors to be fabricated in planar technologies, and they played an important role in the development of these technologies. For instance, rectifiers[2] that could be used as photodiode solar cells[1] were the first devices fabricated by the diffusion of boron into n-type silicon wafers.[3] Even though they were designed as rectifiers without any attempt at optimization for solar conversion, these solar cells were the most efficient ever reported up to that time.

Because the existing germanium photodiode technology was transferred to silicon as soon as good quality silicon became available (See Ref. 4 for review), it is difficult to identify the first application of silicon planar technology to the fabrication of photodiodes for the

---

A portion of this chapter has been published: J. Geist and A. Russell Schaefer, Planar Silicon Photosensors: An overview, Proc. Third Int. Forum ASIC and Transd. Tech. (ASICT' 90, May 20-23, 1990, Banff, Canada, University of Alberta, Edmonton), pp. 32-38 (1990).

measurement and detection of optical radiation. The devices described by Madden and Gibson[5] would seem to qualify even though they were intended to measure high energy particles. Also, photodiode arrays developed for use in vidicons appear to be the first sensors that were fabricated with planar silicon technology to have more than one sensor on a chip.[6]

There are three different ways to improve the level of sensor integration obtainable with planar silicon technology. These are the integration of a number of sensors on a single chip, the integration of both sensing and signal processing functions on a single chip, and the integration of separate on-chip functions into a single structure, rather than implementing the separate functions in isolated devices communicating through metal interconnects. The CCD imaging array was the first integrated sensor to embody all of these aspects on a single chip. In fact, imaging was anticipated as an important potential application in the original proposal for the CCD array,[7] and demonstrated with one of the first CCD devices, an 8-bit shift register.[8]

Planar silicon photosensors continue to be a rich area of sensor research and development. From the point of view of integrated sensors, photosensor research can be divided into five areas. The first three are the traditional areas of photosensor research: 1) the accuracy with which the sensor output can be related to the sensor input, 2) the minimum optical signal that can be detected, and 3) the speed with which the optical signal is transduced into an electrical signal for further processing. The last two areas are specific to integrated sensors: 4) the level of integration as measured by the number of photosensors on a chip, and 5) the level of integration as measured by

the complexity of the on-chip processing of the photosensor signal before leaving the chip.

This thesis is a contribution to the first area described above. The goal here is to develop a high-accuracy silicon-photodiode model, and to demonstrate its suitability for supporting the use of silicon photodiodes in applications requiring the smallest errors and the estimation of reliable uncertainties to associate with these errors.

1.1 SILICON PHOTODIODE SELF-CALIBRATION

During the last fifteen years, the great strides made in silicon photodiode fabrication and characterization have resulted in similar improvements in the accuracy and precision available from silicon photodiodes. During the first half of this period, some high-quality silicon photodiodes were capable of being used at a level of accuracy and precision that exceeded that available from the radiometric standards and techniques in existence at that time.[9] As a result, new techniques based on amplitude-stabilized lasers and self-calibration experiments were developed, as was a new generation of conventional radiometric instrumentation and techniques.[10]

Silicon photodiode self-calibration, which is reviewed in chapter 2 and in Ref. 10, refers to the process of determining a photodiode's photon-to-electron transduction efficiency directly from the diode's electro-optical characteristics without reference to any radiometric standards. Consequently, the self-calibrated silicon photodiode can itself serve as a primary radiometric standard.

Optical radiation detectors that can serve as primary radiometric

standards are called absolute detectors or absolute radiometers.[11] Until the advent of silicon self-calibration, all absolute detectors were thermal detectors, most having an electrical heater built into their radiation receivers. Thus, it is appropriate to refer to high quality silicon photodiodes that can be self-calibrated as absolute silicon photodiodes.

Silicon self-calibration is more convenient than a conventional radiometric calibration for two reasons. The first is that most of the equipment needed for self-calibration is already familiar to people with a technical background. This is not the case with many conventional radiometric instruments, such as blackbody simulators, standard lamps, and radiation thermopiles. The second reason is that there is no need to become familiar with the nomenclature, standards, and techniques of traditional radiometry. This is important because traditional radiometry is very arcane. Indeed, it has been asserted that RADIOMETRY is an acronym for Revulsive, Archaic, Diabolical, Invidious, Odious, Mystifying, Exotic Terminology Regenerating Yawns,[12,13] and this characteristic has limited its use in many potential applications.

Not only is it more convenient to self-calibrate a silicon photodiode than to resort to a conventional radiometric calibration, but it is also more accurate. It was almost two years after the introduction of self-calibration that radiometric accuracy superior to that achieved with self-calibrated photodiodes was demonstrated, and the instrument achieving it was not a conventional absolute radiometer, but a new type requiring liquid helium for its operation.[14] Conventional approaches to radiometry have yet to demonstrate the accuracy obtained

with self-calibration.[15,16]

The accuracy achieved with self-calibration demonstrates its high level of development as an experimental technique. Yet its power and scope are severely limited by the fact that a comprehensive, high accuracy model of an absolute silicon photodiode has never been developed.

The original idea to use silicon photodiodes as absolute radiometric standards was based on the realization that the crudest of models would support an accuracy in the red end of the visible spectrum that was outstanding for that time,[17,18] and self-calibration retained these crude models throughout its development. As a result, self-calibration is not based on a comprehensive theory or model of an absolute silicon photodiode, but relies instead upon a number of isolated theoretical results and models. Moreover, many of these models are qualitative rather than quantitative.

Even though they do not allow a rigorous uncertainty to be estimated for the final self-calibration result, the existing models have generally proven satisfactory for supporting self-calibration in all but the most demanding applications.[10] However, they do limit the accuracy of the extrapolation of the results of a calibration (self- or otherwise) at one wavelength to another wavelength. This is a problem because the highest-accuracy liquid-helium absolute detectors that have been developed[19,20] since self-calibration was introduced can only be used with laser radiation. The simplest way to transfer this accuracy to non-laser applications would be to calibrate a radiometer incorporating three silicon photodiodes in a multiple reflection

configuration[19] at a few laser lines, then to interpolate the calibrations over the visible and near infrared spectrum. It has already been demonstrated that there is a very favorable propagation of error associated with the extrapolation of the quantum efficiency of a silicon photodiode from a spectral region of relatively high loss to a region of lower loss.[17] However, the improvement in accuracy can only be quantified at the level of accuracy of the model used for the extrapolation.

1.2 PHOTODIODE MODELS

Existing semiconductor device models, including those for solar cells, will not by themselves serve as high accuracy photodiode models. These models are designed to cover a very large range of behavior rather than to describe as accurately as possible the short circuit quantum efficiency of a photodiode. On the other hand, it is the short circuit quantum efficiency and the accuracy with which it can be quantified that determine the accuracy available from a photodiode. In fact, the uncertainties incurred with semiconductor device models are not quantified during their development, nor from an analysis of the data that is built into the model, but during their use, and by comparison with the measured characteristics of the devices being modeled.

1.2.1 EXTINCTION COEFFICIENT SPECTRUM

A comprehensive model of an absolute photodiode must describe the electro-optical properties of the photodiode. The theory needed to calculate the distribution with which carriers are photogenerated in a photodiode is well developed.[22] It is essentially the same theory that is used to calculate the transmittance of interference filters,

namely the theory of the reflection, transmission and absorption of electromagnetic radiation through multiple layers having different (complex) indexes of refraction. The fraction of the incident radiation that is reflected from the photodiode depends on both the real and imaginary parts of the index of refraction of silicon, but the relative distribution with which the carriers are photogenerated within the photodiode depends only upon the imaginary part. The latter is called the extinction coefficient.

A number of different spectra of the extinction coefficient have been published, and there are surprisingly large differences among them. Even the differences in the extinction coefficient spectra that have been selected for inclusions in handbooks,[23,24] differ enough to cause intolerably large differences in high-accuracy modeling of silicon photodiodes. Therefore, three chapters of this thesis are devoted to determining what extinction coefficient spectrum should be used, and the uncertainty associated with it.

1.2.2 SEMICONDUCTOR DEVICE MODELS

It is not possible to review the great number of models describing the carrier transport in photodiodes and solar cells that have been developed over the years. They span the spectrum from simple, one-dimensional models having completely analytic solutions in closed form to two dimensional, finite-difference and finite-element models in which the drift-diffusion equations[25] are solved by iterating to self-consistency. But even the latter models are no more accurate than the physics that they incorporate. For instance, the drift-diffusion equations are approximations to the more accurate Boltzmann transport equations, which, in turn, are approximations to averages over the

results of quantum mechanical calculations.[25]

1.2.2.1 REPRESENTATIVE ANALYTIC MODELS

Hovel[26] has developed a solar cell model that is representative of one end of the spectrum of models. It consists of a single, closed-form, analytic expression for the short-circuit photocurrent from a pn-junction-diode solar cell irradiated by monochromatic radiation. In order to derive this expression Hovel was forced to make a number of simplifying assumptions. For instance, he assumed that the diode consisted of three regions, that each region was uniformly doped, and that the electronic transport properties were also uniform throughout each region. Pointing out that the model applied only to the case of low injection of carriers across the junction, he considered only the transport of the photogenerated excess carriers under the influence of the equilibrium electric field that is built into the diode, and used the depletion approximation to describe the latter.

The very nature of the approximations that Hovel used in order to obtain analytic solutions forced him to neglect a number of physical effects that are known to be important at high doping concentrations. These include Fermi-Dirac statistics,[27] the concentration dependence of the minority carrier mobility,[28] and band-gap narrowing.[29] He also was forced to exclude hot carrier[30] and quantum[31] effects that might be important in describing the competition between the collection of the photogenerated carriers by the junction and their recombination at the oxide-silicon interface.

With the inclusion of non-essential simplifications, Hovel's model has been proven very useful in the analysis and interpretation of the

results of silicon self-calibration experiments.[17] In fact, Ref. [17] demonstrates that very different models can produce virtually identical internal quantum efficiency curves in the visible spectral region, but that the values of the same physically meaningful parameters will be quite different for the different models. This is a qualitative argument for a favorable propagation of error from regions of higher recombination loss to regions of lower recombination loss. However, since it is not possible to determine a quantitative error to associate with Hovel's simplifying assumptions, an uncertainty analysis can not be carried out.

Some progress on a generalized analytic photodiode model has been reported by Verdebout.[32] His model includes only one recombination mechanism, that associated with the oxide-silicon interface. This is known to be the major front region recombination mechanism affecting high quality silicon photodiodes.[33] Verdebout expresses the short circuit quantum efficiency in terms of integral transforms involving the equilibrium field and the transmittance of the incident radiation through the diode volume. Like Hovel's model, Verdebout's is very restricted in the physical effects that it can consider, but it has the advantage that it accounts for the actual front region doping distribution.

1.2.2.2 REPRESENTATIVE NUMERICAL MODELS

A simple numerical model of excess carrier transport has been used in an attempt to differentiate between surface and volume recombination in one type of p^+nn^+ silicon photodiode.[33] While this model could have been generalized to encompass a wider variety of physical effects, only those that were also handled by Verdebout's later

generalized analytic model were actually incorporated. Still later, Verdebout[34] used a similar numerical model, but included a carrier mobility that depended upon carrier concentration, and a simplified model of hot-carrier transport, in an attempt to demonstrate the importance of this type of transport to an accurate description of photodiode quantum efficiency in inversion layer photodiodes.

A much more comprehensive one-dimensional numerical model called PC-1D has been developed by Basore *et al.*[35] to run on IBM PC-compatible computers equipped with numerical co-processors. Even though this model is one dimensional and runs on personal computers, it is a good representative of the finite-difference and finite-element models. It was inspired by sophisticated models developed for large computers at Purdue University,[36] and is based on those models in many ways. A very wide range of physical phenomena has been incorporated into PC-1D, and this program is an excellent candidate for a high-accuracy photodiode model.

Two different types of error can be distinguished in the use of PC-1D for high-accuracy photodiode modeling: the error associated with the numerical algorithms used by PC-1D, and the error associated with the physical models used by PC-1D.

Two chapters of this thesis are devoted to quantifying the error associated with numerical algorithms used by PC-1D by comparison with the analytic model and the integral transform model that were specially developed for the purpose of testing the accuracy of numerical solutions of the drift-diffusion equations. One of the models is a generalization of the models of Hovel and Verdebout. While this model

lacks the sophistication of the physical models that are used by PC-1D, it handles photodiode models just complex enough to be very similar to those that PC-1D would encounter in high-accuracy photodiode modeling. It is a virtue of PC-1D that almost all of its models can be modified by changing user-accessible parameters, or replaced by data contained in user-provided files. Thus the sophisticated physical models of PC-1D can be replaced by the same simplified physical models used by the generalized Hovel model, and simulations of the same photodiode can be compared. Since the numerical accuracy of the generalized Hovel model is not in question, the numerical accuracy of PC-1D can be tested in this way.

The ability to modify or replace almost all of the physical models that are used by PC-1D with alternate models is also useful in studying the errors associated with these models. The results of simulating the same photodiode structure with different models of a particular physical phenomena establish practical uncertainties to associate with the physical errors inherent with the models. The integral transform model serves to identify the relatively few physical models among the large number used by PC-1D that need to be investigated in this way.

1.3 ORGANIZATION OF THESIS

The remaining chapters of this thesis are organized as follows: Chapter 2 presents a detailed review of silicon self-calibration and other high-accuracy applications of silicon photodiodes, including the demand for higher accuracy and more rigorous uncertainty analyses. Chapters 3, 4 and 5 describe investigations culminating in a formula that represents the best present knowledge of the silicon absorption

coefficient spectrum from 440 nm to 900 nm. Chapters 6 and 7 describe investigations of the numerical accuracy of PC-1D in calculating equilibrium carrier concentrations and steady-state photocurrents. Chapter 8 considers the suitability of PC-1D for high-accuracy photodiode modeling, and describes programs written specifically to support its use in this application. Chapter 9 describes the analysis of oxide-bias data for three different types of photodiodes with the help of PC-1D and the support programs described in Chapter 8. Nominal values for the charge stored in the oxide and the surface recombination velocity at the oxide-silicon interface for two of the photodiode types are derived, and a nominal internal quantum efficiency of 0.9997 ±0.0003 from 440 nm to 460 nm for one of the photodiode types is derived. Chapter 10 derives two functions: one for extrapolating the internal quantum efficiency of one type of photodiode from a short wavelength greater than 440 nm to longer wavelengths, and another for extrapolating the internal quantum efficiency from a long wavelength less than 960 nm to shorter wavelengths for the same type of photodiode. Together these functions can be used to interpolate the internal quantum efficiency of this type of photodiode over the 440 nm to 860 nm spectral region with an uncertainty of 0.0003. Chapter 11 concludes the thesis by tying together the results of the previous chapters.

The extrapolation formulae derived in Chapter 10, the nominal value for the internal quantum efficiency derived in Chapter 9, the formula for the absorption-coefficient spectrum derived in Chapter 5, and the high-accuracy absorption-coefficient value reported in Chapter 4 all meet recognized needs in the area of high accuracy applications of silicon photodiodes. Other original results, such as the formulae in

Chapter 6 for the carrier concentration in uniformly doped, charge-accumulated material, the integral-transform approximation to the internal quantum efficiency in Chapter 7, the programs described in Chapter 8 to support the use of PC-1D in high-accuracy photodiode modeling, and the demonstration in Chapter 3 that the absorption coefficient spectrum of silicon is a smooth function of wavelength are of less general use, but were essential for obtaining the other more general results. With the exception of the programs, these results are also interesting in their own right as demonstrated by their publication as journal articles.

REFERENCES FOR CHAPTER 1

1. D. M. Chapin, C. S. Fuller, and G. L. Pearson, A new silicon p-n junction photocell for converting solar radiation into electrical power, J. Appl. Phys. **25**, 676-677 (1954).
2. G. L. Pearson and C. S. Fuller, Silicon p-n junction power rectifiers and lightning protectors, Proc. Inst. Radio Engrs. **42**, 760 (1954).
3. C. S. Fuller and J. A. Ditzenberger, Diffusion of boron and phosphorus into silicon, J. Appl. Phys. **25**, 1439-1440 (1954).
4. G. Bertolini and A. Cochi, Semiconductor Detectors, (John Wiley & Sons, NY, 1968).
5. T. C. Madden and W. M. Gibson, Rev. Sci. Inst. **34**, 50-55 (1963).
6. M. H. Crowell, T. M. Buck, E. F. Labuda, J. V. Dalton, and E. J. Walsh, A camera tube with a silicon diode array target, Bell Syst. Tech. J. **46**, 491-495 (1967).
7. W. S. Boyle and G. E. Smith, Charge coupled semiconductor devices, Bell Syst. Tech. J. **49**, 587-593 (1970).
8. M. F. Tompsett, G. F. Amelio, and G. E. Smith, Charge coupled 8-bit shift register, Appl. Phys. Lett. **17**, 111-115 (1970).
9. E. F. Zalewski and J. Geist, silicon photodiode absolute spectral response self-calibration, Appl. Opt. **19**, 1214-1216 (1980).
10. J. Geist, Current status of, and future directions in silicon photodiode self-calibration, SPIE Proc. **1109**, 246-256 (1989).
11. F. Hengstberger, Absolute radiometry: Electrically calibrated thermal detectors of optical radiation, (Academic Press, San Diego, 1989).
12. R. C. Hilborn, Radiometry and the detection of optical radiation (review of book with this title), Am. J. Phys. **52**, 668-669 (1984).
13. C. F. Bohren, Multiple scattering of light and some of its

observable consequences, Am. J. Phys. **55**, 524-533 (1987).

14. T. J. Quinn and J. E. Martin, A radiometric determination of the Stefan-Boltzmann constant and thermodynamic temperature between -40°C and +100°C, Phil. Trans. Roy. Soc. Lond. **A 316**, 85-189 (1985).
15. N. P. Fox and J. E. Martin, The intercomparison of two cryogenic radiometers, Int. Conf. Optical Radiometry, NPL, London, Inst. Phys. Conf. Ser. no. **92**, 31-37 (1988).
16. C. C. Hoyt, P. J. Miller, P. V. Foukal, and E. F. Zalewski, Comparison between a side-viewing cryogenic radiometer and self-calibrated silicon photodiodes, SPIE **1109**, 236-245 (1989).
17. J. Geist and E. F. Zalewski, The quantum yield of silicon in the visible, Appl. Phys. Lett. **35**, 503-506 (1979).
18. J. Geist, E. F. Zalewski and A. R. Schaefer, Spectral response self-calibration and interpolation of silicon photodiodes, Appl. Opt. **19**, 3795-3799 (1980).
19. J. E. Martin, N. P. Fox and P. J. Key, A cryogenic radiometer for absolute radiometric measurements, Metrologia **21**, 147-155 (1985).
20. P. V. Foukal, C. Hoyt, H. Kochling, and P. Miller, Cryogenic absolute radiometers as laboratory irradiance standards, remote sensing detectors, and pyroheliometers, Appl. Opt. **29**, 988-993 (1990).
21. N. P. Fox and J. E. Martin, Comparison of two cryogenic radiometers by determining the absolute spectral responsivity of silicon photodiodes with an uncertainty of 0.02%, Appl. Opt. **29**, 4686-4693 (1990).
22. M. Born and E. Wolf, Principles of Optics, (Pergammon Press, New York, 3rd edition, 1965), pp. 66 and 627.
23. D. F. Edwards, Silicon (Si), in Handbook of Optical Constants, E.

D. Palik, ed., 547 (Academic Press, Orlando, 1985).

24. D. E. Aspnes, Optical functions of intrinsic Si: Table of refractive index, extinction coefficient and absorption coefficient vs energy (0 to 400 eV), in Properties of Silicon, EMIS Datareviews No. 4, 72 (INSPEC, Institute of Electrical Engineers, London, 1988).
25. S. Selberherr, Analysis and simulation of semiconductor devices, (Springer-Verlag, New York, 1984), page 12.
26. H. J. Hovel, Solar Cells, Semiconductors and Semimetals, (Ed. R. K. Willardson and A. C. Beers, Academic Press, New York, 1975), pp. 15-30.
27. S. Selberherr, Analysis and simulation of semiconductor devices, (Springer-Verlag, New York, 1984), pp. 24-27 and references therein.
28. H. S. Bennett, Hole and electron mobilities in heavily doped silicon: comparison of theory and experiment, Solid-State Electron. **26**, 1157-1166 (1983) and references therein.
29. H. S. Bennett and J. R. Lowney, Physics for numerical simulation of silicon and gallium arsenide transistors, Solid-State Electron. **33**, 675-691 (1990), and references therein.
30. G. Baccarani, M. Rudan, R. Guerrieri and P. Ciampolini, Physical models for numerical device simulation, Chapter 4 in Process and device Modeling (ed. W. L. Engl, Elsevire, New York, 1986), pp. 137-139, and references therein.
31. Y. Ohkura, Quantum effects in Si n-MOS inversion layers at high substrate concentration, Solid-State Electron. **33**, 1581-1585 (1990).
32. J. Verdebout, Semiquantitative model for the oxide bias experiment and its application to the study of p^+nn^+ photodiode degradation,

Appl. Opt. **23**, 4339-4344 (1984).

33. J. Geist, Silicon photodiode front region collection efficiency models, J. Appl. Phys. **51**, 3993-3995 (1980).

34. J. Verdebout, Analysis of the oxide-bias experiment on the basis of different models for the internal quantum efficiency of p^+nn^+ photodiode, Advances In Absolute Radiometry, Proc. of an Int. Meeting, 66-69 (Atmospheric and Environmental Research, Inc. Cambridge, MA, June 24-25, 1985).

35. P. A. Basore, D. T. Rover and A. W. Smith, PC-1D version 2: enhanced numerical solar cell modeling, 20th IEEE Photovoltaic Specialists Conference - 1988, pub. # 0160-8371/88/0000-0389 (IEEE, NY, 1988). pp. 389-396.

36. M. S. Lundstrom, R. J. Schwartz and J. L. Gray, Transport equations for the analysis of heavily doped semiconductor devices, Solid-State Electronics **24**, 195-202 (1981).

2. SILICON PHOTODIODE SELF-CALIBRATION

Silicon self-calibration is the name coined for determining the external quantum efficiency of a silicon photodiode from the material and device properties of the diode, rather than by comparison with some radiometric standard.[1] Following its introduction almost eleven years ago, silicon self-calibration has been widely studied, tested and used. The purpose of this Chapter is to review the current status of silicon self-calibration. First, the classical self-calibration procedure is described. Then the applications and validation of the classical procedure are reviewed. Finally, the quest for higher accuracy will be discussed. That quest has led to new approaches to self-calibration that require quantitative photodiode models that can support uncertainty analyses.

2.1 THE CLASSICAL SELF-CALIBRATION PROCEDURE

The quantum efficiency $Q(\lambda)$ at wavelength λ of most silicon photodiodes can be written[2] as

$$Q(\lambda) = A(\lambda)\, Y(\lambda)\, F(\lambda), \qquad (1)$$

where $A(\lambda)$ is the absorptance of the active area of the photodiode for photons of wavelength λ, $Y(\lambda)$ is the quantum yield for electron-hole pair production[3,4] for absorption of photons of wavelength λ, and $F(\lambda)$ is the collection efficiency factor of the diode junction for carriers photogenerated by absorption of photons of wavelength λ.

Assuming that negligible radiation is transmitted to the rear of the

---

A version of this chapter has been published: J. Geist, Current status of, and future directions in silicon photodiode self-calibration, SPIE Proc. 1109, 246-256 (1989).

photodiode, the absorptance can be expressed as

$$A(\lambda) = 1 - \rho(\lambda), \qquad (2)$$

where $\rho(\lambda)$ is the reflectance of the photodiode. Assuming that there is no recombination in the depletion region and no spatial dependence over the active surface of the photodiode, the collection efficiency factor can be expressed as

$$F(\lambda) = 1 - \Delta_f(\lambda) - \Delta_r(\lambda), \qquad (3)$$

where $\Delta_f(\lambda)$ and $\Delta_r(\lambda)$ describe loss mechanisms confined to the front and rear regions of the photodiode, respectively. The front region is that between the front surface of the photodiode and the depletion region; the rear region is that between the depletion region and the rear surface of the photodiode. The assumption that the collection deficiency (one minus the collection efficiency) is zero in the depletion region between the front and rear regions is an excellent approximation for the type of high quality photodiodes used in self-calibration, and self-calibration will only work as well as this assumption is satisfied. The terms $\Delta_f(\lambda)$ and $\Delta_r(\lambda)$ will be called the front-region and rear-region collection deficiency factors in this thesis.

The absorption coefficient of silicon decreases from a maximum of over 100 μm^{-2} at wavelengths less than 350 nm to less than 0.01 μm^{-2} at wavelengths greater than 950 nm. Therefore, the fraction of the radiation absorbed in the front region decreases dramatically and that absorbed in the rear region increases dramatically as the radiation wavelength is increased from 350 to 950 nm. Therefore, $\Delta_f(\lambda)$ also decreases dramatically and $\Delta_r(\lambda)$ increases dramatically with

increasing wavelength λ.

Silicon photodiode self-calibration is based on the assumption that $Y(\lambda)$ is unity over most of the visible spectral region, and that $\rho(\lambda)$, $\Delta_f(\lambda)$ and $\Delta_r(\lambda)$ can be determined from simple relative measurements on some types of photodiodes. A relative measurement is one whose result is a dimensionless ratio, and therefore, does not require calibration against a standard of any type.

For an ideal photodiode $A(\lambda)$ and $F(\lambda)$ are unity, and $\rho(\lambda)$, $\Delta_f(\lambda)$ and $\Delta_r(\lambda)$ are zero. Relative measurements to determine $\rho(\lambda)$, $\Delta_f(\lambda)$, and $\Delta_r(\lambda)$ are called self-calibration experiments or measurements. Such experiments have the advantage that a relative error of some given magnitude in either $\rho(\lambda)$ or $\Delta(\lambda)$ contributes a much smaller relative error to $A(\lambda)$ and $F(\lambda)$ for near ideal diodes because $\rho(\lambda)$ and $\Delta(\lambda)$ are much less than unity for these diodes. The most common self-calibration experiments are reviewed below.

2.1.1 THE OXIDE-BIAS SELF-CALIBRATION EXPERIMENT

The most difficult of the self-calibration experiments is the so-called oxide bias experiment.[1] In this experiment the relative response of a photodiode under constant irradiation is measured as a function of bias voltage applied to the oxide.[5] Under certain conditions this allows determination of $\Delta_f(\lambda)$.[6]

The key ideas of this experiment are shown in Figs. 2.1 and 2.2. Figure 2.1 shows the experimental set up for both the oxide bias experiment and the reverse bias experiment. Figure 2.2 plots a typical curve of the relative increase in photocurrent as a function

of oxide bias. The apparent saturation of response with increasing oxide bias was originally taken as an indication that the recombination of photogenerated carriers at the oxide-silicon interface had been completely eliminated,[1] and the small residual quantum deficiency not accounted for in the oxide bias experiment was attributed to recombination in the volume of the front region.[5,3] The ratio of the photocurrent at zero bias to that at saturation is used in the self-calibration formula[1] to calculate the quantum efficiency at zero bias.

It has been shown that the shoulder in the relative response versus bias curve is associated with the flat-band condition (zero surface potential) at the oxide-silicon interface rather than the onset of saturation of response due to elimination of interface recombination.[7] In fact, the appearance of saturation is an illusion, because a small fraction of the zero-bias interface recombination remains, and is not completely eliminated until the application of bias voltages large enough to cause breakdown of the oxide.[7] Nevertheless, the assumption that the elimination of interface recombination accompanies the saturation of photocurrent with oxide-bias voltage continued to be used in analyzing self-calibration experiments, because no more realistic models were available until the completion of the work reported in this thesis.

Both water electrodes and corona discharge have been used to apply oxide bias. Corona discharge, while satisfactorily employed[8] in a very dry atmosphere, proved unsatisfactory[9,10] in other environments. Since application and removal of a water drop can permanently change the reflectance properties of the front surface of the diode,[8,11] and

since application of bias across the oxide can permanently reduce the internal quantum efficiency of the diode,[12,9] the water drop also has its limitations. Reference 9 describes precautions to minimize the errors caused in self-calibration by these effects, and high accuracies have been achieved.

Studies have been made of the mechanisms causing the degradation of the short wavelength responsivity of silicon photodiodes as a result of oxide bias,[13,7] and as a result of environmental conditions[14,15] such as humidity, temperature and ultraviolet radiation. It is clear from these studies that the best stability of quantum efficiency will be achieved with diodes that are hermetically sealed. This seems to preclude the oxide bias experiment, and generally complicates self-calibration. One resolution of this difficulty is to use photodiodes without windows for self-calibration and to transfer the calibration from these photodiodes to other photodiodes with windows to maintain the calibration over long periods of time. This is the key message of ref. 9, and the same procedure is often used with scales realized with electrical substitution radiometers. However, windows on hermetically sealed photodiodes must be purposely wedged to avoid interference effects if the diodes are to be used with laser radiation. With perfectly parallel windows and highly collimated, highly monochromatic radiation, interference effects can cause the reflectance of the window to vary by as much as 16% as the angle of incidence is varied over a very small range.

The oxide bias experiment is not usually carried out on inversion layer (induced junction) photodiodes because the strong surface field associated with the inversion layer repels most of the photogenerated

minority carriers from the oxide-silicon interface before they can recombine there. The result is that $\Delta_f(\lambda)$ is very close to zero at short wavelengths[16]. Consequently, $\Delta_f(\lambda)$ is assumed to be zero when self-calibrating this type of photodiode, so the oxide-bias experiment is not considered necessary.

2.1.2 THE REVERSE BIAS SELF-CALIBRATION EXPERIMENT

The reverse bias experiment[1] is simpler than the oxide bias experiment. In this experiment the relative response of a photodiode under constant irradiation is measured as a function of reverse bias voltage.[5] Under certain conditions the reverse bias experiment allows the determination of $\Delta_r(\lambda)$ in a silicon photodiode.[17,18]

The key ideas of this experiment are illustrated in Figs. 2.1 and 2.3. Figure 2.1 shows the experimental set up for the reverse bias and oxide bias experiments. Figure 2.3 plots a typical curve of the relative increase in photocurrent as a function of reverse bias. The depletion region grows toward the rear of the photodiode with increasing reverse bias. Therefore, a saturation of the relative increase in the photocurrent with reverse bias, if it can be obtained before the breakdown voltage is reached, is interpreted to mean that only a negligible fraction of the incident radiation penetrates into the rear region of the photodiode where recombination of the photogenerated carriers can take place.

Not only can recombination in the rear region of the photodiode increase $\Delta_r(\lambda)$ from its ideal value of zero, but it can also cause it to vary as a function of photocurrent. Non-linearities and anomalous response times are the result.[18-20] Self-calibration can correct for

these effects provided that a saturation of response with increasing bias can be achieved as illustrated in Figs. 2.2 and 2.3.[17]

2.1.3 THE REFLECTANCE SELF-CALIBRATION EXPERIMENT

Measurement of the diode reflectance is quite simple for collimated laser radiation[21], particularly when it is intensity-stabilized[22]. Laser intensity stabilizers and controllers are available commercially.[23,24] Two schemes for measuring the reflectance of the photodiode with uncollimated radiation have also been described.[25,26] The first of these achieved uncertainties in $1-\rho(\lambda)$ of well under one percent. The second, which attempted to extend the ideas of ref. 21 to uncollimated radiation, did not. Apparently some aspect of the ideal geometry envisioned in ref. 26 was not actually realized in the experimental apparatus.

A device consisting of four inversion layer photodiodes mounted in a multiple reflectance configuration to yield negligible reflectance loss for highly collimated sources of radiation has been developed.[27] This device (UDT QED 100) and a similar device (UDT QED 200) having only three photodiodes, but accommodating larger f-number radiation such as from a monochromator or a standard lamp, are available commercially.[28] There is no need to measure the reflectance of the QED 100 or 200 except in applications requiring uncertainties less than about ± 0.2%. Because they require neither oxide-bias (since $\Delta_f(\lambda)$ is very close to zero) nor reflectance measurements, these devices are particularly convenient in the short wavelength region where $\Delta_r(\lambda)$ is very close to unity. However, they cannot be used without incurring significantly reduced accuracy at the longer wavelengths, because the photocurrent does not saturate with

increasing reverse bias in this spectral region.

2.2 APPLICATION AND VALIDATION OF THE CLASSICAL PROCEDURE

Since 1980, some national laboratories have adopted silicon self-calibration as the basis for their spectral power and/or detector spectral responsivity scales. Others have used it as a convenient means of checking their scales based on the thermal physics of electrical substitution radiometers (ESR's).[29-34] The results of within-laboratory comparisons of silicon self-calibration and conventional ESR's are summarized in Table 2.1.

Seven of eleven national laboratories participating in a 1985 comparison of detector spectral responsivity used self-calibration to realize a scale of this quantity.[35] The remainder used ESR's. Eight of the eleven laboratories agreed in their assessment of radiant power at the helium neon laser wavelength to within a range of ±0.2% as shown in Fig. 2.4. Only one of the laboratories using self-calibration fell outside of this range. Finally, laboratories that derive their scales by calibration against standards obtained from other laboratories have also used self-calibration to verify the calibration.[36]

A number of approaches for using silicon self-calibration as the basis for spectral irradiance measurements have been investigated. An integrating-sphere/interference-filter radiometer was calibrated with an estimated uncertainty of ± 0.25% against a self-calibrated silicon photodiode using amplitude stabilized dye laser radiation as a source.[37] A different type of filter radiometer was constructed from interference filters and a QED 200.[38] The calibration of this

radiometer consisted of the measurement with a ± 0.3% uncertainty of the transmittance of the interference filters in a commercial spectrophotometer whenever the radiometer was disassembled. Finally, the spectral response of monochromator-based radiometers has been calibrated at various laser lines against a self-calibrated photodiode.[39,40] In all of these cases, the estimated uncertainties of the calibrations ranged between ± 0.2% and ± 0.4%, the calibrated radiometer was used to measure the radiation from a standard source, and agreement within the combined uncertainty was achieved. However, it should be noted that some of the uncertainties quoted are estimates of three-standard deviations, and the agreement achieved is not good enough to be consistent with the confidence interval normally associated with three-standard deviations.

The Swiss Federal Office of Metrology used a QED 200 and a broadband photopic filter to realize its standard of luminous intensity.[41] The scale obtained in this way agrees with the world mean value of this quantity to within 0.2%.[42] For comparison, the US scale of this quantity, which was realized by comparison with gold-point blackbody radiation, differed from the world mean by 0.6%.[42]

2.3 THE QUEST FOR HIGHER ACCURACY

Self-calibration was introduced with an uncertainty estimate of 0.05% at 633 nm on the basis of a largely qualitative uncertainty analysis. Since this was much smaller than the uncertainty estimates associated with any other radiometric technique that had been validated in the visible spectral region at that time, it was not possible to test the estimated uncertainty.

While the estimated uncertainty for self-calibration remained much smaller than that claimed for other instruments being used routinely in the visible region, there was little reason to be concerned about the qualitative nature of the uncertainty analysis. In fact, self-calibration was routinely used to validate other less simple approaches that had been developed in various laboratories, as described in the last section. However, as the accuracy of these other techniques was improved, and as the potential accuracy of cryogenic ESR's came to be appreciated, the need for a more reliable uncertainty for self-calibration began to grow.

In fact it was the desire to test the accuracy of self-calibration that lead to the modification of the NPL cryogenic-cavity radiation thermometer[43] for use as an ESR for laser radiation.[44] Once modified, the potential for using this type of radiometer to realize high accuracy scales in the visible spectral region became clear. As was the case during the early days of self-calibration, there is currently no easy way to test the ±0.005% uncertainty for the recently developed NPL cryogenic cavity ESR. A number of problems limit the present level of verification to ±0.02%.[44]

One of the goals of present self-calibration research is to reduce the uncertainty associated with self-calibration to the levels comparable to those demonstrated for cryogenic ESR's. This involves both new self-calibration techniques and a much more quantitative uncertainty analysis.

Fox[30] reported obtaining agreement at the 0.02% level in a preliminary comparison of the classical self-calibration of an EG&G[45] UV444B and

the NPL cryogenic ESR. Hoyt[46] has reported comparable agreement between classically self-calibrated Hamamatsu[47] 1337 photodiodes and a CRI[48] cryogenic ESR. However, in each case the agreement was much better than the uncertainty that could be associated with the intercomparison.

Fox and Martin[44] have used a multiple-reflection radiometer as a transfer standard to intercompare the two NPL cryogenic ESR's at the 0.02% uncertainty level. Presumably, this level of transfer accuracy is available from this device at other wavelengths because both $\Delta_f(\lambda)$ and $\Delta_r(\lambda)$ are small for the 1337 type of photodiode used in this device. However, calibrations at a great number of wavelengths (every 10 nm, for instance) would appear necessary to assure this level of accuracy over the spectral region for which the 1337 is optimized. On the other hand, if a quantitative model of the quantum efficiency of the 1337 photodiode were available to support quantum efficiency interpolation or extrapolation with a sufficiently small uncertainty, then calibration at as few as two wavelengths may suffice.

Hoyt *et al.* have demonstrated the feasibility of extrapolating the quantum efficiency of 1337-type photodiodes from 442 nm to 633 nm.[49] Their work was carried out in connection with an intercomparison of the CRI cryogenic ESR with a new high accuracy self-calibration technique[49] being developed by Zalewski. Zalewski's technique is designed to use the results of high accuracy photodiode modeling as the basis for the extrapolation. For the intercomparison reported in Ref. 49, he used preliminary results obtained in connection with the work reported later in this thesis.

In ref. 49 Zalewski also showed that he could measure the reflectance of a QED 200 radiometer with an uncertainty of ±0.001% at 442 nm, but he was forced to assume that $\Delta_f(442nm) = 0$ for this device. As mentioned previously, he could not assign a reliable uncertainty to that assumption. While qualitative[16] models suggest that there is negligible interface recombination of photogenerated carriers in this type of diode, a quantitative model is needed to determine a value for $\Delta_f(\lambda)$ and an uncertainty estimate to associate with that value. This, of course, is the goal of this thesis.

Table 2.1. Summary of intralaboratory comparisons of self-calibration with electrical substitution radiometers. The first column contains the author reporting the comparison; the second, the wavelengths used in the comparison; the third, the ratio of the radiant power measured by the ESR's to that measured by the self-calibrated photodiodes; the fourth, the number of ESR's used; the fifth, the number of self-calibrated silicon photodiodes used; and the sixth, the reference number in this chapter.

AUTHORS	λ (nm)	ESR/SCP	# ESR	# SCP	Ref.
Zalewski and Geist	633	0.9994	1	2	1
Li Tong-Bao	633	1.0010	5	3	29
Fox	676	1.0000	1	2	30
Boivin and McNeely	476	0.9999	3	2	31
	531	0.9993			
	568	0.9992			
	647	0.9995			
	676	1.0000			
Gardner and Wilkinson	458	1.0003	1	3	32
	488	1.0011			
	514	1.0022			
	633	1.0001			
Faaland and Naiman	633	1.0047	1	1	33
	633	1.0037			

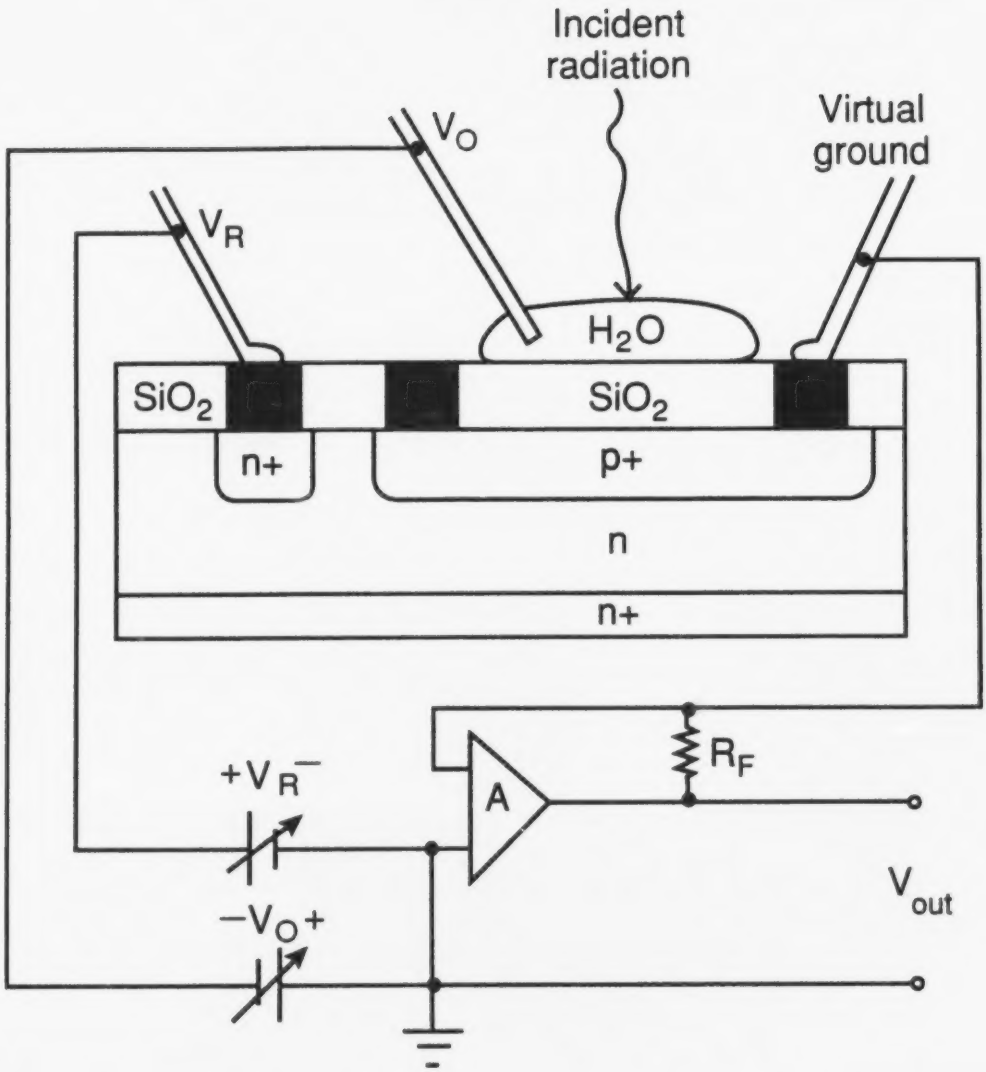

Figure 2.1 Schematic cross-section of a photodiode set up for the oxide bias V_O and reverse bias V_R self-calibration experiments. The drop of water on the oxide serves as a removable, transparent electrode, and the operational amplifier A is connected in the current-to-voltage converting (transimpedence) configuration with the feedback resistor R_F.

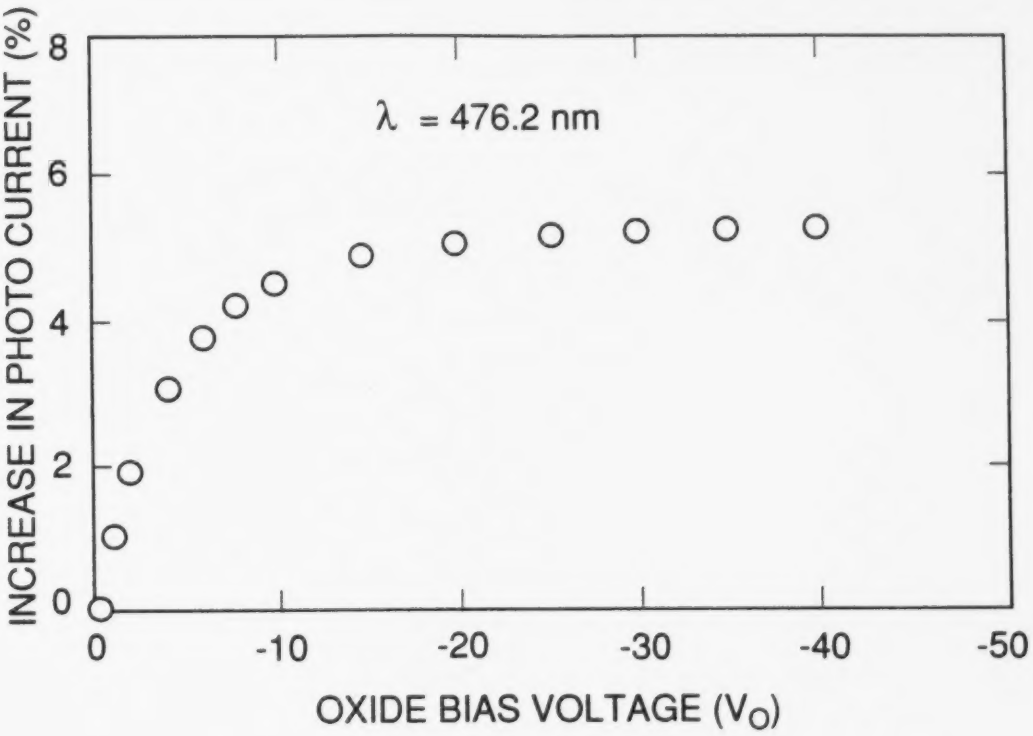

Figure 2.2 Typical result of application of oxide-bias in self-calibration configuration of Fig. 2.1 when p^+n photodiode is irradiated with short wavelength visible radiation.

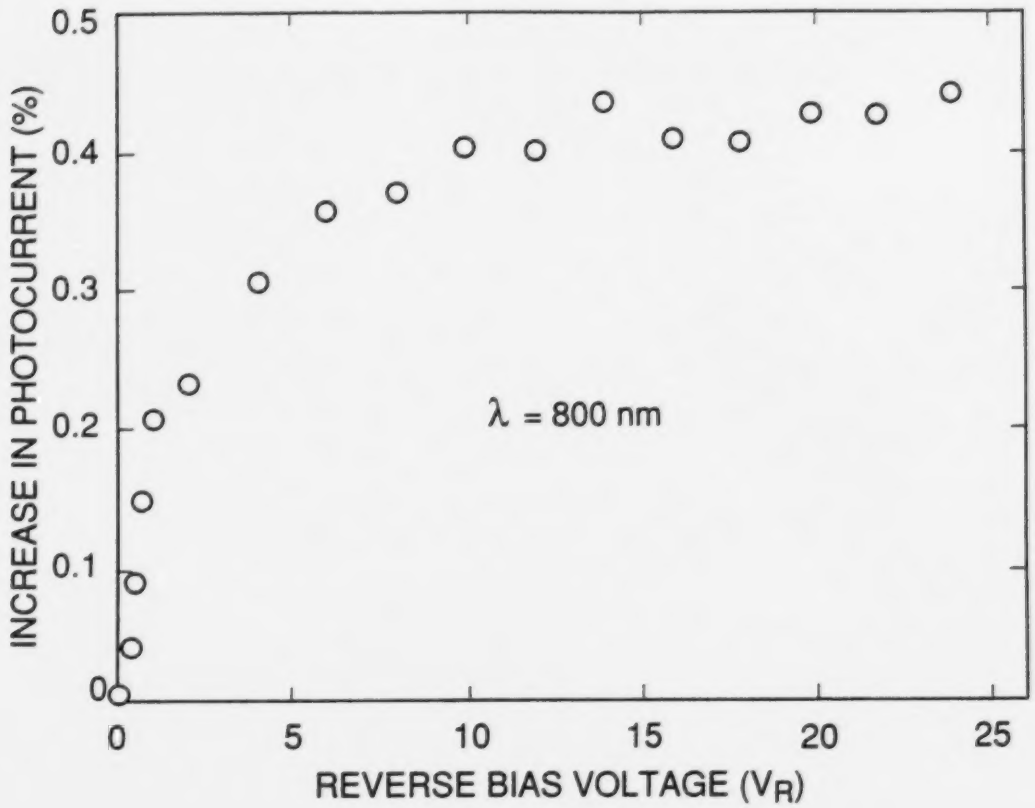

Figure 2.3 Typical result of application of reverse bias in self-calibration configuration of Fig. 2.1 when p+n photodiode is irradiated with long wavelength visible or near infrared radiation.

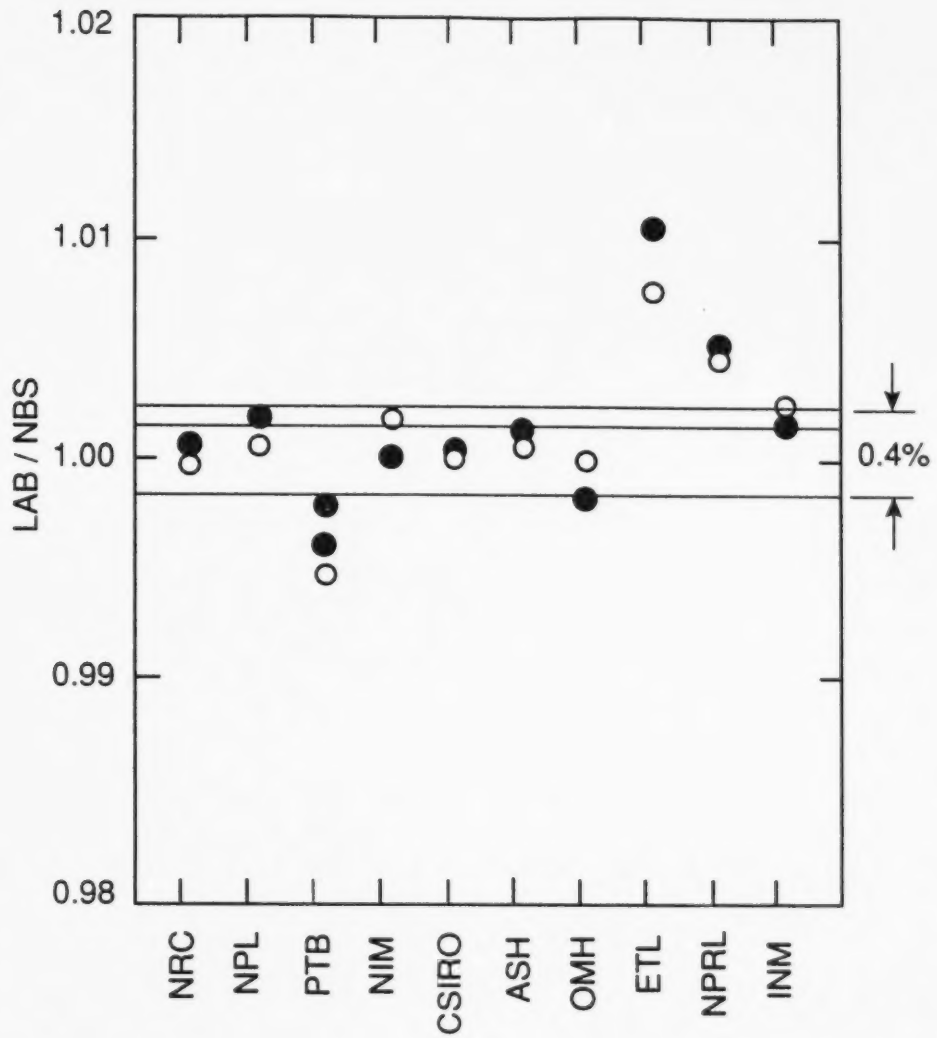

Figure 2.4 Summary of a 1985 interlaboratory comparison of absolute detector calibration capability at 633 nm.[35] The National Research Council (NRC) of Canada, the UK National Physical Laboratory (NPL), the Physikalisch-Technische Bundesanstalt (PTB) of West Germany, and South Africa's National Physical Research Laboratory (NPRL) used ESR's to realize their scale. The US National Bureau of Standards (NBS), the National Institute of Metrology (NIM) of the Peoples Republic of China, Hungary's Office of Metrology (OMH) and Academy of Science (ASH), Japan's Electro-Technical Laboratory (ETL), and the National Institute Metrology (INM) of France used silicon self-calibration. The Commonwealth Scientific and Industrial Research Organization (CSIRO) of Australia used both techniques; the results were identical at the scale of figure.

REFERENCES FOR CHAPTER 2

1. E. F. Zalewski and J. Geist, Silicon detector absolute spectral response self-calibration, Appl. Opt. **19**, 1214-1216 (1980).

2. J. Geist, W. K. Gladden and E. F. Zalewski, Physics of photon-flux measurements with silicon photodiodes, J. Opt. Soc. **72**, 1068-1075 (1982).

3. F. J. Wilkinson, A. J. D. Farmer, and J. Geist, The near ultraviolet quantum yield of silicon, J. Appl. Phys. **54**, 1172-1174 (1983).

4. J. Geist and C. S. Wang, New calculations of the quantum yield of silicon in the near ultraviolet, Phys. Rev. **B27**, 4841-4847 (1983).

5. J. Geist, E. F. Zalewski, and A. R. Schaefer, Spectral response self-calibration and interpolation of silicon photodiodes, Appl. Opt. **22**, 3795-3799 (1980).

6. J. Geist, Silicon photodiode front region collection efficiency models, J. Appl. Phys. **51**, 3993-3995 (1980).

7. J. Verdebout, Semiquantitative model for the oxide bias experiment and its application to the study of p^+nn^+ photodiode degradation, Appl. Opt. **23**, 4339-4344 (1984).

8. J. Geist, A. J. D. Farmer, P. J. Martin, F. J. Wilkinson, and S. J. Collocott, Elimination of interface recombination in oxide passivated silicon p^+n photodiodes by storage of negative charge on the oxide surface, Appl. Opt. **21**, 1130-1135 (1982).

9. P. J. Key, N. P. Fox and M. L. Rastello, Oxide-bias measurements in the silicon photodiode self-calibration technique, Metrologia **21**, 81-87 (1985).

10. A. R. Schaefer, personal communication (1984).

11. A. R. Schaefer, Reflectance and external quantum efficiency change of a silicon photodiode after surface cleaning, Appl. Opt. **18**, 2531 (1979).

12. E. F. Zalewski, Recent developments in the techniques for the self-calibration of silicon photodiodes, In Proc. 10th IMEKO Int. Symposium on Photon Detectors - 1982, 127-136 (IMEKO SECRETARIAT H-1371, Budapest, POB. 457).

13. J. Verdebout and R. L. Booker, Degradation of native oxide passivated silicon photodiodes by repeated oxide bias, J. Appl. Phys. **55**, 406-412 (1984).

14. R. Korde and J. Geist, Stable, high quantum efficiency, uv-enhanced silicon photodiodes by arsenic diffusion, Solid-State Electronics **30**, 89-92 (1987).

15. R. Korde and J. Geist, Quantum efficiency stability of silicon photodiodes, Appl. Opt. **26**, 5284-5290 (1987).

16. J. Geist, E. Liang, and A. R. Schaefer, Complete collection of minority carriers from the inversion layer in induced junction diodes, J. Appl. Phys. **52**, 4879-4881 (1981).

17. J. M. Palmer, Near-infrared limitations to silicon photodiode self-calibration, Proc. SPIE **499**, 7-14 (1984).

18. A. R. Schaefer, E. F. Zalewski, and J. Geist, Silicon detector nonlinearity and related effects, Appl. Opt. **22**, 1232-1236 (1983).

19. J. L. Gardner and F. J. Wilkinson, Response time and linearity of inversion layer silicon photodiodes, Appl. Opt. **24**, 1531-1534 (1985).

20. K. D. Stock, Si-photodiode nonlinearity in the infrared, Appl. Opt. **25**, 830-832 (1986).

21. L. E. Larson and M. E. Mickelson, A super optical power meter, Am. J. Phys. **53**, 1108-1110 (1985).

22. J. B. Fowler, M. A. Lind and E. F. Zalewski, NBS Tech. Note 987 (U.S. Government Printing Office, Wash. DC 20402, 1979).

23. W. Kuhr and E. Yeng, Optimization of sensitivity and separation in capillary zone electrophoresis with indirect fluorescence detection, Anal. Chem. **60**, 2642-2646 (1988).

24. Available from Cambridge Research and Instrumentation, Cambridge, MA 02139.

25. C. G. Hughes, Silicon photodiode absolute spectral response self-calibration using a filtered tungsten source, Appl. Opt. **21**, 2129-2132 (1982).

26. R. L. Booker and J. Geist, Induced junction (inversion layer) photodiode self-calibration, Appl. Opt. **23**, 1940-1945 (1984).

27. E. F. Zalewski and C. R. Duda, Silicon photodiode device with 100% external quantum efficiency, Appl. Opt. **22**, 2867-2873 (1983).

28. Available from United Detector Technology, Hawthorne, CA 90250.

29. Li Tong-Bao, Checking the accuracy of absolute radiometers with technique of silicon photodiode self-calibration, in Proc. 10th IMEKO Int. Symposium on Photon Detectors - 1982, pp. 137-144 (IMEKO SECRETARIAT H-1371, Budapest POB. 457).

30. N. P. Fox, Uses of a cryogenic radiometer in absolute radiometry, in Proc. Advances in Absolute Radiometry, 1985, pp. 56-59 (Atmospheric and Environmental Research, Cambridge, MA).

31. L. P. Boivin and F. T. McNeely, Electrically calibrated absolute radiometers suitable for measurement automation, Appl. Opt. **25**, 554-561 (1986).

32. J. L. Gardner and W. J. Brown, Silicon radiometry compared with the Australian radiometric scale, Appl. Opt. **26**, 2431-2435 (1987).

33. R. W. Faaland and M. L. Naiman, Laser power measurement standards: A comparison of two scales, IEEE Trans. Instr. Meas. **IM-36**, 455-457 (1987).

34. E. F. Zalewski, The NBS photodetector spectral response calibration transfer program, NBS Special Publication 250-17 (US Govt. Printing Office, Washington, 1988).

35. E. F. Zalewski, Comparison of the national standards of absolute spectral responsivity, BIPM Com. Cons. Phot. and Radiometrie **11**, 165-179 (1986).

36. W. Wobrock and R. Eiden, Direct solar radiation: spectrum and irradiance derived from sun-photometer measurements, Appl. Opt. **27**, 2253-2260 (1988).

37. A. R. Schaefer, R. D. Saunders and L. R. Hughey, Intercomparison between independent irradiance scales based on silicon photodiode physics, gold-point blackbody radiation, and synchrotron radiation, Opt. Eng. **25**, 892-896 (1986).

38. R. J. Bruening, Spectral irradiance scales based on filtered absolute silicon photodetectors, Appl. Opt. **26**, 1051-1057 (1987).

39. E. F. Zalewski and W. K. Gladden, Absolute spectral irradiance measurements based on the predicted quantum efficiency of a silicon photodiode, Optica Pura Y Aplicada **17**, 133-140 (1984).

40. K. D. Mielenz, R. D. Saunders, and J. B. Shumaker, Spectro-radiometric determination of the freezing temperature of gold, J. Res. NIST **95**, 49-67 (1990).

41. J. Bonhoure, Report on the sixth comparison of national standards of luminous intensity and of luminous flux, BIPM Com. Cons. Phot. and Radiometrie **11**, 125-160 (1986), page 156-158.

42. J. Bonhoure, Sixth comparison of national standards of luminous intensity and of luminous flux (1985), Metrologia **24**, 157-162 (1987).

43. T. J. Quinn and J. E. Martin, A radiometric determination of the Stefan-Boltzmann constant and thermodynamic temperatures between -40°C and +100°C, Phil. Trans. Royal Soc. London **A316**, 85-189 (1985).

44. N. P. Fox and J. E. Martin, Comparison of two cryogenic radiometers by determining the absolute spectral responsivity of silicon photodiodes with an uncertainty of 0.02%, Appl. Opt. **29**, 4686-4693 (1990).

45. Available from EG&G Electro-Optics, Salem, MA 01970.

46. C. C. Hoyt, personal communication.

47. Available from Hamamatsu, Bridgewater, NJ 08807-0910.

48. Available from Cambridge Research and Instrumentation, Cambridge,

MA 02139.

49. C. C. Hoyt, P. J. Miller, P. V. Foukal, and E. F. Zalewski, Comparison between side-viewing cryogenic radiometer and self-calibrated silicon photodiodes, SPIE Proc. 1109, 236-245 (1989).

3. SHAPE OF THE SILICON ABSORPTION COEFFICIENT SPECTRUM

This and the following two chapters are concerned with obtaining a simple equation that accurately represents the room temperature silicon absorption coefficient spectrum over the visible and near visible spectral region. The purpose of this chapter is to refute claims that this spectrum is not locally smooth and featureless in the visible, and by implication, unsuitable for representation by a simple equation. The purpose of Chapter 4 is to accurately determine the value of this spectrum at 633 nm to help to decide which of a number of published spectra is the most accurate, and therefore, the most suitable for representation. Chapter 5 describes the equation chosen to represent the silicon absorption coefficient at room temperature, and discusses its accuracy.

Certain authors[1,2] claim to have observed features in the visible silicon absorption spectrum that would make it difficult to represent with a simple analytic function. This chapter presents new dye-laser-based measurements with improved resolution and precision in the region around 760 nm (1.631 eV) where both sets of authors claimed to see features. The high-quality data described in this chapter show a smooth absorption coefficient spectrum with no discernible features in this spectral region.

Forman, Thurber, and Aspnes[1] (FTA) reported features in the optical density spectra of silicon that they associated with photon-energy thresholds of the second indirect transition from the $\Gamma_{25'}$ valence

---

A version of this chapter has been published: J. Geist, A. Migdall, and H. Baltes, "Shape of the silicon absorption coefficient spectrum near 1.63 eV", Appl. Opt. 29, 3548-3554 (1990).

band to the L_1 conduction band critical point in the silicon band structure. They reported an abrupt change of slope near 760 nm in spectra of samples taken at 4 K, 77 K, 300 K, and 373 K. They attributed this feature to the photon-energy threshold of the above transition involving the simultaneous emission of a phonon.

FTA also reported detecting an abrupt change of slope at 830 nm, but only in their 373 K spectrum. This they attributed to the indirect transition that involves the absorption of a transverse-optical (TO) phonon. Since the difference in energy between 760-nm and 830-nm photons, which is 0.138 eV, is about twice the TO phonon energy at the L_1 point in silicon, FTA concluded that they had detected the second indirect transition associated with the absorption and emission of TO phonons. Hulthen and Nilsson[2] (HN) checked the results of FTA using photoconductivity measurements. They reported finding small bumps, rather than abrupt changes in slope, in unnormalized data at the wavelengths reported by FTA. In the text of their paper, HN stated that these features were removed by normalization, but they retracted this in a note added in proof. They further reported having detected features at 589 and 626 nm that remained after normalization. They attributed these to the same transitions that FTA claimed to see.

3.1 PHYSICAL BASIS FOR THE ABSORPTION COEFFICIENT SPECTRUM

Macfarlane, McLean, Quarrington, and Roberts[3,4] (MMQR) have reported a high-resolution study of the photon-energy thresholds of the first indirect transition for optical absorption in silicon and germanium. (The latter will be referred to simply as thresholds in the remainder of this chapter.) According to MMQR, neither localized bumps as shown in Fig. 1 of the HN paper nor abrupt changes in a constant slope

extending over a broad spectral region of optical density as shown in Fig. 1b of the FTA paper are what would be expected at a threshold of the second indirect transition.

MMQR found that the largest threshold of the first indirect transition in the absorption coefficient of silicon was associated with the emission of a TO phonon. They also found that this threshold could be approximated by the temperature-dependent Gaussian broadening of a term in the absorption coefficient spectrum that they denoted by $\alpha_2(h\nu-E_0)$.

This term can be approximated by the following empirical relation:

$$\alpha_2(h\nu-E_0) = K_1\, L(h\nu-E_0)^{1/2} + K_2\, L(h\nu-E_0-0.0055eV)^{M}, \quad (1)$$

where E_0 is the empirically-determined temperature-dependent threshold energy (1.2135 eV at 4.2 K), $K_1 = 18.08\ cm^{-1}\ eV^{-1/2}$, $K_2 = 1656.09\ cm^{-1}\ eV^{-M}$, $M = 1.59356$, and $L(x)$ is x for positive x, but is zero otherwise. Equation (1) differs from eq. 6 of Ref. 3 by 6% or less over the first 50 meV above E_0.

The feature associated with the threshold of the first TO phonon-emission-assisted transition in silicon is caused by the "turn-on" of the first term in eq. (1) for $h\nu > E_0$. It is quite distinct at 4.2 K, but becomes less distinct with increasing temperature for two reasons. First, the broadening associated with increasing temperature smooths out the most prominent aspect of the feature, the square root dependence that extends over the first 20 meV. Second, the feature has an amplitude of about 2 cm^{-1}. At 4.2 K, it is superimposed on a background of 1 cm^{-1}, but at 291 K, it is superimposed on a background

of 10 cm^{-1}.

Even though this feature is small compared to the background, MMQR could still resolve it in the absorption spectra at temperatures as large as 415 K because the feature occurs near the threshold for absorption, where the background slope from which it must be distinguished is still quite small. This is not the case for the second indirect transition. Here, the background slope of the absorption coefficient spectrum is very large due to the first indirect transition.

3.2 EXPERIMENTAL PROCEDURE

A detailed description of the facility used for the measurements reported in this chapter has been described previously.[5] Figure 3.1 gives a diagram of the facility. The radiation source was a ring dye-laser that was pumped by a CW Kr^+ ion laser. For these measurements, LD700 was used as the laser dye. The output intensity of the dye laser was actively stabilized using an electro-optic modulator. One beam splitter directed the output beam from the laser to a Michelson-interferometer wavemeter that determined the wavelength of the light with an accuracy of 0.001 nm, and two wedged beam splitters directed the stabilized beam to two photodiodes. The output of the first photodiode was fed back to the modulator to achieve stabilization, and the output of the second was recorded to monitor the stabilized beam power.

The sample was a wafer of high-purity silicon of greater than 10-kΩ-cm resistivity, nominal 100-μm thickness, and 2.5-cm diameter, with polished, scratch-free optical surfaces on both faces. The sample was

mounted on a jig fastened to a silicon photodiode with its surface oriented 45° to the incoming laser radiation as shown in Fig. 3.2. The inside of the jig was coated with a specular black paint having a reflectance of 3% at 760 nm, so the multiply-reflected radiation was assumed to be negligible. The sample was at room temperature for the measurements reported here.

The same specular black paint was used to fix the silicon wafer to the jig and the jig to the detector to assure that the assembly was light-tight. Thus, the only way for radiation to reach the photodiode was to pass through the silicon wafer. This assured that geometrically stray light did not affect the measurements.

The photodiode assembly was mounted in a box that was light-tight except for a small aperture through which the laser radiation was introduced, as shown in Fig. 3.2. The measurements were carried out with the room lights off. Thus, there was negligible radiation of wavelengths other than the dye laser radiation incident on the silicon wafer, thereby assuring that spectrally stray light did not affect the measurements.

Before the silicon wafer and jig were fixed to the silicon photodiode, the photodiode was positioned in the direct radiation beam and the ratio R_b of the photocurrent from the monitor photodiode to that from this photodiode was recorded as the dye laser photon energy was scanned from about 1.61 to 1.65 eV. The measured ratio was approximately 4% and was constant to within a tenth of a percent of the ratio over this energy range. After these measurements, the photodiode was fixed to the jig and wafer, and then mounted in the box

as described above, and the measurements were repeated.

The absorption coefficient $\alpha(\nu)$ of the silicon in the wafer was then determined using

$$\alpha(\nu) = - \ln(R_p(\nu) R_b/(1-\rho(\nu))^2) \cos \theta'/d, \qquad (2)$$

where $R_p(\nu)$ is the measured ratio of the photocurrent from the photodiode behind the wafer to that from the monitor photodiode, d is the thickness of the wafer, θ' is the angle of propagation inside the wafer, and $\rho(\nu)$ is the reflectance of the wafer for the angle θ' inside the wafer and for the polarization state of the radiation.

The wafer thickness was measured with a double-probe micrometer. The result was 84 ± 3 μm due to thickness variations in the region where the radiation was incident on the wafer. The quantity $(1-\rho(\nu))^2$ was calculated[6] for both polarizations by interpolating values from the literature[7] for $n(\nu)$ and $k(\nu)$, the real and imaginary parts of the index of refraction of silicon. For each polarization, the values varied less than 0.25% over the spectral range from 1.61 to 1.65 eV. Since this variation is negligible compared to the almost factor-of-four change in wafer transmittance over the same spectral range, $\rho(\nu)$ was approximated by the constant value 0.46 over this spectral region.

3.3 RESULTS

The results are shown in Fig. 3.3, where they have been normalized to give $\alpha = 1160$ cm^{-1} at 1.6313 eV.[8,9] The data consist of 88 points, but they cannot all be distinguished in Fig. 3.3. Different data points for the same photon energy usually fell on top of each other to within the resolution of the figure. No features or abrupt changes in

slope are apparent from visual inspection of the data in Fig. 3.3. A change in slope as large as that reported by FTA would be easily seen in these data.

Various simple models were used in fitting the data shown in Fig. 3.3. The same models were also applied to data that simulated the effect of an energy threshold of the second indirect transition. This data was obtained by adding $\alpha_2(h\nu-E_2)$ in eq. (1) to the measured data, where E_2 = 1.634 eV. The idea behind including the simulated data in the fits was to test the sensitivity of the various models and the fitting procedure to the presence of a threshold of the second indirect transition.

The simulation is based on the fact that the joint density of states and matrix elements for the second indirect transition involving the emission of a TO phonon are comparable to that for the first. With this assumption, a photon-energy threshold of the second indirect transition for optical absorption occurring at 1.634 eV could be simulated by using the corresponding term from the first indirect transition. However, by using eq. (1) directly without applying a correction for temperature broadening as described in Refs. 3 and 4, the term that is appropriate to 4.2 K rather than 300 K was used. There is not much difference between these terms, but the real threshold would be more difficult to detect than the simulated threshold.

3.3.1 DESCRIPTION OF MODELS

All of the models that were fit to the measured and simulated data had the form

$$\alpha(\nu) = A_0 + A_1 (h\nu - E_1) + A_2 (h\nu - E_1)^2 + A_3 (h\nu - E_1)^3 + C\, \alpha_2(h\nu - E_2 - \Delta E_2), \quad (3)$$

where $E_1 = 1.629$ eV, $E_2 = 1.634$ eV, and A_0, A_1, A_2, A_3, C, and ΔE_2 were either set equal to zero or adjusted by a nonlinear fitting program[10] depending upon the specific hypotheses being tested. (See Table 3.1.) The first four terms in eq. (3) represent a Taylor series expansion about the point $h\nu = E_1$. The last term represents the TO phonon emission term of the second indirect transition with threshold energy $E_2+\Delta E_2$, subject to the assumption that eq. (1) is a good approximation to this term.

Table 3.1 compares the results of the fits of different models based on eq. (3) to both the measured and the simulated data. The values of the fitting parameters, their estimated standard deviations, and the residual standard deviation of the fits are all listed in the table.

It is clear that a Taylor series expansion of the data shown in Fig. 3.3 must contain at least a constant and linear term. Thus, Model 1 in Table 3.1, which consists of the first two terms of a Taylor series expansion about the point $E_1 = 1.629$ eV, was fit to the experimental data. Both of the free parameters, A_0 and A_1, are significant in both models, as is to be expected from Fig. 3.3. The residual standard deviation of the fit to the measured data is less than two thirds as large as that to the simulated data, indicating that the model fits the measured data better than the simulated data. The top graph in Fig. 3.4 shows the residuals for the fit of Model 1 to the measured data, and the second graph shows the residuals for the fit of the same model to the simulated data. A systematic trend in the residuals is

evident in the second graph, and may also be present in the first.

Since the absorption coefficient of silicon has a highly non-linear dependence on photon energy, a quadratic term in the Taylor series with a coefficient significantly different from zero is a possibility that must be considered. Thus, Model 2, which consists of the first three terms of the Taylor series expansion, was also fit to the experimental data.

3.3.2 COMPARISON OF MODELS

The F statistic[11], which assesses the reduction in the sum of the squares for error that is gained by going from a restricted case (Model 1, for instance) to a more general case (Model 2, for instance), was used to compare the different models. A large F statistic is associated with a significant reduction in the sum of squares for error, indicating that the fit of the data is improved by the additional parameter in the more general model. The F statistic for Model 1 versus Model 2 for the case of the measured data is 22.76, while that for the case of the simulated data is 186.14. Both F statistics are very significant at the 99% probability level indicating that the fits to both data sets are improved by the addition of the quadratic term.

The third graph in Fig. 3.4 shows the residuals of the fit of Model 2 to the measured data, and the fourth shows the residuals of the fit of the same model to the simulated data. No large-scale systematic trends are evident, but there does appear to be a small oscillation with a period of approximately 0.02 eV. This could be caused by a larger than expected periodic systematic error in the measurement of

the dye-laser wavelength.

The last two graphs in Fig. 3.4, which are flat except for the periodic variation mentioned above, suggest that nothing would be gained by adding another term to the Taylor series expansion of the absorption coefficient spectrum. Model 3 tests this hypothesis. Both the residual standard deviations of the fits of this model to the measured data and to the simulated data are larger than those for Model 2, showing that the hypothesis is correct.

No threshold of the second indirect transition is apparent in the residuals of the fit of Model 2 to either the measured data or the simulated data in the last two graphs in Fig. 3.4. Model 4, which includes a threshold of the indirect transition with threshold energy $h\nu = E_2 = 1.634$ eV (holding $\Delta E_2 = 0$), tests for the presence of a threshold at this photon energy. In the case of the fit of Model 4 to the simulated data, both A_2 and C are marginally significant, whereas C is not significantly different from zero in the case of the fit to the measured data. The F statistic for Model 2 versus Model 4 for the case of the measured data is 0.24, which is not significant at the 90% confidence level, while that for the simulated data is 6.03, which is significant at the 97.5% confidence level, but not at the 99% level. Thus the fit of the first three terms in a Taylor series expansion to the measured data is not improved significantly by the addition of a term describing a threshold of the second indirect transition at E_2, while the fit to the simulated data is significantly (at the 95% confidence level) improved by this addition.

Model 5, which adds the free parameter C to the two-term Taylor series

expansion of Model 1, tests the improbable, but not impossible, case where the detailed nature of the joint density of states for the indirect transition is locally linear in the vicinity of $h\nu = E_1 = 1.629$ eV, but that a threshold of the indirect transition occurs at $h\nu = E_2 = 1.634$ eV. The F statistic for Model 1 versus Model 5 for the measured data is 19.44, while that for the simulated data is 246.68. Therefore, this model fits the measured and simulated data as well as Model 2. It is also of interest to calculate the F statistics for Model 5 versus Model 4. For both the measured data and for the simulated data, the F statistic is 2.92, which is significant at the 90% confidence level. Thus adding a quadratic term to a model that contains a constant term, a linear term, and a term to describe the threshold of the second indirect transition at 1.634 eV results in a marginal (significant at the 90% confidence level) improvement of the fit.

The F statistic results are summarized in Table 3.2. They imply the following: If a quadratic term is added to Model 1, then it is found to result in a significant improvement in the fit to both data sets. If a term to describe the second indirect transition is added to the resulting model, it is found to contribute no significant improvement to the fit to the measured data, but to contribute a significant (at the 95% confidence level) improvement to the fit to the simulated data. Thus, if Model 2 correctly describes the shape of the silicon absorption spectrum in the vicinity of 1.635 eV in the absence of a threshold of the second indirect transition, and if a threshold of the second indirect transition associated with the emission of a TO phonon is present at the expected level and photon energy, it should have contributed an improvement to the fit to the measured data that was

significant at the 95% confidence level. In fact, it was found to contribute no improvement at all.

Similarly, if a term to describe the onset of the second indirect transition is added to Model 1, it is found to result in a significant improvement to the fit to both data sets. If a quadratic term is now added to this model, it is found to contribute a marginally significant (90% confidence level) improvement to the fit to both data sets.

Since there is no *a priori* reason to expect a contribution from the threshold of the second indirect transition in the measured data, and since there is an *a priori* reason to expect a contribution from a quadratic term in the measured data, these results do not support the detection of the onset of the second indirect transition.

Also, the fact that Model 5 fits the measured data as well as Model 2 is somewhat misleading since there is no *a priori* reason to expect that $E_2 = 1.634$ eV in the measured data, even if there were an *a priori* reason to expect the onset of the indirect transition somewhere in the vicinity of 1.634 eV. A fairer test would be to treat ΔE_2 as a free parameter. This is done in Model 6. The fitting procedure was unstable for this model. There were many local minima in the residual standard deviation, and the final value of the model parameters and residual standard deviation depended upon the starting value of ΔE_2. The parameter values shown in Table 3.1 for Model 6 had the lowest residual standard deviation that was found by systematically varying the starting value of ΔE_2 between -0.02 and 0.03. For all of the starting values of ΔE_2 that were tested, the parameter values fell

within their estimated uncertainties in Table 3.1. Neither C nor ΔE_2 was significantly different from zero in any of these fits. This result is very important. It means that the threshold in the simulated data cannot be detected unless the threshold energy is already known.

3.4 CONCLUSIONS

There are four specific conclusions that can be drawn from the results presented in this chapter: 1) the first two terms of a Taylor series expansion do not explain all of the effects seen in the data, 2) the simulated photon-energy threshold of the second indirect transition in the optical absorption spectrum can be unambiguously identified in the simulated data only if the simulated threshold energy is known in advance and fixed during the fitting procedure, 3) the measured data are explained as well by curvature in the absorption coefficient as by a photon-energy threshold of the second indirect transition at some fixed energy, 4) the measurements and data analysis techniques described in this chapter are not sensitive enough to detect unambiguously a threshold of the expected magnitude occurring at an unknown photon energy in the measured data, even if it is present.

Three factors contribute to the fourth conclusion. First, the residual effect that is not modeled by the first two terms in the Taylor series expansion is of the same order as the precision of the data. Second, the residual effect of the simulated threshold is rather accurately modeled by the sum of the linear and quadratic terms of the Taylor series expansion of the first indirect transition. Third, the simulated threshold, lacking the temperature broadening appropriate to 300 K, is probably easier to detect than the actual TO phonon emission

threshold of the second indirect transition at 300 K. All of these problems are even more severe at 2.1 eV, where HN claim to have detected thresholds of the second indirect transition.

It is unlikely that absorption coefficient data of substantially improved precision can be easily obtained. The fit of Model 2 to the absorption coefficient data shown in Fig. 3.3 is characterized by a relative residual standard deviation of less than 5 parts in 10^4. This is the most precise ever reported for a semiconductor in the region of a band-to-band transition. While it is true that there is an unexplained oscillation of small amplitude in the measured data that might be removed by improvements in the experimental techniques, it is unlikely that this improvement would reduce the standard deviation of the fit enough to change the conclusions reported above.

Fitting data over an extended spectral range would allow the inclusion of data for which the effect of the second indirect transition was much larger than the precision of the data. However, it would also require more terms of the Taylor series to account for the curvature associated with the terms of the first indirect transition. As more terms are added to the Taylor series, it can more accurately approximate the effect of the threshold. Thus, the increased size of the effect might be compensated by the increased difficulty in distinguishing the effect from curvature in the absorption coefficient data. Consequently, extending the spectral range does not appear promising.

In connection with considerations of a broader spectral region, note that the Weakliem and Redfield[9] (WR) absorption coefficient spectrum shows a dip between 1.4 and 1.5 eV. In Chapter 5 a model describing

the large energy shape of the transverse-optical (TO) and transverse-acoustic (TA) phonon-assisted first indirect transitions is used to fit the WR data to obtain an accurate analytic representation of that data set.[8] While not reported in Chapter 5, models having four threshold terms to describe the second indirect transition were tested and rejected. Thresholds for abrupt changes in slope were obtained at 1.43 eV, 1.83 eV, and 2.21 eV, the fourth threshold being pushed above the greatest photon energy in the WR data set. Notice, however, that these thresholds are not consistent with either TO or TA phonon-assisted transitions, because the energy differences are far too large. Also, note that the WR data were not measured at a sufficiently dense set of photon energies to resolve the fine detail described by eq. (1) of this chapter.

In the fits of the rejected models to the WR data, it appeared that the abrupt changes in slope were being used by the fitting program to compensate for the deviation from parabolic shape of the bands away from the band edge. The three thresholds and the corresponding strengths of the abrupt changes in the slope of the curve required a total of six parameters to describe the data. Indeed, when the model of the second indirect transition was replaced by a model specifically chosen to describe the increase in the joint density of states, only four parameters were needed to achieve the same residual standard deviation of the fit to the WR data.

It appears that the background absorption coefficient, that is, the slope and the curvature associated with the first indirect transition, overwhelms the effect of the thresholds of the second indirect transition. This suggests that the contribution of the second

indirect transition to the absorption coefficient will never be resolved unless the contribution from the first indirect transition can be accurately subtracted from the spectrum. Clearly this requires much more accurate knowledge of the joint density of states for the first indirect transition and, therefore, of the details of the silicon band structure than is currently available. In principle, such knowledge could be obtained from first-principles quantum mechanical calculations, or from a non-optical measurement technique. However, the required accuracy is beyond the current state of the art.

Nevertheless, both the theoretical and the experimental evidence suggests that the silicon absorption spectrum for photon energies greater than the energy thresholds of the first indirect transition is a smooth (to within a tenth of one percent) function of photon energy over the region of the indirect transition. Therefore, it should be possible to represent that spectrum by a simple analytic function that is based on the physics of the absorption process with an uncertainty of no more than a few percent over most of the spectral region of the indirect transition. Indeed, this goal is achieved by the fit to the WR data given in Chapter 5. But first it is necessary to verify the accuracy of the WR data. This is done by comparing the WR data with other sets of data including a high accuracy value at the 633 nm HeNe laser line that was derived from measurements described in the next chapter.

TABLE 3.1. Coefficients of nonlinear, least-squares adjustments of the parameters in the model described by eq. (3) to the measured absorption coefficient data shown in Fig. 3.3 and to artificial data containing a simulated threshold of the second indirect transition. The units of the parameters A_0, A_1, A_2, A_3, and C are such that the units of $\alpha(\nu)$ are cm^{-1} when eV are the units of energy. The uncertainties associated with each parameter are standard deviations estimated by the fitting program, and RSD is the residual standard deviation of the fit. Constants not listed are 0.

	MEASURED ABSORPTION COEFFICIENT		SIMULATED ABSORPTION COEFFICIENT	
	VALUE	UNCERTAINTY	VALUE	UNCERTAINTY
Model 1				
A_0 =	1150.62	0.057	1151.02	0.094
A_1 =	4233.40	5.794	4333.18	9.501
RSD =		0.497		0.815
Model 2				
A_0 =	1150.44	0.064	1150.48	0.066
A_1 =	4210.85	6.983	4266.71	7.228
A_2 =	2723.04	569.9	8028.75	588.5
RSD =		0.444		0.459
Model 3				
A_0 =	1150.47	0.076	1150.49	0.079
A_1 =	4207.25	9.737	4265.01	9.394
A_2 =	2217.78	1003.	7823.10	996.6
A_3 =	35527.2	62810.	14562.0	57350.
RSD =		0.446		0.462
Model 4				
A_0 =	1150.45	0.066	1150.45	0.066
A_1 =	4218.17	21.09	4217.50	20.99
A_2 =	3402.48	1986.	3329.74	1976.
C =	-0.129937	0.3576	0.883050	0.3553
RSD =		0.446		0.446
Model 5				
A_0 =	1150.44	0.066	1150.44	0.066
A_1 =	4188.13	11.65	4187.63	11.67
C =	0.453731	0.1041	1.45867	0.1043
RSD =		0.451		0.451
Model 6				
A_0 =	1150.45	0.064	1150.48	0.064
A_1 =	4189.16	11.16	4192.88	11.09
C =	0.457144	7.2	1.45866	20.28
ΔE_2 =	0.00031	0.2582	0.00040	0.2272
RSD =		0.451		0.451

TABLE 3.2. The F statistics (F stat) comparing related models from Table 3.1, where n is the number of degrees of freedom for fitting each model to the data of Fig. 3.3, and Dn is the reduction in the number of degrees of freedom between the models being compared.

		Measured data			Simulated data		
Models	new term	F stat	n	Dn	F stat	n	Dn
1 vs 2	A2	22.76	85	1	186.14	85	1
2 vs 4	C	0.24	84	1	6.03	84	1
1 vs 5	C	19.44	85	1	246.68	84	1
5 vs 4	A2	2.92	84	1	2.92	84	1

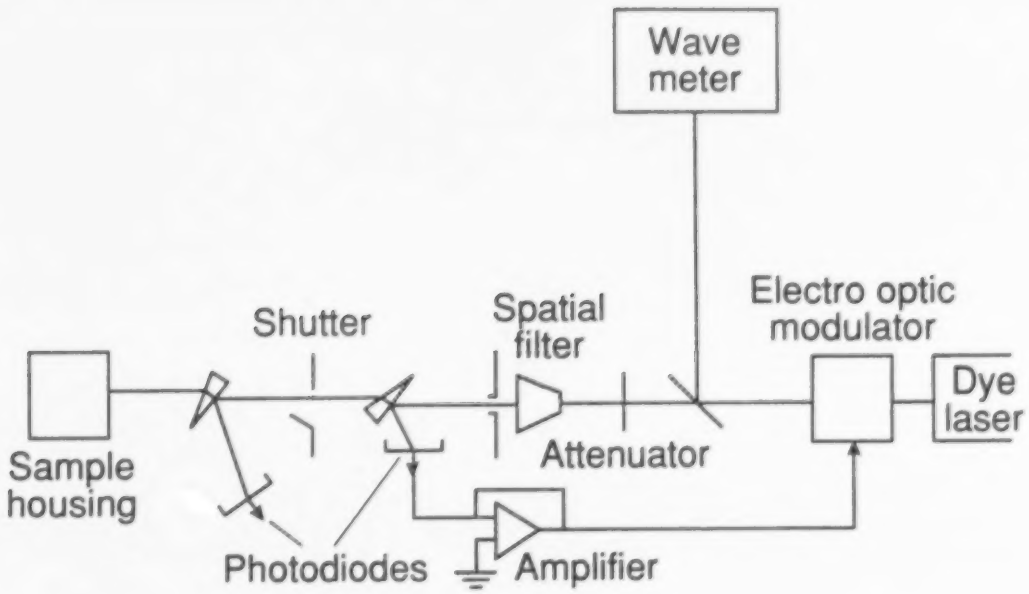

FIGURE 3.1. A schematic diagram of the apparatus used to measure the transmittance of a thin silicon wafer mounted in front of a silicon photodiode in the sample housing as shown in Fig. 3.2. The radiation proceeds from the dye laser through the electro-optic modulator through the spactial filter through the shutter to the sample and detector mounted in the sample housing. The dye laser was pumped with a Kr^+ ion laser, the electro-optical modulator was used to stabilize the amplitude of the dye laser radiation, the wavemeter was used to measure the wavelength of the laser radiation, and the spatial filter was used to produce a clean beam of radiation for the measurement.

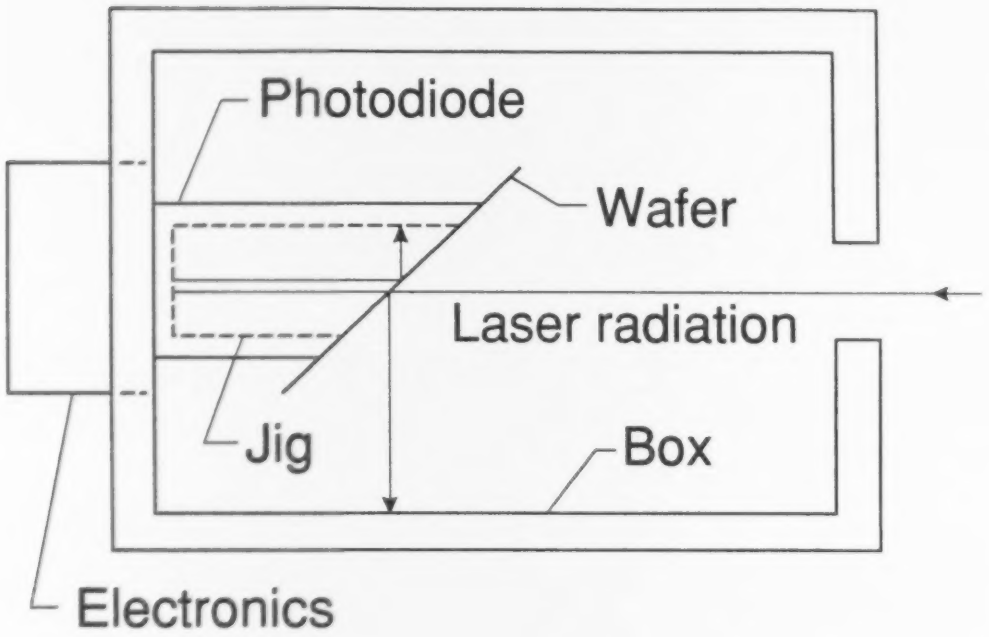

FIGURE 3.2. A schematic view into the box housing the assembly consisting of the silicon wafer, mounting jig, and silicon photodiode. The detector was mounted on the electronics package, which was mounted with a light-tight seal in a hole in the box.

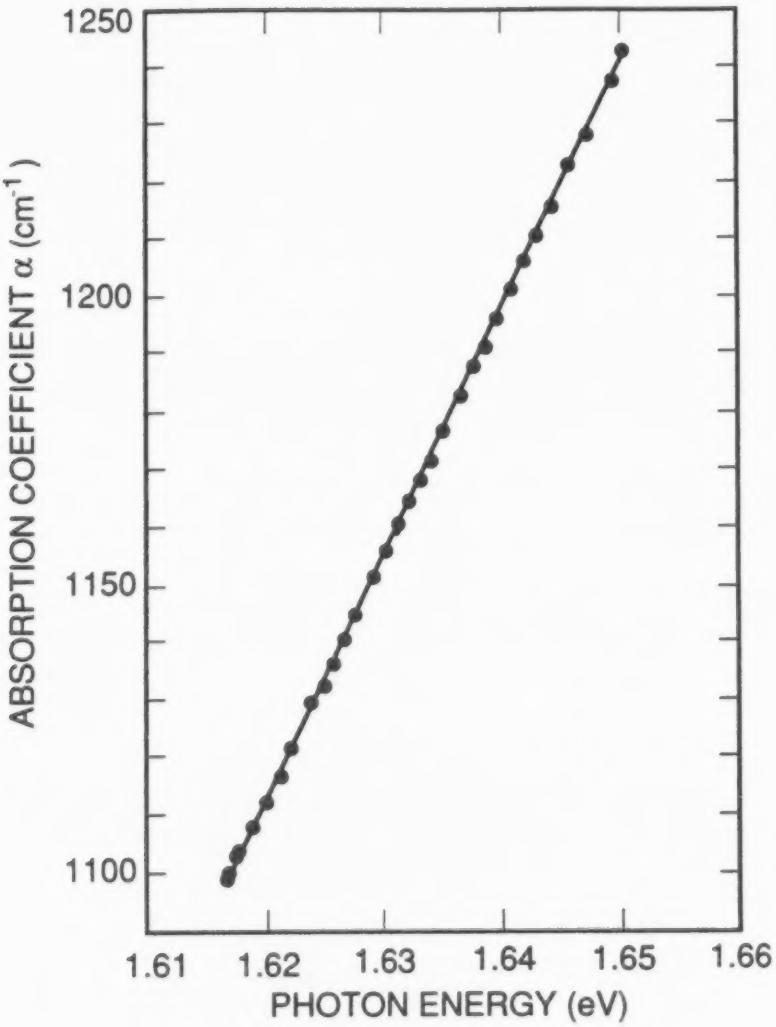

FIGURE 3.3. High-resolution, high-precision, room-temperature, silicon absorption coefficient data (filled circles) normalized to 1160 cm^{-1} at 1.6313 nm. The curve is the fit to the data of Model 2 described in this chapter.

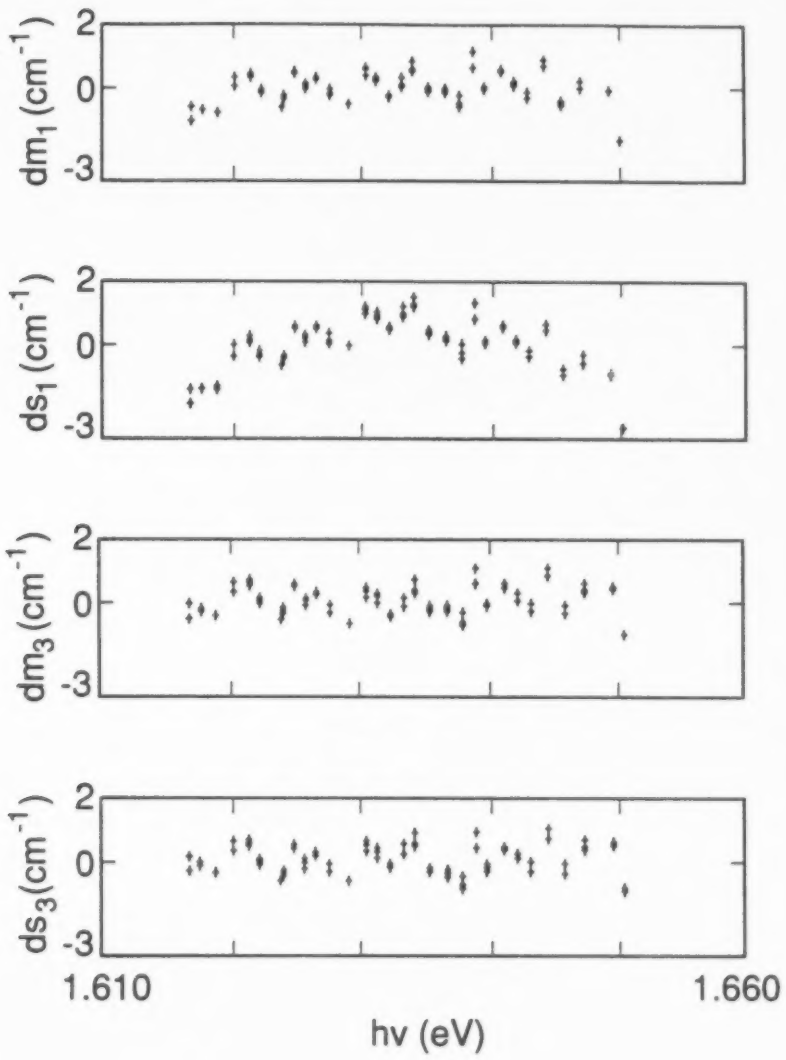

FIGURE 3.4. The residuals between Model 1 and the measured data (dm_1), Model 1 and the simulated data (ds_1), Model 2 and the measured data (dm_3), and Model 2 and the simulated data (ds_3). Some residual curvature is evident in the plot of ds_1, less in the plot of dm_1, and none in the plots of dm_3 and ds_3.

REFERENCES FOR CHAPTER 3

1. R. A. Forman, W. R. Thurber and D. E. Aspnes, Second indirect band gap in silicon, Solid State Communications **14**, 1007-1010 (1974).

2. R. Hulthen and N. G. Nilsson, Investigation of the second indirect transition of silicon by means of photoconductivity measurements, Solid State Communications **18**, 1341-1343 (1976).

3. G. G. Macfarlane, T. P. McLean, J. E. Quarrington and V. Roberts, Fine Structure in the Absorption-Edge Spectrum of Si, Phys. Rev. **111**, 1245-1254 (1958).

4. G. G. Macfarlane, T. P. McLean, J. E. Quarrington and V. Roberts, Exiton and phonon effects in the absorption spectra of Germanium and Silicon, J. Phys. Chem. Solids **8**, 388-392 (1959).

5. A. R. Schaefer and K. L. Eckerle, Spectrophotometric tests using a dye-laser-based radiometic characterization facility, Appl. Opt. **23**, 250-256 (1984).

6. M. Born and E. Wolf, "Principles of Optics" (Pergamon Press, Oxford, 3rd edition, 1965), page 632.

7. D. E. Aspnes and A. A. Studna, Dielectric functions and optical parameters of Si, Ge, GaP, GaAs, GaSb, InP, InAs, and InSb from 1.5 to 6.0 eV, Phys. Rev. **B27**, 985-1009 (1983).

8. J. Geist, A. Migdall and H. P. Baltes, Analytic representation of the silicon absorption coefficient in the indirect transition region, Appl. Opt. **27**, 3777-3779 (1988).

9. H. A. Weakliem and D. Redfield, Temperature dependence of the optical properties of silicon, J. Appl. Phys. **50**, 1491-1493 (1979), and personal communication of data plotted therein.

10. J. J. Filiben, DATAPLOT, Introduction and Overview, US Government Printing Office, Wash. DC, June 1984.

11. J. Netter and J. Wasserman, Applied Linear Statistical Models (Richard D. Irwin, Inc., Homewood, IL, 1974), 77-84.

4. AN ACCURATE VALUE FOR THE SILICON 633 nm ABSORPTION COEFFICIENT

The absorption coefficient α is related to the imaginary part of the index of refraction k, also called the extinction coefficient,[1] by

$$\alpha = 4 \pi k/\lambda, \qquad (1)$$

where λ is the vacuum wavelength of the incident radiation, and is related to the photon energy $h\nu$ of the radiation by

$$\lambda h\nu = 1.23985 \text{ eV } \mu\text{m}. \qquad (2)$$

For silicon, k spectra have been derived from a Kramers-Kronig analysis of reflectance data,[2] by inversion of ellipsometric data,[3] and from α spectra derived from transmission measurements.[4,5] Neither ellipsometric nor reflectance measurements are well suited for determining small values of k, so for silicon most k values quoted below 2.5 eV have been determined from transmission measurements. Since the differences among the various data sets are fairly large, Taft[6] found it necessary to measure the absorption coefficient at the Hg 546.1 nm line (2.27 eV) to reduce ellipsometric data on oxide films on silicon wafers. However, at the present time there is no consensus as to the correct spectra. This is illustrated by the fact that two recent compilations contain spectra that differ by much more than 20% at some wavelengths in the visible.[7,8]

A version of this chapter has been published: J. Geist, A. R. Schaefer, J-F Song, Y. H. Wang, and E. F. Zalewski, An accurate value for the absorption coefficient of silicon at 633 nm, J. Res. NIST 95, 549-558 (1991).

This chapter reports a measurement similar to that of Taft at the 633 nm HeNe laser line. The purpose of these measurements was twofold. First, there was a need to fit an analytic function to one of the existing data sets. A value at 633 nm would establish the accuracy of the various data sets at the midpoint of the wavelength range of interest, and complement Taft's value at 546 nm. Second, this measurement offered the opportunity to test the use of 1) an amplitude-stabilized laser as a radiation source, 2) extremely linear silicon photodiodes as the radiation detectors, 3) recently perfected etching techniques for sample preparation, and 4) state-of-the-art mechanical measurements of sample thickness in high-accuracy absorption-coefficient measurements.

The advantage of using amplitude-stabilized lasers with extremely linear photodiodes is that very precise transmission measurements can be carried out over a very large range of transmittance values with very high wavelength accuracy and resolution. This was demonstrated recently in connection with a search for evidence of the second indirect gap in the silicon absorption coefficient spectrum reported in the previous chapter.[9] The work reported here supplements that work by showing what additional steps are necessary to achieve high accuracy. Combining the techniques described in this chapter with those described in Chapter 3 should allow high-precision, high-accuracy measurements over a large range of transmittance.

There are two reasons why a large range of transmittance is desirable. Since the absorption coefficient of silicon changes by many orders of magnitude over the region of the indirect transition, the dynamic range over which accurate transmittances can be measured determines

the number of samples needed to cover the whole spectral range. Also, there are certain advantages that accrue directly from calculating the absorption coefficient from small values of transmittance. The transmission of an optically thick sample (negligible multiple reflections) is given by the simple expression

$$t = (1-r_f)\,(1-r_b)\,\exp(-\alpha\, x), \qquad (3)$$

where r_f and r_b are the reflectances of the front and back surfaces of the sample, respectively, and x is the sample thickness. Therefore, the total differential of α can be written as

$$\frac{d\alpha}{\alpha} = -\frac{dx}{x} - \frac{1}{\alpha\, x}\left[\frac{dt}{t} + \frac{dr_f}{(1-r_f)} + \frac{dr_b}{(1-r_b)}\right]. \qquad (4)$$

Each of the terms inside the brackets in eq. (4) represents the relative error in a measured quantity due to various sources of random and systematic errors affecting the measurements. As t is decreased, the terms in the brackets remain independent of t until noise in the transmitted signal becomes the largest source of error. Thus, the relative uncertainty in α will have its minimum value at the largest value of x (smallest transmittance) for which the relative uncertainties in the transmittance and reflectances remain independent of the transmittance t.

The following sections describe the silicon sample, the optical measurements, the mechanical measurements, the data reduction, and the uncertainty analysis that were used to derive the absorption and extinction coefficient values reported here.

4.1 SILICON SAMPLE

The transmittance of a 2 cm by 2 cm by 13 μm free standing film of silicon was used for the measurements reported here. It was prepared as follows: A uniform thickness, p-type, epitaxial layer doped with 10^{14} B atoms per cm^3 (50 Ω-cm resistivity) was grown to a nominal thickness of 15 μm on a front-side polished 100 mm diameter p^+ (0.01 Ω-cm) silicon wafer with (100) surface orientation. The rear surface of the wafer was polished. A nominal 25 by 25 mm square sample was cut from the wafer, and masked with wax so as to leave the central 2 cm by 2 cm area of heavily doped substrate exposed. The masked sample was then mounted on a sapphire carrier disk and etched in a rotating-drum mixture of 1 part hydrofluoric acid, 3 parts nitric acid, and 8 parts acetic acid.[10] After eight hours, it was removed and cleaned. The result was a 2 cm by 2 cm free standing film, nominally 15 μm thick, suspended from a square silicon frame 0.64 mm thick and 2 mm wide.

The sample was glued onto a flexible piece of plastic over a 2 cm by 2 cm hole cut in the plastic so that the etched side faced the plastic. The plastic served as a convenient handle for aligning and mounting the sample, and as a strain relief for the sample during handling. Although the sample was reasonably robust due to the frame, it still could be damaged by rough handling, and the plastic served to protect it.

4.2 EXPERIMENTAL MEASUREMENTS

4.2.1 ABSOLUTE TRANSMISSION AND REFLECTION MEASUREMENTS

The absolute transmission measurements were carried out using the experimental setup shown in Fig. 4.1. A HeNe laser emitting 633 nm radiation was used as the source of radiation. The beam was passed through an electro-optical modulator and focused with a microscope objective onto a pin-hole aperture in an opaque screen. The radiation diffracted through the pin hole was collimated with a beam-expanding telescope to produce an Airy disk about 6 mm in diameter. An opaque screen with a 6 mm diameter hole (Airy Filter) was aligned with the first dark ring in the Airy pattern so that only the Airy disk passed through the aperture. This provided a fairly clean and uniform beam of about 40 μW. A beam splitter reflected some of this radiation to a photodiode whose output controlled the transmittance of the modulator so as to maintain a constant power in the beam to within about 0.1% over a period of hours.[11]

The amplitude-stabilized laser beam passed through the sample-holder section of a computer-controlled translation stage (which provided horizontal and vertical motion, and rotation about a vertical axis) and was incident on a photodiode having a 1 cm by 1 cm active area that was located in position T in Fig. 4.1. The photocurrent I_0 from this photodiode was measured with a high-accuracy digital voltmeter and a transimpedance amplifier. In this and all other photocurrent measurements, the measured value was corrected by subtracting the dark current that was measured with the laser light shuttered and the rest of the apparatus in the same configuration as during the photocurrent measurement. The dark current contributed negligibly to I_0, but it contributed a few percent to the transmitted signal.

4.2.1.1 DIRECT TRANSMITTANCE AND REFLECTANCE

The plastic sheet to which the sample was attached was positioned on the sample holder such that the laser radiation was incident on the etched side of the sample, and the bottom and top sides of the sample were parallel to one, and perpendicular to another of the directions of motion of the translation stage on which the holder was mounted. The plastic sheet was fastened to the sample holder in this position with removable transparent tape. In this position the photodiode was 29 cm from the sample. The stages were then translated so that the 6 mm diameter HeNe radiation beam was centered on the nominal center of the sample, and the photocurrent $I_d(j,k)$ (where $j = -1, 0, 1$, and $k = -1, 0, 1$) due to the directly transmitted radiation was recorded as a function of the position of the sample over a 3 by 3 grid of points on the sample having a 2 mm grid spacing, with the center of the grid pattern coincident with the nominal center of the sample.

The sample was removed from the sample holder, rotated 180° about a vertical axis, remounted, and centered as described above. The translation stage was rotated about 9° off perpendicular to the direction of the laser beam to allow the reflectance of the sample to be measured by the photodiode in position R in Fig. 4.1. The resulting photocurrent I_r reflected from the nominal center of the sample was recorded. The photodiode was relocated to position T in Fig. 4.1, but at 12 instead of 29 cm from the sample, and the photocurrent I from the radiation directly transmitted through the center of the sample was measured.

The photocurrent I was 1.7% greater than $I_d(0,0)$, which was measured

at the nominal center of the sample when the etched side of the sample faced the laser and the photodiode was 29 cm from the sample. This difference could be caused by a failure to irradiate exactly the same area of the sample when aligning the laser beam with the nominal center of the sample, or by the different angle of incidence for the different measurements. It could also be caused by slightly more scattered radiation falling on the photodiode when located 12 cm from the sample than when located 29 cm from the sample. In any event, the difference between I and $I_d(0,0)$ was not due to laser drift: After the measurement described above, the sample was removed from the sample holder and I_0 was remeasured. The two measurements of I_0 agreed to within 0.1%, indicating the stability of the amplitude-stabilized laser beam.

4.2.1.2 SCATTERED TRANSMITTANCE

A scattermeter package[12] consisting of a box-shaped array of photodiodes with a 1 cm by 1 cm hole in the center of the array as shown in Fig. 4.2 was used to measure the transmitted radiation that was scattered out of the directly transmitted beam. First, the photodiode used to measure the directly transmitted radiation was removed. Then, with the sample still out of the sample holder, the scattermeter was aligned in the beam so that it collected all of the beam on its interior surface, and the photocurrent I_{s0} was recorded. Next, the sample was remounted with the etched surface facing the scattermeter, and recentered. The scattermeter was then located 10 cm from the sample as shown in Fig. 4.3, so that the 1 cm by 1 cm opening in the top of the scattermeter was 12 cm from the sample in the position previously occupied by the photodiode measuring the directly transmitted radiation. The photocurrent I_{s1} was recorded. The

scattermeter was then moved so that its base was only 2.2 cm from the sample, care being taken to keep the directly transmitted beam in the center of the 1 cm by 1 cm opening in the top of the scattermeter 4.2 cm from the sample. The photocurrent I_{s2} was then recorded. The results, which are $I_{s1}/I_{s0} = 0.060\%$ and $I_{s2}/I_{s0} = 0.094\%$, were used in the calculation of the total transmittance as described next.

4.2.1.3 TRANSMITTANCE AND REFLECTANCE DATA REDUCTION

The transmittance t(j,k) of the sample was calculated for the same 9 points of the 3 by 3 grid from

$$t(j,k) = \frac{I_d(j,k)}{I_d(0,0)} \left[\frac{I}{I_0} + \frac{I_{s1}}{I_{s0}} + \frac{I_{s2}}{I_{s0}} \right], \qquad (5)$$

where the first term in the brackets is the contribution to the transmittance from the directly transmitted beam that was measured with the set up of Fig. 4.1, and the last two terms in the brackets are the contributions from the scattered transmittance that was measured with the set up of Fig. 4.3.

Equation (5) is based on the following assumptions: 1) The relative transmittance as a function of position on the sample surface is independent of the distance from the sample at which it is measured, 2) The transmittance of the sample is independent of whether the radiation is transmitted from the etched surface to the polished surface, or vice versa, and 3) that the transmitted radiation that is scattered is proportional to the directly transmitted radiation. The t(j,k) values calculated from eq. (5) are listed in Table 4.1.

The polished side of the sample, which faced the laser beam, was

smooth enough to reflect specularly with negligible scattering. Moreover, when the radiation was incident on the polished side of the sample, the fraction that was reflected from the etched side was attenuated by $(1-r)^2 \exp(-2 \alpha x)$ (which is less than 2×10^{-4}) as it was transmitted through the polished face of the sample to the etched face, and back again. Therefore, the scattered component of radiation reflected from the etched surface was negligible compared to the radiation reflected specularly from the polished surface, and no attempt was made to measure it.

The reflectances of both faces of the sample were calculated as

$$r_b = r_f = I_r/I_0 = 0.3454, \qquad (6)$$

under the assumption that the roughness of the etched surface was not large enough to change the reflectance of the surface significantly, even though it was large enough to scatter a significant amount of radiation out of the directly transmitted beam. How this assumption was tested is described in the next section.

4.2.2 MECHANICAL MEASUREMENTS

4.2.2.1 SURFACE ROUGHNESS

The characterization of the roughness of the etched surface of the sample was carried out by measuring the roughness along five lines located on the sample as shown in Fig. 4.4 using the NIST Stylus/Computerized System,[13] in which a high-resolution TALYSTEP stylus instrument is calibrated on the 200,000X vertical magnification range against a 0.0291 μm step-height standard that was measured interferometrically. To allow the fine structure of the surface to be resolved, a stylus width of 0.15 μm with a loading of 0.15 mgf (1.5

μN) was used. The TALYSTEP ISO filter (2CR) was used, and the cut-off wavelength was 0.0976 mm (25% attenuation). The traversing speed was 0.122 mm/s over a distance of 0.4 mm. Since the instrument's high-frequency response is 85 Hz, the surface profile could be detected over a wavelength range extending from about 1.44 μm (corresponding to the frequency response of the instrument) to 97.6 μm (the filter cut-off wavelength). The root-mean-square surface roughnesses R_q over this wavelength range varied from 7.2 to 10.0 nm for the five lines, while the arithmetic average roughness R_a varied from 6.3 to 8.1 nm. This is not large enough to disturb the mechanical thickness measurements described next, nor to change the reflectance of the surface by as much as one percent, but it is large enough to scatter both transmitted and reflected radiation significantly out of the respective direct and specular directions.

4.2.2.2 SAMPLE THICKNESS

A high accuracy, laser-interferometer micrometer (a GCA LASERULER) that had a resolution of 0.01 μm and an estimated uncertainty of ± 0.13 μm was used to measure the thickness of the sample. The micrometer was fitted with a hemispherical, steel-tipped probe, 0.2 inches (5.1 mm) in diameter, and a steel surface plate with a nominal diameter of 130 mm was centered under the probe. The digital output from the laser-interferometer that was connected to the probe shaft was set to zero when the probe was driven against the surface plate with the probe-driving mechanism. The probe was then raised from the surface plate and driven against it, and the zero point height recorded six times. The probe was again raised, the sample placed on the surface plate with its polished surface down, and the probe driven to within a millimeter of the etched surface. In this position, the

sample location was adjusted to be nominally centered under the probe as determined by sighting along the diagonals of the sample.

The probe was then lowered and raised six times, and the sample thickness was recorded each time. The zero point thickness measurements were then repeated six times. The thickness h was calculated from the difference of the mean of the thickness measurements and the mean of zero point measurements. The value determined in this way was h = 12.86 ± 0.02 μm, where the stated uncertainty is one standard deviation of the reported value. The purpose of this value was to serve as a consistency check on the data on the variation of thickness over the sample that is described next.

The laser-interferometer micrometer had no provision for precise sample alignment and centering. The following procedure was used to assure that the thickness measurements were carried out in such a way that they could be approximately aligned with the 3 by 3 grid where the direct transmittance was measured: A small piece of graph paper was fastened to the surface plate with removable transparent tape in such a way that one corner of the plastic sheet to which the sample was fastened fell in the center of the graph paper when the sample was nominally centered under the micrometer probe. The graph paper did not extend under the sample for any position of the sample that allowed the probe to touch the etched surface of the sample. The plastic sheet was then aligned so that one edge was parallel to one of the lines on the graph paper, one corner was aligned with a point where horizontal and vertical lines on the graph paper crossed, and the micrometer probe was located over the etched portion of the sample near one corner. The plastic sheet was then translated over an 8 by 8

grid with a 2 mm grid spacing and the height z(m,n), m = 0, ..., 7, n = 0, ..., 7, of the sample measured at each grid point. After the measurement of z(m,n) at each grid point, the plastic sheet was returned to the starting point (0,0) and the thickness z(0,0;m,n) was remeasured to monitor indirectly any zero drift in the digital readout of the micrometer.

When the measurements described above were completed, the plastic sheet was removed and a zero point reading was taken. The zero-point reading had drifted by 0.32 μm during the set of 64 grid point and 64 reference point measurements, but the reference point measurements indicated that the zero-point reading had reached even larger values a few times during the measurements. Therefore, the reference point measurements were used in making the zero-point corrections to the thickness map data.

The plastic sheet was then alternately aligned at the point (1,3) and removed three times, so that three measurements of sample thickness followed by three measurements of the zero point value could be recorded. The thickness h(1,3) = 12.79 ± 0.00 μm of the sample at the point (1,3) was calculated as the mean of the sample thickness measurements minus the mean of the zero point readings. The uncertainty was calculated in the same way as it was for the measurement at the nominal center of the sample that was described at the beginning of this section.

Finally, the thickness h(m,n) of the sample at each grid point was calculated as

$$h(m,n) = h(1,3) + [z(m,n) - z(0,0;m,n)] - [z(1,3) - z(0,0;1,3)]. \quad (7)$$

In this equation h(1,3) is the value of 12.79 μm measured at the grid position (1,3), [z(m,n) - z(0,0;m,n)] is the relative variation in thickness measured at the grid points (m,n), and [z(1,3) - z(0,0;1,3)] is a correction to make h(m,n) = h(1,3) when (m,n) = (1,3).

Table 4.2 shows the h(m,n) data obtained from eq. (7). Figure 4.5 shows as crosses the approximate location of the 8 by 8 grid where the h(m,n) data were measured on the sample as determined by observing the location of the sides of the micrometer probe relative to the corners of the sample after the measurement described above was completed. For comparison, Fig. 4.5 also shows as x's the nominal location of the transmittance measurements reported earlier in this paper. The circled x is the point (0,0) for the transmittance data, and it is also the nominal location of the thickness measurement reported earlier in this section as a consistency check. That value, h = 12.86 ± 0.02 μm, agrees to within 0.1 μm with the expected value on the basis of the data shown in Table 4.2.

4.2.2.3 ELASTIC COMPRESSION CORRECTION

All of the silicon thicknesses reported so far contain an error due to the elastic compression of the hemispherical probe tip and the surface that it contacts under the load of a thickness or zero-reference measurement. The true thickness of the sample h_t is related to the difference h between the sample-in and sample-out measurement by $h_t = h + \Delta h$, where $\Delta h = \alpha_2 - \alpha_1$ as is illustrated in Fig. 4.6. The subscript 1 applies to the steel surface plate, and the subscript 2 applies to the silicon sample. To calculate Δh, the equation for the

elastic compression α_i of a sphere in contact with a flat surface,

$$\alpha_i = \frac{(3 \pi p [V_{flat\ i} + V_{sphere}])^{2/3}}{2 D^{1/3}}, \qquad (8)$$

was used. In eq. (8), p is the total applied force, D is the diameter of the sphere, and

$$V_j = (1 - \sigma_j^2)/ (\pi E_j), \qquad (9)$$

where σ_j is Poisson's ratio of the j^{th} material, and E_j is the modulus of elasticity of the j^{th} material.[14]

Reference [14] gives 0.956×10^{-8} in^2/lbf (1.39 pm^2/N) for V_{steel}. References [15] and [16] give 0.44 and 1.56×10^6 lbf/in^2 (3.0 and 10.8 GN/m^2) for σ_{Si} and E_{Si}, respectively, without indicating the crystallographic direction to which the values actually apply. For forces applied to a silicon (100) surface, E_{Si} is given by

$$E_{Si} = (C_{11} + 2 C_{12}) (C_{11} - C_{12})/(C_{11} + C_{12}), \qquad (10)$$

where C_{kl} are the tensor stiffness constants of silicon.[17] Reference [18] gives values for C_{kl} from which $E_{Si} = 18.9 \times 10^6$ lbf/in^2 (130 GN/m^2) was calulated. The diameter of the tip of the hemispherical probe was measured to be 0.20 inches (5.1 mm), and the force applied during a thickness measurement was measured to be 0.154 lbf (0.658 N). Using the above values, $\Delta h = 0.035$ μm was calculated and assigned plus or minus this value as a conservative uncertainty.

4.3. DATA REDUCTION AND UNCERTAINTY ANALYSIS

4.3.1 ABSORPTION COEFFICIENT

An absorption coefficient value was calculated for each of the transmittance measurements by inverting eq. (3) with $r_f = r_b = 0.3454$, to obtain

$$\alpha(j,k) = \frac{-\ln(t(j,k)/[(1-r_f)(1-r_b)])}{x(j,k)+\Delta h}, \qquad (11)$$

where

$$x(j,k) = \frac{\left[\sum_{m=j+2}^{m=j+5}\sum_{n=k+2}^{n=k+5} w(m-j-3,n-k-3)\ h(m,n)\right]}{108}, \qquad (12)$$

for $j = -1, 0, 1$, $k = -1, 0, 1$, and where the weights $w(u,v)$ for $u = -1, 0, 1, 2$, $v = -1, 0, 1, 2$ are listed in Table 4.3. These weights, which were chosen to be the proportional to the areas shown in Fig. 4.7, average the measured sample thickness over approximately the same 6 mm diameter area in the center of the sample as was used in the transmittance measurements. Table 4.4 lists the resulting average thicknesses $x(j,k)$, and Table 4.5 lists the absorption coefficient values obtained from eq. (11).

4.3.2 UNCERTAINTY ANALYSIS

The uncertainty in the absorption coefficient can be calculated from the total differential in eq. (4). First consider the sources of error that are common to every point (j,k). These sources of error include systematic radiometric errors in both the direct and the scattered transmittance measurements, and in the reflectance measurement, uncertainties associated with using the reflectance measured

from the polished side of the sample to represent that from the etched side, and with using the sum of the measured scattered transmittances to represent the true scattered transmittance. Inaccuracies in the laser micrometer and the calculation of the depth Δh to which the micrometer probe penetrates into the silicon during the thickness measurement are also sources of error common to all of those measurements. These sources of error and uncertainty estimates for them are listed in Table 4.6. Also listed there is the quadrature sum of their contributions to the relative uncertainty in the absorption coefficient according to eq. (4).

Referring to Table 4.6 and eq. (4), recall that the measured sample thickness was approximately 13 μm. Since the uncertainty associated with the laser micrometer is 0.13 μm, it contributes 1% to the uncertainty in the absorption coefficient. Similarly, the 0.035 μm uncertainty assigned to the compression of the silicon, the surface plate and the probe tip contributes 0.27%.

There is a 1% uncertainty associated with the transmittance-photocurrent ratios because the gain of the current-to-voltage converter was 100 times greater for the measurements of the numerator photocurrents than for the denominator photocurrents, and 1% is the between-range gain accuracy of the transimpedance amplifier used. An uncertainty of 25% of the measured components of the scattered transmittance was used as a conservative estimate of the error associated with the use of the sum of these quantities for the true scattered transmittance. Since the sum of the measured components of the scattered transmittance was about 15% of the total measured transmittance, the relative uncertainty is about 3.8%. An uncertainty of less than 0.1% is associated with

the reflectance ratio since the same gain was used for both the numerator and the denominator photocurrents in this measurement. However, an uncertainty of 1% was associated with r_b to allow for the possibility that it was smaller than r_f due to the roughness of the etched surface. According to eq. (4), each of these uncertainties is multiplied by a factor of $1/\alpha x$ (about 1/4 for this sample and wavelength) in its contribution to the uncertainty in the absorption coefficient, as shown in the table.

Sources of error that contribute differently to the absorption coefficient values at the different points (j,k) are the random errors in the measurements of the transmittance, reflectance, and thickness. The first two errors are negligible at 0.1% or less. The third error might not be negligible, but its actual contribution to the data reported here cannot be distinguished from the error associated with the variation in thickness of the sample as a function of position over its surface.

It is not really clear how to estimate the uncertainty to be associated with the variations in sample thickness. The thickness averaging procedure was designed to eliminate errors from this source. However, the procedure is not perfect because the transmittance values and the average thicknesses do not weight the same parts of the sample in the same way. The transmittance values weight the points of the sample within a 6 mm diameter region according to the intensity of the Airy disk. The average thickness weights 13 points on a 2 mm by 2 mm grid nonuniformly to approximate equal weighting of all points in a 6 mm diameter region. Furthermore, the centers of the corresponding regions over which the transmittance and thickness averages were

computed are only approximately aligned.

Plus or minus the half-range of the data listed in Table 4.5 is a conservative estimate of the uncertainty to associate with both the random errors in the measurement of, and the variations in, the sample thickness. This results in a contribution of 0.76% to the relative uncertainty in the absorption coefficient. When this is added in quadrature with the relative uncertainties reported in Table 4.6, an overall uncertainty of 1.94% is obtained.

The average of the values in Table 4.5 is $\alpha = 3105\ cm^{-1}$. Thus, this value is reported here as the absorption coefficient of silicon at a photon energy of 1.9587 eV, or vacuum wavelength of 633.00 nm with an estimated (one-standard-deviation equivalent) uncertainty of ±2%. This corresponds to a value of $k = 0.01564$ for the extinction coefficient with the same uncertainty.

4.3.3 COMPARISON WITH EXISTING DATA

Figure 4.8 compares the data reported here at 1.96 eV (filled diamond) with some of the more noteworthy data previously reported in the 1.9 to 2.3 eV spectral region. The open circles are the handbook data of Ref. [7] and the closed circles are the handbook data of Ref. [8]. The dashed line is the data (for which no tabulated values were published) of Ref. [4], and the full line is data (for which no tabulated values were published) of Ref. [5]. The open diamond is the value reported in Ref. [6], along with the reported uncertainty. The value reported here is the closed diamond.

The result reported here has an estimated uncertainty that is signifi-

cantly smaller than the other results shown in Fig. 4.8, due to combining a higher quality sample with more accurate and precise thickness and transmittance measurements. Two uncertainties dominate the uncertainties listed in Table 4.6. These are the measurement of the thickness of the sample and the measurement of the scattered component of the transmittance. It should be possible to improve both of these measurements to reduce the overall uncertainty to below 1%, either by using more accurate instrumentation, and/or by improving the sample quality. In either case it would be necessary to obtain a more accurate laser micrometer.

Other desirable improvements in instrumentation would include a more accurate scattermeter, and a precision translator that clamps onto both the surface plate used in the thickness measurements and the sample holder used in the transmittance measurements. The latter would allow precise alignment of the areas weighted by the thickness and transmittance measurements, as well as a finer density of points for the thickness measurements.

Improvements in the sample preparation procedure that resulted in a sample having a more uniform thickness and a smoother rear surface would eliminate the requirement for the improved scattermeter and the translation stage. However, at the present time, it is not clear how to improve in the sample preparation procedure to provide a smoother rear surface and a more uniform thickness.

The data of Ref. [5] agree with the value reported here to within the uncertainty of this value. Furthermore, the difference between the value reported by Taft[6] at 514 nm and the data of Ref. [5] at the same

wavelength is not large enough relative to estimated uncertainty in the former to be a source of concern. Thus, of the data shown in Fig. 4.8, the data of Ref. [5] appear to be the most suitable for representation by a simple equation. The next chapter describes an equation that was fit to the data of Ref. [5], and how well this equation agrees with other selected data sets.

TABLE 4.1. The absolute transmittance t(j,k) measured on the silicon sample described in this paper.

t(j,k)			
\j k\	-1	0	1
1	0.00802	0.00778	0.00824
0	0.00786	0.00783	0.00816
-1	0.00766	0.00768	0.00800

TABLE 4.2. The thickness h(m,n) of the sample at points located at the approximate positions indicated in Fig. 4.5.

\m n\	0	1	2	3	4	5	6	7
	h(m,n) in μm							
7	10.97	11.59	11.49	11.99	12.11	11.75	13.29	10.70
6	12.42	12.66	12.80	12.58	12.60	12.56	12.24	11.68
5	12.89	12.82	13.15	12.83	12.44	12.66	12.76	11.93
4	12.94	13.01	12.79	12.81	12.54	12.80	12.88	11.84
3	12.97	12.79	12.71	12.96	12.81	12.79	12.85	11.80
2	12.95	13.05	12.95	12.66	13.02	12.88	12.50	11.68
1	12.95	12.90	13.05	13.14	12.73	12.58	12.56	11.59
0	12.17	12.61	12.68	12.74	12.55	12.30	11.97	11.36

TABLE 4.3. The weights w(u,v) used in calculating average thickness of the sample over the regions irradiated during the transmittance measurements.

108·w(u,v)				
v\ u\	-1	-0	1	2
2	0	3	1	0
1	7	16	14	1
0	11	16	16	3
-1	2	11	7	0

TABLE 4.4. The average thickness x(j,k) of the sample over the same areas for which the transmittance data are shown in Table 4.1.

---------- x(j,k) in μm ----------

\j k\	-1	0	1
-1	12.87	12.75	12.69
0	12.84	12.78	12.79
1	12.89	12.88	12.81

Table 4.5. The absorption coefficients $\alpha(j,k)$ of silicon at 633 nm determined from the data in Tables 4.1 and 4.4.

$\alpha(j,k)$ in cm^{-1}			
\j k\	-1	0	1
1	3114	3106	3090
0	3114	3123	3128
-1	3099	3089	3081

Table 4.6. The sources of error and associated uncertainty estimates for the sources of error that are common to the thickness and transmittance measurements at all points on the sample.

Source of error	Estimated uncertainty	
dx/x		times 1
micrometer accuracy	1.00%	1.00%
compression correction	0.27%	0.27%
dt/t		times $1/\alpha x$
$I_d(j,k)/I_d(0,0)$	1.0%	0.25%
I/I_0	1.0%	0.25%
I_{s1}/I_{s0}	1.0%	0.25%
I_{s2}/I_{s0}	1.0%	0.25%
$(I_{s1}+I_{s2})/I_{s0}$ for true scatter	3.8%	0.95%
$dr_f/(1-r_f)$		times $1/\alpha x$
I_r/I_0	$<$ 0.1%	0.02%
$dr_b/(1-r_b)$		times $1/\alpha x$
use of r_f for r_b	1.0%	0.25%
sum in quadrature	-	1.79%

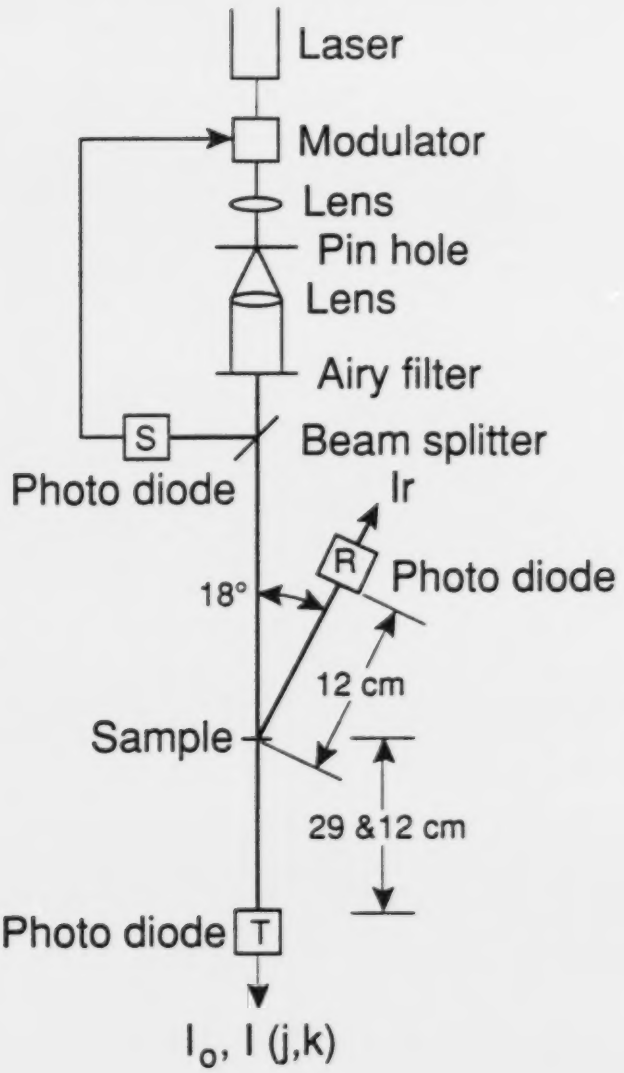

FIGURE 4.1. Apparatus for measuring the transmittance and reflectance of the silicon sample at the 633 nm HeNe laser line. The photodiodes S, R, and T are used to stabilize the output power in the laser beam, to measure the reflectance, and to measure the transmittance of the sample, respectively.

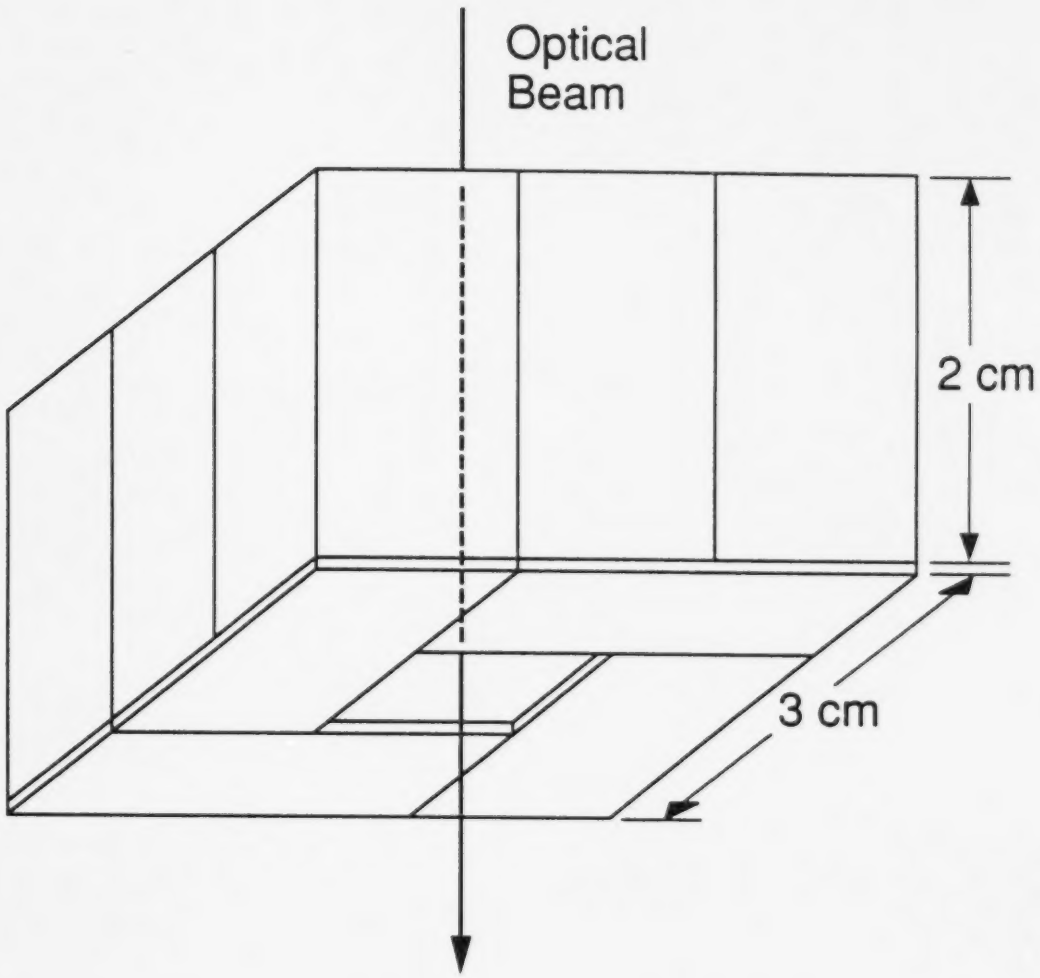

FIGURE 4.2. Illustration of the box-shaped scattermeter made from an array of photodiodes to measure the scattered component of the transmitted HeNe laser radiation.

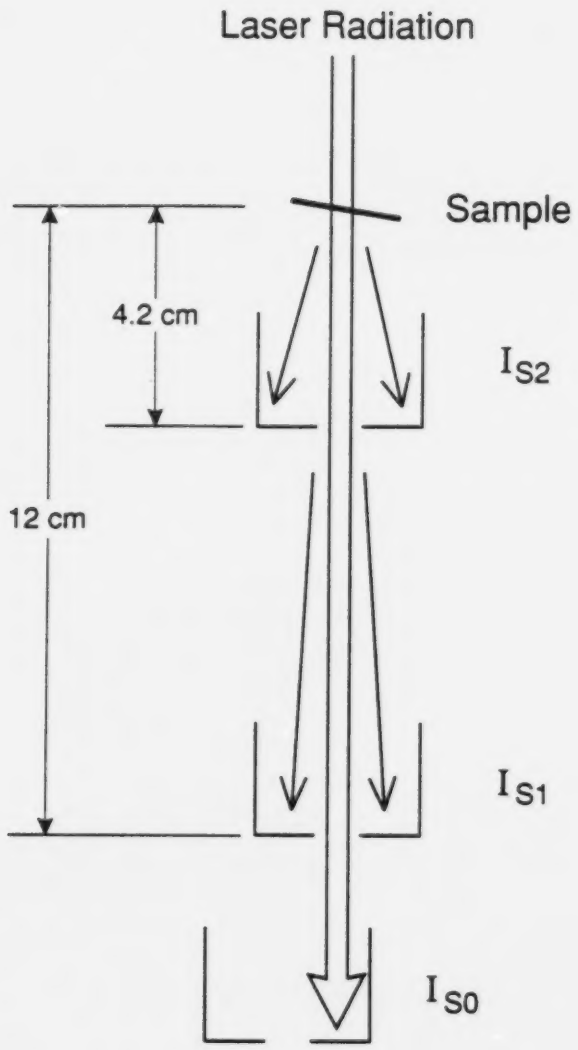

FIGURE 4.3. Illustration of the use of the scattermeter shown in Fig. 4.2 to measure some scattered components of the transmitted HeNe laser radiation.

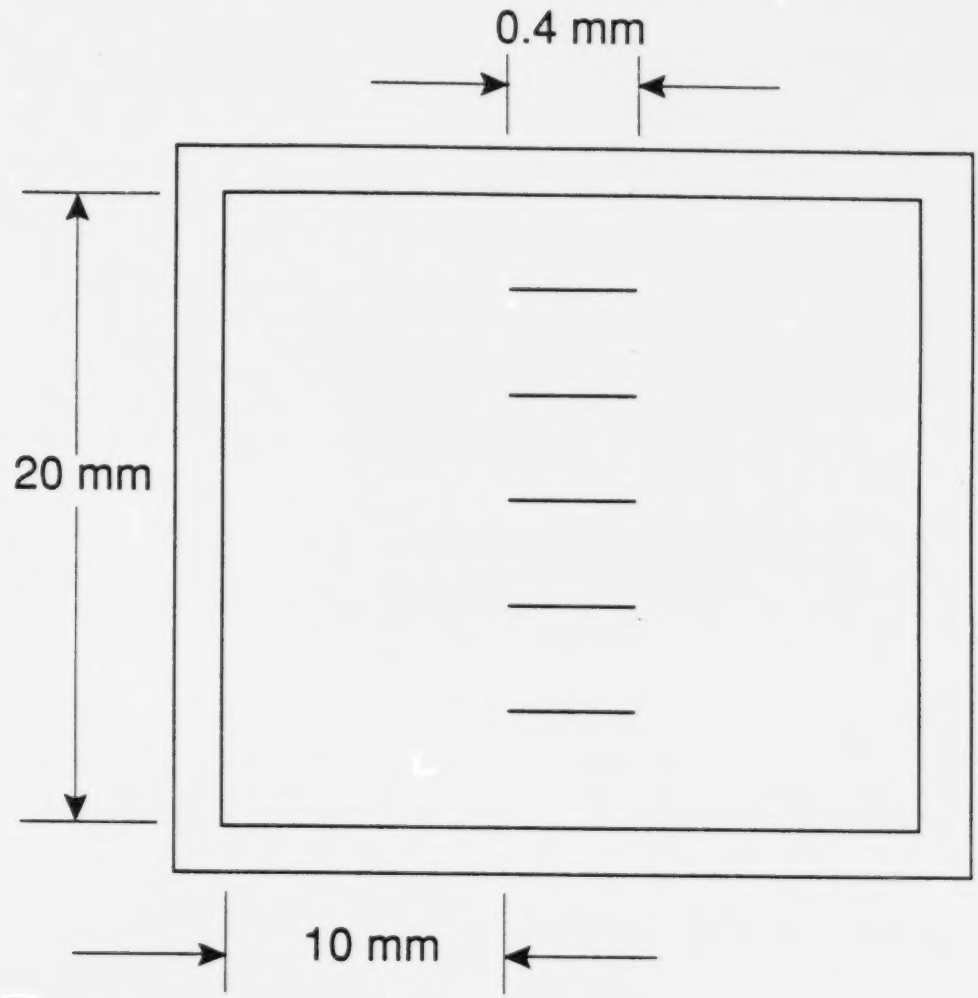

FIGURE 4.4. Illustration of the location on the sample of the surface roughness measurements. Note that the length of the surface roughness scans is exaggerated in this figure.

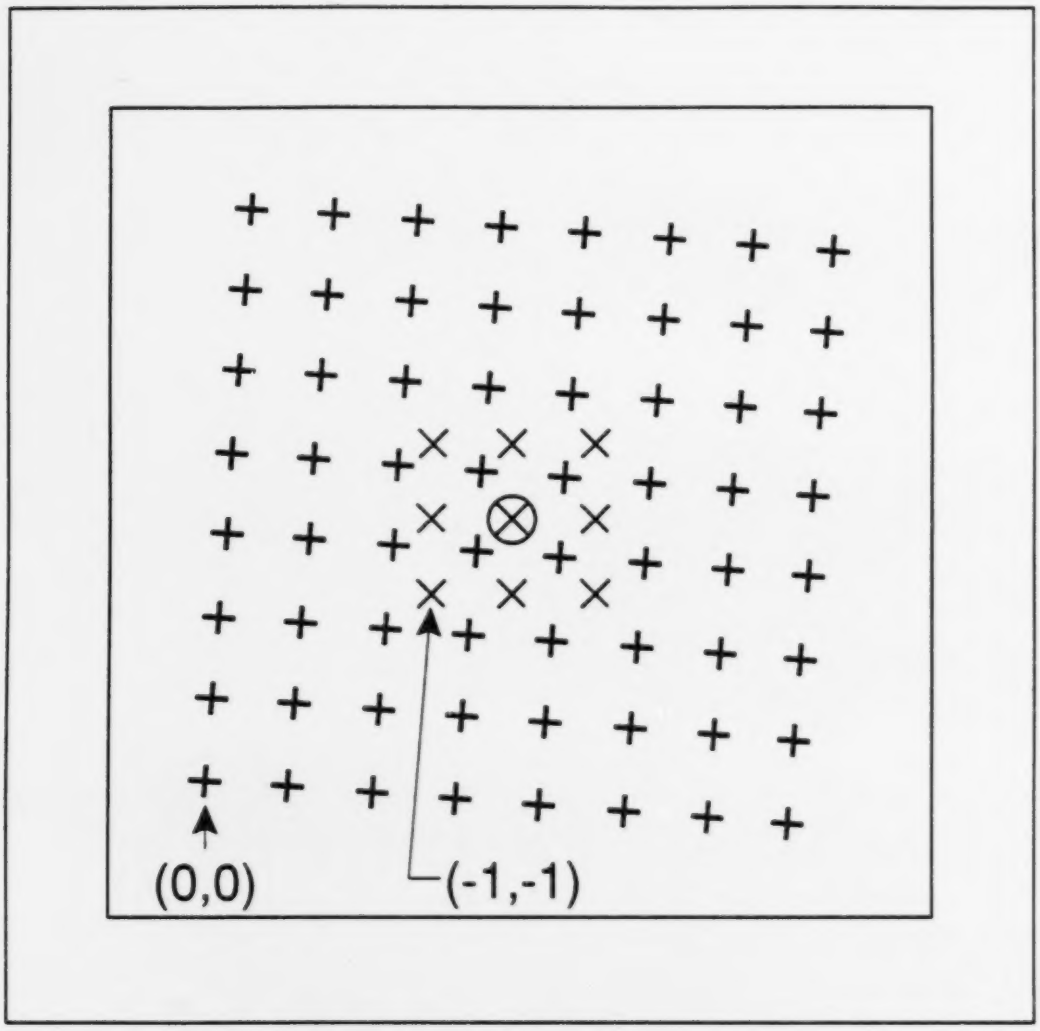

FIGURE 4.5. Approximate relative locations of the thickness measurements (+) and the transmittance measurements (x) relative to the center (circled x) of the sample.

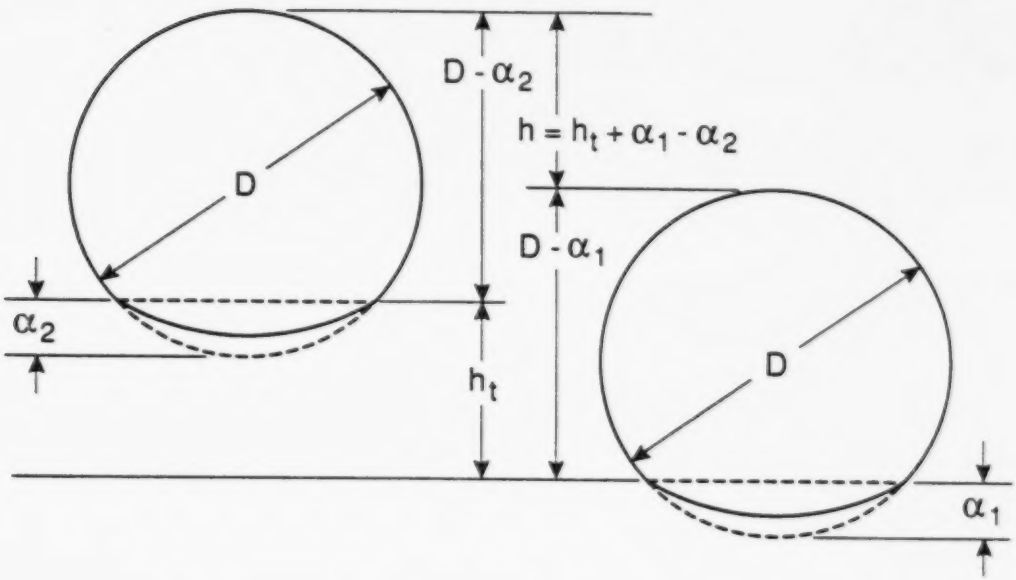

FIGURE 4.6. Illustration showing the relation between the true thickness h_t of the sample and the measured thickness h due to the difference in compression between the sample-in and sample-out measurements with the laser micrometer. The quantity α_1 is the compression when the probe tip presses against the silicon sample with a given force. The quantity α_2 is that when the probe tip presses against the surface plate with the same force.

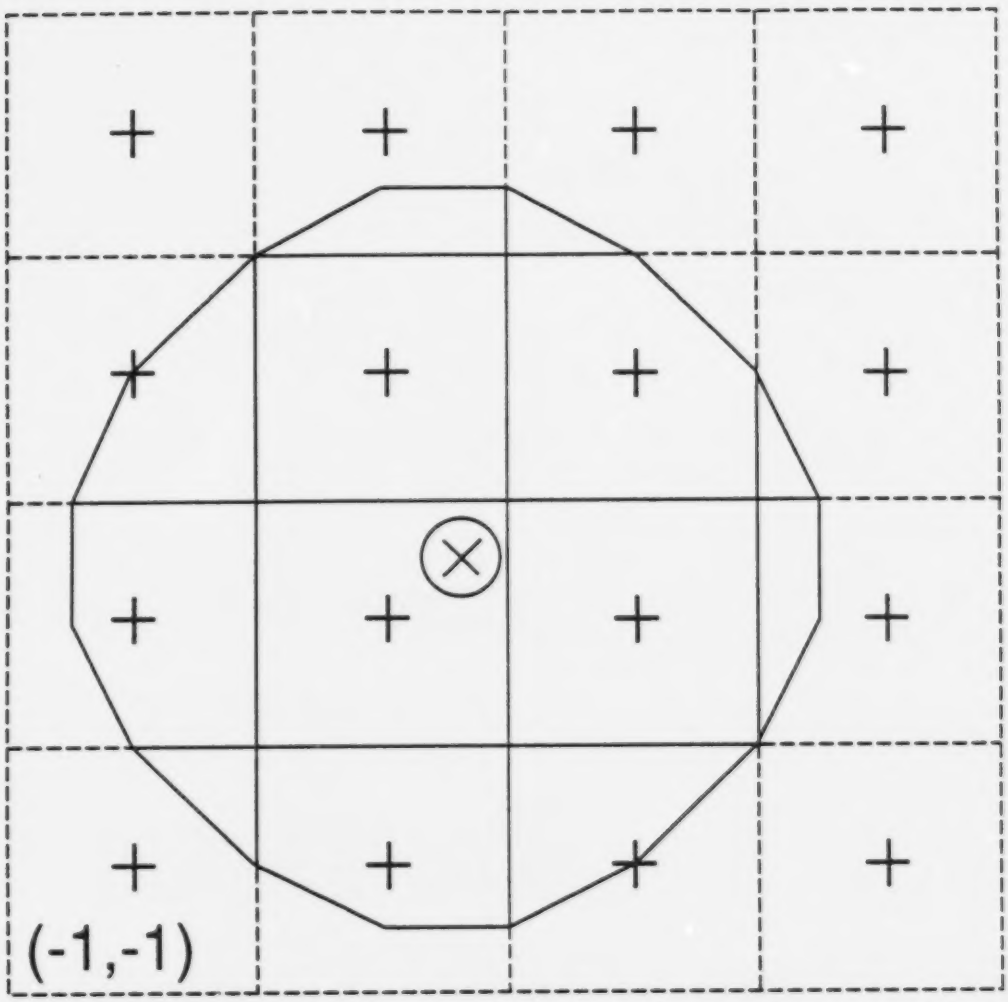

FIGURE 4.7. A polygon of average 6 mm diameter centered on the point that was the center of the nominal 6 mm diameter area irradiated by the laser beam during the transmission measurements. In calculating the average thickness of the sample that was appropriate for the transmission measurement, the thickness at each point (plus sign) where the thickness was measured was weighted by the area enclosed by the solid line surrounding that point.

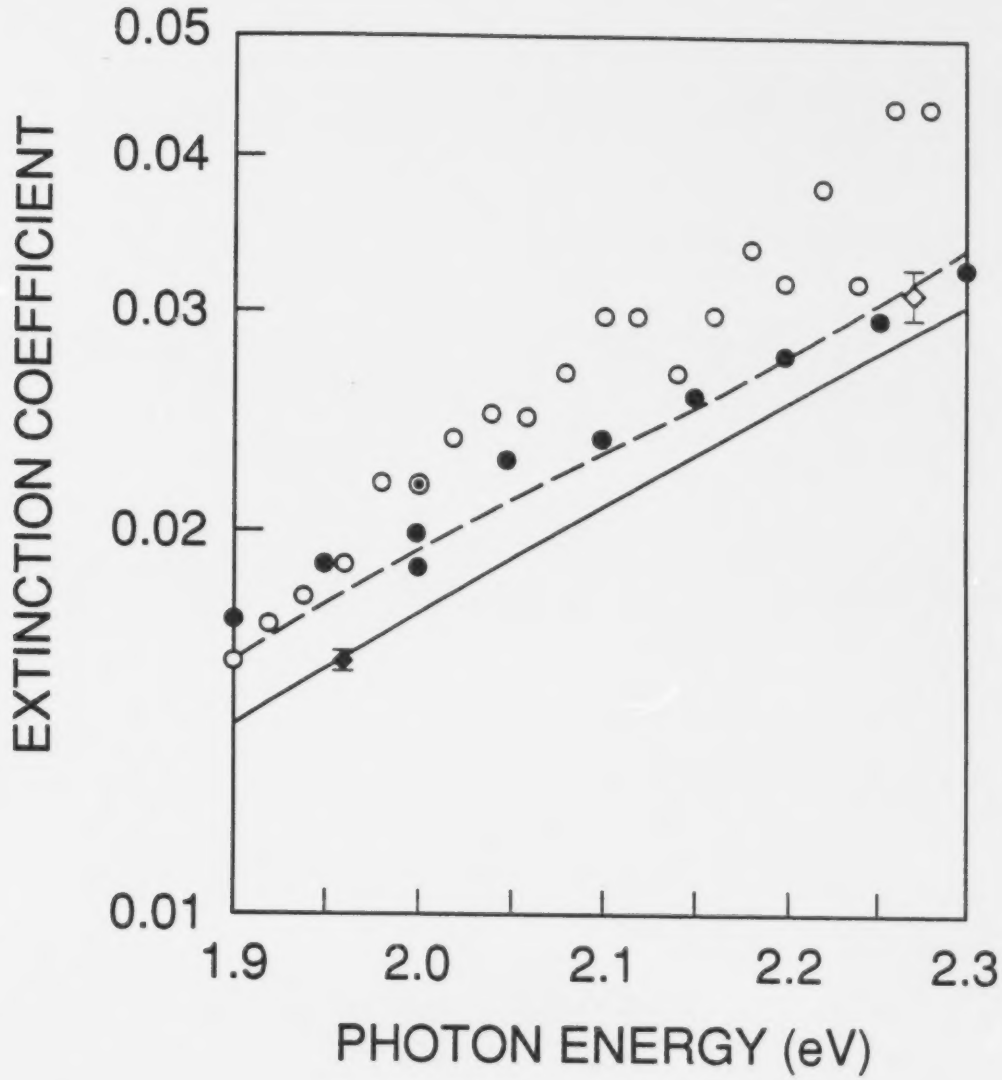

FIGURE 4.8. Comparison of Handbook data (open circles from Ref. [7] and closed circles Ref. [8]), published data reported without tabulation (dashed line from Ref. [4] and continuous line from Ref. [5]), and a single point transmittance measurement (open diamond from Ref. [6]) with the value (closed diamond) reported at 633 nm here.

REFERENCES FOR CHAPTER 4

1. M. Born and E. Wolf, "Principles of Optics, 3rd Edition", page 614 (Pergamon Press, NY, 1965).

2. H. R. Philipp, Influence of oxide layers on the determination of the optical properties of silicon, J. Appl. Phys. **43**, 2835-2839 (1972), and personal communication of spectral values.

3. D. E. Aspnes and A. A. Studna, Dielectric function and optical parameters of Si, Ge, GaP, GaAs, GaSb, InP, InAs, and InSb from 1.5 to 6.0 eV, Phys. Rev. **B27**, 985-1009 (1983).

4. W. C. Dash and R. Newman, Intrinsic optical absorption in single-crystal germanium and silicon at 77°K and 300°K, Phys. Rev. **99**, 1151-1155 (1955).

5. H. A. Weakliem and D. Redfield, Temperature dependence of the optical properties of silicon, J. Appl. Phys. **50**, 1491-1493 (1979), and private communication of spectra values.

6. E. A. Taft, The optical constants of silicon and dry oxygen oxides of silicon at 5461 A, J. Electrochem. Soc. **125**, 968-971 (1978).

7. D. F. Edwards, Silicon (Si), in Handbook of Optical Constants, ed. E. D. Palik, pages 547-569 (Academic Press, Orlando, ISBN 0-12-544420-6, 1985).

8. D. E. Aspnes, Optical functions of intrinsic Si: table of refractive index, extinction coefficient and absorption coefficient vs energy (0 to 400 eV), in Properties of Silicon, EMIS Datareviews (sic) Series No. 4, pages 72-79 (INSPEC, Institution of Electrical Engineers, London, ISBN 0-85296-475-7, 1988).

9. J. Geist, A. Migdall, and H. Baltes, Shape of the silicon absorption coefficient spectrum near 1.63 eV, Appl. Opt. **29**, 3548-3554, (1990).

10. W. C. Dash, Evidence of dislocation jogs in deformed silicon, J. Appl. Phys. **29**, 705-709 (1958).

11. W. Kuhr and E. Yeng, Optimization of sensitivity and separation in capillary zone electrophoresis with indirect fluorescence detection, Anal. Chem. **60**, 2642-2646 (1988).

12. R. Koehler, J. L. Luther, and J. Geist, Reflectometer for measurements of scattering from photodiodes and other low scattering surfaces, Appl. Opt. **29**, 3130-3134 (1990).

13. E. C. Teague, Evaluation, revision, and application of the NBS Stylus/Computer System for the measurement of surface roughness, NBS Technical Note 902, April, 1976.

14. M.J. Putlock and E.G. Thwaite, Elastic compression of spheres and cylinders at point and line contacts, National Standards Laboratory Technical paper No. 25, (CSIRO, Australia, 1969).

15. W.J. McGregor Tegart, Elements of Mechanical Metallurgy, page 92

(MacMillan, NY, 1966).

16. W. L. Forsythe, Smithsonian Physical Tables, 9th Edition, page 190 (Smithsonian Institution, Washington DC, 1954).

17. L. D. Landau and E. M. Lifshitz, Theory of Elasticity: Volume 7 of Course of Theoretical Physics, 3rd Edition, page 37 (Pergamon Press, NY, 1986).

18. C. T. Lynch, Handbook of Materials Science, Volume III: Nonmetallic Materials and Applications, page 160 (CRC Press, Cleveland, OH, 1975).

5. ANALYTIC REPRESENTATION OF THE SILICON ABSORPTION COEFFICIENT

The absorption coefficient of silicon over most of the indirect transition region is essential for modeling silicon solar cells and photodiodes. Interpolation using a table of experimentally determined values covering this spectral region is cumbersome because the absorption coefficient increases many orders of magnitude over the entire region. To avoid interpolation errors significantly larger than the experimental error in the absorption coefficient data, either the table must be very large or the interpolating formula must be based upon the spectral dependence of the absorption coefficient. Therefore, a compact analytical expression for the absorption coefficient that represents the experimental data at the level of accuracy inherent in the data is highly desirable.

5.1 PREVIOUS WORK

Rajkanan, Singh and Shewchun[1] (RSS) and Palmer[2] have developed analytic models of the silicon absorption coefficient spectrum for modeling silicon solar cells and photodiodes, respectively. RSS used a twelve parameter equation to describe the variation of the silicon absorption coefficient as a function of wavelength and temperature, while Palmer[2] fitted a seven parameter equation to the absorption coefficient data of Weakliem and Redfield[3] (WR) at a temperature of 298 K. Palmer's equation is more accurate than that of RSS near room temperature. Even so, it still differs from the WR data by almost 20% in the vicinity of 1.25 and 1.5 eV, and by more than 20% near the band edge.

A version of this chapter has been published: J. Geist, A. Migdall, and H. P. Baltes, Analytic representation of the silicon absorption coefficient in the indirect transition region, Appl. Opt. 27, 3777-3779 (1988).

The results of the last chapter suggest that the WR data are more accurate than Palmer's equation. The purpose of this chapter is to describe a new eleven parameter equation that was fit to the WR data by using standard non-linear least squares fitting techniques. This equation is useful from 1.05 eV to 2.8 eV, and is considerably more accurate than either Palmer's or that of RSS, particularly near the band edge.

5.2 NEW EQUATION

The eleven parameter equation for the absorption coefficient of silicon at 298 K is

$$\alpha(h\nu)/h\nu = \sum_{i=1}^{2}\sum_{j=1}^{2} \{C_{i,j}\,[L(h\nu-\varepsilon_i + (-1)^j\, d\varepsilon_i)]^2\} + C_3\,[2\,L(h\nu-\varepsilon_3)]^{(N+dN\,h\nu)} \qquad (1)$$

where

$$L(\varepsilon) = (\varepsilon + |\varepsilon|)/(2\ \text{eV}), \qquad (2)$$

and the values of $C_{1,2}$, $C_{1,1}$, $C_{2,2}$, $C_{2,1}$, C_3, ε_1, $d\varepsilon_1$, $d\varepsilon_2$, ε_3, N and dN are given in Table 5.1. The units of the C parameters in Table 5.1 give α in cm^{-1} when eV is the unit of energy.

Equation (1) is an approximation to the theoretical expression for the absorption coefficient of silicon that is discussed by McLean[4]. Roughly speaking, the double sum in eq. (1) describes the indirect transition from the parabolic region near the maximum of the valence band to the parabolic region near the minimum of the conduction band across the energy gap ε_1. The sum is made up of four terms to describe the emission (j = 1) and the absorption (j = 2) of transverse

optical (TO) phonons (energy = $d\varepsilon_1$) and transverse acoustical (TA) phonons (energy = $d\varepsilon_2$). The last term in eq. (1) is an attempt to describe the smooth increase beyond the quadratic dependence, as described by McLean[5]. This increase is to be expected from the increasing density of states in the conduction band due to the deviation of the bands from parabolic shape at the higher energies. However, much of the detail described by McLean has been left out in order to reduce the theoretical expression to something practical, which is the sole purpose of this work.

5.3 QUALITY OF FIT TO WR DATA

Figure 5.1 compares eq. (1) (continuous line) with the WR data at 298 K (filled circles), and with the RSS equation evaluated at that same temperature (dashed line). The quality of the fit over the entire spectral range is evident. The standard deviation of one minus the ratio of the values calculated from eq. (1) to the experimental values of WR for the same photon energies is 2.5%, and the maximum difference is less than 10%. On the other hand, the agreement between the RSS equation and the WR data is good only near 1.15 and 2.5 eV, and the difference exceeds 50% near the band edge and over a broad region extending from 1.4 eV to 1.9 eV.

Palmer's equation is not shown in Fig. 5.1, because the difference between his equation and the WR data is not easily resolved at the scale of that figure. Figure 5.2 compares the relative errors in Palmer's equation with the relative errors in eq. (1) normalized to the 298 K experimental WR data set. This figure shows the higher accuracy of eq. (1) over the entire spectral range. It also shows that both equations have difficulty fitting the data in a small region

above 1.4 eV and near the band edge.

Equation (1) is a more accurate representation of the WR data than Palmer's not only because it has more parameters, but also because it more closely resembles the theoretical expression for the absorption coefficient. Equation 1 also has a term to describe the deviation of the conduction band from parabolic shape above 1.4 eV. No such term was included in the RSS equation.

5.4 COMPARISON WITH OTHER DATA

The previous chapter showed that the WR data is accurate to within 2% in the vicinity of 1.96 eV. However, this does not imply equivalent accuracy at lesser and greater photon energies. In fact, that same chapter described the difficulty of preparing and measuring the thickness of silicon samples that are thin enough to allow accurate transmission measurements at photon energies greater than 2 eV. On the other hand, samples thicker than those used by WR are needed in order to assure high accuracy in the very low absorption coefficients at photon energies near the band edge. Thus the range over which the WR data were taken is not necessarily the range over which eq. (1) is useful. In fact, the only way to determine the range over which eq. (1) can be used is to compare it with data that is more reliable than the WR data at the endpoints of the range.

The most accurate absorption coefficient data near the silicon band edge appears to be that of MacFarlane, McLean, Quarrington and Roberts[6,7] (MMQR). This data is based on the transmittance of samples as thick as 1 cm. Figure 5.3 shows a comparison of eq. (1) (dashed line) and the 298 K WR data (large open and filled circles)

with the data of MMQR near the silicon band edge. The continuous lines and small circles in Fig. 5.3 represent the MMQR data for the indicated sample temperatures. This figure shows that eq. (1) is not useful below 1.05 eV. It also shows the level of agreement between the 298 K WR data set and the 291 K MMQR data set in the region of low absorption coefficient where the WR data is subject to large relative errors because their samples were quite thin for this spectral region.

The large filled circles in Fig. 5.3 represent the absorption coefficient values at 298 K that WR derived from a sample 250 μm thick. The large open circles in Fig. 5.3 represent the absorption coefficient values at the same temperature that WR derived from a sample 800 μm thick. There appears to be more noise in the WR data for both samples than in the data of MMQR. As pointed out above, this was expected: Any error in the transmission data from which the absorption coefficient is derived is divided by the optical depth, which is the product of the absorption coefficient and the sample thickness. There also appears to be more noise in the WR data from the 250 μm sample (large circles) than in that from the 800 μm sample (large squares). This too was expected. For instance, the optical depth of the 800 μm sample is 0.013 at 1.06 eV, and that of the 250 μm sample is 0.004 at the same wavelength. This results is a significant amplification of any errors inherent in the measurement procedure, whether they are random or systematic.

Except for the greater apparent noise, the WR data from the 800 μm sample fits the systematic features of the MMQR data. However, these features would not be apparent without the MMQR data as a guide due to the much courser wavelength sampling of the WR data.

Above 2.5 eV the absorption coefficient of silicon is so large that it can be accurately determined from reflectance measurements. These do not require thin samples. Absorption coefficient data reported by Philipp[8], which are based on reflectance measurements, and which were corrected for the presence of a native oxide on the silicon surface, appear to be the most accurate available in the 2.5 to 3.0 eV spectral region. Figure 5.4 compares eq. (1) with the data of Philipp[8]. Notice that the difference is approximately 12% at 1.96 eV where eq. (1) is known to be accurate to within ±2% as reported in the previous Chapter.[9] Between 1.8 and 2.8 eV the differences fall with the range given by 12% ± 4%. Above 2.8 eV the differences between Philipp's data and the values calculated from eq. (1) are almost certainly due to errors in the latter. Therefore, 2.8 eV seems to be the upper end of the range of usefulness of eq. (1).

5.5 CONCLUSION

Equation 1 of this chapter appears to be an accurate representation of the silicon absorption coefficient spectrum at 298 K over the 1.05 to 2.8 eV spectral region. The absolute value of the spectrum is reproduced to within ±2 % at 633 nm,[9] but the error could be larger at other photon energies, particularly near the low and high energy end of the spectral range. Over most of the 1.05 to 2.8 eV spectral range the shape of the spectrum appears to be reproduced to within ±4%. However, near 1.05 eV the error associated with eq. (1) could be as large as 10%. Near 1.4 eV the error might also be as large as 10%, but both theory and the experimental results of Chapter 3 suggest that the WR data is in error at this photon energy.[10]

TABLE 5.1. Parameters for use in eq. (1) to describe the absorption coefficient of silicon from 1.05 to 2.8 eV. The right most digits in these parameters are not significant, but were retained to maximize the precision of the fits.

PARAMETER	VALUE
ε_1	1.09969 eV
$d\varepsilon_1$	0.0583148 eV
$C_{1,2}$	483.916 cm^{-1} eV
$C_{1,1}$	5030.02 cm^{-1} eV
$d\varepsilon_2$	0.0220161 eV
$C_{2,2}$	79.4079 cm^{-1} eV
$C_{2,1}$	1634.30 cm^{-1} eV
ε_3	1.40985 eV
C_3	1046.08 cm^{-1} eV
dN	1.23084 eV^{-1}
N	0.394122

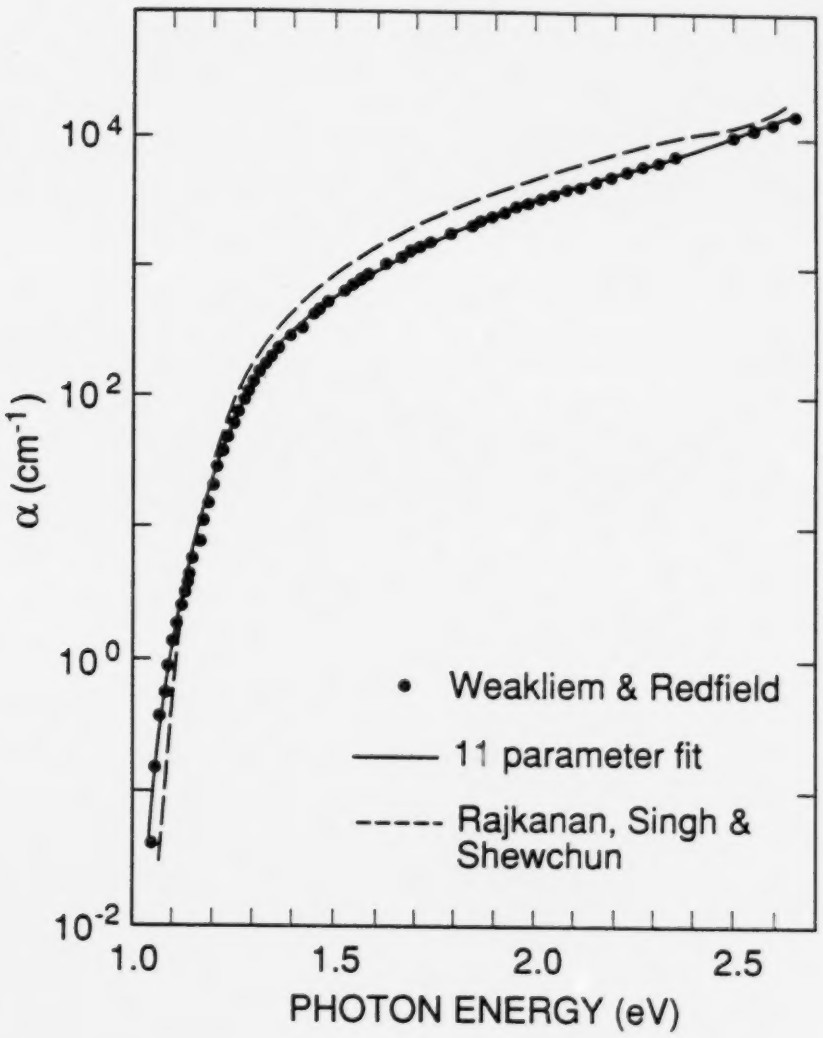

FIGURE 5.1. Comparison of Weakliem and Redfield's experimental silicon absorption coefficient data at 298 K (filled circles) with eq. (1) of this Chapter using the eleven parameters given in Table 5.1 (continuous line) and with the equation of Ref. [1] (dashed line).

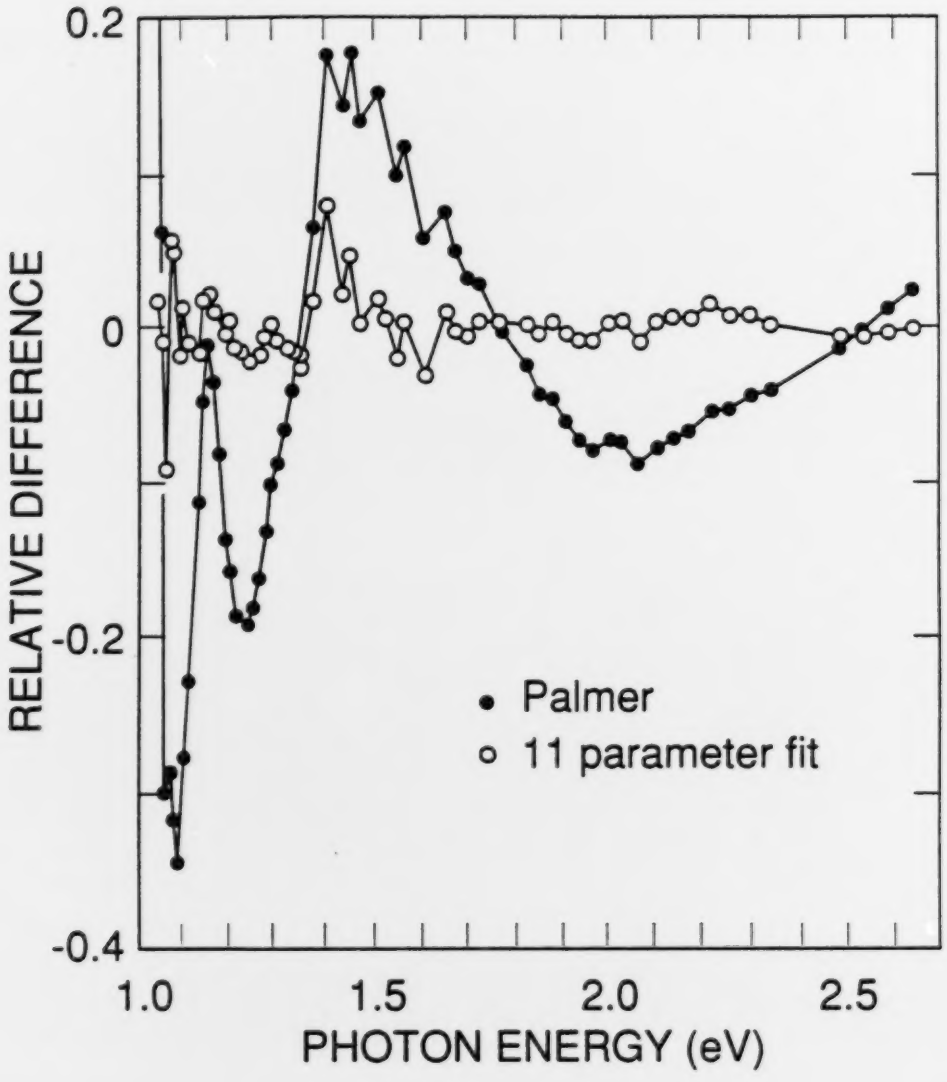

FIGURE 5.2. Comparison of the ability of the seven parameter equation of Ref. [2] (filled circles) and the eleven parameter eq. (1) of this Chapter (open circles) to represent Weakliem and Redfield's 298 K silicon absorption coefficient data.

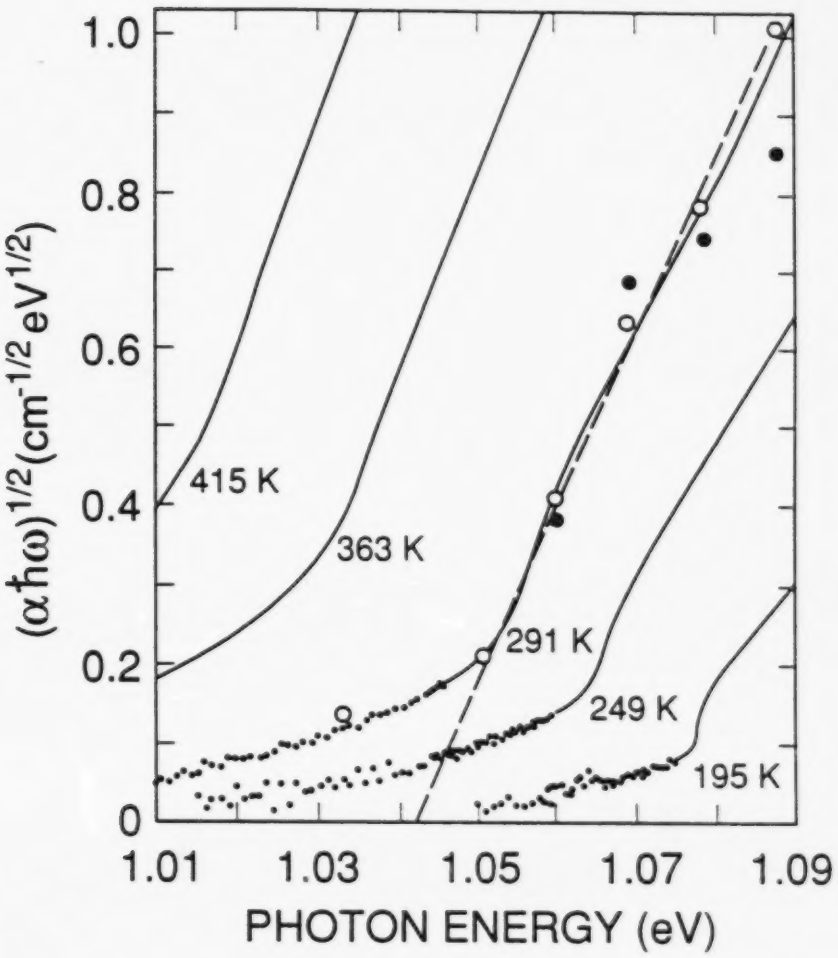

FIGURE 5.3. Comparison near the absorption band edge of Weakliem and Redfield's 298 K silicon absorption coefficient data (large filled circles for the 250 μm sample and large open circles for the 800 μm sample), eq. (1) representing their data (dashed line), and the more detailed data set of MacFarlane, McLean, Quarrington and Roberts (small circles and continuous lines).

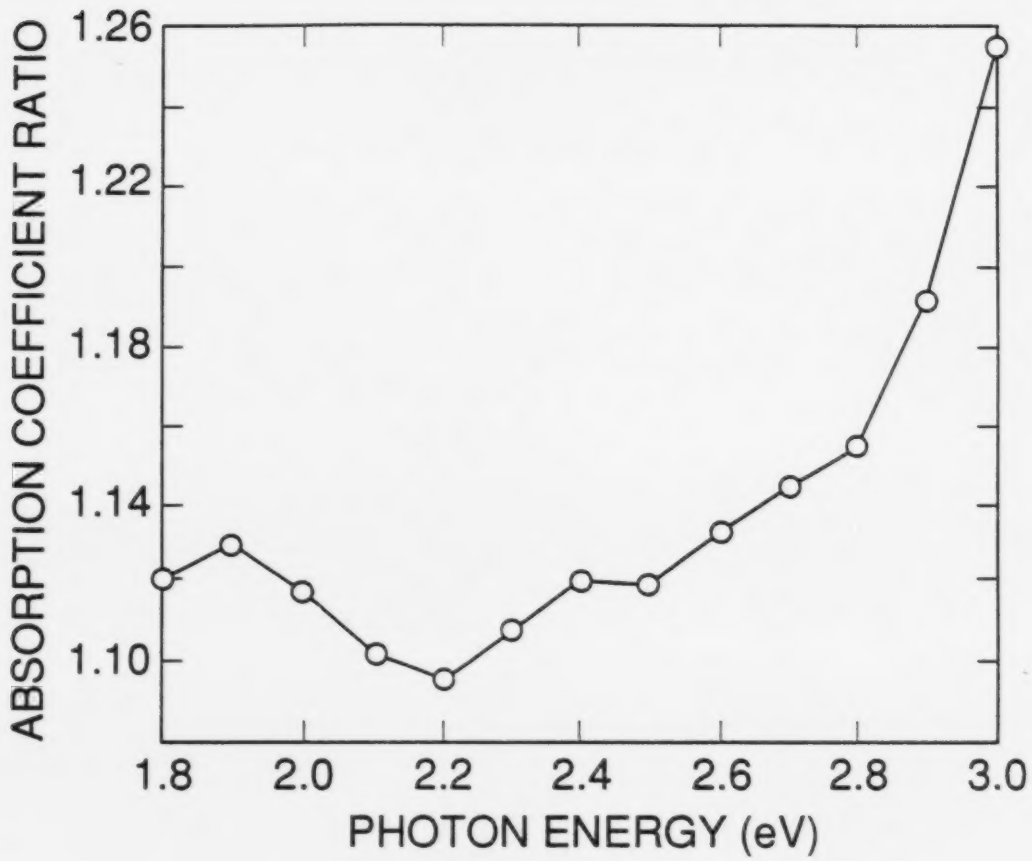

FIGURE 5.4. The ratio of Philip's absorption coefficient values[8] to those calculated from eq. (1) of this Chapter.

REFERENCES FOR CHAPTER 5

1. K. Rajkanan, R. Singh, and J. Shewchun, Absorption coefficient of silicon for solar cell calculations, Solid-State Electr. **22**, 793-795 (1979).

2. J. M. Palmer, Near-infrared limitations to silicon photodetector self-calibration, Proc. SPIE **499**, 7-14 (1984).

3. H. A. Weakliem and D. Redfield, Temperature dependence of the optical properties of silicon, J. Appl. Phys. **50**, 1491-1493 (1979), and personal communication.

4. T. P. McLean, The absorption edge spectrum of semiconductors, Progress in Semiconductors **5**, 53-102 (Ed. A. F. Gibson, John Wiley, 1960).

5. Ref. 4, page 99.

6. G. G. Macfarlane, T. P. McLean, J. E. Quarrington and V. Roberts, Fine Structure in the Absorption-Edge Spectrum of Si, Phys. Rev. **111**, 1245-1254 (1958).

7. G. G. Macfarlane, T. P. McLean, J. E. Quarrington and V. Roberts, Exiton and phonon effects in the absorption spectra of Germanium and Silicon, J. Phys. Chem. Solids **8**, 388-392 (1959).

8. H. R. Philipp, Influence of oxide layers on the determination of the optical properties of silicon, J. Appl. Phys. **43**, 2835-2839 (1972), and personal communication.

9. J. Geist, A. Russell Schaefer, J-F Song, Y. H. Wang, and E. F. Zalewski, An accurate value for the absorption coefficient of silicon at 633 nm, J. Res. NIST **95**, 549-558 (1990).

10. J. Geist, A. Migdall, and H. Baltes, Shape of the silicon absorption coefficient spectrum near 1.63 eV, Appl. Opt. **29**, 3548-3554 (1990).

6. TESTING THE ACCURACY OF QUANTUM EFFICIENCY CALCULATIONS

This chapter and the next are concerned with testing the numerical accuracy of iterative solutions of the drift-diffusion equations for photodiodes. This chapter develops an new expression for the internal quantum efficiency of a photodiode in terms of an integral transform of the photon-absorption rate density in the photodiode. The kernel of the transform contains the normalized, equilibrium majority-carrier distribution in the front region of the photodiode. This result is useful for two reasons.

First, it shows that the internal quantum efficiency is very sensitive to the shape of the equilibrium majority-carrier concentration in the front region of the photodiode. Therefore, any iterative solution of the drift-diffusion equations that is to calculate accurate photodiode quantum efficiencies will have to accurately reproduce the variations of the equilibrium majority carrier-concentration in the photodiode. This requirement is particularly stringent for silicon photodiodes in the vicinity of the oxide-silicon interface where strong surface fields can cause the equilibrium majority-carrier concentration to vary over many orders of magnitude in less than one nanometer.

The next chapter describes a technique for testing the ability of programs that solve the drift-diffusion equations to accurately calculate the equilibrium majority-carrier distribution in the presence of surface fields. This chapter develops a technique for verifying that programs that pass the test of the next chapter also

---

A version of this chapter has been published: J. Geist and H. Baltes, High accuracy modeling of photodiode quantum efficiency, Appl. Opt. **28**, 3929-3939 (1989)

calculate accurate steady-state photocurrents. Together these techniques provide a simple, reliable way to verify the numerical accuracy achieved by iterative calculations of the internal quantum efficiency of high-quality silicon photodiodes.

The technique derived in this chapter is used in Chapter 10 to verify the numerical accuracy of the internal quantum efficiency calculated by a semiconductor device modeling program, Version 2 of PC-1D[1,2], for a case where very high accuracy is required. The numerical accuracy of the equilibrium majority-carrier concentrations calculated by Version 2 of PC-1D is verified in the next chapter. The remainder of the introduction to this chapter compares the conventional analytic and iterative approaches to solving the drift-diffusion equations, and relates the integral transform approach of this chapter to those approaches.

There are two widely used approaches to calculating the short-circuit, steady-state photocurrent in a planar solar cell or photodiode using the drift-diffusion equations that describe the generation, recombination, and transport of carriers within such a device. The first is to model the device as a one-dimensional structure consisting of two field-free regions of uniform doping surrounding a fully depleted region. Hovel[3] has derived a very useful analytic expression for the short-circuit photocurrent with this model under the assumption that the photogenerated carrier transport is governed by the equilibrium fields. The second approach is an iterative, numerical solution of the drift-diffusion equations for the doping distributions actually existing in the diode.

Unfortunately, neither approach is particularly well suited for estimating the uncertainty associated with the calculated short-circuit photocurrent. Such an estimate is crucial to silicon photodiode self-calibration[4] and other high accuracy measurement applications of high-quality photodiodes. Reliable uncertainties of the order of 100 parts per million (ppm) are currently needed to support self-calibration research[5], and uncertainties of the order of 10 ppm may eventually be required.

The main problem with Hovel's analytic expression for the short-circuit photocurrent is the assumption of a uniformly doped, field-free front region. The other two parts of Hovel's model, namely the fully depleted region and the uniformly doped back region, are representative of high-quality silicon photodiodes. But these devices rarely, if ever, have uniformly doped and field-free front regions. Instead, naturally inverted[6], diffused, or implanted front regions are typical. This means that some error is incurred by replacing the actual dopant distribution in the front region with a constant value when using the analytic expression to model this type of photodiode. Placing bounds on this error is extremely difficult.

The main problem with iterative solutions of the drift-diffusion equations is the complexity of these equations. Because it is not clear how the various material parameters interact with the parameters describing the diode structure to produce the photocurrent, the error analysis is not straightforward. However, the success of Hovel's analytic expression in describing the behavior of solar cell and photodiode quantum efficiency suggests that the short-circuit

photocurrent is determined by the equilibrium properties of the diode. If this is so, a modified version of Hovel's expression might provide sufficient accuracy to verify the accuracy of iterative solutions of the drift-diffusion equations.

To test this idea, this chapter develops an alternative to Hovel's expression for the contribution to the short-circuit photocurrent arising in the front region of a photodiode. In one way the new expression is more general than Hovel's because it accommodates arbitrary front region doping distributions. In another way it is less general than Hovel's because it neglects volume (but not interface) recombination. The new expression is well suited to the analysis of high quality photodiodes because such photodiodes have almost no recombination of photogenerated minority carriers within the volume of the front region[5]. Moreover, the small amount of volume recombination in the front region is well approximated by surface recombination[5].

The remainder of this chapter is organized as follows: Section 6.1 is an analysis of a typical high quality silicon photodiode using Version 1 of PC-1D. Specifically, the equilibrium carrier concentrations and mobilities as a function of position in the diode are calculated because they are needed later in the chapter. The short-circuit photocurrent for the photodiode in the absence of recombination is also calculated to for artificially large recombination rates. These results are needed for the error analysis in Section 6.3.

Section 6.2 derives the new expression for the contribution from the front region of a high quality photodiode to the short-circuit

photocurrent. Section 6.3 examines the accuracy of the new expression. The sources of errors that are common to the new expression and the iterative solutions of the drift-diffusion equations are distinguished from those that are unique to the new expression, and the latter are shown to be smaller than the former for a particular type of photodiode of interest to self-calibration research.

6.1 ITERATIVE NUMERICAL SOLUTIONS WITH PC-1D

Table 6.1 lists nominal characteristics for the Hamamatsu 1337 silicon photodiode. This diode is typical of the type of high quality photodiode currently in use. Version 1 of PC-1D[7] was used to carry out numerical calculations on the diode specified in Table 6.1. Before the results of these calculations are described, the features of Version 1 of PC-1D are summarized.

Version 1 of PC-1D is a menu-driven program that carries out iterative, numerical solutions of the drift-diffusion equations for one-dimensional models of diodes and transistors under equilibrium, steady-state, and transient conditions on IBM PC-compatible computers having a numerical coprocessor installed. It accommodates a numerical grid of up to 80 points, and has about 14-digit numerical accuracy available during its calculations. PC-1D also contains rather sophisticated physical models of the optical and electronic properties of silicon and gallium arsenide. Moreover, the user can modify the parameters in these models, and in some cases replace the model with a table of data. PC-1D calculates over 30 different device properties and produces both plots and numerical values of these properties when desired.

6.1.1 EQUILIBRIUM RESULTS

The values listed in Table 6.1 were entered into PC-1D as the first step in modeling the photodiode described therein. As the second step, the equilibrium properties of the diode were calculated using the default silicon material models built into PC-1D. Figures 6.1 and 6.2 show the carrier concentrations and carrier mobilities for the photodiode at equilibrium. The equilibrium carrier concentrations and mobilities are needed in Section 6.2 to demonstrate the use of the new expression to calculate the internal quantum efficiency of the photodiode.

6.1.2 INTERFACE AND VOLUME RECOMBINATION

The assumption that there is little recombination occurring within the volume of the front region of a high quality photodiode, and that it can be modeled as surface recombination is central to the derivation of the new expression. Therefore, PC-1D is used to demonstrate the validity of this assumption before the derivation of the new expression for the short-circuit photocurrent is attempted.

Previous measurements[8,9] of photocurrent as a function of oxide bias in high quality photodiodes have been interpreted to show that the front region volume recombination was large enough to decrease the internal quantum efficiency by 0.6% at 350 nm. But later work[10] showed that most, if not all, of the 0.6% was actually due to incomplete accounting for the approximately 15% front surface recombination, due to a misinterpretation of the experimental data. In fact, it is very difficult to distinguish experimentally between front surface recombination and front region volume recombination in

high quality photodiodes.

To estimate the volume recombination occurring in the front region of the photodiode of Table 6.1, the Shockely-Hall-Read (SHR) lifetime was set to the default value of 10^{-4} s, and the surface recombination velocity was reset to zero. For this case PC-1D calculated the 300 nm to 500 nm quantum efficiency for the photodiode of Table 6.1 to be 10 ppm less than for the case of no recombination. To achieve higher precision, the calculations were repeated with the SHR lifetime decreased by a factor of ten to 10^{-5} s. In this case, the quantum efficiency was 65 ppm below unity between 300 and 450 nm. This shows that the PC-1D default SHR lifetime reduces the quantum efficiency at 300 nm by about 7 ppm.

Whatever the exact value of the SHR recombination, the work reported in Refs. 11 and 12 suggests that its effect can be modeled by surface recombination for wavelengths greater than 400 nm. Version 1 of PC-1D cannot be used to demonstrate this for SHR recombination since it uses the same SHR lifetime in the rear and front regions of the diode. This causes the back region of the diode, as well as the front region, to contribute to the shape of the internal quantum efficiency spectrum at long wavelengths when SHR recombination is present. This distorts the shape of the quantum efficiency curve from what it would be if only front region recombination were active. However, Version 1 of PC-1D can be used to demonstrate this point for Auger recombination.

Figure 6.3 compares the internal quantum deficiencies calculated from the short-circuit photocurrents obtained from PC-1D using artificially high Auger recombination and surface recombination. The reason for

using artificially large recombination is to minimize the effect of the ± 10 ppm precision of PC-1D. In each case the SHR lifetime was set to the unrealistically large value of 10^4 s. For the case labeled Surface, the electron and hole Auger recombination cross sections were zero, while the surface recombination velocity was 1.4×10^7 cm/s. This value is a factor of 1000 greater than the value of 1.4×10^4 that produces the correct order of magnitude quantum deficiency in the short wavelength region of the visible. For the case labeled Auger, the surface recombination velocity was zero and the hole Auger recombination cross-section rate was 3.49×10^{-26} cm^6/s. This value is a factor of 2×10^5 greater than the PC-1D default value of 1.8×10^{-31} cm^6/s.

The curves in Fig. 6.3 are plotted as quantum deficiencies because this quantity is linearly related to the recombination rate at small recombination rates, and because this is the important quantity when determining the uncertainty in self-calibration experiments. Notice that the differences between the Auger and Surface curves in Fig. 6.3 are very small at wavelengths greater than 400 nm. In fact, these curves fall within 3% of each other at all wavelengths greater than 400 nm, but differ by almost 20% below 350 nm.

The key idea here is the following: If the product of the absorption coefficient and the doping distribution depth scale is less than one, then any recombination associated with the doping distribution, be it Auger or SHR, has nearly the same effect on the quantum deficiency as has recombination localized at the front surface. This idea was demonstrated for unrealistically large recombination parameters so that the small differences could be distinguished. For realistic

recombination parameters, these differences are negligible.

6.2 NEW EXPRESSION FOR PHOTOCURRENT

Four assumptions form the basis of the derivation of an integral transform expression for the contribution of the front region to the short-circuit photocurrent in a high quality photodiode. These are:

i) the photodiode has a one-dimensional, planar geometry,

ii) the photocurrent is linearly related to the incident photon flux,

iii) the oxide-silicon interface at the front of the photodiode is the only place in the front region where the photogenerated minority carriers recombine, and

iv) the excess minority carrier concentration due to photogeneration is zero at the boundary between the front region and the depletion region.

The first assumption is valid for large area diodes with planar geometries such as are typical of high quality silicon photodiodes. The second assumption differentiates measurements of photon fluxes with photodiodes, where linearity is a virtue, from solar conversion, where the photodiode must generate enough voltage to drive the photocurrent through a load. The latter case is an intrinsically nonlinear mode of operation. The third assumption is the mark of a high quality photodiode, as was pointed out in Section 6.1. The fourth assumption, which was introduced by Hovel, is required to derive a closed form expression for the photocurrent. Presently, this assumption introduces errors that are small compared to other errors that are common to both the numerical models and our approximate expression. Improvements in the physical models incorporated in

future versions of PC-1D might reduce the latter errors to the point where the errors associated with the fourth assumption become important.

The approach to deriving the integral transform expression is to calculate the contribution to the photocurrent from the region between $x = 0$ and $x = x_1$ for the metallurgical junction-diode structure shown in Fig. 6.4. This quantity will be calculated in the limit of zero photocurrent, observing that the photocurrent does not perturb the built-in electric field from its equilibrium value in this limit.

Notice that Fig. 6.4 depicts an n on p diode structure, rather than the p on n structure of the Hamamatsu 1337. For convenience, the new expression is derived for the former structure, and then generalized to cover both p on n and n on p structures. The structure of Fig. 6.4 is one dimensional in accordance with assumption i) above. The point $x = 0$ represents the oxide silicon interface. The point x_1 represents the location where the excess minority carrier concentration is assumed to be zero. This was assumption iv) above. The choice of the actual value for x_1 is somewhat arbitrary. It serves to define the boundary between the front region and the depletion region. Later in this section, a criterion is introduced to allow x_1 to be chosen to meet some desired numerical accuracy in the calculation of the photocurrent. The point x_c, which is not labeled in Fig. 6.4, represents the point where the minority and majority carrier concentrations cross. This is not the same as the metallurgical junction where the dopant concentrations cross.

Assume now that the one-dimensional, steady-state operation of the planar silicon photodiode structure shown in Fig. 6.4 is described by

the six drift-diffusion equations,

$$\frac{d^2\phi(x)}{dx^2} = -\left[\frac{q}{\kappa\ \varepsilon_0}\right] [p(x) - n(x) + N_D^+(x) - N_A^-(x)], \tag{1}$$

$$J_n(x) = -q \left[\mu_n(x)\ n(x) \frac{d\phi(x)}{dx} - D_n(x) \frac{dn(x)}{dx}\right], \tag{2}$$

$$J_p(x) = -q \left[\mu_p(x)\ p(x) \frac{d\phi(x)}{dx} + D_p(x) \frac{dp(x)}{dx}\right], \tag{3}$$

$$\frac{dJ_n(x)}{dx} = q\ [R_n(x) - G_n(x)], \tag{4}$$

$$\frac{dJ_p(x)}{dx} = -q\ [R_p(x) - G_p(x)], \tag{5}$$

and

$$J_T(x) = J_n(x) + J_p(x). \tag{6}$$

Equation 1 is the Poisson equation that relates the electric potential $\phi(x)$ at the point x to the concentrations of holes p(x), electrons n(x), ionized donors $N_D^+(x)$, and ionized acceptors $N_A^-(x)$. The quantity q is the quantum of electric charge, κ is the dielectric constant of silicon, and ε_0 is the permittivity of free space. Equations 2 and 3 are the current density equations that relate the respective electron and hole current densities $J_n(x)$ and $J_p(x)$ to the gradients of the electric potential and the carrier concentrations through the electron and hole mobilities $\mu_n(x)$ and $\mu_p(x)$ and diffusion

coefficients $D_n(x)$ and $D_p(x)$. Equations 4 and 5 are the steady-state continuity equations that describe the gradients of the current densities in terms of the steady-state carrier recombination and generation rate densities $R(x)$ and $G(x)$, which depend upon the incident irradiation. Equation 6 states that the total current $J_T(x)$ is made up of the sum of the electron and hole currents.

At equilibrium,

$$J_T(x) = J_n(x) = J_p(x) = 0, \tag{7}$$

and eqs. 1 through 3 can be solved using standard numerical techniques such as are implemented in PC-1D. We assume that the solution is available and denote the equilibrium distributions of electrons, holes and the electric potential by $n_0(x)$, $p_0(x)$, and $\phi_0(x)$, respectively.

It is convenient for what follows to define the normalized electron and hole concentrations as

$$\hat{n}_0(x) = n_0(x)/n_0(0), \tag{8}$$

and

$$\hat{p}_0(x) = p_0(x)/p_0(0). \tag{9}$$

Thus

$$\frac{d\phi_0(x)}{dx} = -\left[\frac{D_p(x)}{\mu_p(x)}\right]\left[\frac{1}{\hat{p}_0(x)}\right]\frac{d\hat{p}_0(x)}{dx}. \tag{10}$$

Approximate solutions to eqs. 1 through 6 can be obtained as follows: First seek a solution for which $d\phi(x)/dx$ is accurately approximated by

$d\phi_0(x)/dx$ when $x < x_1$. Then show that the exact location of x_1 is immaterial to the final result. All that is necessary is that x_1 be large enough that there is negligible probability that a front region minority carrier at x_1 will return to the front surface and recombine there.

The assumption that $d\phi(x)/dx = d\phi_0(x)/dx$ for $x < x_1$ is equivalent to assumption ii) above, that the device is operating in the linear regime of photocurrent. Indeed, linearity means that the ratio of the photocurrent to the incident flux is independent of flux level. Thus the limiting case of zero photocurrent can be used, because $d\phi(x)/dx = d\phi_0(x)/dx$ in this case.

The assumption that $d\phi(x)/dx = d\phi_0(x)/dx$ in eq. 3 is used to obtain an approximate expression relating $p(x)$ to $J_p(x)$ through the equilibrium hole concentration $p_0(x)$. Then eqs. 4 and 5 can be used to relate $J_p(x)$ and $J_n(x)$ to the incident photon flux, thereby obtaining the desired approximate solutions.

6.2.1 APPROXIMATE CARRIER CONCENTRATION

First assume that the equilibrium distributions $p_0(x)$, $n_0(x)$, and $d\phi_0(x)/dx$ are known, and that the irradiation of the photodiode with photons causes a photocurrent to flow without changing $d\phi(x)/dx$ from the equilibrium distribution $d\phi_0(x)/dx$. It is easy to show that

$$p(x) = p_0(x) + \frac{\hat{p}_0(x)}{q} \int_x^{x_1} \frac{ds\ J_p(s)}{\hat{p}_0(s)\ D_p(s)}$$

$$= \hat{p}_0(x) \left[\frac{p_0(x_1)}{\hat{p}_0(x_1)} + \frac{1}{q} \int_x^{x_1} \frac{ds\, J_p(s)}{\hat{p}_0(s)\, D_p(s)} \right] \qquad (11)$$

satisfies eq. 3, subject to the assumption that

$$d\phi(x)/dx = d\phi_0(x)/dx. \qquad (12)$$

To see this, differentiate both sides of eq. 11, express the result in the form

$$\frac{dp(x)}{dx} = \frac{d\hat{p}_0(x)}{dx} \frac{p(x)}{\hat{p}_0(x)} - \frac{1}{q} \frac{J_p(x)}{D_p(x)}, \qquad (13)$$

and use eq. 10 to transform eq. 13 to the form

$$\frac{dp(x)}{dx} = -\left[\frac{\mu_p(x)}{D_p(x)}\right] p(x) \frac{d\phi_0(x)}{dx} - \frac{J_p(x)}{q\, D_p(x)}, \qquad (14)$$

which when substituted into eq. 3 verifies that eq. 11 is indeed a solution. Notice that eq. 11 incorporates assumption iv) above, which is equivalent to $p(x_1) = p_0(x_1)$.

6.2.2 PHOTOCURRENTS

The next step in obtaining an approximate solution to eqs. 1 through 6 is to use eqs. 4 and 5 to express $J_n(x)$ and $J_p(x)$ in terms of the incident photon flux. Assume that the probability that the photogenerated minority carriers will recombine between $x = 0$ and x_1 is negligible in comparison to the probability that they will either be transported past x_1 by the built-in electric field $-d\phi(x)/dx$ or that they will recombine at the oxide-silicon interface at $x = 0$.

This is assumption iii) above. Also recall that electrons and holes are always generated and recombine as pairs. Thus, eqs. 4 and 5 can be rewritten as

$$\frac{dJ_n(x)}{dx} = - J\, a(x), \qquad (15)$$

and

$$\frac{dJ_p(x)}{dx} = J\, a(x). \qquad (16)$$

The quantity J a(x) in these equations expresses the rate of carrier generation due to the absorption of photons by silicon, with J representing the current density that the incident photon flux would cause in a device having 100% quantum efficiency, and a(x) representing the density per unit length, per photon with which the photons are absorbed at the point x.

For monochromatic radiation in a device with zero reflectance at its back surface,

$$a(x) = \alpha \exp(-\alpha x), \qquad (17)$$

where α is the wavelength-dependent absorption coefficient of silicon. More complicated expressions for a(x), including both polychromatic photon fluxes and multiple reflections between the front and back surfaces of the photodiode can be substituted for a(x) as appropriate. To allow for these cases, define the more general expression,

$$A(x) = 1 - \int_0^x a(s)\, ds, \qquad (18)$$

where a(s) might be given by a much more complex expression than eq. (17). Notice that $A(x_1)$ is the fraction of the flux incident on the front surface of the photodiode that is not absorbed in the front region of the photodiode. Also notice that if a(x) is given by eq. 17, then

$$A(x) = \exp(-\alpha x). \qquad (19)$$

To find the actual current densities in the front region due to the absorption of photons in that region, eqs. 15 and 16 must be integrated. Thus, for the structure shown in Fig. 6.4,

$$J_n(x) = \int_{x_1}^{x} \frac{dJ_n(s)}{ds}\, ds = J\,[A(x) - A(x_1)] + J_n(x_1), \qquad (20)$$

and

$$J_p(x) = \int_{0}^{x} \frac{dJ_p(s)}{ds} = J\,[1 - A(x)] - J_i, \qquad (21)$$

where $J_i = -J_p(0)$ is the interface recombination current, and $J_n(x_1)$ is the contribution to the photocurrent arising within the depletion and back regions of the diode. Hovel's expression[3] could be used for $J_n(x_1)$, as could an iterative, numerical solution for that part of the diode.

Substituting eqs. 20 and 21 into eq. 6 gives

$$J_T(x) = -J_1 + J\,[1 - A(x_1)] + J_n(x_1), \qquad (22)$$

which is independent of x, as it should be, due to conservation of charge.

6.2.3 COMBINING THE SOLUTIONS

Examine the first term in eq. 22, the interface recombination current density, in more detail. It is usual to approximate the total number of carriers recombining at the interface per unit time and area by the product of a surface recombination velocity S_p and the concentration of excess minority carriers at the interface, so

$$J_1 = q\,S_p\,[p(0) - p_0(0)]. \qquad (23)$$

Now set x = 0 in the first expression on the right-hand side of eq. 11, and use eq. 9 to replace $\hat{p}_0(0)$ by 1 to obtain

$$p(0) = p_0(0) + \frac{1}{q}\int_x^{x_1} \frac{ds\,J_p(s)}{\hat{p}_0(s)\,D_p(s)}. \qquad (24)$$

Next substitute eq. 24 into eq. 23 to obtain

$$J_1 = \Gamma_p \int_0^{x_1} \frac{ds\,J_p(s)}{\hat{p}_0(s)\,\hat{D}_p(s)}, \qquad (25)$$

where

$$\Gamma_p = S_p/D_p(0), \qquad (26)$$

and

$$\hat{D}_p(x) = D_p(x)/D_p(0). \qquad (27)$$

Now substitute eq. 21 into eq. 25, substitute eq. 25 into eq. 22, and rearrange the result to obtain

$$J_i = J\,[\Gamma_p\, I_p\{1\} - \Gamma_p\, I_p\{A\}]/[1 + \Gamma_p\, I_p\{1\}], \qquad (28)$$

and,

$$J_T = J\left[\frac{[1 + \Gamma_p\, I_p\{A\}]}{[1 + \Gamma_p\, I_p\{1\}]} - A(x_1)\right] + J_n(x_1), \qquad (29)$$

where

$$I_p\{A\} = \int_0^{x_1} \frac{ds\, A(s)}{\hat{P}_0(s)\, \hat{D}_p(s)}, \qquad (30)$$

is an integral transform of the function A(x), and the curly brackets {} indicate that I_p is a functional[13] that depends upon all of the values of the function A(x), rather than a function that depends upon a single value of A. Notice that $I_p\{1\}$ means $I_p\{A(x)=1\}$.

Equation 29 expresses the total photocurrent J_T in an n on p photodiode in terms of J, the photocurrent produced at 100% quantum efficiency, $A(x_1)$ the fraction of the incident flux not absorbed in the front region, two integral transforms of the equilibrium concentration of the front region minority carrier within the

photodiode, and $J_n(x_1)$, the contribution to the photocurrent arising from points $x > x_1$ in the diode.

Assuming that the front region is uniformly doped and that the depletion approximation is valid, as done by Hovel[3], and further assuming that there is no recombination of the photogenerated minority carriers within the volume of the front region, then eqs. 31 and 32 can be reduced to Hovel's results for the case of a n-type front region with his parameter $L_p = \infty$.

Finally, notice that the solution to eqs. 1 through 6 for the case of a p on n junction is obtained by replacing every occurrence of p with n, and vice versa in eqs. 26 through 30. Therefore, both cases are covered by replacing every occurrence of p by m, and n by M in eqs. 26 through 30, where m stands for front region minority carrier, and M stands for front region majority carrier. Also notice that the result can be expressed directly in terms of the quantum deficiency $QD = 1 - J_T/J$. The important results are

$$QD = \frac{\Gamma_m \left[I_m\{1\} - I_m\{A\} \right]}{\left[1 + \Gamma_m \, I_m\{1\} \right]} + A(x_1) - \frac{J_M(x_1)}{J}, \qquad (31)$$

and

$$I_m\{A\} = \int_0^{x_1} \frac{ds \; A(s)}{\hat{m}_0(s) \; \hat{D}_m(s)} \quad , \qquad (32)$$

where, again, m represents the front region minority carrier, M

represents the front region majority carrier, J is the photocurrent that would be produced by the incident radiation at 100% quantum efficiency, $A(x_1)$ is the fraction of the flux entering the diode that is not absorbed in the front region, $J_M(x_1)$ is the contribution to the photocurrent that arises in the depletion and back regions of the diode, and the carets over the front region minority carrier concentration and diffusion coefficient indicate that these quantities are normalized to unity at $x = 0$, the oxide-silicon interface. For use in modeling high quality silicon photodiodes, Γ_m can be considered a parameter whose value is determined experimentally. As mentioned earlier, Hovel's expression could be used for $J_M(x_1)$.

Assume that the photodiode is much thicker than the reciprocal absorption coefficient for 700-nm radiation, and that there is no recombination of photogenerated excess carriers at points $x > x_1$, so that $J_M(x_1)/J$ is equal to $A(x_1)$ in eq. 31. This confines attention to the front region of the diode.

Also, if A(x) is given by eq. 19, then there is a one-to-one correspondence between the values of the parameter α and the functions A(x). Therefore, the functional $I_m[A]$ can be replaced by the function $I_m(\alpha) = I_m\{\exp(-\alpha x)\}$. In this case the functional $I_p[1]$ is replaced by $I_m(0) = I_m(\alpha = 0) = I_m\{1\}$. This nonessential simplification will be used to discuss the errors associated with eqs. 31 and 32 in the next section.

The kernel of the integral defining $I_m(0)$ is a monotonically decreasing function for $0 \leq x \leq x_c$, so increasing x_1 will never increase the value of $I_m(0)$ relative to its value when $x_1 = x_c$ by more

than $(x_c - x_1)/(\hat{m}_0(x_1)\ \hat{D}_m(x_1)$. This observation makes a useful criterion for choosing x_1 to be the smallest value of x_1 which satisfies

$$(x_c - x_1)/(\hat{m}_0(x_1)\ \hat{D}_m(x_1)) < \beta\ I_m(0), \qquad (33)$$

where x_c is the point at which the electron and hole concentrations are equal. This will assure that $I_m(0)$ is approximated to within a fraction β of its value when $x_1 = x_c$.

The internal quantum efficiency of the diode specified in Table 6.1. was calculated from the equilibrium majority-carrier concentration computed by PC-1D with eqs. 31 through 33, and from the short-circuit photocurrent computed directly by PC-1D. The same silicon absorption coefficient data and the same surface recombination velocity (which corresponds to $\Gamma = 0.4005\ \mu m^{-1}$) were used in both the calculations, and a value of $\beta = 0.001$, which gives $x_1 = 0.52\ \mu m$, was used.

The approach used to approximate the integrals in eq. 31 was the following: A single five-parameter function was fit to the $\hat{D}_m(x)$ data obtained from PC-1D, and four overlapping functions, which depended on anywhere from four to seven parameters, were fit to the $\hat{m}(x)$ from PC-1D. These analytic approximations were then integrated over a much finer grid than provided by PC-1D.

The results of these calculations of the quantum deficiency are compared in Fig. 6.5. The former are labeled This work, while the latter are labeled PC1D Default. Notice that the curves labeled Default and This work agree quite well over the entire spectral range. The difference between them is less than 4% except at 650 nm, where it

is 9%. In fact, this difference appears to be due to a 20-ppm error in Version 1 of PC-1D. In this connection, notice that the PC-1D Default curve has a slight dip at 650 nm. Similar curves produced by PC-1D for slightly different values of the parameters did not have a dip at this wavelength. The fact that the new expression can locate errors at this level of accuracy is an indication of its usefulness.

6.3 ACCURACY OF THE APPROXIMATION

A number of sources of error affecting internal quantum deficiency calculations have been identified. These include:

i) the assumption that $m(x_1) = m_0(x_1)$,

ii) the assumption that $d\phi(x)/dx = d\phi_0(x)/dx$,

iii) the assumption that any front region recombination not localized at the front surface is properly modeled,

iv) the numerical accuracy with which the quantum deficiency is calculated, and

v) the accuracy of the physical models used in calculating the quantum deficiency.

The first two sources of error affect only calculations of the quantum deficiency that are based on eqs. 31-33, and will be considered first.

6.3.1 ASSUMPTION THAT $m(x_1) = m_0(x_1)$

There is no way to estimate the uncertainty associated with this source of error, except by comparison with the results of an iterative solution of the drift-diffusion equations including photogeneration. Figure 6.5 presents such a comparison. The small differences of less than 4% between the quantum deficiencies shown in that figure could be caused by this source of error, but they could also be the result of numerical inaccuracy in either the approximations for $I_m(\alpha)$ and $I_m(0)$,

or the photocurrents calculated by PC-1D. These sources of error are discussed later. In any case, ±4% is a conservative estimate of the uncertainty associated with the assumption that $m(x_1) - m_0(x_1) = 0$.

6.3.2 USE OF EQUILIBRIUM ELECTRIC FIELD

It is quite difficult to estimate the uncertainty to be associated with the approximation of $d\phi(u)/du$ by $d\phi_0(u)/du$ in point ii) above. However, it is clearly true that $d\phi(u)/du = d\phi_0(u)/du$ in the limit of zero incident photon flux density. Furthermore, any change in the internal quantum efficiency with increasing photon flux density is called a nonlinearity. Consequently, if the photon flux density is small enough so that the nonlinearity is less than some value ξ, then the error caused by the approximation of $d\phi(u)/du$ by $d\phi_0(u)/du$ is also less than ξ. Typical high quality photodiodes show non-negligible nonlinearities at flux densities between 100 $\mu W/cm^2$ and 10 mW/cm^2. These nonlinearities are caused by two dimensional effects. The short-circuit photocurrent calculated by PC-1D for the photodiode of Table 6.1 shows no evidence of nonlinearity even at significantly higher flux densities. Therefore, the errors associated with this approximation are negligible.

Those sources of error that are common to any calculation of the quantum deficiency, no matter the approach, are considered next.

6.3.3 FRONT REGION VOLUME RECOMBINATION

Since there is no sensitive experimental technique that can detect small amounts of front region volume recombination in the presence of interface recombination, it is necessary to associate some uncertainty with the front-region volume recombination. Equations 31-33 cannot be

used to estimate an uncertainty associated with this source of error. They were derived by assuming that all of the recombination was localized at the interface. On the other hand, an iterative solution of the drift-diffusion equations with photogeneration can be used to estimate uncertainties due to this source of error. Figure 6.3 is useful in this regard.

Figure 6.3 compares the shape of the quantum deficiency curves for the diode described in Table 6.1 for two cases: all of the recombination loss is caused by an artificially large Auger recombination rate, and all of the recombination loss is caused by an artificially large surface recombination velocity. For wavelengths between 400 nm and 700 nm, the two curves can be made to fall within ± 2% of each other. On the other hand, if the wavelength range is extended to include 300 nm, then the two curves cannot be made to fall within less than ± 20% of each other. This means that if some of the recombination occurring in the front region of the diode is not localized at the front surface, but is distributed as the Auger recombination mechanism is distributed, then modeling it as surface recombination will cause an error no larger than ± 2% in extrapolating the quantum deficiency between 400 and 700 nm, and this number will serve as a conservative uncertainty for this source of error. On the other hand, if extrapolations from 300 nm to greater than 400 nm were under consideration, an uncertainty of ± 20% would be required.

The cross section for Auger recombination is proportional to the majority carrier concentration. Therefore it tends to be concentrated near the oxide-silicon interface. This is also a good model for the SHR recombination. When SHR recombination in the front region is not

negligible in a high-quality silicon photodiode, it is because there is residual damage in the silicon caused by the incorporation of the front region dopant into the photodiode. Such residual damage also tends to be proportional to the dopant concentration.

6.3.4 NUMERICAL ACCURACY

This chapter will not attempt to directly determine the uncertainty to be associated with the total photocurrent calculated from an iterative solution of the drift-diffusion equations with photogeneration. Basically, this task requires that the equations be solved with ever smaller grid sizes until certain differences associated with the potentials at adjacent grid points scale as the square of the grid size. Then the uncertainties in the potential can be calculated and propagated through the equations to determine the uncertainty in the total photocurrent.

One important result of such an analysis will, however, be mentioned. The standard algorithms used to solve the steady-state drift-diffusion equations iteratively calculate the total current at each point in the photodiode by taking the difference of two numbers. One of these numbers scales with the majority carrier concentration at each point; the other scales with the larger of the minority carrier concentration and the photogeneration rate at each point. The net result is that the maximum precision of the steady-state photocurrent increases as the number of digits used to store the numbers being differenced is increased, and as the photogeneration current is increased, but decreases as the doping concentration is increased. This means that the limiting precision with which the total photocurrent can be calculated varies with location in the photodiode.

As a result, algorithms that have more than adequate precision deep within the photodiode where the doping concentration is low can have inadequate precision in the front region of the photodiode where the doping concentration is many orders of magnitude larger. This is true even if the potential is calculated to the same precision at all points within the photodiode, and independent of the precision with which the equilibrium carrier concentrations can be calculated. For this reason the equilibrium carrier concentrations are often calculated from algorithms that are based on the assumption that the total photocurrent is identically zero. As a result, steady-state solutions for carrier concentrations obtained for the equilibrium conditions of zero photogeneration and zero applied voltage do not always agree in every digit with the equilibrium solutions obtained under identical conditions with the same program.

By way of contrast, the numerical accuracy of the quantum deficiencies calculated from eqs. 31-33 will depend upon a) the numerical accuracy with which the equilibrium minority carrier concentration and mobility have been calculated from an iterative numerical solution of the drift-diffusion equations for the conditions of equilibrium, and b) the accuracy with which $I_m\{A\}$ and $I_m\{1\}$ can be calculated from these results using eq. 32. No uncertainty analysis for a) will be attempted here; the important point is that the accuracy is limited by factors that are completely different from those that limit the accuracy of the iterative, numerical solution.

To determine an uncertainty to be associated with the integration process itself, we compared the values of $I_m(0)$ obtained when

different functions were used to approximate the equilibrium minority carrier concentrations calculated from PC-1D. The different values of $I_m(0)$ fell within a range of ± 5%, which contributes an uncertainty of about ± 10 ppm at 300 nm. Moreover, this uncertainty decreases with increasing wavelength because $I_m(\alpha)$ and $I_m(0)$ become correlated as the product of the absorption coefficient and the doping scale depth decrease below unity.

From the above discussion, it should be clear that there is no direct relation between the numerical accuracy obtained when calculating the quantum efficiency from the equilibrium carrier concentrations, and that obtained when calculating the quantum efficiency from the steady-state photocurrent, even when the same program is used to calculate the steady-state photocurrent and the carrier concentration. Thus, the two different approaches described in this chapter for determining the internal quantum efficiency in a photodiode are quite independent of each other. It is true that the integral transform approach is dependent upon the accuracy with which the iterative approach can calculate equilibrium carrier concentrations, but the accuracy of the latter can be tested independently, as shown in the next chapter. Therefore, it is quite reasonable to assume that the level of agreement obtained between the quantum deficiency curves obtained by the two different approaches as shown in Fig. 6.5 is indicative of the numerical accuracy of the individual approaches, and not the result of a coincidence associated with the factors common to the two approaches.

6.3.5 ACCURACY OF PHYSICAL MODELS

In the past, it has been very difficult to assign a useful uncertainty for this source of error. However, eqs. 31-32 make this a simpler task, not only for the new expression for the quantum deficiency, but also for quantum deficiencies derived from iterative solutions of the drift-diffusion equations. Equation 32 shows that the photocurrent depends upon the diode material parameters and device parameters in a rather simple way, and the error analysis need be concerned only with the minority carrier concentration, the minority carrier mobility, and the absorption coefficient.

In principle, the absorption coefficient should not be a significant source of error for a silicon photodiode. Chapters 4 and 5 point out, however, that this is not the case.[14,15] The formula used by PC-1D to calculate the default silicon absorption coefficients was chosen because it covers the large temperature range needed for modeling solar cells, and it is apparently accurate enough for solar cell modeling. However, it is not accurate enough for modeling high-accuracy applications of silicon photodiodes. Study of the error propagation associated with the more accurate formula[14] of Chapter 5 will be postponed to Chapter 10.

Since PC-1D has a model of the dependence of the minority carrier mobility on the majority carrier concentration[16] that is based on experimental measurements, the major source of error affecting the kernel of the integral in eq. 32 is the dependence of the minority carrier concentration upon various other effects not well modeled by PC-1D (or any semiconductor device model at the present time). These include tunneling[17] and the dependence of band-gap narrowing on both the dopant concentrations and the carrier concentrations in the

sharply graded front-region[18]. It would be unreasonable to expect that the actual values of $\hat{m}(x)$ fall very close to those calculated by PC-1D. It may not be possible to put reasonably tight uncertainties on these sources of error considering the current state-of-the-art of modeling these effects. The fact that both $\hat{m}(x)$ and $\hat{D}_m(x)$ are normalized to unity where they make the greatest contribution to $I_m(\alpha)$ and $I_m(0)$ turns out to be very helpful in this regard.

The estimation of an uncertainty for the two effects described above is postponed until Chapter 10. However, without the new expression for the internal quantum efficiency that is contained in eqs. 31-33, the estimates obtained there would not be possible. Even a complete parametric analysis with PC-1D might not suffice because the most important effects are not particularly well parametrized by PC-1D.

The results of this section show that determining the actual shape of the absorption coefficient spectrum and the product of the minority carrier distribution and the minority carrier diffusion coefficient are the most important source of error in modeling the internal quantum deficiency above 400 nm.

6.4 CONCLUSION

An integral transform expression for the contribution to the internal quantum deficiency from the front region of a high quality silicon photodiode has been derived. This expression depends upon the incident photon flux, the density per photon with which the radiation is absorbed within the diode, the equilibrium minority carrier concentration as a function of position, and the diffusion coefficient for minority carriers as a function of position in the diode front

region. The new expression becomes more accurate as the incident flux on the photodiode is decreased, and as the quantum efficiency approaches unity, and it has two virtues for use in high-accuracy modeling of silicon photodiodes: 1) It supports a rather transparent error propagation from the physical parameters associated with a photodiode to the quantum efficiency of the diode. 2) It supports a consistency check of the numerical accuracy of the steady-state photocurrent and equilibrium carrier concentration in a photodiode.

The new expression is remarkably accurate, despite the fact that it is based upon some assumptions that are not rigorously true. It has been shown to agree to within 4% with the quantum deficiency calculated directly by Version 1 of PC-1D for the photodiode described in Table 6.1. In Chapter 10, it is used to test the accuracy of Version 2 of PC-1D in a particular application, and agreement within 2×10^{-5} is obtained. This meets the present needs for accuracy testing of programs for solving the drift-diffusion equations for high-accuracy photodiode modeling.

TABLE 6.1 Nominal front region diode parameters characteristic of the Hamamatsu 1337 photodiode.

SUBSTRATE	
thickness	300 μm
doping	5×10^{12} atomic P cm^{-3}
FRONT DIFFUSION	
surface concentration	5×10^{18} atomic B cm^{-3}
diffusion shape	complementary error function
diffusion depth scale	0.055 μm
junction depth	0.209 μm
active area	1 cm^2

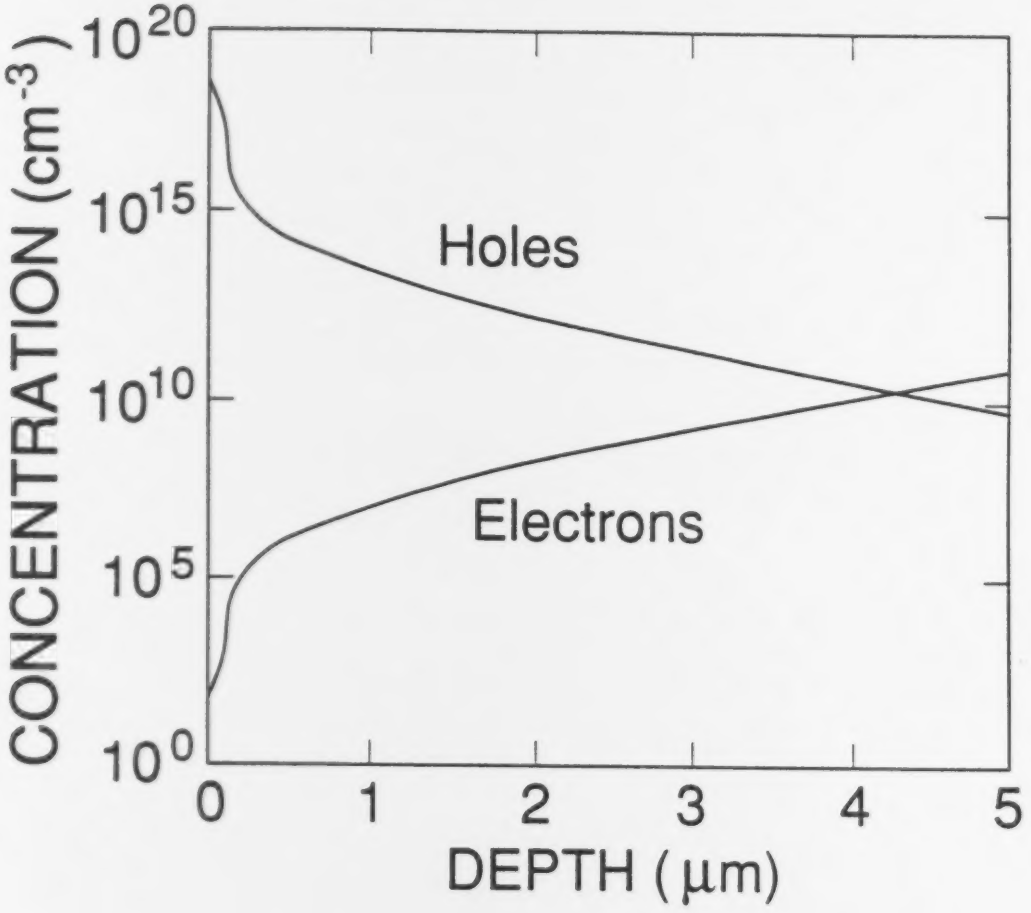

FIGURE 6.1 Equilibrium electron and hole concentrations $n_0(x)$ and $p_0(x)$ as a function of depth in the photodiode described in Table 6.1 according to the PC-1D semiconductor-device model.

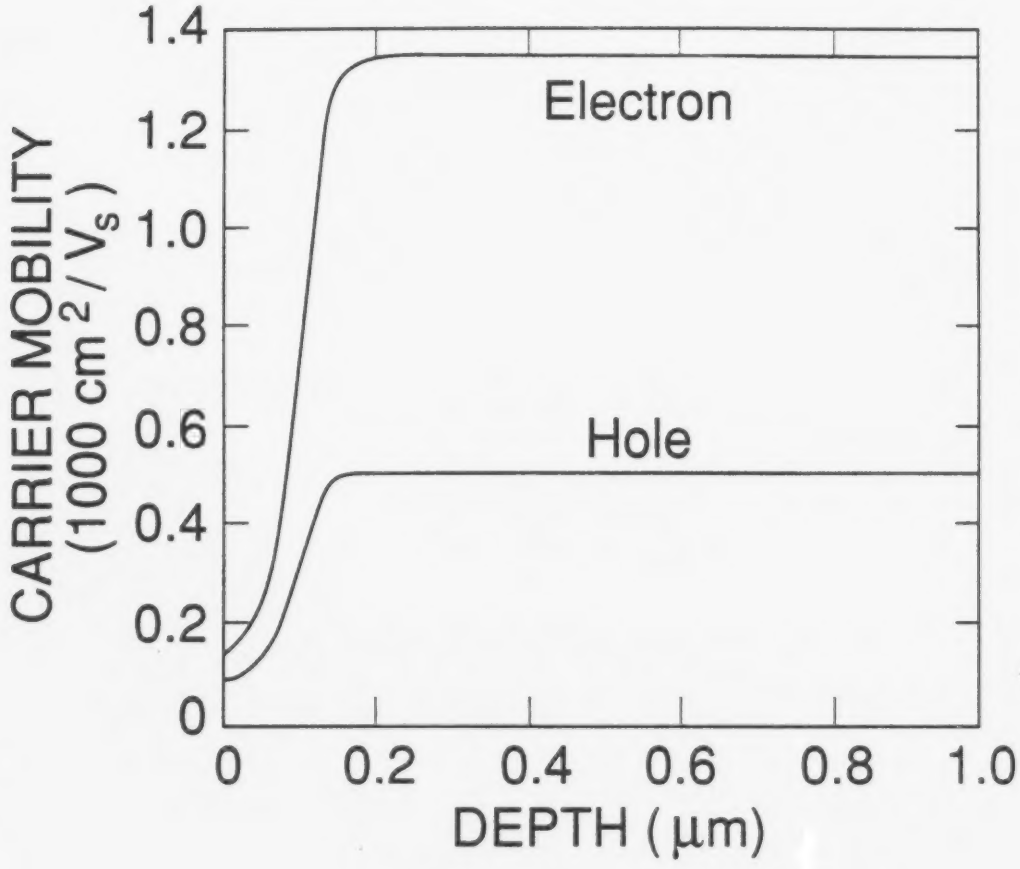

FIGURE 6.2 Carrier mobilities for electrons and holes at thermal equilibrium as a function of depth in the front region of the photodiode described in Table 6.1 according to the PC-1D semiconductor-device model.

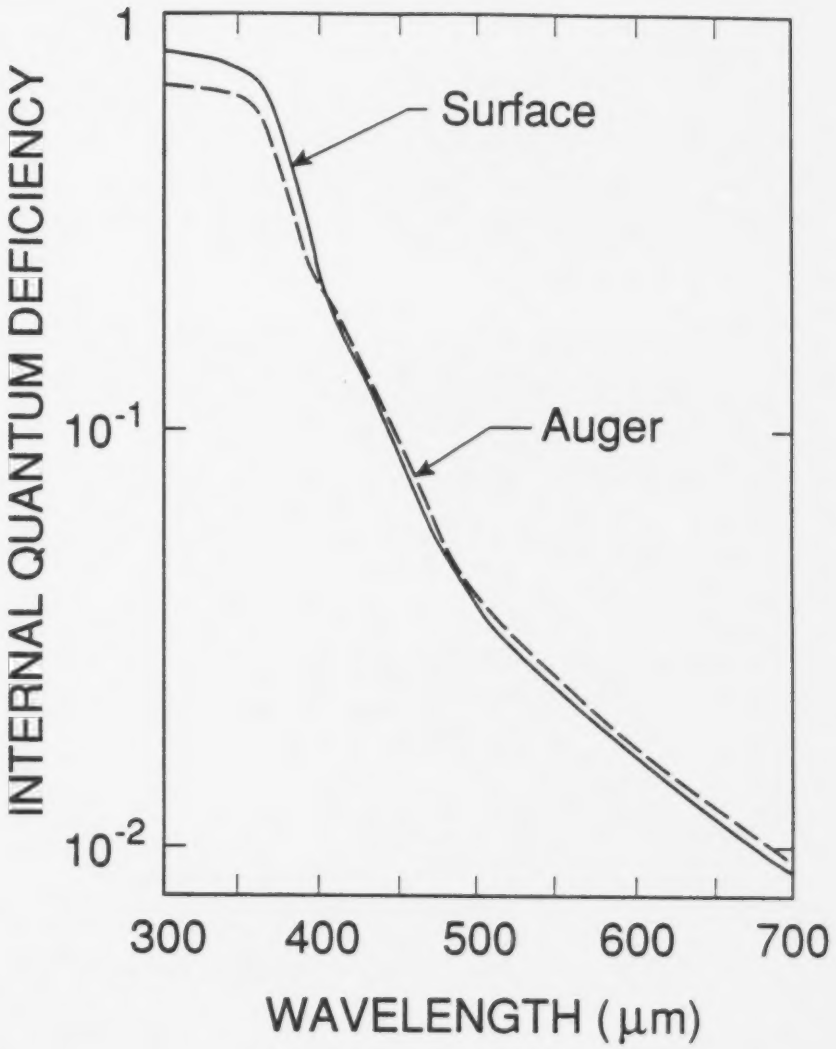

FIGURE 6.3 Comparison of the shape of the quantum deficiency curve for the diode described in Table 6.1 when the recombination losses are entirely due to Auger recombination in the volume of the front region (Auger) with the shape for the same diode when the recombination losses are entirely due to surface recombination (Surface). The recombination losses were set artificially large and adjusted to make the curves cross at λ = 400 nm.

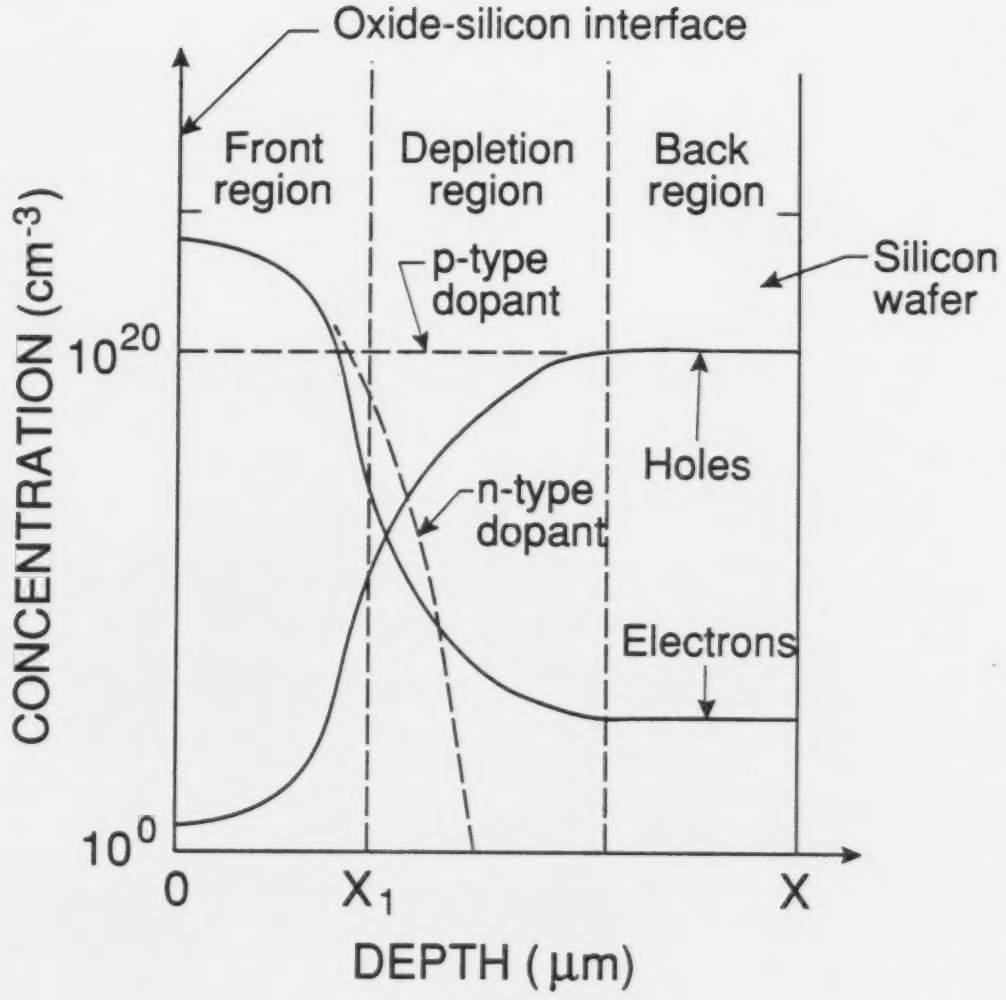

FIGURE 6.4 Doping and carrier concentrations, and partition into regions in a typical high quality planar silicon photodiode. The point x_1 is the point where the excess photogenerated carrier concentration is assumed to be zero, and is used to define the location of the interface between the front and depletion regions.

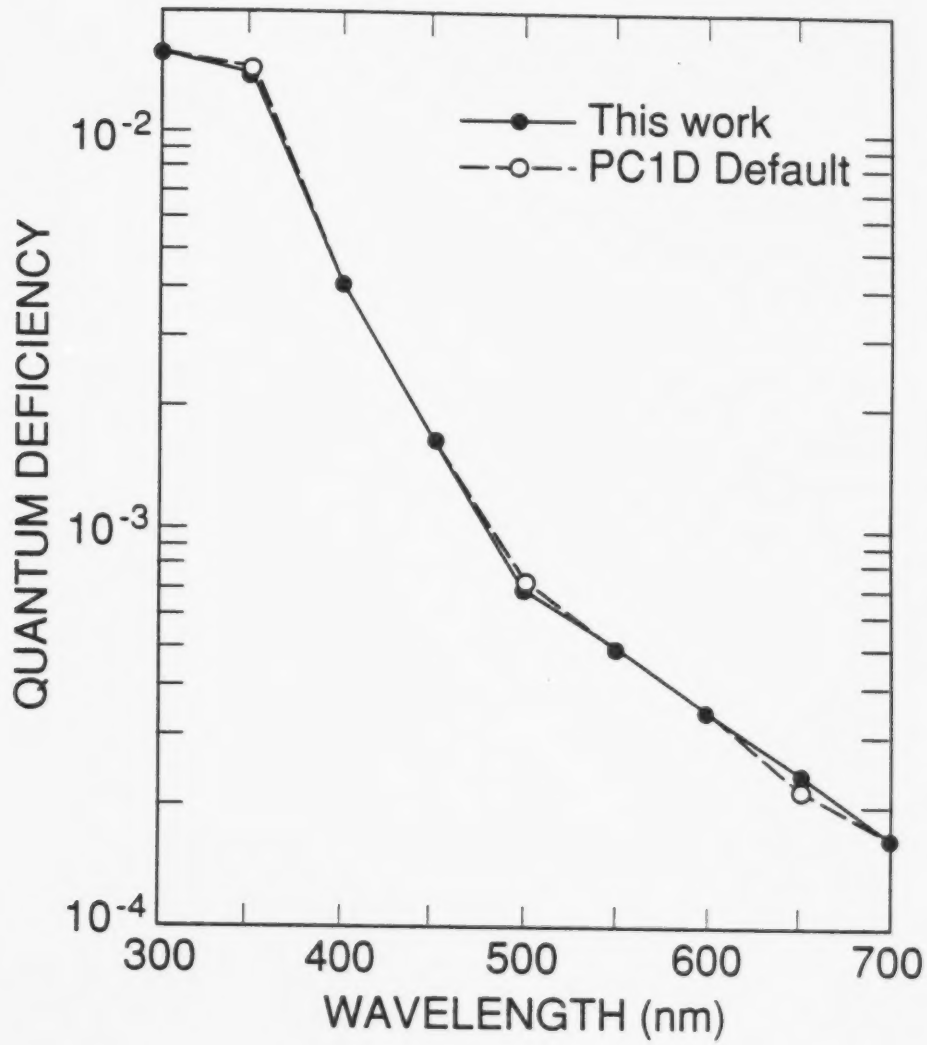

FIGURE 6.5 Comparison of the quantum deficiency curve calculated for the photodiode described in Table 6.1 by PC-1D with S = 1.4×10^4 cm/s (PC1D Default) with the value calculated from eqs. 31-33 (This work) for the same material parameters and device parameters.

REFERENCES FOR CHAPTER 6

1. P. A. Basore, PC-1D version 2: enhanced numerical solar cell modeling, 29th IEEE Photovoltaic Specialists Conference - 1988, 389-396 (pub. # 0160-8371/88/0000-0389, IEEE, NY, 1988).

2. PC-1D is available from Iowa State University Research Foundation (ISURF), Ames, IA 50011, copyright 1985.

3. H. J. Hovel, Solar Cells, in R. K. Willardson and A. C. Beers, Eds., Semiconductors and Semimetals, **11**, 1-254 (Academic Press, New York, 1975), page 15.

4. E. F. Zalewski and J. Geist, Silicon photodiode absolute spectral response self-calibration, Appl. Opt. **19**, 1214 (1980).

5. J. Geist, Current status of and future directions in silicon photodiode self-calibration, SPIE **1109**, 246-256 (1989).

6. T. E. Hansen, Silicon uv-photodiode using natural inversion layers, Physica Scripta **18**, 471 (1978).

7. Version 1 of PC-1D was replaced by Version 2 shortly after the work reported in this chapter was completed. The major advantages of Version 2 over Version 1 are the following: 1) Version 2 can use up to 150 finite elements compared to 80 in Version 1. 2) Version 2 allows arbitrary surface charge concentrations to be specified compared to a choice of no surface charge, weak inversion or strong inversion in Version 1. 3) Version 2 can be run in batch mode to access the highest levels of precision and accuracy available from PC-1D, which are not accessible from the menu driven interface. 4) Version 2 allows three different regions having different physical and material properties to be defined.

8. J. Geist, E. F. Zalewski and A. R. Schaefer, Spectral responsivity self-calibration and interpolation of silicon photodiodes, Appl. Opt. **22**, 3795-3799 (1980).

9. F. J. Wilkinson, A. J. D. Farmer and J. Geist, The near ultraviolet quantum yield of silicon, J. Appl. Phys. **54**, 1172-1174 (1983).

10. J. Verdebout, Semiquantitative model for the oxide bias experiment and its application to the study of p^+n^+ photodiode degradation, Appl. Opt. **23**, 4339-4344 (1984), page 4344.

11. J. Geist, Silicon photodiode quantum efficiency models, J. Appl. Phys. **51**, 3993-3995 (1980).

12. J. R. Lowney and J. Geist, Comparison of models of the built-in electric field in silicon at high donor densities, J. Appl. Phys. **55**, 3624-3627 (1984).

13. F. Riesz and B. Sz.-Nagy, Functional Analysis, (Frederick Ungar, New York, 1965).

14. J. Geist, A. Migdall and H. P. Baltes, Analytic representation of the silicon absorption coefficient in the indirect transition region, Appl. Opt. **27**, 3777-3779 (1988).

15. J. Geist, A. R. Schaefer, J-F. Song, Y. H. Wang, and E. F. Zalewski, An accurate value for the absorption coefficient of silicon at 633 nm, J. Res. NIST **95**, 549-558 (1990).

16. H.S. Bennett, Hole and electron mobilities in heavily doped silicon: comparison of theory and experiment, Solid-State Electronics, **26**, 1157-1166 (1983).

17. Y. Ohkura, Quantum effects in Si n_MOS inversion layers at high substrate concentrations, Solid-State Electron. **33**, 1581-1585 (1990).

18. J. R. Lowney and H. S. Bennett, Limitations of isotropic theory of band-gap narrowing in Si and Ge devices, in IEEE 1987 Bipolar Circuits and Technology Meeting, 157-159 (ed. Janice Jopke, Cat. No. 87CH2509-8, IEEE, Piscataway, NJ 08854, 1987).

7. TESTING THE ACCURACY OF EQUILIBRIUM CARRIER CONCENTRATIONS IN THE PRESENCE OF SURFACE FIELDS

This and the preceding chapter are concerned with testing the numerical accuracy of iterative solutions of the semiconductor drift-diffusion equations for photodiodes. Such testing is essential if quantum efficiency calculations accurate to 100 parts per million (ppm) are to be achieved.[2] The preceding chapter shows that the majority carrier concentration at the front-surface oxide-silicon interface is one of the major factors determining the short wavelength quantum efficiency of high quality silicon photodiodes.[1] Large surface fields, which are present at the oxide-silicon interface of the silicon photodiodes used in high accuracy applications, create large, nonlinear majority carrier concentration gradients in the photodiode. The accurate simulation of such gradients presents the greatest challenge to the numerical algorithms that are used to solve the drift-diffusion equations. This chapter shows how to test the accuracy of the calculated majority carrier distribution in the presence of surface fields, and also shows that Version 2 of the semiconductor device modeling program PC-1D[3-4] is suitable for high accuracy applications.

Figure 7.1 shows majority carrier concentrations that were calculated with PC-1D [3,4] for uniformly doped silicon samples, 300 μm thick, having zero rear-surface charge density and a front-surface interface-charge density of 10^{13} q/cm^2, where q is the elementary unit of

---

A version of this chapter has been published: J. Geist, J. R. Lowney, C. R. James, and A. M. Robinson, Testing the accuracy of calculated equilibrium carrier concentrations in the presence of surface fields, J. Appl. Phys. 70, 236-242 (1991).

charge. The curves shown in Fig. 7.1 are typical of those that must be calculated when modeling the quantum efficiency of a photodiode by solving the drift-diffusion equations numerically. The numerical difficulties in the vicinity of the surface field near the oxide-silicon interface are obvious from this figure.

The approach developed in this chapter for testing the accuracy of the numerical results shown in Fig. 7.1 is 1) to derive a differential equation for the majority-carrier concentration in uniformly doped material in the presence of a surface field under assumptions that can be easily incorporated in any numerical model whose accuracy is to be tested, 2) to obtain analytic solutions to this differential equation for the special case of intrinsic material, 3) to express the solutions to the differential equation for the case of extrinsic material as the product of the solutions for the case of intrinsic material and another function that will be called a product function, 4) to derive separate differential equations for the product function for charge-accumulated material as well as charge-depleted and inverted material, 5) to solve the differential equation for the product function appropriate to heavily doped material with a charge-accumulated front surface, and 6) to fit a simple analytic expression to the product function.

The analytic solutions for intrinsic material are rigorous within the framework of the assumptions made in deriving them, and the product of the analytic solution for intrinsic material and the analytic expression for the product function for heavily doped material is accurate to well within 100 ppm for doping concentrations above 10^{12} cm^{-3}. On the other hand, the product function for the case of charge

depletion or inversion at the front surface is not a simple function, and offers no advantages, so its development is not completed in this chapter.

An alternative to the method developed in this paper is to derive the carrier concentrations from the solutions to the differential equations for the electric potential,[5,6] but this is less suitable for accuracy testing. It is the approach used by Version 2 of PC-1D, (and most, if not all, other iterative, numerical solvers of the drift-diffusion equations) and subtle errors associated with the particular approach could be common to both the algorithms of PC-1D and the algorithms that would be used in this chapter. Also, working directly with the carrier concentration produces better physical insight, at least in the case of charge accumulation at the interface.

7.1 DIFFERENTIAL EQUATIONS FOR CARRIER CONCENTRATIONS

Most semiconductor device models assume that the majority carrier mobility depends only upon dopant concentration. Actually this assumption is limiting because the free-carrier screening radius depends upon the carrier concentrations. Similarly, many models treat the effects of band-gap narrowing and Fermi-Dirac statistics through an effective intrinsic carrier concentration n_{ie} that is assumed to depend only upon the dopant concentration. This is also a limitation because n_{ie} depends upon the carrier concentrations as well as the dopant concentrations.[7] However, these assumptions are convenient for testing the numerical accuracy of semiconductor device models that either implement or allow them.[8] Specifically, these assumptions satisfy the Einstein relation in uniformly doped material. The Einstein relation, $D\,q = k\,T\,\mu$, connects the majority carrier

diffusion constant D and mobility μ, where k is Boltzmann's constant, and T is the thermodynamic temperature.

The crucial assumption for the approach developed here is that the device is a uniformly doped, one-dimensional, semi-infinite medium in which the carrier mobility is independent of carrier concentration, and for which the Einstein relation is valid. For this particular case, Poisson's equation and the current density equations, which govern the equilibrium carrier concentrations, can be written as

$$\frac{d^2\phi(x)}{dx^2} = -\frac{q}{\kappa\,\varepsilon_0}\left[p(x) - n(x) + N_D^{+} - N_A^{+}\right], \qquad (1)$$

$$\frac{d\phi(x)}{dx} = \frac{k\,T}{q}\,\frac{1}{n(x)}\,\frac{dn(x)}{dx} = -\frac{k\,T}{q}\,\frac{1}{p(x)}\,\frac{dp(x)}{dx}, \qquad (2)$$

where $\phi(x)$ is the electric potential, κ is the dielectric constant of silicon, ε_0 is the permittivity of free space, n(x) and p(x) are the free electron and hole concentrations, respectively, and N_D^{+} and N_A^{+} are the ionized donor and acceptor concentrations, respectively. These equations can be combined into the single equation

$$\frac{d}{dx}\left[\frac{1}{M(x)}\,\frac{dM(x)}{dx}\right] = \frac{q^2}{k\,T\,\kappa\,\varepsilon_0}\left[M(x) - \frac{n_{ie}^{\,2}}{M(x)} - M_{ion}\right], \qquad (3)$$

where M(x) is the majority carrier concentration and M_{ion} is the absolute value of $N_D^{+} - N_A^{-}$. If the minority-carrier concentration is desired, it can be calculated from the definition of the effective intrinsic carrier concentration,

$$n_{ie}^2 = m(x)\, M(x), \qquad (4)$$

which is valid at equilibrium, and which is used in deriving eq. (3). Now let

$$M_\infty = \lim_{x \to \infty} M(x), \qquad (5)$$

$$x_s = \left[\frac{2 \kappa \varepsilon_0 k T}{q^2 M_\infty} \right]^{1/2}, \qquad (6)$$

which is the square root of two times the Debye length, and

$$u = (x+x_0)/x_s, \qquad (7)$$

where x_0 is a positive constant to be determined by the boundary conditions. Also, let

$$\beta = n_{ie}/M_\infty, \qquad (8)$$

and

$$f(u) = M(x)/M_\infty. \qquad (9)$$

In this case, eq. (3) can be written in the dimensionless form,

$$\left[\frac{f'(u)}{f(u)} \right]' = 2 \left[f(u) - \beta^2/f(u) - (1-\beta^2) \right]. \qquad (10)$$

7.2 SOLUTIONS

It can be verified by substitution and expansion using the hyperbolic function identities that both

$$f(u) = \coth^2(u), \qquad (11)$$

and

$$f(u) = \tanh^2(u) \qquad (12)$$

are solutions of eq. (10) when $\beta = 1$. Therefore, $M(x) = M_{\infty} \coth^2(u) = n_{ie} \coth^2(u)$ for charge accumulation in intrinsic material, and $M(x) = M_{\infty} \tanh^2(u) = n_{ie} \tanh^2(u)$ for charge depletion in intrinsic material. Also, n_{ie} is equal to the intrinsic carrier concentration for intrinsic material.

To treat the case where β is not equal to 1, let

$$y(u) = f^{1/2}(u), \qquad (13)$$

which leads to

$$\left[\frac{y'(u)}{y(u)}\right]' = [y^2(u) - \beta^2/y^2(u) - (1-\beta^2)]. \qquad (14)$$

Equation (14) has an analytic solution for $\beta = 0$, but that solution cannot satisfy the boundary conditions imposed by eq. 3.[9]

To simplify the analysis of eq. (14), let

$$y(u) = r(\beta,u) \coth u, \qquad (15)$$

for the case of charge accumulation at the interface, and

$$y(u) = q(\beta,u) \tanh u, \qquad (16)$$

for the case of charge depletion or inversion at the interface. The resulting differential equations for r and q are

$$[r'/r]' = (r^2-1) \coth^2 u + (1-\beta^2/r^2) \tanh^2 u - (1-\beta^2), \qquad (17)$$

and

$$[q'/q]' = (q^2-1)\tanh^2 u + (1-\beta^2/q^2)\coth^2 u - (1-\beta^2). \qquad (18)$$

The Maclaurin series for $r(\beta,u)$ and $q(\beta,u)$ do not exist unless $\beta = 1$, as shown for $r(\beta,u)$ Ref. [9]. Nevertheless, it was possible to obtain numerical solutions to eq. (17) using a Fortran subroutine[10] that solves a two-point boundary-value problem for a system of ordinary differential equations with a Newton-iteration technique. The values of $r(\beta,10^{-6})$ and $r(\beta,100)$ were set to unity and used as the boundary values, since $r(\beta,u)$ approaches unity as u approaches zero and as u approaches infinity, as shown in Ref. [9]. The absolute error tolerance for the solutions was set to 10^{-5} and the mesh size was 1000 points. The solutions for the limiting cases of $\beta = 0$ and $\beta = 1$ are shown in Fig. 7.2.

Intrinsic material is described by $\beta = 1$, but no physically realizable situation is described by $\beta = 0$ because M_- cannot be infinite, nor can n_{ie} be zero. However, Fig. 7.3 shows that $r(0,u)$ is an excellent approximation to $r(\beta,u)$ for realistic values of β ranging from 10^{-10}, which corresponds to a realistic upper limit of 10^{20} cm^{-3} for the electrically active doping concentration, to 0.1. For the latter case, which corresponds to a doping concentration of about 10^{11} cm^{-3}, the maximum error is less than 0.1%. Moreover, $1 < r(\beta,u) < 1.1$, and it is only in the small region of u from 0.1 to 10 that $r(\beta,u)$ differs significantly from 1. As illustrated in Fig. 7.2, the fact that the function $r^2(\beta,u)$ is such a small perturbation to $M_- \coth^2 u$ means that considerable physical insight into the nature of charge accumulation can be obtained by considering only the behavior of $\coth^2 u$.

The function $r(0,u)$ for $0.01 \leq u \leq 8.3$ is well approximated by

$$r(u) = 1 + a\,u^n \exp(-k\,u) \sum_{j=0}^{5} b_j\,u^j, \qquad (19)$$

where the values of a, n, b_0, ... , b_5, and k, which were obtained from a nonlinear least-squares fit, are given in Table 7.1. The residual standard deviation of the fit of eq. (19) to r(0,u) is 20 ppm, and the largest deviation is 52 ppm, which occurs at u = 0.5. This means that the majority carrier concentration in accumulated silicon that is uniformly doped to greater than about 2×10^{12} cm^{-3} is approximated by

$$M(x) = M_\infty\, r^2([x+x_0]/x_s)\, \coth^2([x+x_0]/x_s) \qquad (20)$$

to well within 100 ppm when x_s is given by eq. (6) and x_0 is chosen to satisfy the boundary conditions. Therefore, the difference between M(x) in eq. (20) and the results of a numerical solution of the drift-diffusion equations for the same device parameters gives the error in the latter.

No numerical solution of eq. (18) was attempted for the case of charge depletion and inversion. Unlike $r^2(\beta,u)$, which was shown to be a small perturbation of $M_\infty \coth^2(u)$, $q^2(\beta,u)$ is not a small perturbation of $M_\infty \tanh^2(u)$. If anything, $\tanh^2(u)$ is a small perturbation of $M_\infty\, q^2(\beta,u)$. This is shown in Fig. 7.4, which plots $q^2(10^{-9},u) = M(u)/[M_\infty \tanh^2(u)]$ as a function of x, where M(u) was calculated as p(x) by PC-1D with $N_a = 10^{19}$ cm^{-3}, $N_{ss} = 10^{13}$ cm^{-2}, $u = (x+x_0)/x_s$ as defined in eq. (7). Also, the value of x_s was calculated from eq. (6) and x_0 was chosen to make $M_\infty \tanh^2(u) = p(x)$ when x = 0 at the front surface. (The point at x = 0 is plotted at $x = 10^{-11}$ m in Fig. 7.4 to accommodate the logarithmic scale, and is connected by a dashed line to the rest of the calculated points.) Because $q^2(\beta,u)$ varies by

orders of magnitude from the ideal value of unity, this approach to depletion and inversion is not as useful as it is for accumulation.

In summary, this section 1) described simple analytic solutions to the ordinary differential equation describing both charge depletion and accumulation at an interface in intrinsic material, 2) described a simple, yet accurate analytic approximation to the solution of the ordinary differential equation that describes charge accumulation at the interface of a moderately to heavily doped material, and 3) showed that the approach that is quite successful for charge-accumulated material offers no similar advantages for charge-depleted material.

7.3 BOUNDARY VALUES

This section derives the boundary values that are needed to apply the solutions obtained in the previous section to describe the carrier concentrations in a semi-infinte semiconductor bounded by a charged surface. Let $q\,N_{ss}$ be the surface charge density on the surface at x = 0 of the semi-infinite semiconductor. At equilibrium,

$$N_{ss} = \int_0^\infty dx\,[M(x) - n_i^2/M(x) - M_{ion}],$$

$$= -\frac{k\,T\,\kappa\,\varepsilon_0}{q^2}\,\frac{1}{M(0)}\,\frac{dM(x)}{dx}\bigg|_{x=0}, \qquad (21)$$

where eqs. (1) and (3) were used to obtain the right hand side of eq. (21).

The majority carrier concentration for the case of charge accumulation at the front surface of a uniformly doped material at equilibrium is

described by eq. (20) where x_0 is the solution to

$$N_{ss}/(M_\infty x_s) = \operatorname{sech}(x_0/x_s)\,\operatorname{csch}(x_0/x_s) - r'(\beta,x_0/x_s)/r(\beta,x_0/x_s). \quad (22)$$

The second term on the right-hand side of eq. (22) is zero for intrinsic material, and can be set equal to zero with little error even in the case of extrinsic material. In fact,

$$x_0 \sim x_s^2 \frac{M_\infty}{N_{ss}} = \frac{2 \kappa \varepsilon_0 k T}{q^2 N_{ss}}, \quad (23)$$

is also an excellent approximation for both intrinsic and extrinsic material.

If an exact solution is required, it is useful to rewrite eq. (22) in the form

$$u_0 = 0.5 \operatorname{arcsinh}(2 R/[1 + R\, r'(\beta,u_0)/r(\beta,u_0)]), \quad (24)$$

where

$$R = M_\infty x_s/N_{ss}, \quad (25)$$

and

$$u_0 = x_0/x_s. \quad (26)$$

Equation (24) can be solved iteratively starting with $u_0 = R$ as the zero order solution.

This completes the development of an approach for testing the ability of numerical algorithms to produce accurate values for the majority

carrier concentrations in the presence of surface fields. Before applying this approach to test the accuracy of Version 2 of PC-1D in the next section, consider the following quote from Ref. 11: "The more the surface is accumulated, the thinner will be the accumulation layer (effectively, the Debye length at the surface will be reduced by the added carriers); ..." The ease with which Appendix D of Ref. 9 shows the error in this widely held picture of charge accumulation by using the equations developed thus far in this chapter suggests that these equations provide considerable physical insight into the process of charge accumulation.

7.4 APPLICATION

The results derived above are used here to test the accuracy of the accumulated equilibrium majority-carrier concentrations calculated by Version 2 of PC-1D in Fig. 7.1. Figure 7.5 compares the relative differences between the values plotted in Fig. 7.1 and the values calculated from eqs. (20), (22), and (24). For the heavily doped case, $\beta^2 \sim 2\text{x}10^{-18}$, so according to Fig. 7.3, $r(0,u)$ is identical to $r(\beta,u)$ to well within the accuracy of eq. (19), so the largest error in the use of $r(u)$ defined in eq. (19) to approximate $r(\beta,u)$ falls below the 100-ppm resolution of Fig. 7.5. The errors are even smaller for the intrinsic approximation to the extremely lightly doped case.

In other words, to within the accuracy of Fig. 7.5, the relative differences plotted in that figure are the numerical errors inherent in the solutions obtained from PC-1D for the cases considered. The error for both the intrinsic case and for the heavily doped case changes sign at a depth a little greater than 1 nm; the errors for the two cases are very similar for shallower depths. The differences in

the errors at depths above 1 nm primarily reflect the fact that the carrier concentration approaches its asymptotic value much more rapidly with increasing depth in the case of heavily doped material than in the case of intrinsic material.

Table 7.2 compares the electron concentrations at a positively charged surface in intrinsic silicon as calculated by PC-1D with the more accurate values calculated from eqs. (20) and (24) for various values of N_{ss}. The value for the ratio x_0/x_s was obtained by solving eq. (24) for the case of intrinsic material, and the value obtained from the approximation in eq. (23) is also shown for comparison. These values could just as well have been calculated from the equations given in Refs. [5] and [6], but were calculated from the equations developed here for completeness. On the other hand, the results shown in Fig. 7.5 could not have been obtained so easily from those references, as it would be necessary to solve their equations numerically, and to independently validate the accuracy of the solutions.

The differences between the values of the electron concentration n(0) at the interface as calculated from eq. (20) and (24) and as calculated by PC-1D increase with increasing surface-charge density N_{ss}. This is to be expected because the accuracy with which finite elements can approximate the majority carrier concentration near the interface is determined by the deviation from linearity of the electrostatic potential over the finite elements. Assuming that the function is to be approximated over the domain from $x = 0$ to $x = x_1$ by a fixed number of elements of variable width, the error will scale as $\coth^2([x+x_0]/x_s) \approx ([x+x_0]/x_s)^2$, which increases by two orders of

magnitude for each entry in Table 7.2. This is the reason that the error is so large when $N_{ss} = 10^{14}$ cm^{-2}. Fortunately, N_{ss} will be less than 10^{13} cm^{-1} for most, if not all, practical applications involving photodiodes.

7.5. CONCLUSION

The physical assumptions that are the basis for the finite element equations in Version 2 of the semiconductor device simulation program PC-1D have been used to derive an ordinary differential equation to describe the carrier concentration in a uniformly doped semiconductor having a charged surface. The solution for the case of intrinsic material is a simple analytic function. The solution for the case of charge accumulation at the interface is the product of the same analytic function and a function that never differs from unity by more than 10%, and has very simple properties. The solution for the case of charge depletion and inversion at the interface can also be written as the product of a simple analytic function and another function, but the properties of the latter are complex enough and the variations of the function large enough that there seems to be no advantage to this procedure.

The solutions derived in this paper for the cases of intrinsic material and heavily doped material have been compared with the numerical solutions obtained from PC-1D for the same parameter values. Numerical errors, which approached 10% at the highest surface-charge concentration of interest, and which decreased to 1% within 1 nm of the surface, were observed. This level of error makes PC-1D suitable for modeling the highest accuracy applications of silicon photodiodes presently of interest.

It is important to realize that only the numerical accuracy of the solutions obtained from PC-1D for the case of surface accumulation has been tested here. It is possible that errors caused by assumptions and approximations in the physical models employed in PC-1D may exceed the numerical errors illustrated in Fig. 7.5 and Table 7.2. Version 2 of PC-1D accounts for the effects of band-gap narrowing and Fermi-Dirac statistics through an effective intrinsic carrier concentration n_{ie} that depends only upon doping concentration, but does not account for net charge. This is a significant source of error in a heavily doped region that is partially depleted. Another potentially serious source of error is the quantum mechanical behavior of the carriers (tunneling) that causes the majority-carrier concentration to deviate from that predicted by the drift-diffusion equations within about 1 nm of a charged surface. It is of interest to estimate the uncertainties associated with these sources of error, but such estimates are beyond the scope of this thesis.

TABLE 7.1 Parameters for use in eq. (19).

Name	Value
a	0.442160
n	1.70167
b0	1.00000
b1	0.830148
b2	0.0193164
b3	-0.0028197
b4	0.0124375
b5	-0.00015632
k	2.2584

TABLE 7.2 A comparison of the calculated electron concentration at the oxide-silicon interface n(0) in intrinsic silicon at 300 K as a function of the surface charge density N_{ss} at the interface. The comparison is between the numerical algorithms of PC-1D and the more accurate solutions of eqs. (20) and (24). The approximate value of x_0/x_s obtained from eq. (23) is also compared with the numerical value obtained from eq. (24). The values of n_{ie} and κ were 1.45×10^{10} cm^{-3} and 11.9, respectively, for both calculations.

N_{ss}	x_0/x_s	x_0/x_s	eq.11 n(0)	PC-1D n(0)
cm^{-2}	eq. (23b)	eq. (23c)	cm^{-3}	cm^{-3}
10^9	7.02157E-2	6.99870E-2	2.96995E12	2.96960E12
10^{10}	7.02157E-3	7.02157E-3	2.94113E14	2.94687E14
10^{11}	7.02157E-4	7.02157E-4	2.94103E16	3.02322E16
10^{12}	7.02157E-5	7.02157E-5	2.94103E18	3.15814E18
10^{13}	7.02157E-6	7.02157E-6	2.94103E20	3.27771E20
10^{14}	7.02157E-7	7.02157E-7	2.94103E22	6.07962E22

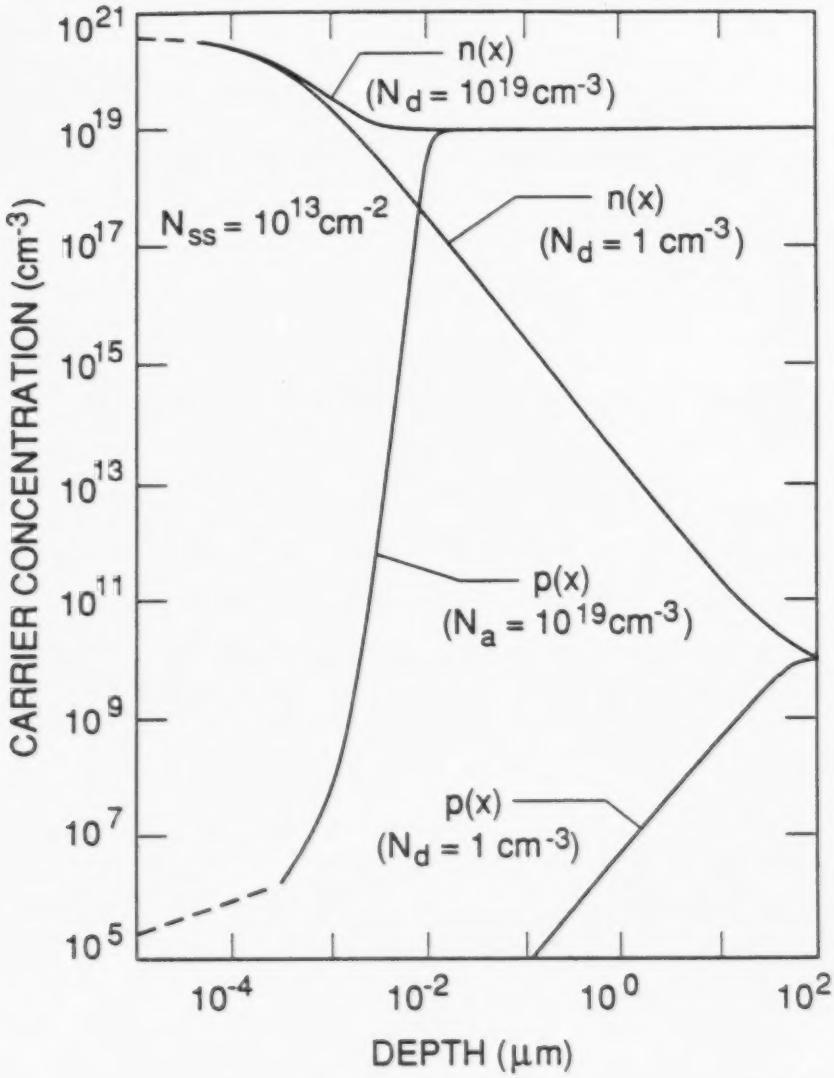

FIGURE 7.1 A comparison of the electron n(x) and hole p(x) concentrations near an oxide-silicon interface with a positive, trapped charge number density corresponding to $N_{ss} = 10^{13}$ cm^{-2} for nearly intrinsic silicon, for silicon with a donor density $N_d = 10^{19}$ cm^{-3}, and for silicon with an acceptor density $N_a = 10^{19}$ cm^{-3}.

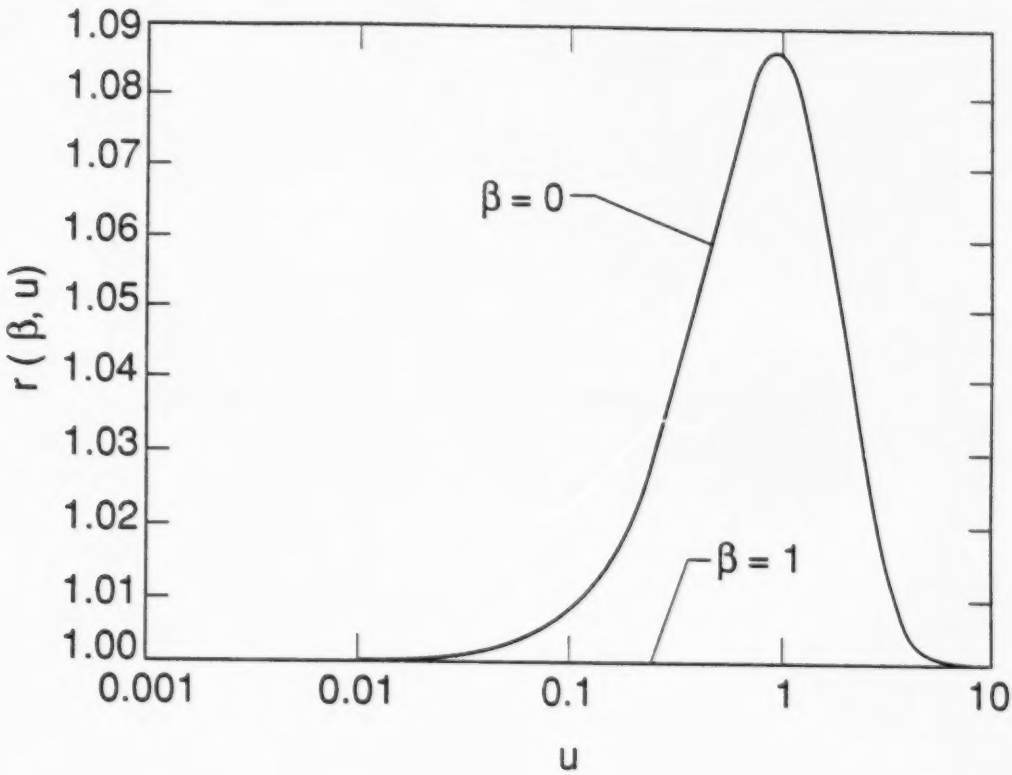

FIGURE 7.2 The function $r(\beta,u)$ whose square modulates $M_\infty \coth^2 u$ in describing the surface-accumulated majority-carrier concentration in a uniformly doped semiconductor for the limiting values $\beta = 0$ and $\beta = 1$.

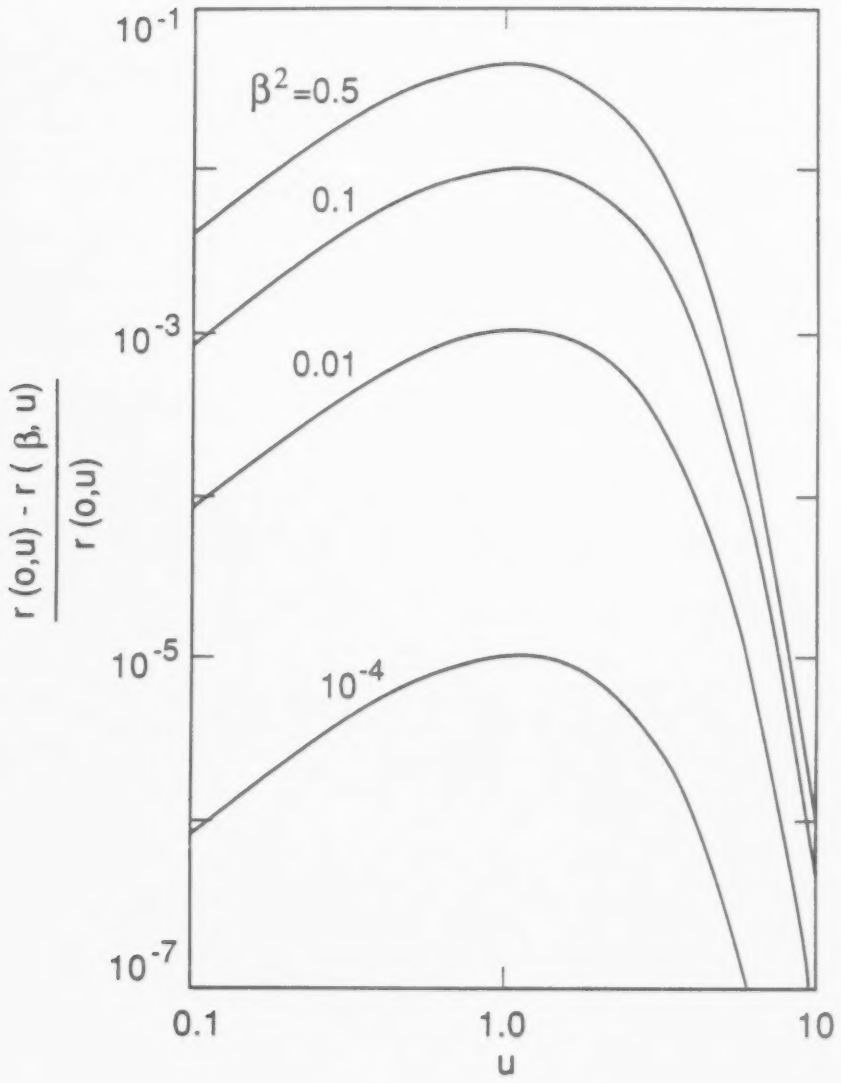

FIGURE 7.3 The relative error incurred by approximating $r(\beta,u)$ by $r(0,u)$ for various values of β^2 as a function of the dimensionless parameter u.

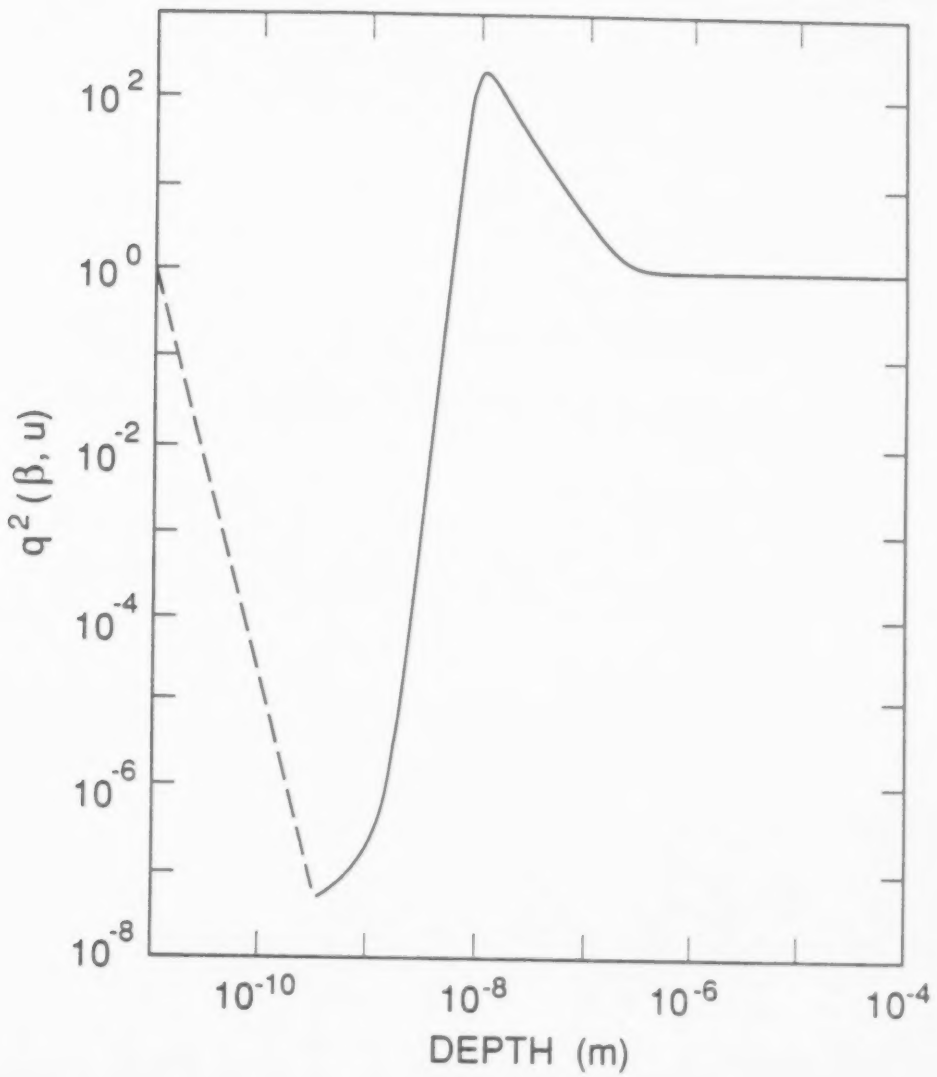

FIGURE 7.4 An approximation to $q^2(\beta,u)$ for $\beta = 1.45\ 10^{-9}$ obtained as the ratio of the carrier concentration calculated by PC-1D to $M_\infty \tanh^2(u)$ that shows that this function varies over ten orders of magnitude to modulate $M_\infty \tanh^2(u)$ in describing the surface-depleted and inverted majority-carrier concentrations in a heavily doped semiconductor. As a result, its use offers no advantage over previous approaches.

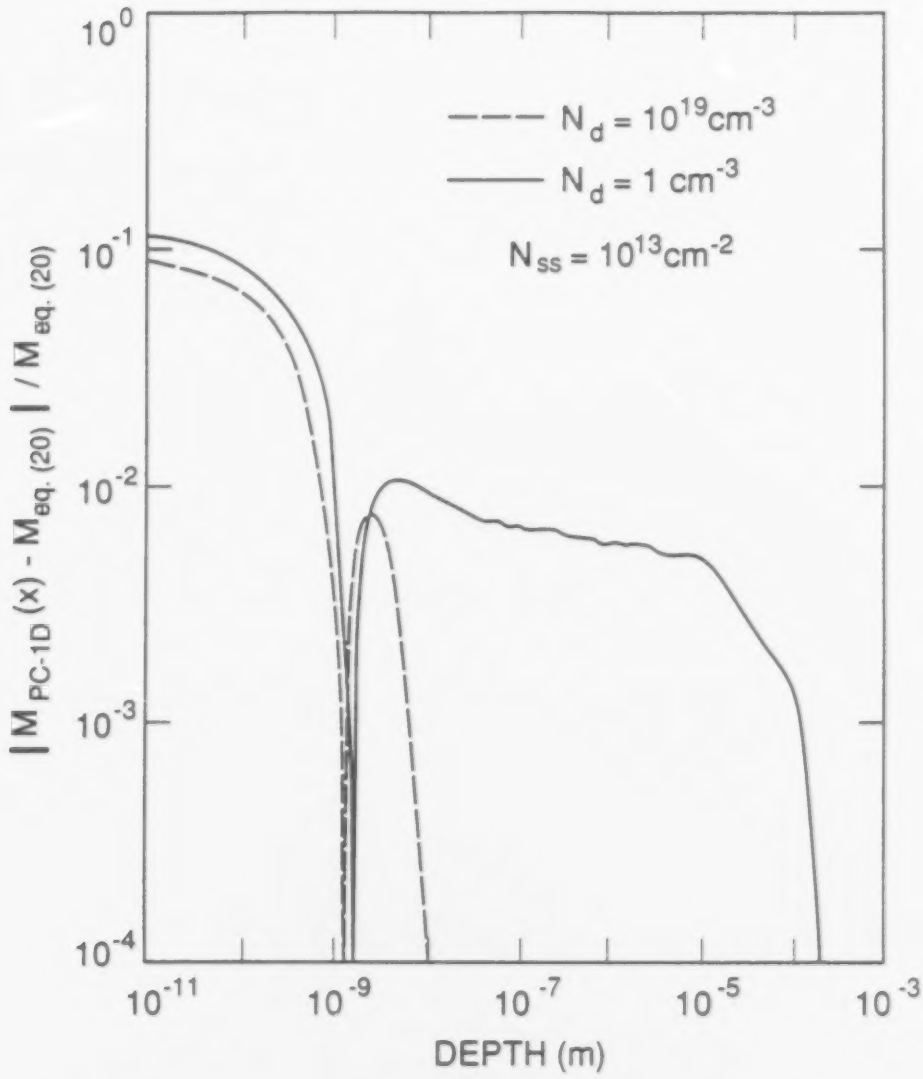

FIGURE 7.5 The absolute values of the relative differences between accumulated carrier concentrations calculated from PC-1D and from eqs. (20) and (24) of this paper for heavily doped and nearly intrinsic material.

REFERENCES FOR CHAPTER 7

1. J. Geist and H. Baltes, High accuracy modeling of photodiode quantum efficiency, Appl. Opt. **28**, 3929-3939 (1989).

2. J. Geist, Current status of, and future directions in, silicon photodiode self-calibration, Proc. SPIE **1109**, 246-256 (1989).

3. P. A. Basore, D. T. Rover and A. W. Smith, "PC-1D Version 2: Enhanced numerical solar cell modeling," 12th IEEE Photovoltaic Specialists Conference, 389-396 (publication 0160-8371/88/0000-0389, IEEE, Piscataway, NJ 08854, 1988).

4. Available from ISU Extension Software Service, Ames, IA 50011.

5. R. H. Kingston and S. F. Neustadter, Calculation of the space charge, electric field, and free carrier concentration at the surface of a semiconductor, J. Appl. Phys. **26**, 718-720 (1955).

6. C. E. Young, Extended curves of the space charge, electric field, and free carrier concentration at the surface of a semiconductor, and curves of the electrostatic potential inside a semiconductor, J. Appl. Phys. **32**, 329-332 (1961).

7. J. R. Lowney, The effect of electron-hole plasmas on the density of states in silicon and GaAs, J. Appl. Phys. **66**, 4279-4283 (1989).

8. Actually, it is possible to run PC-1D and many other device modeling programs in an iterative mode that allows better approximations to be calculated external to PC-1D for both the mobility and n_{ie} after each iteration and used as input for the next iteration, if desired.

9. J. Geist, J. R. Lowney, C. R. James, and A. M. Robinson, Testing the accuracy of calculated equilibrium carrier concentrations in the presence of surface fields, J. Appl. Phys. **70**, 236-242 (1991).

10. Subroutine D02GAF, NAG Fortran Library, Numerical Algorithms Group Inc., Downers Grove, IL 60515-1263.

11. R. S. Muller and T. I. Kamins, Device Electronics for Integrated Circuits, (2nd edition, John Wiley & Sons, NY, 1986) p. 389.

8. HIGH-ACCURACY MODELING OF SILICON PHOTODIODE WITH PC-1D

This is the first of three chapters specifically devoted to modeling the internal quantum efficiency of silicon photodiodes for various high accuracy applications. The modeling is carried out with Version 2 of PC-1D[1,2]. It was shown in Chapter 7 that this program accurately reproduces the majority carrier distribution in the presence of strong surface fields, a property shown to be essential for high accuracy modeling in Chapter 6. This Chapter is concerned with developing tools to optimize the use of PC-1D for high accuracy modeling, and with incorporating into PC-1D the absorption coefficient data of Chapter 5 that was selected on the basis of the results described in Chapters 3 and 4. The next two chapters describe the use of PC-1D to model three different types of silicon photodiodes in two different high-accuracy applications.

PC-1D[1,2] is a computer program for numerical modeling of the electrical performance of one-dimensional semiconductor devices including photogeneration. It is optimized for solar cell modeling, and runs on IBM-PC compatible computers equipped with a numerical coprocessor. Version 2 of PC-1D includes realistic models of most of the semiconductor material and device properties that are important for high-accuracy applications of photodiodes. Consequently, Version 2 of PC-1D has potential as a tool for supporting these applications.

Unfortunately, for reasons that have to do with the difference between the applications for high-accuracy photodiodes and those for solar

---

A version of this chapter has been published: J. Geist, D. Chandler-Horowitz,, A. M. Robinson, and C. R. James, Numerical modeling of silicon photodiodes for high-accuracy applications, Part I. Simulation programs, J. Res. NIST **96**, 463-469 (1991).

cells, it is not easy to achieve the highest accuracy of PC-1D through its standard user interface. However, the designer of Version 2 of PC-1D anticipated this problem and included the option to run it in batch mode in a way that does allow access to the highest levels of numerical precision and accuracy that are available from PC-1D.

This chapter reports the development of a program shell for PC-1D that provides a batch-mode user interface optimized for high-accuracy modeling of photodiodes. The shell consists of three programs. The first is a program that prepares the input for PC-1D, the second is a program that reads the output from PC-1D, and the third is a MS-DOS batch file program that supervises the sequential execution of PC-1D and the other two programs.

The remainder of this chapter reviews the properties of Version 2 of PC-1D and describes the new program shell for high-accuracy modeling of photodiodes. Typical applications are described in Chapters 9 and 10.

8.1 DESCRIPTION OF PC-1D

Version 2 of PC-1D is an interactive, graphical, semiconductor-device simulation program that solves the fully-coupled, drift-diffusion (electron and hole transport) equations in one dimension. Its principal limitations are that it supports no more than three regions of possibly different materials, and that it is a one-dimensional model with a maximum of 150 finite elements. Within these constraints the program is very versatile. It is beyond the scope of this thesis to describe its full capability, but details can be found in Ref. 2.

Both the IBM Pascal source code and the executable code are available for PC-1D. The latter requires an IBM PC-compatible computer equipped with at least 512 kbytes of random access memory (RAM), a 80X87 coprocessor chip, a CGA, VGA, or EGA compatible graphics adapter, and a matching display. To use the shell described in this chapter, batch mode operation is necessary, which requires an MS-DOS compatible operating system (Version 3.1 or greater).

Only one of the interactive modes of PC-1D is of interest for the purposes of this chapter, the one that allows the creation and saving of parameter files. Parameter files contain all of the information needed by PC-1D to model a specific, user-defined device. These files are stored in binary format under user-defined names with .PRM as their extension. Included in the parameter file are the names of other data files needed by PC-1D to model the device.

8.1.1 OPENING MENU

Figure 8.1 shows the opening menu when PC-1D is run in the interactive mode. An overview of the options mentioned in this menu is appropriate for what follows. The first, second, and fourth options, "Proceed with Solution", "Preview / Examine", and "Output Graphs:" are used in the interactive modeling mode, and are of no concern here. The "Solution Mode:", "Base Voltage:", "Collector Voltage:", and "Light:" options are used to set the electrical and optical conditions under which the simulation will be run. For the purposes of this thesis, it does not matter what selections are made for these options; they will be set to the correct values by the high-accuracy photodiode modeling shell when it is run.

The "Simulation Parameters:" option is used to load parameter files in the interactive mode, but it is also used to save parameter files, which is of interest to the use of PC-1D in batch mode. The "Reinitialize:" and "Number of Finite Elements:" options allow details of the numerical procedures to be modified to a certain extent. Normally, 150 finite elements, the maximum allowed, will be needed for high-accuracy modeling. It will sometimes be necessary to use this menu option in order to force PC-1D to use all 150 elements. Reinitialization is probably desirable, except perhaps when simulating a reverse-bias experiment.

The remaining options define the detailed nature of the device and external circuit to be modeled. All of the parameters obtained from the internal models built into PC-1D are adjusted to the values appropriate for the temperature entered following the "Temperature:" heading at the bottom of the opening menu. The user, of course, must assure that any user-defined parameters or data files are consistent with the chosen temperature. The "Area:" option is straightforward. The "Thickness:" option allows three different regions to be defined, each having its own thickness, material, and doping properties. If the thickness of a region is set to zero, it is not included in the solution, and it is not explicitly indicated following the "Thickness:" heading.

8.1.1.1 MATERIALS PROPERTIES

Selection of the "Materials:" heading of the opening menu allows such properties as the carrier mobilities, band-gap narrowing, Auger recombination cross sections, and absorption coefficient to be adjusted. For each region, a set of three files having the extensions

.MAT, .INR, and .ABS are needed. These files are 1) an ASCII file that is the main material file, 2) an ASCII file containing wavelength versus real index of refraction data, and 3) an ASCII file containing wavelength versus absorption-coefficient data, respectively. All of the file names are stored in the parameter (PRM) file. In default operation, the INR and ABS files will have the same name as the MAT file. The user has the option of associating alternate ABS and INR files with a given MAT file in a particular parameter file, even though they have different names. If this is done, asterisks follow the MAT file names in the "Materials:" option heading, as shown in Fig. 8.1. Other material properties are included in internal models. Some of these allow the user to specify the values of the parameters in the equations defining the models, and most can be replaced by user-supplied ASCII files having the appropriate extensions. The internal model of the absorption coefficient of silicon, which is discussed next, is an example.

The default absorption-coefficient data in the SI.ABS file of Version 2 of PC-1D are not accurate enough for high-accuracy modeling of silicon photodiodes over the 400 nm to 900 nm spectral region.[3] Indeed, Chapters 3 through 5 of this thesis are concerned with choosing a suitable spectrum. Two data sets of higher accuracy were calculated and stored in files named SIL_WEAK.ABS and SIL_PHIL.ABS. The first data set was calculated by using eq. 1 of Ref. [3], which was fitted to the data of Ref. [4] over the spectral range from 470 to 1180 nm. This is the spectrum selected in Chapter 5. The second data set was calculated by interpolation of the data of Ref. [5]. The first set is believed to be more accurate above 450 nm; the second below 450 nm.

The ratios of the data in SIL_PHIL.ABS to that in SIL_WEAK.ABS are plotted over the 400-nm to 900-nm spectral range in Fig. 8.2. The difference can be characterized conservatively as 12% ± 4% over the spectral region from 440 nm to 780 nm, growing much larger outside that spectral region. The value of 12% is a convenient average offset because it is the difference between the two data sets at 633 nm. At that wavelength the value calculated from eq. 1 of Ref. [3] agrees with a recent measurement[6] to within the ±2% uncertainty associated with the measurement.

One material property not modeled by PC-1D is the quantum yield for electron-hole pair production.[7] It may differ significantly from unity outside the 400 to 900 nm spectral region,[8] but no high accuracy models currently exist outside that region.[7,9] This is the main reason that the modeling described in Chapters 9 and 10 is confined to the 400 to 900 nm spectral region. However, other problems, such as larger uncertainties in the available absorption-coefficient data at shorter wavelengths and uncertainties in the fraction of the radiation reflected by the rear surface of the photodiode at the longer wavelengths also contribute to a significant deterioration in accuracy outside that spectral region.

8.1.1.2 DEVICE PROPERTIES

The "Doping:" heading of the opening menu of PC-1D allows either an internal doping model or an external file containing doping concentrations for each region of the device being modeled. The internal model consists of two front and two rear dopant distributions, as well as a uniform background dopant. The

distributions can be chosen from uniform, complementary error, and Gaussian functions, and the parameters defining the maximum value, its location, and the width of the distributions can be adjusted. If tabular doping data are to be used, they are read from a user-generated ASCII file containing a depth, an n-type dopant concentration, and a p-type dopant concentration on each line, and having .DOP as its extension.

The shape of the equilibrium majority carrier-concentration near the front-surface oxide-silicon interface is very important to high-accuracy photodiode modeling.[10] It is necessary to use external files to model the front region doping in p^+n type photodiodes to force PC-1D to devote enough finite elements to the front region to accurately approximate the majority carrier concentration there.

The "Recombination:" heading of the opening menu of PC-1D allows the defect-related recombination in the volume and at the surfaces of the device to be modeled. (Auger recombination is considered a material property and covered under the "Materials:" heading.) Shockley-Hall-Read (SHR) recombination through a single energy-level trap state is used as the model for volume recombination. Either an internal model or a user-defined table of depths and electron and hole lifetimes (equivalent to cross sections in the SHR model) in an external ASCII file with the extension .TAU can be used to model the volume recombination. With the internal model, the user may choose a single electron lifetime, a single hole lifetime, and a single trap energy relative to mid-gap for each region. With the external model, a trap level at mid-gap is used with the lifetime data in the external ASCII file.

The restriction of the SHR model to a single-energy state prevents PC-1D from accurately fitting the measured[11] variation of quantum efficiency with flux (i.e., nonlinearity) at 950 nm for an EG&G UV444B photodiode as illustrated in Fig. 8.3. The simulated data in Fig. 8.3 were calculated using a mid-gap state with equal electron and hole lifetimes. Even though the simulated and experimental data agree in the low flux limit and again at a high flux level, their shapes are very different. Better agreement can be achieved at low flux levels at the cost of a worse fit at the higher flux levels by moving the state away from mid-gap, and by using different electron and hole lifetimes as illustrated in Fig. 8.4. It is expected that the proper distribution of SHR trap levels over the band gap would result in an accurate simulation of the nonlinearity of this type of photodiode, but the actual distribution is unknown.

It should be possible to develop an external lifetime model based on a parametrized distribution of SHR recombination states, and to adjust the parameters to fit the nonlinearity data shown in Figs. 8.3 and 8.4. However, it would be necessary alternately to use PC-1D to calculate the carrier concentrations and then the external model to calculate the lifetimes appropriate to these carrier concentrations, and to iterate to self-consistency. This procedure is too complex and time consuming to be practical at the current time.

The failure of the SHR model in Version 2 of PC-1D to describe the nonlinearity of this type of photodiode casts some doubt on its ability to model accurately the reverse-bias self-calibration experiment.[12,13] This point is addressed in more detail in Chapters 9

and 10.

In the case of surface recombination the "Recombination:" option allows the choice of one of two internal models, a surface-recombination velocity model, and a saturation-current density model, but does not accommodate a user-defined data file. The choice of the surface-recombination velocity model allows the user to adjust the hole- and electron-recombination velocities as well as the energy-level of a single-energy surface state.

The "Surfaces:" option allows the user to choose the surface charge at the front and back surfaces of the device. For modeling the oxide-bias self-calibration experiment,[12,13] the surface charge is the algebraic sum of any charge trapped in the oxide during fabrication of the photodiodes and the charge stored on the oxide surface by the voltage applied to the transparent electrode used in the oxide-bias experiment.

The "Circuit:" option of the main menu of PC-1D allows the user to define a circuit in which the device is to operate. For the case of a photodiode, the emitter and base are connected, the collector is disconnected, and the connections to the device are made at the front and back surfaces. Keeping the collector disconnected forces the "Collector Voltage:" option to zero, as shown in Fig. 8.1. Setting the internal resistance R_b to some non-zero value in the Main Menu of PC-1D allows the effect of series resistance to be simulated.

8.2 THE PHOTODIODE MODELING SHELL PROGRAMS

The photodiode modeling shell for Version 2 of PC-1D is designed to

allow simulation of oxide-bias and reverse-bias, self-calibration experiments, nonlinearity measurements, and internal quantum efficiency spectra, while accessing the highest accuracy and precision available from PC-1D. It consists of three program files. The first program, a short MS-DOS Batch program named RUN_PC1D.BAT, is listed in Fig. 8.5. The other two programs, MAKE_PRM.EXE and READ_PDF.EXE, were complied with Version 5.5 of Turbo Pascal from the listings contained in Appendices 1 and 2, respectively, of this thesis.

8.2.1 OPERATION OF RUN_PC1D.BAT

RUN_PC1D.BAT first tests whether or not the files MAKE_PRM.EXE, PC-1D.EXE, and READ_PDF.EXE exist. If not, it issues an error message, and terminates execution at :STOP. If all three files do exist, RUN_PC1D deletes the temporary file TEMP.DAT. This is a precaution in case a previous nonstandard termination left this file in existence. RUN_PC1D then enters the loop between :LOOP and GO TO LOOP. Once in this loop, it transfers control to MAKE_PRM.EXE.

MAKE_PRM.EXE first tests the existence of TEMP.DAT. If TEMP.DAT does not exist, then MAKE_PRM.EXE prompts the user to define the photodiode experiment to be simulated. Examples of the questions and typical answers are shown in Fig. 8.6. The questions and answers are clear and require no explanation. If the file option rather than the keyboard option is chosen to define the independent variables for the experiment to be simulated, then the program asks for the file name instead of the start, stop, and step values for the independent variable. Once MAKE_PRM.EXE has obtained all of the necessary information, it writes that information into the file TEMP.DAT, creates the temporary parameter file TEMP.PRM, and passes control back

to RUN_PC1D.BAT.

RUN_PC1D.BAT now tests the existence of TEMP.DAT. If it does not exist, RUN_PC1D terminates execution. If TEMP.DAT does exist, then RUN_PC1D passes control to PC-1D.EXE. This program reads TEMP.PRM (the first TEMP on the command line following PC-1D), carries out the simulation defined therein, writes a table having a depth, an electron current, a hole current, and a total current on each line in the file TEMP.PDF (the second TEMP on the command line), and returns control to RUN_PC1D.BAT. Note that PDF files are the standard ASCII format HP plotter output files generated by PC-1D.

RUN_PC1D.BAT now passes control to READ_PDF.EXE. This program reads the total photocurrent at the depth specified in the definition of the experiment to be simulated (See Fig. 8.6) from file TEMP.PDF, and appends it to the output file specified in response to the prompt from MAKE_PRM.EXE. READ_PDF.EXE then returns control to RUN_PC1D.BAT.

On subsequent passes through the loop, MAKE_PRM.EXE finds that TEMP.PRM does exist, reads the necessary information from this file, and writes updated TEMP.DAT and TEMP.PRM files. The information about when to exit the loop is in TEMP.DAT, and when MAKE_PRM.EXE determines that this time has come, it deletes TEMP.DAT, triggering RUN_PC1D.BAT to terminate execution.

8.2.2 FEATURES OF MAKE_PRM AND READ_PDF

MAKE_PRM.EXE and READ_PDF.EXE are designed to compensate for traits of PC-1D that make the latter less than ideal for high-accuracy modeling of photodiodes. The first trait is that PC-1D.EXE calculates the

internal quantum efficiency from the sum of the photocurrent and the dark current occurring under reverse or forward bias. This is probably not a problem in solar cell modeling where very high accuracy is not required, but it is a problem for modeling high-accuracy applications of silicon photodiodes. As a result, MAKE_PRM.EXE calculates and stores the appropriate dark currents for all simulations that have a nonzero bias voltage V_{bb}, and READ_PRM.EXE reads them and subtracts them from the appropriate total currents when calculating the quantum efficiency. This is simulated as a shutter-closed/shutter-open measurement sequence by MAKE_PRM.EXE.

Even though the total current is a constant throughout a photodiode, it must be calculated at each finite element in the photodiode. The numerical precision with which it can be calculated depends upon the majority carrier concentration in the element where it is being calculated. This is caused by the nature of the numerical algorithm, which involves the difference of two large numbers that scale with doping concentration. This effect is illustrated in Fig. 8.7, which shows the variation in the total current computed by PC-1D as a function of depth in the front region of a p^+n type photodiode irradiated by 1 $\mu W/cm^2$ of 440-nm radiation. This result was obtained by running PC-1D through its standard user interface and could not be obtained by running PC-1D with the shell just described, since carrier concentration as a function of depth is not an output supported by the shell. The decrease in the noise in the data with increasing distance from the front surface of the photodiode is evident in the figure.

PC-1D.EXE calculates the quantum efficiency from the total current at either the front or the rear of the photodiode at the discretion of

the user. Since these are usually the regions where the majority carrier concentration is greatest, PC-1D often calculates the quantum efficiency from values of the total photocurrent that are not the most precise available to it. This loss of precision, which occurs even in the absence of dark current, is the reason that MAKE_PRM.EXE asks the user to choose the depth at which the total photocurrent will be read from the TEMP.PDF file. This depth should be somewhere in the interior of the photodiode where the doping concentrations are low and the effect of surface fields on the carrier concentrations is small or negligible.

Very high precision is available under these conditions. The internal quantum efficiency was calculated by RUN_PC1D for the same type of photodiode used to generate the data in Fig. 8.7. With all of the loss (recombination) mechanisms set to zero, the quantum efficiency was 6 parts per million (ppm) above unity ± 1 ppm for 1 $\mu W/cm^2$ irradiation throughout the 400-nm to 900-nm spectral region. This result was obtained by assuming the somewhat large thickness of 400-μm for this photodiode to minimize the fraction of the incident radiation penetrating to the rear of the photodiode. PC-1D does not permit a reflectance of 100% at the rear surface of the diode. With a more typical 300-μm thick photodiode under the same conditions, the quantum efficiency was reduced a few ppm at the longest wavelengths.

Since PC-1D does not model the oxide passivation on the front surface of the photodiode, it is necessary to vary the oxide-trapped charge N_{ss} to simulate the effect of applying a voltage across the oxide in the silicon self-calibration experiment. First, the value of N_{ss} must be chosen to simulate the oxide-fixed charge. To this value must be

added the charge appropriate to the application of oxide bias according to the formula for the charge density stored on a capacitor as a function of thickness, dielectric constant, and applied voltage. It is this sum that PC-1D must use as N_{ss} when simulating the effect of oxide bias on a photodiode. The bookkeeping for the values of N_{ss} chosen to simulate the oxide-fixed charge and the changes in N_{ss} needed to simulate the combined effect of the fixed charge and the applied oxide bias are handled by MAKE_PRM.EXE.

8.3 CONCLUSIONS

The semiconductor device modeling program PC-1D and some programs to enhance its use in the high-accuracy modeling of silicon photodiodes have been described. The features of PC-1D that suit it for high-accuracy photodiode modeling have been described, and the features of the support programs that compensate for features of the PC-1D user interface that are less than ideal for this application have also been described. Examples of the use of these programs in photodiode modeling in different types of high-accuracy applications are given in Chapters 9 and 10.

PC-1D PROGRAM CONTROL

Proceed with Solution

Preview / Examine (None)

Simulation Parameters: 1337_NEW

Output Graphs: Specified

Reinitialize: Yes

Number of Finite Elements: 150

Solution Mode: Equilibrium

Temperature: 25 C

Area: Uniform 1 cm2

Thicknesses: 1 m, 299 um

Materials: SI*, SI*

Doping: 1337, Internal

Recombination: Internal

Surfaces: Charged, Neutral

Circuit: Vbb

Base Voltage: Zero

Light: 10 uW/cm2

Photogeneration: Monochrome 440 nm

Reflectance: 0, 0.85

FIGURE 8.1 The opening menu of PC-1D when run in the interactive mode.

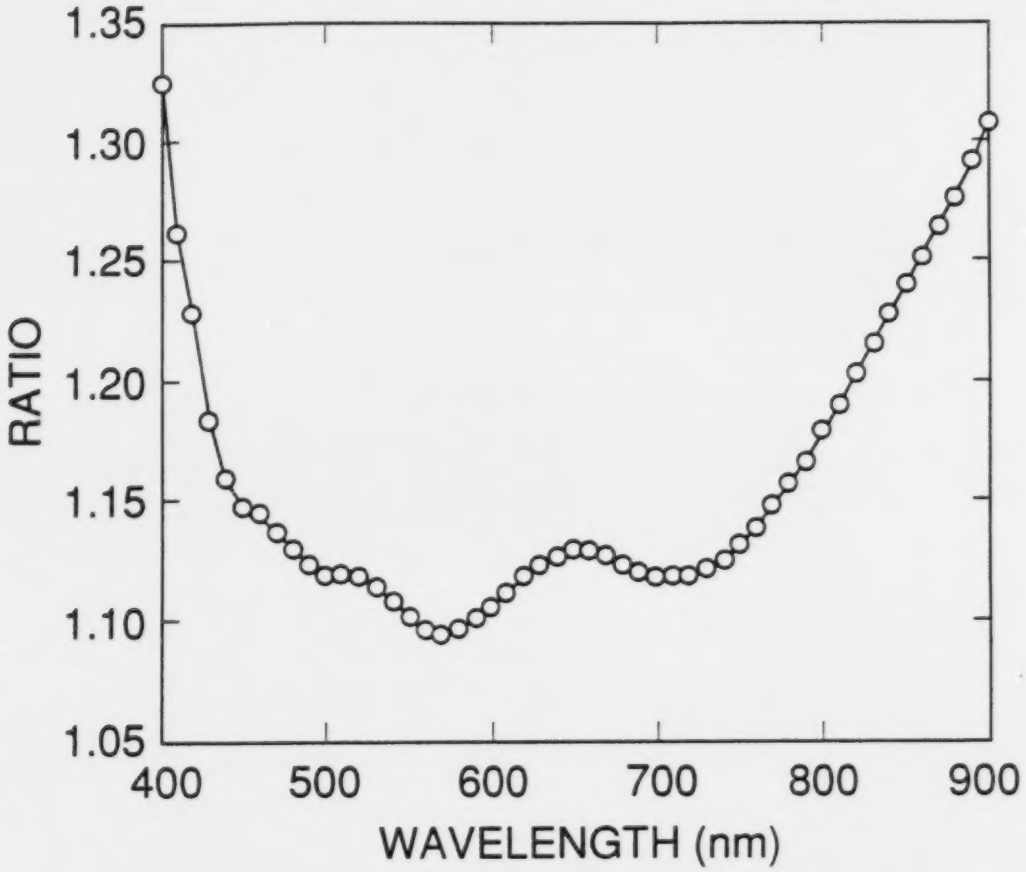

FIGURE 8.2 Ratios of the absorption coefficient data interpolated from Ref. 5 to those calculated from eq. 1 of Ref. 3 that were fit to the data of Ref. 4.

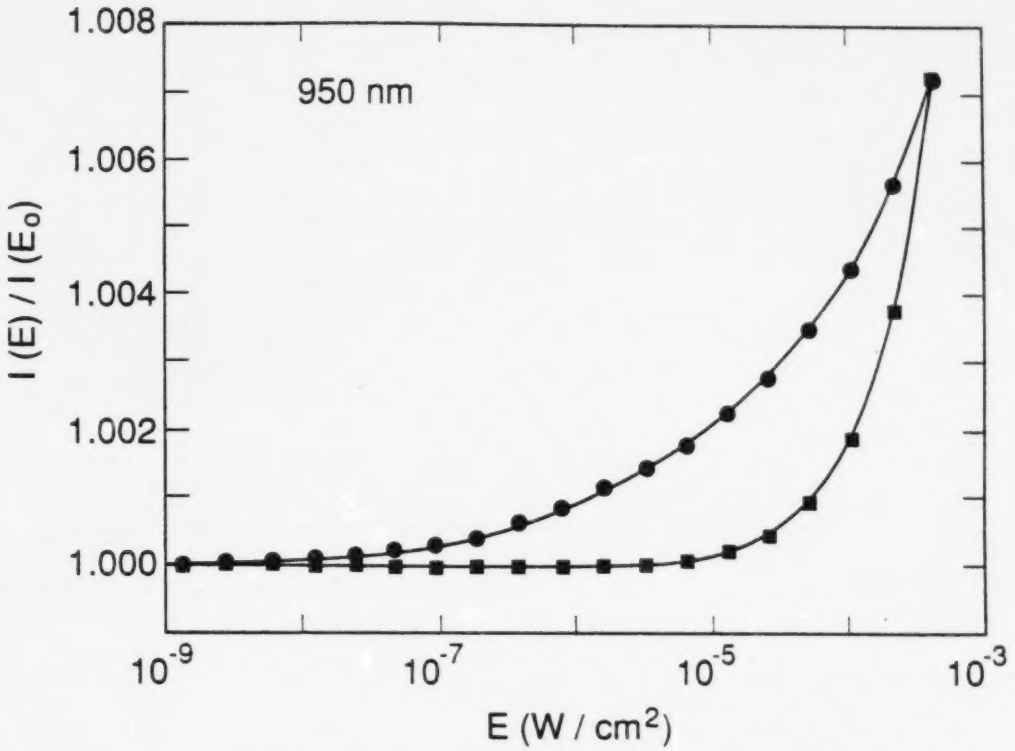

FIGURE 8.3 Comparison of experimental (filled circles) and simulated (filled squares) linearity measurements on an EG&G UV444B (444B) photodiode at 950 nm using a single SHR trap level at mid-gap with electron and hole lifetimes of 74.04 μs. I(E) is the photocurrent as a function of the incident irradiance E, and $E_0 = 10^{-9}$ W/cm^2 is the irradiance to which the linearity measurements are referenced.

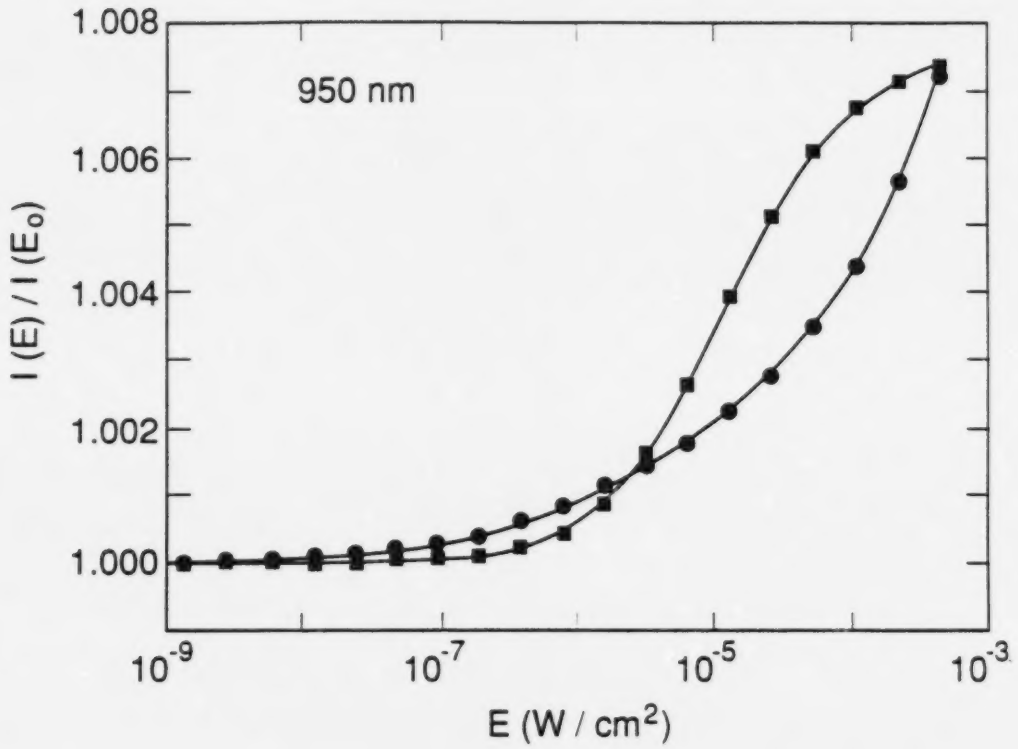

FIGURE 8.4 Comparison of experimental (filled circles) and simulated (filled squares) linearity measurements on an EG&G UV444B (444B) photodiode at 950 nm using a single SHR trap level 0.1796 eV above mid-gap with electron and hole lifetimes of 900 ms and 700 μs, respectively. I(E) is the photocurrent as a function of the incident irradiance E, and $E_0 = 10^{-9}$ W/cm^2 is the irradiance to which the linearity measurements are referenced.

```
IF NOT EXIST MAKE_PRM.EXE GOTO ERROR1
IF NOT EXIST PC-1D.EXE GOTO ERROR2
IF NOT EXIST READ_PDF.EXE GOTO ERROR3
DEL TEMP.DAT

:LOOP
     MAKE_PRM.EXE
     IF NOT EXIST TEMP.DAT GOTO STOP
     PC-1D TEMP TEMP
     READ_PDF.EXE
     GOTO LOOP

:ERROR1
     REM MAKE_PRM.EXE not found.
     GOTO MESSAGE

:ERROR2
     REM PC-1D.EXE not found.
     GOTO MESSAGE

:ERROR3
     REM READ_PDF.EXE not found.
     GOTO MESSAGE

:MESSAGE
     TYPE RUNPC1D.DOC
     GOTO STOP

:STOP
```

FIGURE 8.5 Listing for the MSDOS batch file RUN_PC1D.BAT that supervises the execution of the programs MAKE_PRM.EXE, PC-1D.EXE, and READ_PDF.EXE for high-accuracy photodiode modeling.

```
Parameter file (including PRM extension) defining photodiode:
1337_new.prm
Complete path to file in which to store QE results:
test.dat
Type of experiment to simulate?
(O)xide bias (Volts) scan?
(R)everse bias (Volts) scan?
(W)avelength (nm) scan?
(P)hoton energy (eV) scan?
(L)inearity (W/cm^2) scan?
Enter letter here: w
Start, stop, and stop values from
  (K)eyboard or all values from (F)ile? k
First value for scanned parameter: 400
Stop value for scanned parameter: 900
Step size for scanned parameter: 10
Incident irradiance (W per sq. cm): 1e-5
Oxide bias voltage (V): 0
Reverse bias voltage (V): 0
Non-zero thickness of front surface oxide (nm): 25
Depth at which to get total photocurrent (um): 100
```

FIGURE 8.6 A sample of the screen produced by MAKE_PRM.EXE when RUN_PC1D.BAT is executed.

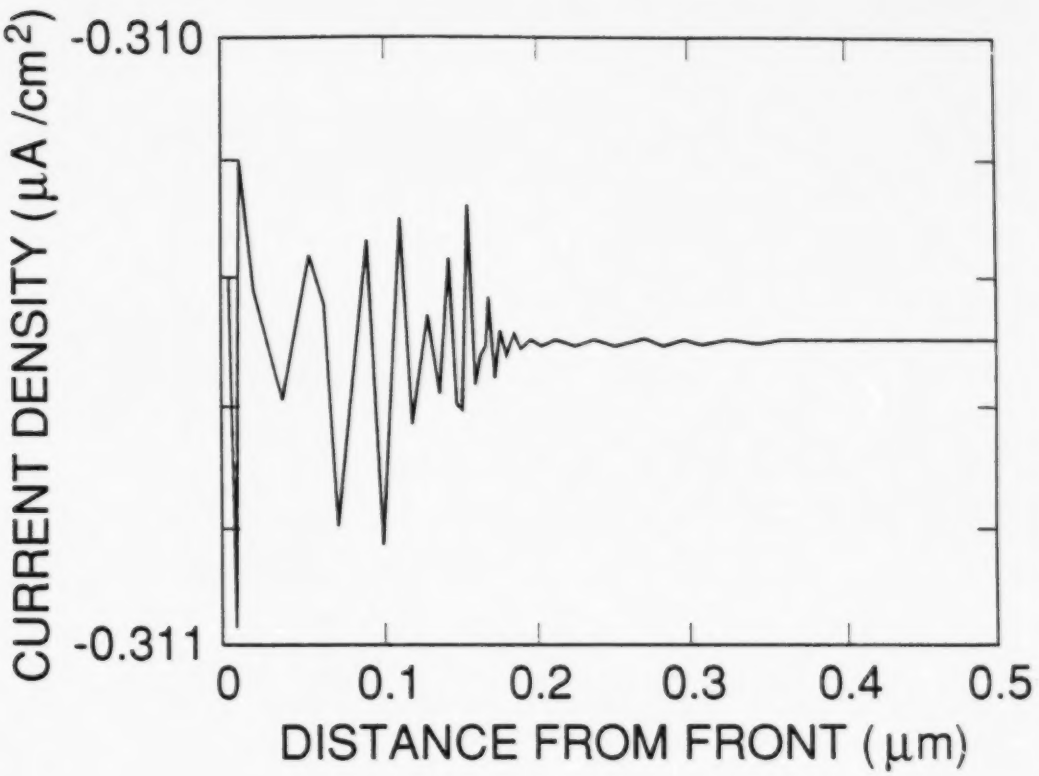

FIGURE 8.7. Variation in the total photocurrent calculated by PC-1D as a function of position in the front region of a Hamamatsu 1337-type photodiode due to the effect of the high front region doping concentration.

REFERENCES FOR CHAPTER 8

1. Available from ISU Extension Software, 108 Atanasoff Hall, Iowa State University, Ames, IA 50011, (505) 294-8658.

2. P. A. Basore, PC-1D version 2: enhanced numerical solar cell modeling, 20th IEEE Photovoltaic Specialists Conference - 1988, (IEEE pub. # 0160-8371/88/0000-0389, NY, 1988), 389-396.

3. J. Geist, A. Migdall, and H. P. Baltes, Analytic representation of the silicon absorption coefficient in the indirect spectral region, Appl. Opt. **27**, 3777-3779 (1988).

4. H. A. Weakliem and D. Redfield, Temperature dependence of the optical properties of silicon, J. Appl. Phys. **50**, 1491-1493 (1979), and personal communication from H. A. Weakliem.

5. H. R. Philipp, Influence of oxide layers on the determination of the optical properties of silicon, J. Appl. Phys. **43**, 2835-2839 (1972), and personal communication.

6. J. Geist, A. R. Schaefer, J-F. Song, Y. H. Wang, and E. F. Zalewski, An accurate value for the absorption coefficient of silicon at 633 nm, J. Res. NIST **95**, 549-558 (1990).

7. J. Geist and C. S. Wang, New calculations of the quantum yield of silicon in the near ultraviolet, Phys. Rev. **B27**, 4841-4847 (1983).

8. J. Geist, W. K. Gladden, and E. F. Zalewski, Physics of photon-flux measurements with silicon photodiodes, J. Opt. Soc. **72**, 1068-1075 (1982).

9. J. Geist, J. L. Gardner, and F. J. Wilkinson, Surface-field-induced feature in the quantum yield of silicon near 3.5 eV, Phys. Rev. **B42**, 1262-1267 (1990).

10. J. Geist and H. Baltes, High accuracy modeling of photodiode quantum efficiency, Appl. Opt. **26**, 3929-3939 (1989). Note there is an error in eq. 31 of this reference. The plus sign in the numerator of the first term in eq. 31 should be replaced by a minus sign.

11. K. D. Stock, Si-photodiode spectral nonlinearity in the infrared, Appl. Opt. **25**, 830-832 (1986), and personal communication.

12. E. F. Zalewski and J. Geist, Silicon photodiode absolute spectral response self-calibration, Appl. Opt. **19**, 1214-1216 (1980).

13. J. Geist, E. F. Zalewski, and A. R. Schaefer, Spectral response self-calibration and interpolation of silicon photodiodes, Appl. Opt. **19**, 3795-3799 (1980).

9. NUMERICAL MODELING OF OXIDE-BIAS SELF-CALIBRATION EXPERIMENTS

This chapter presents the results of high-accuracy simulations of various oxide-bias experiments performed on silicon photodiodes. The simulations were carried out by using PC-1D[1,2] and a set of three programs designed to support the use of PC-1D in this specific application. Both PC-1D and the support programs are described in the previous chapter.[3]

The oxide-bias experiment[4,5,6] consists of recording the ratio of the photocurrent as a function of oxide-bias voltage to the zero-bias photocurrent during irradiation of the photodiode with a stable photon flux. The oxide bias is usually applied with a transparent water-drop electrode. A review is given in Ref. 6.

The remainder of this chapter is organized as follows: Section 9.1 describes the simulation of an oxide-bias, self-calibration experiment on an EG&G UV444B photodiode. The purpose of this simulation is to demonstrate the derivation of an accurate value for the zero-bias quantum efficiency including an uncertainty estimate. Section 9.2 describes the simulation of an oxide-bias experiment on a Hamamatsu 1337 photodiode. The purpose of this simulation is to determine nominal values for the charge trapped in the oxide covering the front surface of the photodiode, and for the surface recombination velocity at the oxide-silicon interface. Section 9.3 describes the simulation of an oxide-bias experiment on a UDT UV100 photodiode. The purpose of this simulation is to determine a nominal high-accuracy value for the

---

A version of this chapter has been published: J. Geist, R. Koehler, R. Goebel, A. M. Robinson, and C. R. James, Numerical modeling of silicon photodiodes for high-accuracy applications: Part II. Interpreting oxide-bias experiments, J. Res. NIST 96, 471-479 (1991).

internal quantum efficiency of this type of photodiode and the nominal wavelength region where this value is valid. Section 9.4 gives the conclusions this chapter.

9.1 EG&G UV444B PHOTODIODE

The EG&G UV444B was the first type of silicon photodiode to be self-calibrated by using the oxide-bias experiment.[5] This photodiode consists of a 300 μm thick, 1.5×10^{13} cm^{-3} phosphorus-doped, n-type silicon substrate with an n^+-type phosphorus diffusion in the rear surface, a p^+-type boron diffusion in the front surface, and a nominally 120 nm thick, thermally grown oxide-passivation layer over the front surface. Figure 9.1 shows the front-region doping profile that was obtained from spreading resistance measurements on a representative UV444B photodiode. Figure 9.1 also shows the equilibrium hole concentration calculated for this doping distribution by using PC-1D.

The rear-region of the UV444B has an n^+-type diffusion that repels minority carriers away from the rear surface of the photodiode where they would otherwise recombine. This so-called minority carrier mirror was not modeled; instead it was assumed that the recombination velocity at the rear of the device was zero. This assumption is not physically realizable, but it results in a mirror for minority carriers at the rear of the device that serves the same function as the n^+-type diffusion. This assumption is useful because it requires fewer finite elements at the rear of the photodiode, thereby leaving more of them available for modeling the front region and depletion region.

Figure 9.2 compares simulated and experimental results of an oxide-bias experiment on a UV444B photodiode for irradiation by a 3 mm diameter spot of 476.2 nm laser radiation through a water-drop electrode. (The apparatus used for the oxide-bias measurements described in this chapter has been described previously.[7]) The absorption-coefficient data in the file SIL_WEAK.ABS, which were calculated from an equation[8] fit to the data measured by Weakliem and Redfield,[9] and which are described in Chapter 5, were used in this simulation. Both the surface recombination velocity S and the number density N_{ss} of the oxide fixed charge were adjusted in the simulation to obtain a good fit to the experimental data in Fig. 9.2.

The procedure used to fit the simulated data to the experimental data shown in Fig. 9.2 was as follows: First, a value of S was chosen, then the value of N_{ss} was adjusted until the average residual of the fit to the photocurrent ratio was zero for the two most negative voltages in the figure. This gave a value of N_{ss} for each value of S that was chosen. The best combination of S and N_{ss} was then obtained by minimizing the residual standard deviation over all of the data shown in Fig. 9.2.

Figures 9.3, 9.4, and 9.5 plot the residuals (differences) between the results of the fits and the experimental results and Table 9.1 lists the residual standard deviation for three different choices of S and N_{ss}. Careful inspection of the figures shows that the combination of S and N_{ss} used for Fig. 9.3 gives a better overall fit than either of the other choices, even though the residual standard deviation for Fig. 9.3 is not very much lower than that for Fig. 9.4 or Fig. 9.5. One reason for the relatively small decrease in residual standard

deviation with the best fit is that the residual standard deviation of all three fits are dominated by the apparent outlier points near -1 V and -10.5 V oxide bias.

The assignment of S = 6000 cm/s and N_{ss} = 1.942 x 10^{12} cm^{-2} with estimated uncertainties of ±1000 cm/s and ±0.070 x 10^{12} cm^{-2}, respectively, is justified by Figs. 9.3, 9.4, and 9.5. When these values are used in the PC-1D model of the UV444B photodiode, the internal quantum deficiency (one minus the internal quantum efficiency) at zero oxide bias is 0.1690 ± 0.0021. The stated uncertainty is the maximum difference between the internal quantum deficiency calculated for the combination of S and N_{ss} used in Fig. 9.3, and those calculated for the combinations of S and N_{ss} used for Figs. 9.4 and 9.5.

The assumption that the average of the last two data points on the right in Fig. 9.3 corresponds to 100% internal quantum efficiency is used with the conventional oxide-bias self calibration. That assumption gives a zero-bias internal quantum deficiency of 0.1634 with no reliable way to estimate the uncertainty associated with that value. Moreover, the result of that assumption differs by 0.0056 from the more accurate value that was determined in the last paragraph by using PC-1D to model the oxide-bias experiment. This difference is about 3.3% of the effect being calculated, and more than 2.5 times the uncertainty associated with the more accurate value.

It must be emphasized that the results reported here are illustrative rather than definitive since the doping distribution data in Fig. 9.1 were obtained from one photodiode, and the oxide-bias data in Fig. 9.2

were obtained from a different photodiode. An additional uncertainty associated with the effect of variations in doping distribution would be needed, or the doping distribution must be measured for the actual photodiode used in the self-calibration.

Because oxide bias voltages large enough to nearly saturate the photodiode response are also large enough to change S or N_{ss}, the oxide-bias measurement is already destructive to a certain extent, and it must be carried out as described in Ref. 10 in order to yield the highest accuracy of which it is capable. Therefore, the sacrifice of the photodiode for a spreading resistance measurement is not as impractical as it might at first seem. Nevertheless, it is inconvenient, and more convenient approaches are being developed.[6]

9.2 HAMAMATSU 1337 PHOTODIODE

Like the EG&G UV444B photodiode, the Hamamatsu 1337 is a p^+nn^+ photodiode, but its front-region doping profile is shallower, its background n-type dopant concentration is 5×10^{12} cm^{-3}, and its oxide-passivation layer has a nominal thickness of 25 nm. Figure 9.6 shows relative front-region doping profiles for six different Hamamatsu 1337 photodiodes taken from four different batches. The curves in Fig. 9.6 were normalized to unity at the oxide-silicon interface because it is the shape of the doping profile rather than the magnitude that has the major effect on the internal quantum efficiency, as discussed in Chapter 6.[11] The measured dopant concentrations at the oxide-silicon interface varied between 2×10^{18} and 1×10^{19} cm^{-3} for the six photodiodes of Fig. 9.6.

Figure 9.7 shows the results of modeling an oxide-bias experiment on a

1337 photodiode at 476.2 nm using the doping profile that correspond to the lower solid curve in Fig. 9.6. The fit shown in Fig. 9. 7 was obtained with $N_{ss} = -3.0 \times 10^{12}$ and $S = 1.835 \times 10^{5}$ cm/s, and gave a zero-bias internal quantum deficiency of 0.003199. It was possible to fit the oxide bias data in Fig. 9.7 just as well when using the doping profile corresponding to the upper solid curve in Fig. 9.6 by using $N_{ss} = -4 \times 10^{12}$ and $S = 1.56 \times 10^{5}$ cm/s. This fit gave a zero-bias internal quantum efficiency of 0.003280, which differs by only 8 parts in 10^{5} from the result based on the lowest curve in Fig. 9.6. As in the case of the UV444B type photodiode, the SIL_WEAK.ABS absorption-coefficient data were used, and the rear of the photodiode was modeled as uniformly doped with zero recombination velocity.

Figure 9.8 compares the internal quantum deficiencies calculated from the doping profile corresponding to the solid curves in Fig. 9.6 by using the values of N_{ss} and S that were obtained from the simulated oxide-bias experiments based on each of those profiles. The fact that the two curves have very similar shapes is very important. It suggests that a single function of wavelength might be used to extrapolate the internal quantum efficiency of any 1337 photodiode, rather than a different function for each different photodiode. This possibility is examined in detail in the next Chapter.

Notice that the sign of the trapped charge in the 1337 photodiode is the opposite of that for the UV444B photodiode, and that the interface recombination velocity is much larger. Both the sign of the trapped charge and the large value of the recombination velocity suggest an oxide prepared by chemical vapor deposition rather than by thermal oxidation; the latter is known to produce trapped positive charge and

a low surface recombination velocity. The modeling carried out here shows that the large negative charge in the oxide more than makes up for the greater surface recombination velocity by effectively repelling minority carriers from the surface.

The fact that the 1337 photodiode has negative rather than positive charge trapped in its oxide is important for its possible use in quantum-efficiency interpolation and extrapolation. If the oxide contained a significant amount of positive charge, as assumed in Ref. 12, the oxide-silicon interface would be depleted of holes, leading to a very large decrease in the energy needed to impact-ionize a valence band electron. However, since the oxide contains negative charge, the positive charge at the interface is accumulated. In this case, even though the charge density is quite large, there is little or no decrease in the energy needed to impact-ionize a valence band electron.[12] This is important because a large decrease in the energy required to impact-ionize a valence band electron might cause the quantum yield[13] for electron-hole pair production of the silicon near the front surface to exceed unity at wavelengths as long as 450 nm. This would limit the usefulness of this type of photodiode for extrapolating and interpolating quantum-efficiency calibrations. If this limitation were encountered, it could only be overcome with a very accurate model of the quantum yield in the presence of surface fields. Such a model appears well beyond the current state of the art.[12]

Even though the uncertainties in the internal quantum deficiency associated with the diode-to-diode variations in doping profile are quite small for the 1337 photodiode, the oxide-bias experiment is

still less than ideal for self-calibration.[6] However, since it is so well suited for interpolating and extrapolating internal quantum-deficiency data, as shown in Chapter 10, all that is needed is a way to calibrate it that works over a limited spectral region near 450 nm and another near 900 nm. The next section illustrates how simulations can be used to predict the internal quantum efficiency of a different type of photodiode with an uncertainty of ± 0.0003 at 450 nm.

9.3 UDT UV100 PHOTODIODE

The UDT UV100 photodiode is usually assumed to have an internal quantum efficiency of unity in the short wavelength portion of the visible.[14] In fact, this assumption is the basis for the use of the QED 100 and QED 200 multiple reflection radiometers,[15] which contain modified UV100 photodiodes, as high-accuracy absolute radiometric standards.

As the state of the art in absolute radiometry improves, the assumption of unit quantum efficiency for the UV100 type photodiode becomes more questionable. What is needed is a nominal internal quantum-deficiency spectrum accompanied by a reliable uncertainty spectrum. Since the 1337 type photodiode can be used to interpolate or extrapolate internal quantum-efficiency calibrations, as shown in Chapter 10, it is necessary to have these spectra only over a limited spectral region above 400 nm. One way to obtain these spectra is to calculate them from nominal characteristics of the UV100 photodiode. The pertinent characteristics can be obtained by fitting numerical simulations of oxide-bias measurements to experimental results as demonstrated in the preceding sections.

The UV100 photodiode is quite different from the UV444B and 1337. Its n^+p junction is not formed by introducing a front-region dopant, but is induced in a 100 Ω cm p-type (approximately 1.3 x 10^{14} cm^{-3}, boron-doped, p-type) silicon substrate by the growth of an oxide passivation layer having a large concentration of trapped positive charge.[16]

Figure 9.9 compares the results of simulated and experimental oxide-bias experiments on a UV100 photodiode. Here, again the absorption-coefficient data in SIL_WEAK.ABS were used, and the rear of the photodiode was modeled as uniformly doped with a surface recombination velocity of zero. Since the UV100 is an n^+p type rather than a p^+n type photodiode, the effect of increasing negative bias is to decrease rather than increase the internal quantum efficiency. However, because the zero-bias quantum efficiency is so close to unity, reducing the quantum efficiency is what is needed to sample the shoulder portion of the curve that contains the majority of the information about the values of N_{ss} and S, as can be seen in the figure.

The values of N_{ss} and S obtained from the fitting the PC-1D results to the measured data in Fig. 9.9 were 1.38 x 10^{12} cm^{-2} and 3.0 x 10^5 cm/s, respectively. These values are used to simulate the internal quantum-deficiency spectra for a nominal UV100 photodiode in Fig. 9.10. The three different curves shown in Fig. 9.10 correspond to minority carrier lifetimes τ of 1 μs, 10 μs, and 81 ms, respectively, in the rear region of the photodiode. The lifetimes of 1 μs and 10 μs give internal quantum deficiencies at 700 nm that bracket the range measured for six typical UV100 type photodiodes[17] and the 81 ms lifetime is the longest lifetime that the default silicon material

model of PC-1D will allow for 100 Ω cm, p-type silicon with a recombination trap at mid-gap.

The region between the curves corresponding to τ = 1 and τ = 10 μs in Fig. 9.10 is the range of nominal internal quantum-deficiency spectra that applies to UV100 type photodiodes and to QED 100 and QED 200 radiometers at zero reverse bias. Figure 9.11 compares the spectrum for τ = 1 μs around its minimum in the 400 to 500 nm spectral region with spectra obtained for the cases where either the front-region surface recombination velocity is doubled, or the positive charge trapped in the oxide is halved. These are conservative limits to associate with the mass production of photodiodes in a controlled planar-silicon fabrication process. These should also be conservative limits for the effects of environmental stress such as humidity, temperature, and irradiation with ultraviolet radiation, for UV100 photodiodes made after 1986.[18,19]

The curves in Fig. 9.11 can be used to estimate uncertainties to be associated with the nominal values of the internal quantum efficiency of the UV100 type photodiode. Summing in quadrature the differences between the nominal spectrum and the other two spectra in Fig. 9.11 produces a somewhat conservative estimate since increases in surface recombination velocity tend to be correlated with increases in trapped charge. In the region from 440 to 460 nm, a nominal value of 0.0003 ± 0.0003 is a practical summary of the results of such an analysis. This result should be considered a one-standard-deviation equivalent, rather than a limit of error, since the whole analysis is based on the results obtained for a single device. Outside the 440 to 460 nm spectral region the uncertainties grow so rapidly that they are not

really practical for high-accuracy applications.

There are a number of errors that have not yet been considered. All of these errors, which are described in detail in the next chapter in connection with the 1337 photodiode, were found to be negligible in the 440 to 460 nm spectral region compared to ±0.0003 for the UV100 photodiode. The reason for this is that all of these errors scale with the magnitude of the internal quantum deficiency, and this quantity is very small for this type of photodiode in this spectral region. This is illustrated in Fig. 9.12 for the uncertainty associated with the absorption coefficient of silicon, which is the largest uncertainty not considered so far.

Figure 9.12 compares the spectrum of Fig. 9.11 for τ = 1 μs, which was based on the absorption-coefficient data in SIL_WEAK.ABS, with the same spectra calculated for identical parameters, but based on the absorption-coefficient data measured by Philipp[20], and described in Chapter 8. When added in quadrature to the ±0.0003 assigned to the variations in N_{ss} and S from diode to diode, the effect of the uncertainty in the absorption coefficient is negligible. This might not remain true if a much larger wavelength interval were considered.

Because of the large long-wavelength quantum deficiency shown in Fig. 9.10, reverse bias is often applied to UV100 photodiodes and QED 100 and 200 radiometers when they are used at the longer wavelengths. By moving the depletion region toward the rear of the photodiode, the reverse bias forces the internal quantum deficiency to approach the lower quantum deficiency limit given by the 81 ms curve in Fig. 9.10.[15,21,22] Reverse bias is also applied to eliminate a saturation

nonlinearity that is sometimes observed with photocurrents above a few microamps. However, recent results[7] suggest that moderate bias levels can cause gain, resulting in an internal quantum efficiency in excess of unity. This effectively precludes the application of moderate reverse bias in high-accuracy applications.

As pointed out in Chapter 8, PC-1D cannot accurately model the reverse-bias self-calibration experiment, but this has no bearing on the accuracy with which PC-1D can model the oxide-bias experiment. The oxide-bias experiment is concerned with the front-region quantum deficiency, the reverse-bias experiment with the rear-region quantum deficiency. These regions are decoupled in photodiodes that have negligible recombination in the depletion region, which is a hallmark of a high quality photodiode. The other hallmark, negligible volume recombination in the front region, causes the details of the recombination process in the front region (surface recombination) to differ significantly from that in the rear-region. Indeed, the next chapter shows that the existing experimental evidence is consistent with the few parts in 10^4 uncertainties derived for the UV100 photodiode in this chapter and for the 1337 photodiode in the next chapter.

9.4 CONCLUSION

This chapter has demonstrated the use of Version 2 of PC-1D.EXE, RUN_PC1D.BAT, MAKE_PRM.EXE, and READ_PDF.EXE to simulate various oxide-bias experiments of interest to high-accuracy applications of silicon photodiodes. In each case, the simulation was used to interpret an oxide-bias experiment, with different sorts of information being sought from the different experiments.

It was shown that the simulations can be used to derive a more accurate internal quantum-deficiency value from an oxide-bias experiment than is available from the conventional data reduction, and that an uncertainty can be associated with the value derived from the simulation based on how well the simulated oxide-bias data can be fit to the experimental data. It was also shown that simulations can be used to determine nominal values for the front-surface recombination velocity and for the charge trapped in the front-surface oxide, and that values for these parameters can be used to determine nominal internal quantum-deficiency spectra for various types of silicon photodiodes.

As well as illustrating these general ideas, some more specific results were also obtained. Firstly, it was shown that a nominal internal quantum deficiency of 0.0003 ± 0.0003 is appropriate for the unbiased UDT UV100 photodiode in the 440 to 460 nm spectral region. Secondly, it was shown that the shape of the internal quantum-deficiency spectrum of the 1337 photodiode is quite independent of typical variations in doping profile. This result suggests that the 1337 might serve to extrapolate high-accuracy calibrations obtained from cryogenic absolute radiometers or from QED radiometers in the 440 to 460 nm spectral region to longer wavelengths with little or no loss of accuracy. The next chapter shows that this is the case.

TABLE 9.1. Comparison of simulated oxide bias results with experimental results for a UV444B type photodiode where Res. Std. Dev. is the standard deviation of the difference between simulated and experimental results.

S (cm/s)	N_{ss} (10^{12} cm^{-3})	Res. Std. Dev.
5000	2.011	0.002233
6000	1.942	0.002076
7000	1.883	0.002093

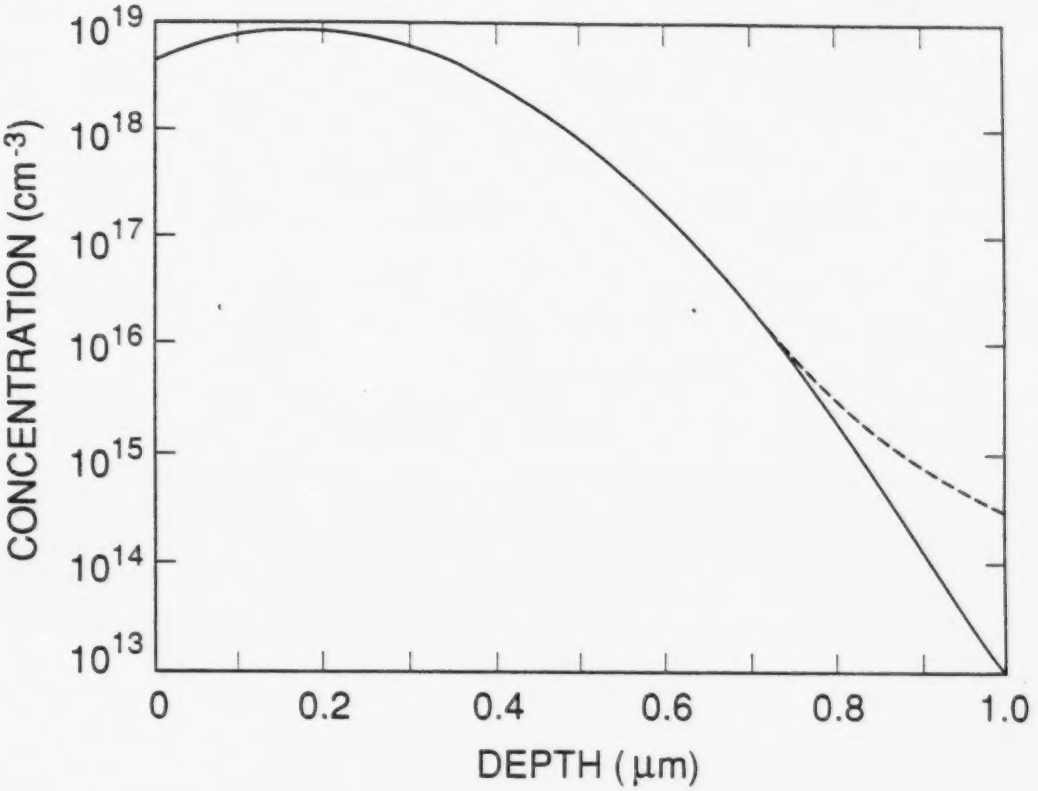

FIGURE 9.1 The front-region boron concentration (continuous line) determined from spreading resistance measurements for a typical EG&G UV444B photodiode, and the equilibrium hole concentration (dashed line) calculated by PC-1D from the boron concentration.

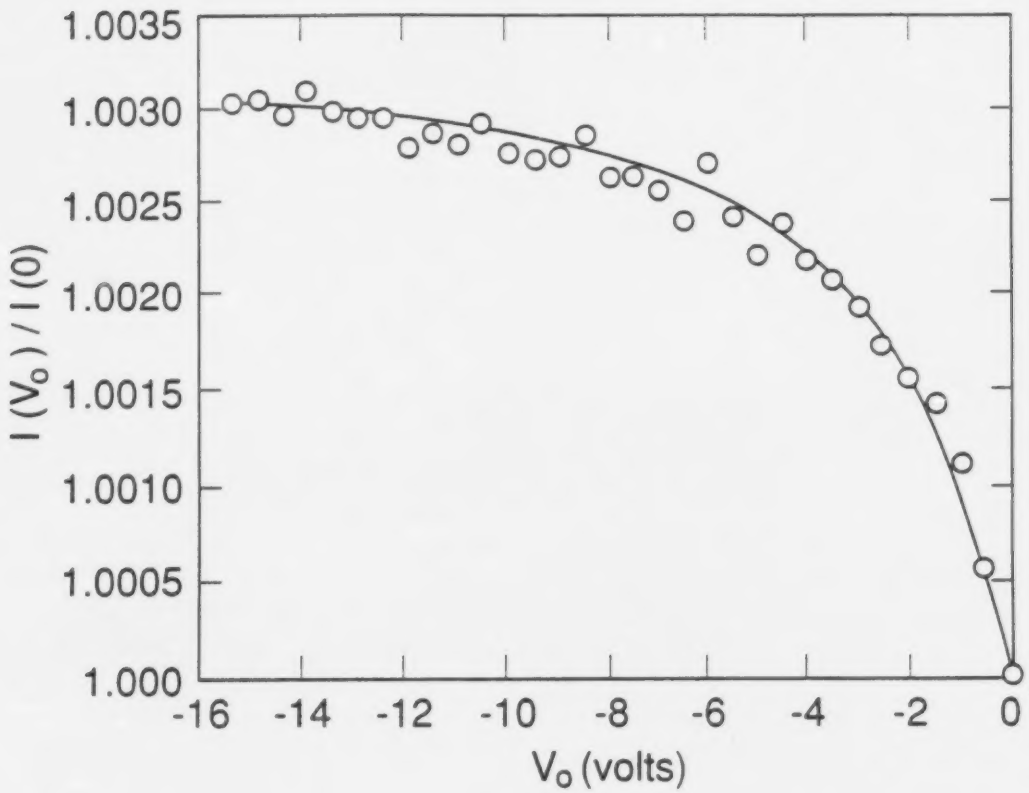

FIGURE 9.2 Ratio of the photocurrent $I(V_o)$ as a function of oxide-bias voltage V_o to the photocurrent $I(0)$ at zero oxide-bias voltage as measured on an EG&G UV444B silicon photodiode (circles) and as calculated with PC-1D (line) with a front-surface recombination velocity S = 6000 cm/s and an oxide trapped charge number density $N_{ss} = 1.942 \times 10^{12}$ cm^{-2}.

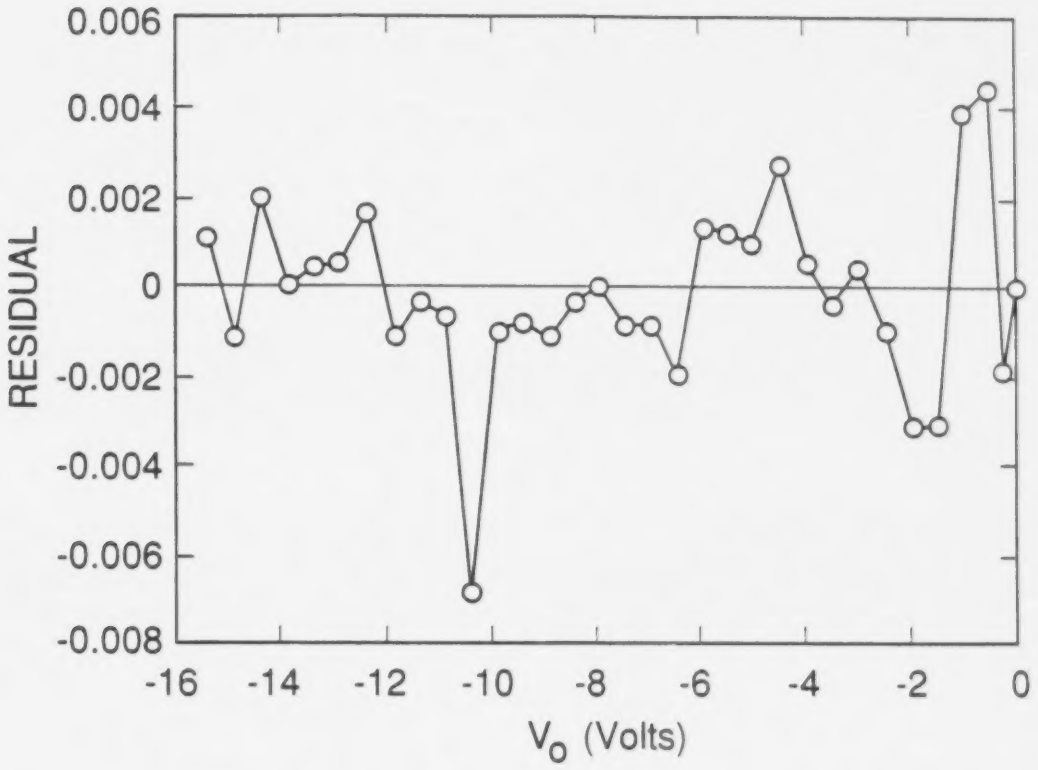

FIGURE 9.3 The residuals between the experimental data of Fig. 9.2 and the simulated data calculated by PC-1D when S = 6000 cm/s and N_{ss} = 1.942 x 10^{12} cm^{-2}.

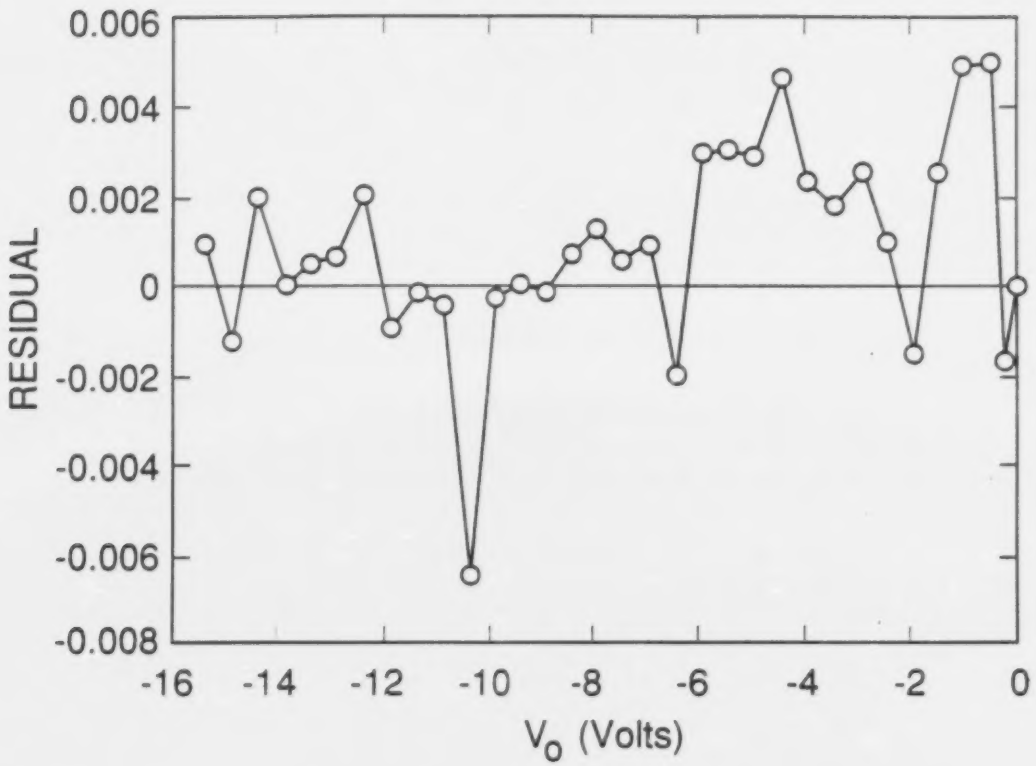

FIGURE 9.4 The residuals between the experimental data of Fig. 9.2 and the simulated data calculated by PC-1D when S = 5000 cm/s and N_{ss} = 2.011 x 10^{12} cm^{-2}.

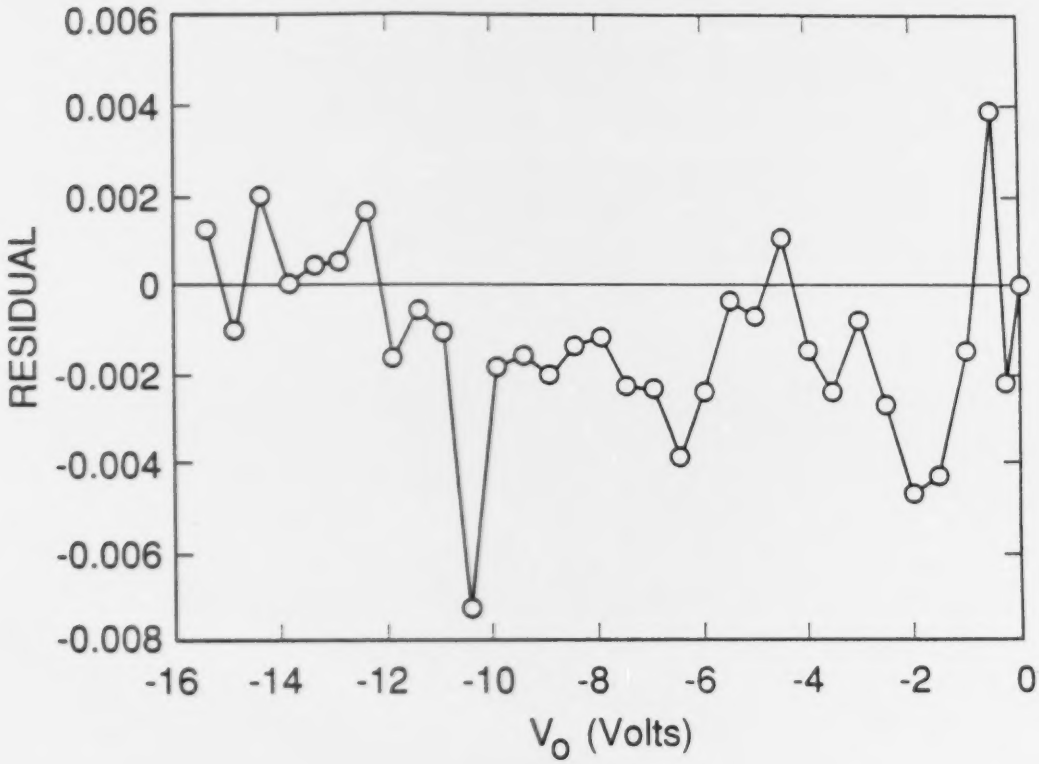

FIGURE 9.5 The residuals between the experimental data of Fig. 9.2 and the simulated data calculated by PC-1D when S = 7000 cm/s and N_{ss} = 1.883 x 10^{12} cm^{-2}.

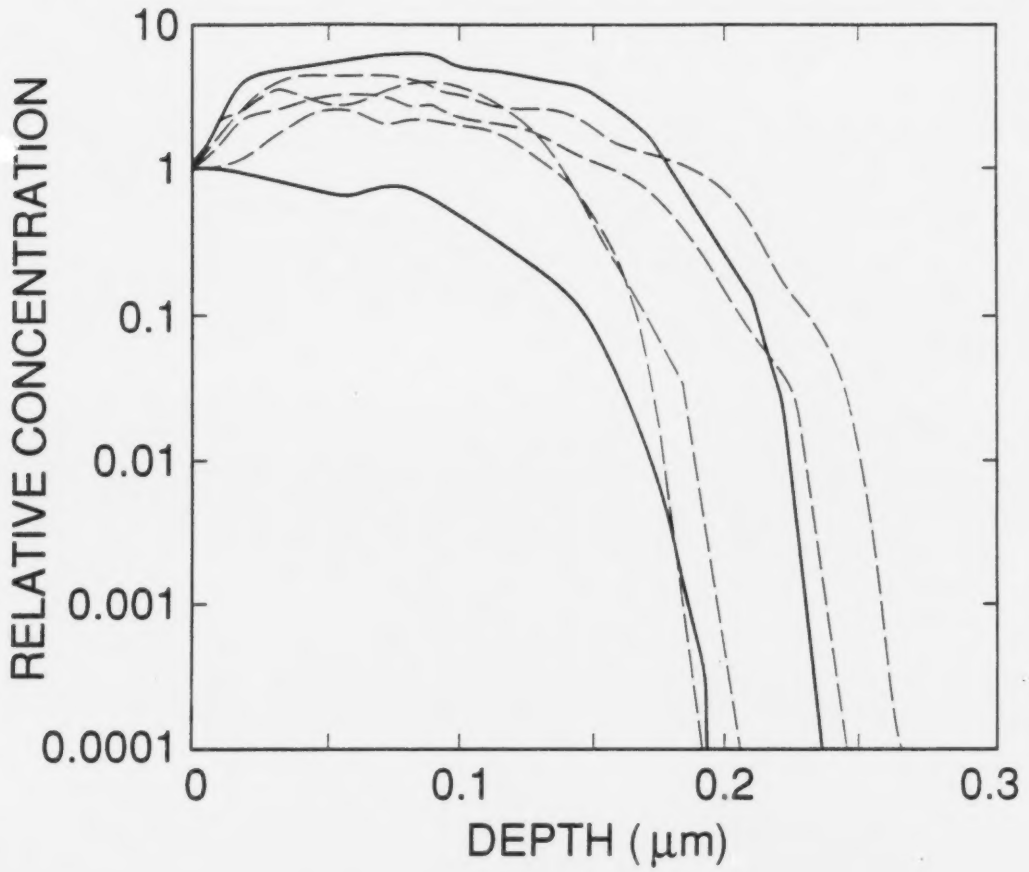

FIGURE 9.6 The relative front-region boron concentration for six typical Hamamatsu 1337 type photodiodes. The two profiles shown with solid lines bracket the other four in their effect on the shape of the internal quantum-deficiency spectrum.

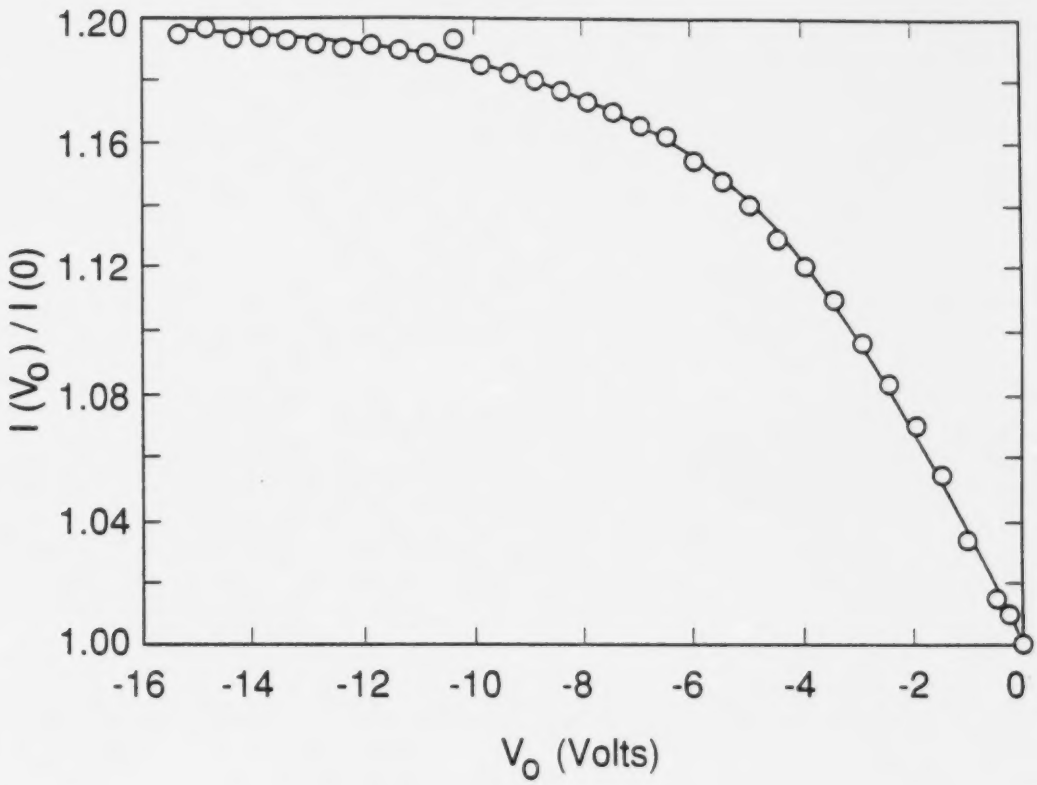

FIGURE 9.7 Ratio of the photocurrent $I(V_o)$ as a function of oxide-bias voltage V_o to the photocurrent I(0) at zero-bias voltage as measured on a Hamamatsu 1337 silicon photodiode (circles) and as calculated with PC-1D for the doping distribution corresponding to the lower solid curve in Fig. 9.6 with S = 1.835 cm/s and $N_{ss} = -3.0 \times 10^{12}$ cm^{-2} (line).

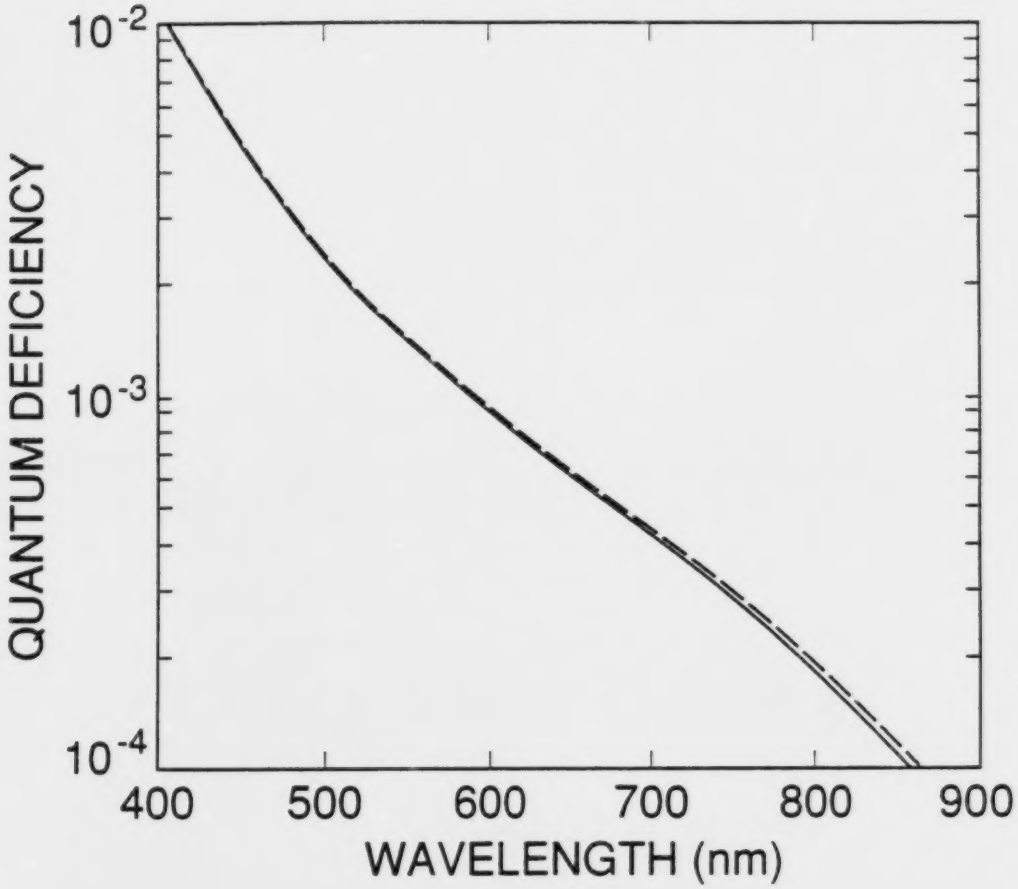

FIGURE 9.8 Simulated internal quantum deficiency spectra for a 1337 photodiode having the oxide-bias data shown in Fig. 9.7. The solid curve is for the doping profile that corresponds to the lower solid curve in Fig. 9.6 with $N_{ss} = -3.0 \times 10^{12}$ and $S = 1.835 \times 10^{5}$ cm/s; the dashed curve is for the doping profile that corresponds to the upper solid curve in Fig. 9.6 with $N_{ss} = -4 \times 10^{12}$ and $S = 1.56 \times 10^{5}$ cm/s.

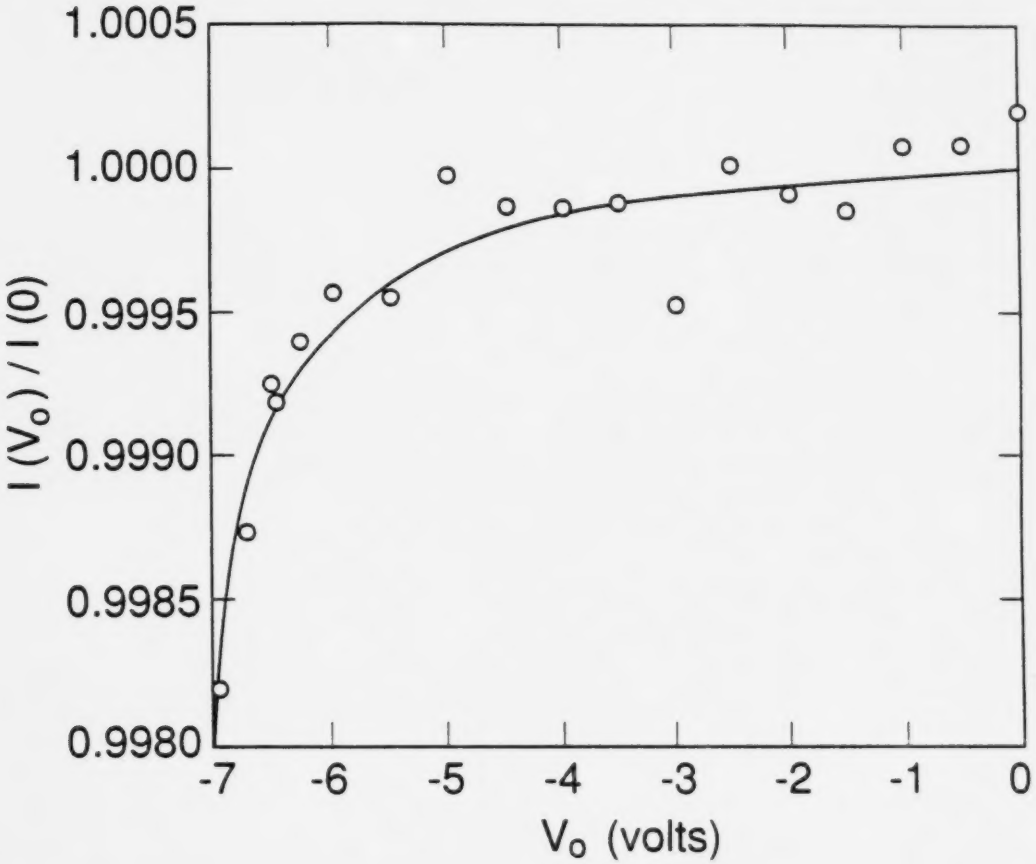

FIGURE 9.9 Ratio of the photocurrent $I(V_o)$ as a function of oxide-bias voltage V_o to the photocurrent $I(0)$ at zero-bias voltage as measured on a typical UDT UV100 silicon photodiode (circles) and as calculated with PC-1D for $S = 3.0 \times 10^5$ cm/s and $N_{ss} = 1.38 \times 10^{12}$ cm^{-2} (line).

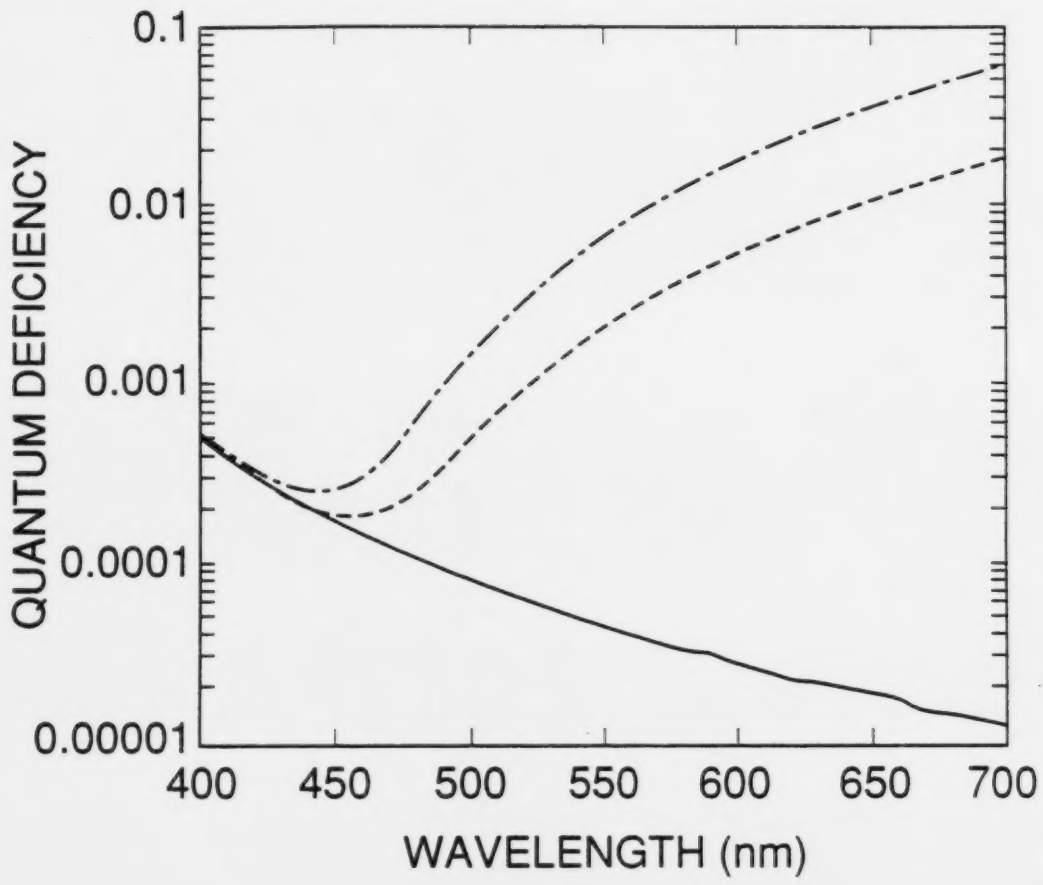

FIGURE 9.10 Internal quantum-deficiency spectra calculated by PC-1D for S = 3.0 cm/s, N_{ss} = 1.38 x 10^{12} cm^{-2}, and rear-region lifetimes τ of 81 ms (solid line), 10 μs (dashed line), and 1 μs (dot-dashed line).

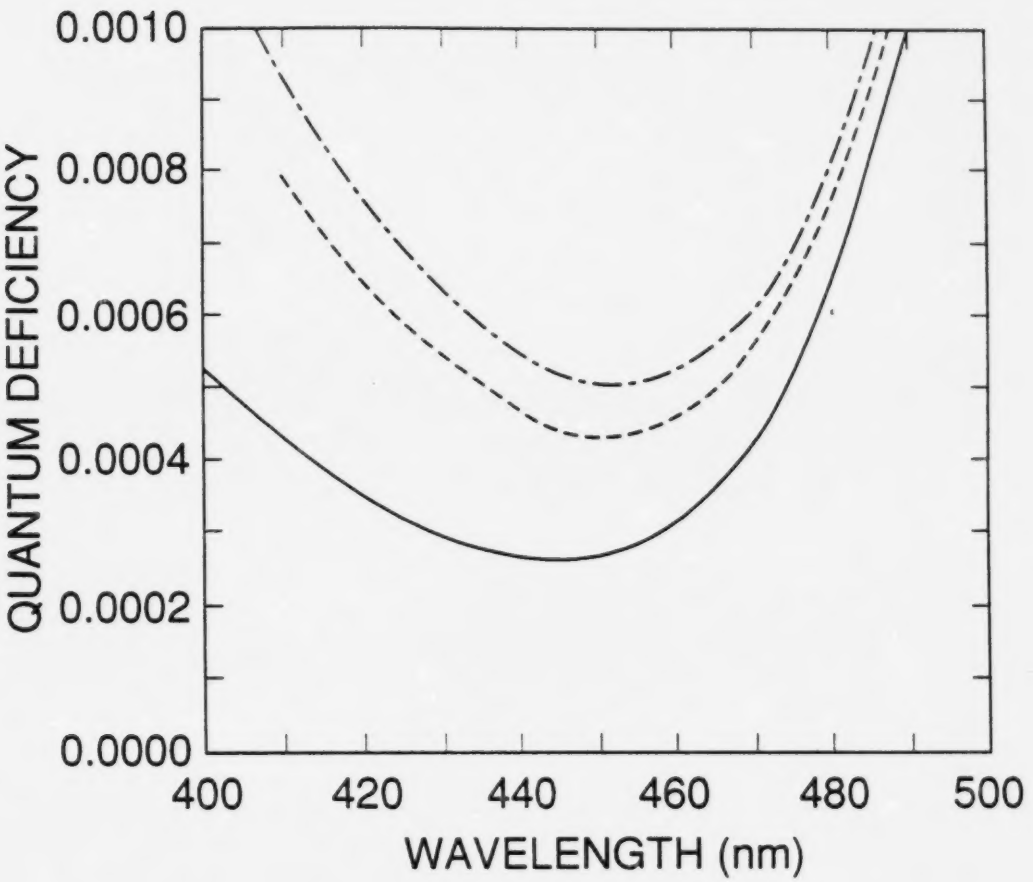

FIGURE 9.11 Internal quantum-deficiency spectra calculated by PC-1D for a rear-region lifetime τ = 1 μs with S = 3.0 x 10^5 cm/s and N_{ss} = 1.38 x 10^{12} cm^{-2} (solid line), with S = 6.0 x 10^5 cm/s and N_{ss} = 1.38 x 10^{12} cm^{-2} (dashed line), and with S = 3.0 x 10^5 cm/s and N_{ss} = 0.69 x 10^{12} cm^{-2} (dot-dashed line).

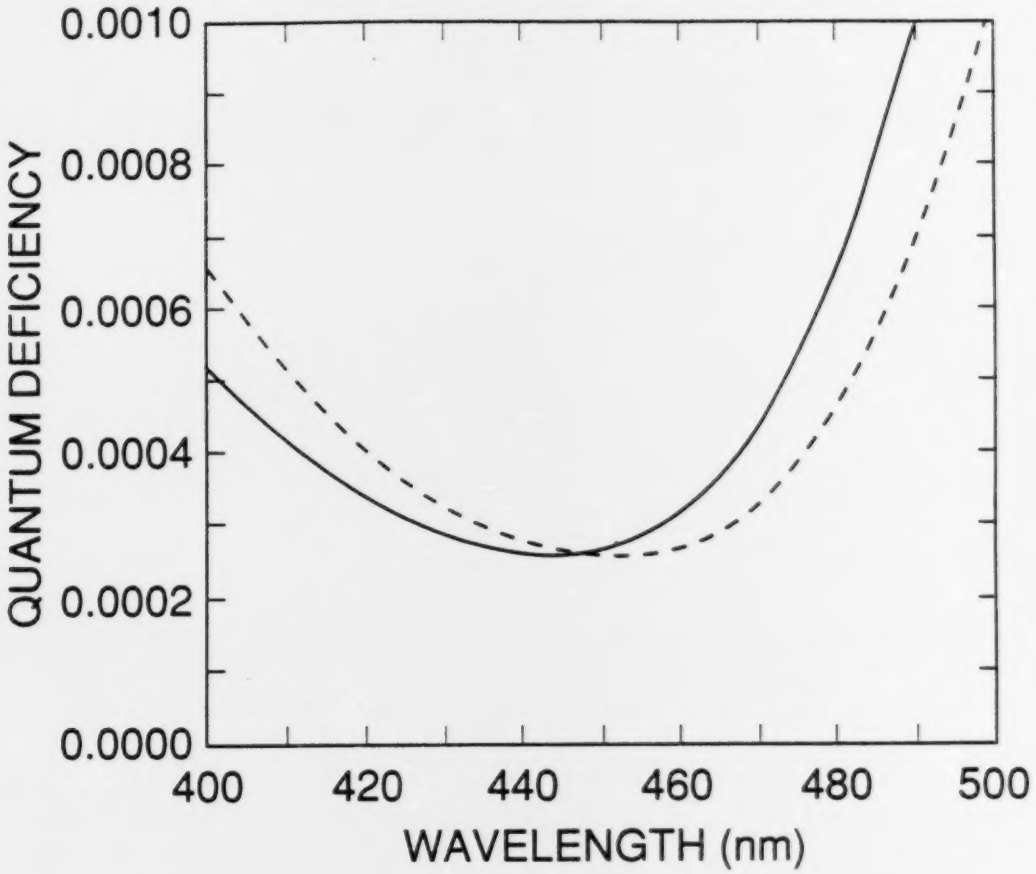

FIGURE 9.12 Comparison of the internal quantum-deficiency spectra calculated for a UV100 type photodiode for a rear-region lifetime τ = 1 μs with S = 3.0 x 10^5 cm/s and N_{ss} = 1.38 x 10^{12} cm^{-2} by using PC-1D with the absorption-coefficient data in the SIL_WEAK.ABS file (solid line), and with the absorption-coefficient data in the SIL_PHIL.ABS file (dashed line). The data in these files are described in more detail in Chapters 4, 5 and 8.

REFERENCES FOR CHAPTER 9

1. Available from ISU Extension Software, 108 Atanasoff Hall, Iowa State University, Ames, IA 50011, (505) 294-8658.

2. P. A. Basore, PC-1D version 2: enhanced numerical solar cell modeling, 20th IEEE Photovoltaic Specialists Conference - 1988, (IEEE, pub. # 0160-8371/88/0000-0389, NY, 1988), 389-396.

3. J. Geist, D. Chandler-Horowitz, A. M. Robinson, and C. R. James, Numerical modeling of silicon photodiodes for high accuracy applications. Part I: Simulation programs, J. Res. NIST **96**, 463-469 (1991)..

4. J. Geist, Silicon photodiode front region collection efficiency models, J. Appl. Phys. **51**, 1172-1174 (1983).

5. E. F. Zalewski and J. Geist, Silicon photodiode absolute spectral response self-calibration, Appl. Opt. **19**, 1214-1216 (1980).

6. J. Geist, Current status of, and future directions in silicon photodiode self-calibration, SPIE **1109**, 246-256 (1989), provides a review of the oxide-bias, self-calibration technique.

7. R. Koehler, R. Pello, and J. Bonhoure, Temperature dependent nonlinearity effects of a QED-200 detector in the visible, Appl. Opt. **29**, 4212-4215 (1990).

8. J. Geist, A. Migdall, and H. P. Baltes, Analytic representation of the silicon absorption coefficient in the indirect transition region, Appl. Opt. **27**, 3777-3779 (1988).

9. H. A. Weakliem and D. Redfield, Temperature dependence of the optical properties of silicon, J. Appl. Phys. **50**, 1491 (1979), and personal communication.

10. P. J. Key, N. P. Fox, and M. L. Rastello, Oxide-bias measurements in the silicon photodiode self-calibration technique, Metrolgia **21**, 81-87 (1985).

11. J. Geist, and H. Baltes, High accuracy modeling of photodiode quantum efficiency, Appl. Opt. **28**, 3929-3939 (1989).

12. J. Geist, J. L. Gardner, and F. J. Wilkinson, Surface induced feature in the quantum yield of silicon near 3.5 eV, Phys. Rev. **42B**, 1262-1267 (1990).

13. J. Geist and C. S. Wang, New calculations of the quantum yield of silicon in the near ultraviolet, Phys. Rev. **27B**, 4841-4847 (1983).

14. J. Geist, E. Liang, and A. R. Schaefer, Complete collection of minority carriers from the inversion layer in induced junction diodes, J. Appl. Phys. **52**, 4879-4881 (1981).

15. E. F. Zalewski and C. R. Duda, Silicon photodiode device with 100% external quantum efficiency, Appl. Opt. **22**, 2867-2873 (1983).

16. T. Hansen, Silicon UV-photodiodes by using natural inversion layers, Phys. Scr. **18**, 471-475 (1978).

17. J. M. Houston and R. B. Saunders, personal communication of data.

18. R. Korde and J. Geist, Stable, high quantum efficiency, uv-enhanced silicon photodiodes by arsenic diffusion, Solid-State Electronics **30**, 89-92 (1987).

19. R. Korde and J. Geist, Quantum efficiency stability of silicon photodiodes, Appl. Opt. **26**, 5284-5290 (1987).

20. H. R. Philipp, Influence of oxide layers on the determination of the optical properties of silicon, J. Appl. Phys. **43**, 2835-2839 (1972), and personal communication.

21. J. Geist, E. F. Zalewski, and A. R. Schaefer, Spectral response self-calibration and interpolation of silicon photodiodes, Appl. Opt. **19**, 3795-3799 (1980).

22. A. R. Schaefer, E. F. Zalewski, and J. Geist, Silicon detector nonlinearity and related effects, Appl. Opt. **22**, 1232-1236 (1983).

10. INTERPOLATING INTERNAL QUANTUM-EFFICIENCY CALIBRATIONS

The previous chapter[1] suggested that the Hamamatsu 1337 photodiode might be conveniently used for interpolating or extrapolating high-accuracy quantum-efficiency calibrations in the 400 to 900 nm spectral region. The idea of quantum-efficiency extrapolation was implicit in the first detailed description of how a silicon photodiode could be used to realize a scale of absolute spectral responsivity,[2] and interpolation was explicitly considered in Ref. 3. Beyond these two publications, however, little progress has been reported in this area until recently.

Hoyt et al.[4] (using early results of the work described in this chapter) used three Hamamatsu 1337 photodiodes to extrapolate a quantum-efficiency calibration that was obtained at 441.6 nm from a UDT QED 100 radiometer to 633.0 nm, and reported an average difference of 0.04% compared to independent measurements based on their electrically calibrated cryogenic cavity radiometer. Even though 0.04% is quite good by conventional radiometric standards, it was, as pointed out in Ref. 4, a factor of two larger than the combined uncertainty estimate for the two measurement techniques being compared, and further study was proposed by Hoyt et al. In this connection, Zalewski and Hoyt[5] have reported a recent, more direct test of the accuracy of the use of the Hamamatsu 1337 photodiode to extrapolate quantum efficiency. The results of this test agreed to within the combined estimated uncertainty, and two errors were

---

A version of this chapter has been published: J. Geist, A. M. Robinson, and C. R. James, Numerical modeling of silicon photodiodes for high-accuracy applications, Part III: Interpolating and extrapolating internal quantum-efficiency calibrations, J. Res. NIST **96**, 481-492 (1991).

discovered in the work reported in Ref. 4. When these errors were corrected, agreement within the estimated uncertainty was obtained.

The purpose of this chapter is to develop formulae and uncertainty estimates for interpolating and extrapolating internal quantum-efficiency calibrations with Hamamatsu 1337 photodiodes. It will be shown that this type of photodiode has characteristics that suit it particularly well to this task over the 440 to 860 nm spectral region. The remainder of this chapter is organized as follows: Section 4.1 investigates the errors associated with the use of relations that are only approximate for the 1337 photodiode, but which simplify both interpolation and extrapolation of the internal quantum efficiency for this type of photodiode. Section 4.2 investigates the various sources of error associated with the actual calculation of internal quantum-deficiency spectra using the semiconductor-device modeling program PC-1D and the support programs described[6] in chapter 8. Finally, section 4.3 compares the results obtained here with experimental measurements and demonstrates agreement within 0.0003.

10.1 ERRORS ASSOCIATED WITH THE QUANTUM-DEFICIENCY APPROXIMATIONS

THE APPROXIMATIONS

For the purposes of extrapolating and interpolating the internal quantum efficiency of Hamamatsu 1337 photodiodes, the internal quantum deficiency can be approximated by a function $\delta(\lambda, N_{ss}, S, \tau_r)$ of wavelength λ and of three recombination-related variables: N_{ss} the charge number density stored in the front-surface oxide, S the surface recombination velocity at the oxide-silicon interface, and τ_r the minority-carrier lifetime in the rear region.

For silicon photodiodes, $\delta(\lambda, N_{ss}, S, \tau_r)$ can be approximated by

$$\delta(\lambda, N_{ss}, S, \tau_r) = K_f(N_{ss},S)\ \delta_f(\lambda) + K_r(\tau_r)\ \delta_r(\lambda), \qquad (1)$$

where

$$\delta_r(\lambda) = 0, \qquad (2)$$

for λ less than some wavelength λ_0.

To see how this is useful for interpolating quantum deficiency measurements, suppose that $\delta(\lambda_f, N_{ss}, S, \tau_r)$ has been measured at wavelength $\lambda_f < \lambda_0$, and $\delta(\lambda_r, N_{ss}, S, \tau_r)$ has been measured at wavelength $\lambda_r > \lambda_0$. The values for $K_f(N_{ss},S)$ and $K_r(\tau_r)$ can then be determined from

$$K_f(N_{ss},S) = \frac{\delta(\lambda_f, N_{ss}, S, \tau_r)}{\delta_f(\lambda_f)}, \qquad (3a)$$

and

$$K_r(\tau_r) = \frac{\delta(\lambda_r, N_{ss}, S, \tau_r) - K_f\ \delta_f(\lambda_r)}{\delta_r(\lambda_r)}, \qquad (3b)$$

and these values can be used in eq. 1 to interpolate the quantum deficiency between λ_f and λ_r. In the above equations $\delta_f(\lambda)$ and $\delta_r(\lambda)$ are functions only of wavelength, and λ_f and λ_r are the wavelengths at which K_f and K_r in eqs. 3a and 3b are to be normalized. Generally, λ_0 will fall between 600 nm and 650 nm.

The subscript f stands for the front of the photodiode since this is the location of the mechanism (recombination at the front-surface oxide-silicon interface) that causes $\delta_f(\lambda)$ to exceed zero. The subscript r stands for the rear of the photodiode since this is the

location of the mechanism (recombination in the volume of the rear region) that cause $\delta_r(\lambda)$ to exceed zero. Therefore, $\delta_f(\lambda)$ and $\delta_r(\lambda)$ will be called the front-region and rear-region internal quantum-deficiency spectra, respectively. The functional dependence of K_f and K_r will be suppressed for the remainder of this paper.

ACCURACY OF THE APPROXIMATIONS

Exactly how accurate eqs. 1-3 are depends upon the particular type of photodiode and the range covered by the parameters. Figure 10.1 illustrates the accuracy of eq. 1 for the 1337 type photodiode (modeled as described in chapter 9) over the 400 to 900 nm spectral region for an internal quantum-deficiency spectrum that is a practical upper limit for this type of photodiode. Figure 10.1 compares the internal quantum-deficiency spectra $\delta(\lambda, 0, S, \infty)$ for S = 71264 cm/s and $\delta(\lambda, 0, 0, \tau_r)$ for τ_r = 1 ms with their sum, and with the internal quantum-deficiency spectrum $\delta(\lambda, 0, 71264 \text{ cm/s}, 1 \text{ ms})$. The latter spectrum and the sum of the two first spectra differ by less than 2×10^{-5} over the entire 400 nm spectral region, and they cannot be distinguished at the scale of the figure. (Any errors with absolute values less than 2×10^{-5} are considered negligible in this chapter.)

Figure 10.2 shows that the $\delta(\lambda_r, N_{ss}, S, \infty)$ spectra have very similar shapes for quite different combinations of N_{ss} and S. Therefore, a single function of wavelength $\delta_f(\lambda)$ can be a good approximation to $\delta(\lambda, N_{ss}, S, \tau_r)$ for any combination of N_{ss} and S. The spectra in Fig. 10.2 were calculated for the range of parameters listed in Table 10.1. Cases 1-3 in that table are based on the front-region doping distribution $N_A(x)$ shown as the dashed curve in Fig. 10.3, and Case 4 is based on that shown as the solid curve in the same figure. Of six

doping distributions measured for different 1337 photodiodes, the two shown in Fig. 10.3 produce the largest change in shape of the internal quantum-deficiency spectrum.[1]

The shapes of the front-region internal quantum-deficiency spectra in Fig. 10.2 are compared in Fig. 10.4 by normalizing all of the spectra to 0.01 at 440 nm and by plotting their differences relative to the normalized spectrum for Case 2. Cases 1 and 3 compared with Case 2 show how the shape of $\delta(\lambda, N_{ss}, S, \infty)$ changes when the whole curve is shifted up or down by over a factor of three by a substantial decrease or increase in N_{ss}.

Case 4 compared with Case 2 shows how the shape of $\delta(\lambda, N_{ss}, S, \infty)$ changes when the dopant distribution is changed from the dashed curve to the solid curve in Fig 10.3. This effect is much larger than that associated with varying N_{ss} and S.

The three spectra in Fig. 10.4 characterize the uncertainties to be associated with the diode-to-diode variations in N_{ss}, S, and $N_A(x)$ when any one of the spectra in that figure is used as $\delta_f(\lambda)$ with K_f = 0.01 in eqs. 1 and 3. These spectra should be multiplied by $K_f/0.01$ if $K_f \neq 0.01$. For the purposes of this chapter, the spectrum for Case 2 in Table 10.1 will be used for $\delta_f(\lambda)$ in eqs. 1 and 3.

The front-region internal quantum deficiency also depends upon two front-region recombination mechanisms not considered above. These are the Auger and SHR mechanisms that become important in the heavily doped front region of the photodiode. Both effects were included in all of the spectra described so far by using the default cross

sections that are built into PC-1D for these recombination mechanisms. The PC-1D default values for the Auger recombination cross sections give an internal quantum-deficiency spectrum with a value of 9×10^{-6} at 400 nm when S = 0 and the SHR cross sections are set to zero. The shape of this spectrum is well modeled by $\delta_f(\lambda)$, as shown in chapter 6.[7] In fact, the research reported in this chapter determined that an uncertainty of ±100% can be tolerated in the Auger cross sections in 1337 photodiodes without causing an error as large as 2×10^{-5} anywhere within the 400 to 900 nm spectral region.

For the doping profile shown as the solid curve in Fig. 10.3, the PC-1D default values for the SHR recombination cross sections give the lifetimes shown in Fig. 10.5 as a function of distance from the oxide-silicon interface in the photodiode when the Auger cross sections are set to zero. These SHR lifetimes shown in Fig. 10.5 give an internal quantum-deficiency spectrum with a value of 6×10^{-5} at 400 nm. The function $\delta_f(\lambda)$ does not model the spectrum for SHR recombination as well it models the spectrum for Auger recombination. Nevertheless, an uncertainty of ±50% in the SHR recombination cross sections can be tolerated without raising the error associated with the use of $\delta_f(\lambda)$ to model this effect to 2×10^{-5} anywhere in the 400 to 900 nm spectral region.

Now consider $\delta_r(\lambda)$. Figure 10.6 shows that the $\delta(\lambda_r, N_{ss}, 0, \tau_r)$ spectra have similar shapes for different values of τ_r, and therefore can be modeled reasonably well by a single function of wavelength $\delta_r(\lambda)$. The shapes of the different $\delta(\lambda_r, N_{ss}, 0, \tau_r)$ spectra are not as similar as are the shapes of the different $\delta(\lambda, N_{ss}, S, -)$ spectra. This is not a problem because the effect being modeled is smaller, so

larger relative errors can be tolerated in the approximations.

The spectra in Fig. 10.6 were calculated for τ_r = 1 ms and 10 ms, with N_{ss} = S = 0. The shapes of the spectra in Fig. 10.6 are compared in Fig. 10.7 by normalizing them to 0.002 at 860 nm and plotting their differences relative to the spectrum for τ_r = 1 ms. The normalization value of 0.002 was chosen as a practical upper limit. The difference spectrum in Fig. 10.7 characterizes the uncertainties to be associated with the variations in rear-region lifetime when the spectrum for τ_r = 1 ms is used as $\delta_r(\lambda)$ with K_r = 0.002 in eqs. 1 and 3. This spectrum should be multiplied by $K_r/0.002$ if $K_r \neq 0.002$. For the purposes of this chapter, $\delta_r(\lambda)$ will be set to zero for $\lambda \leq 620$ nm, and the spectrum for τ_r = 1 ms will be used for $\delta_r(\lambda)$ if $\lambda > 620$ nm.

EXTRAPOLATING FUNCTIONS

A convenient function of wavelength has been fit to the spectrum for Case 2 in Table 10.1, and another to the spectrum for τ_r = 1 ms in Fig. 10.6. These functions, the forms of which were obtained by trial and error, are

$$\delta_f(\lambda) = A_0 [X(\lambda) + A_1 X^2(\lambda) + A_2 Y(\lambda)], \quad (4)$$

and

$$\delta_r(\lambda) = A_0 [1/X(\lambda) - A_2/Y(\lambda)], \quad (5)$$

respectively, where

$$X(\lambda) = \exp(-\lambda/\lambda_0), \quad (6)$$

and

$$Y(\lambda) = \exp(-(\lambda/\lambda_2)^2). \qquad (7)$$

The appropriate values for A_0, A_1, A_2, λ_0, and λ_2 for eqs. 4 and 5 are listed in Table 10.2. The function in eq. 5 becomes negative for $\lambda <$ 620 nm, in which case eq. 5 is replaced with $\delta_r(\lambda) = 0$ as mentioned earlier. The values of A_0 in Table 10.2 normalize $\delta_f(\lambda)$ to 0.01 at 440 nm, and $\delta_r(\lambda)$ to 0.002 at 860 nm, respectively.

With $K_f = 0.5516405$ and $\delta_f(\lambda)$ given by eq. 4, eq. 2 fits the spectrum for Case 2 in Table 10.1 with a residual standard deviation of 2.9×10^{-6} over the 420- to 900-nm spectral region, and never differs from that spectrum by more than 7×10^{-6} over the same spectral region. This translates to less than 10 ppm when the internal quantum deficiency is normalized to 0.01 at 440 nm. Therefore, the error associated with the use of eq. 4 is negligible. The larger variations below 420 nm are negligible with respect to uncertainties already identified and others discussed below.

With $K_r = 1.685081$ and $\delta_r(\lambda)$ given by eq. 5, eq. 2 fits the spectrum shown as a solid line in Fig. 10.6 with a residual standard deviation of 1.4×10^{-5} over the 610 to 900 nm spectral region, and never differs from that spectrum by more than 2.5×10^{-5} over that same spectral range. This translates to less than 1.7×10^{-5} when the quantum deficiency is normalized to 0.002 at 860 nm; thus the error associated with the use of eq. 5 is also negligible.

10.2 ERRORS ASSOCIATED WITH QUANTUM-DEFICIENCY CALCULATIONS

Two types of error associated with the quantum-deficiency values calculated by PC-1D can be distinguished: 1) numerical errors associated with the algorithms used by PC-1D and the limited number of

finite elements available to PC-1D, and 2) physical errors associated with approximations and simplifications in the physical models used by PC-1D. Both types are considered in this section.

NUMERICAL ERRORS

It was shown in chapter 6 that $\delta_f(\lambda)$ is well approximated by

$$\delta_f(\lambda) = \frac{\Gamma\,[\,I(0) - I(\alpha(\lambda))\,]}{1 + \Gamma\, I(\alpha(\lambda))}, \tag{8}$$

$$I(\alpha(\lambda)) = \int_0^{x_1} \hat{k}(x)\, \exp(-\alpha(\lambda)\, x)\, dx, \tag{9}$$

$$\hat{k}(x) = k(x)/k(0), \tag{10}$$

$$k(x) = 1/(m_0(x)\, D_m(x)), \tag{11}$$

$$\Gamma = S/D_m(0), \tag{12}$$

where $\alpha(\lambda)$ is the absorption-coefficient spectrum of silicon, x is the distance from the oxide-silicon interface toward the rear of the photodiode, $m_0(x)$ is the equilibrium minority-carrier concentration at the point x in the front region of the photodiode, and $D_m(x)$ is the equilibrium diffusion constant for the minority carriers at the point x. Note that the sign in the numerator in eq. 8 is correct, and that the sign is incorrect in Ref. 7. Also, note that $\delta_f(\lambda)$ becomes very insensitive to x_1 as x_1 increases beyond some critical value. Thus, the point x_1 has the following interpretation: Once a front-region minority carrier has reached x_1, it has negligible probability of recombining at the front-surface oxide-silicon interface. The point

where the electron and hole concentrations cross is a convenient choice for x_1, but smaller values work as well.[7]

For comparison with PC-1D, the kernel k(x) in eq. 11 must be chosen as

$$k(x) = q\, M_0(x)/(n_{ie}^2(x)\, k\, T\, \mu_m(x)), \qquad (13)$$

where $M_0(x)$ is the equilibrium majority carrier concentration in the front region, $n_{ie}(x)$ is called the effective intrinsic carrier concentration,[8] which in PC-1D includes the effect of Fermi-Dirac statistics, $\mu_m(x)$ is the minority-carrier mobility as a function of position in the front region, k is the Boltzmann constant, and T is the temperature of the photodiode.

Figure 10.8 compares $\exp(-\alpha(400\text{ nm})\, x)$ with the equilibrium functions $M_0(x)$, $n_{ie}(x)$, and $\mu_m(x)$ as calculated by PC-1D over the range $0 < x < 200$ nm for the same photodiode model used to calculate the quantum-deficiency spectra in Fig. 10.3 for Case 2 of Table 10.1. For $x < 10$ nm, N_{ss} determines the shape of $M_0(x)$ by determining the shape of the accumulation layer at the front surface of the photodiode. For 10 nm $< x <$ 180 nm, the front-region doping distribution determines the shape of $M_0(x)$ because $M_0(x)$ follows the doping distribution closely in this region.

The numerical accuracy with which PC-1D calculates $M_0(x)$ within the framework of the drift-diffusion approximations for the conditions of charge accumulation at an oxide-silicon interface as shown in Fig. 10.8 has been studied in chapter 7 and found to be quite good: With a uniform doping density of 10^{19} cm^{-3} and an oxide charge density of 10^{13} cm^{-2}, PC-1D overestimates $M_0(x)$ by about 9% at $x = 0$, decreasing

to within ±1% for $x > 1$ nm. The error in $k(x)$ due to this effect will be estimated by replacing $k(x)$ by

$$k_1(x) = k(x)/(1-0.1\ x/x_0), \tag{14}$$

for $x < x_0$, and

$$k_1(x) = k(x)/0.9, \tag{15}$$

for $x > x_0$ in the kernel of the integral in eq. 9, where $x_0 = 1$ nm.

This still leaves a question about the numerical accuracy with which PC-1D would calculate the steady-state photocurrent if the equilibrium carrier concentration were exact. Equations 8-12 can now be used to answer this question. The uncertainty to be associated with this source of error was estimated as follows: 1) The internal quantum-deficiency spectrum was calculated directly from the PC-1D solution of the steady-state drift-diffusion equations for the total current flowing in the photodiode for the conditions described by Case 2 of Table 10.1. 2) Equations 8-12 were used to calculate the internal quantum-deficiency spectrum from the equilibrium values of $M_0(x)$, $n_{ie}(x)$, and $\mu_m(x)$ that were calculated by PC-1D for the same conditions as in 1) above. The integration was carried out with a generalization of Simpson's rule for non-equidistant points. 3) Both spectra were normalized to 0.01 at 440 nm, and the differences calculated.

There is no reason to believe that the differences obtained in step 3) above, which exceed 2×10^{-5} only at 400 nm and at 900 nm, are caused by errors associated with PC-1D. It is just as likely that they are associated with eqs. 8-12 since these equations were derived from a

number of assumptions that are not rigorously satisfied. The important point is that it is unlikely that either calculation is in error by much more than the differences between them. This suggests that the numerical errors in the photocurrents calculated by PC-1D are negligible at the level of accuracy required for this thesis.

PHYSICAL ERRORS

There are a number of other errors, which are associated with incomplete or approximate physical models built into PC-1D, that also affect the accuracy with which PC-1D calculates the functions defining k(x) in eq. 13. These include quantum-mechanical effects[10] (eg. tunneling) that change the shape of $M_0(x)$ from that calculated from the drift-diffusion approximation for $x < 1$ nm, band-gap narrowing effects[11] associated with heavy doping and large surface-fields[12] that cause $n_{ie}(x)$ to depend upon position in the photodiode, and carrier-carrier and carrier-ion scattering mechanisms[13] that cause $\mu_m(x)$ to depend upon position. It is beyond the scope of this thesis to study each of these sources of error in detail, but the error in k(x) due to all of them combined will be modeled by replacing k(x) by

$$k_2(x) = k(x) \, (1 - 0.1 \log(\hat{k}(x))) \qquad (16)$$

in the kernel of the integral in eq. 9. This allows an error of 10% per decade change in k(x).

The differences between the internal quantum-efficiency spectrum calculated from eqs. 8-13 by replacing k(x) with either $k_1(x)$ or $k_2(x)$ in eq. 9 and the spectrum calculated using k(x) were computed after all three spectra were normalized to 0.01 at 440-nm. No difference exceeded 2×10^{-5} over the entire 400 to 900 nm spectral region.

Therefore, all of these sources of error are negligible with respect to the level of accuracy required for this thesis.

Another source of error that is obvious in eqs. 8-12 is the absorption-coefficient data used in the simulations. As described in chapter 8, the absorption-coefficient data were calculated from an equation[14] that was fit to the data of Weakliem and Redfield.[15] An alternate set of absorption-coefficient data was described by Philipp.[16] Figure 10.9 plots the differences between the internal quantum-deficiency spectra normalized to 0.01 at 440 nm for Case 2 of Table 10.1 when based on the absorption-coefficient data in Ref. 16, and when based on the equation for the absorption coefficient in Ref. 14. These differences will be used as the estimated uncertainties arising from the errors in the silicon absorption-coefficient spectrum when $\delta_f(\lambda)$ is used to extrapolate an internal quantum deficiency of 0.01 from 440 nm to longer wavelengths with a 1337 photodiode. A similar calculation was carried out for the case where S = 0 and τ_r = 1 ms. Both spectra were normalized to 0.002 at 860 nm, and the differences, which are shown in Fig. 10.10, will be used as the estimated uncertainties arising from the uncertainties in the silicon absorption-coefficient spectrum when $\delta_r(\lambda)$ is used to extrapolate an internal quantum deficiency of 0.002 from 860 nm to shorter wavelengths with a 1337 photodiode.

OVERALL UNCERTAINTIES

Figures 10.11 and 10.12 plot the quadrature sum of the difference spectra plotted in Figs. 10.4 and 10.9, and in Figs. 10.7 and 10.10, respectively. The spectrum in Fig. 10.11 plots the estimated (one standard deviation) uncertainty as a function of wavelength that is

associated with the use of $\delta_f(\lambda)$ in eq. 4 to extrapolate a measured internal quantum deficiency of 0.01 from 440 nm to longer wavelengths.

The major sources of error contributing to the uncertainty spectrum in Fig. 10.11 were identified earlier in this chapter as the diode-to-diode variations in $N_A(x)/N_A(0)$ and the uncertainty in the absorption-coefficient spectrum for silicon. A number of other sources of error were also identified with the help of eqs. 8-12, and any that produced differences greater than 2×10^{-5} for 400 nm $< \lambda <$ 900 nm are included in Fig. 10.11. Most did not.

The spectrum in Fig. 10.12 plots the estimated (one standard deviation) uncertainty as a function of wavelength that is associated with the use of $\delta_r(\lambda)$ in eq. 5 to extrapolate a measured internal quantum deficiency of 0.002 from 860 nm to shorter wavelengths. The major sources of error contributing to the uncertainty spectrum in Fig. 10.12 were identified as the change in shape of $\delta_r(\lambda)$ with t_r and the uncertainty in the absorption-coefficient spectrum for silicon. All other sources of error considered were negligible with respect to 2×10^{-5} for 400 nm $< \lambda <$ 900 nm.

No equivalents to eqs. 8-12 were used to guide the error analysis for $\delta_r(\lambda)$. The results of the uncertainty analysis of $\delta_f(\lambda)$ show that the numerical errors in PC-1D will be a negligible source of error in $\delta_r(\lambda)$. This leaves the errors associated with the approximations in the physical models that are built into PC-1D. Some of these were tested, but no tests were possible for the use of a single SHR trap level to model the recombination in the rear region of the photodiode. This could be a non-negligible source of error; it was shown in

chapter 8 that this approximation introduced errors of the order of the effect being modeled in non-linearity simulations on a UV444B type photodiode. A more complete model might make τ_r depend upon position in the photodiode, which might modify the shape of $\delta_r(\lambda)$ and add an uncertainty that is not included in Fig. 10.12. However, the effects being modeled for the case of the 1337 photodiode are not much larger than the estimated uncertainty, and a great deal more work beyond that reported in this thesis will be necessary to answer to this question definitively.

3. COMPARISON WITH EXPERIMENT

FORMULAE

To use the results developed thus far, it is necessary to define the internal quantum-deficiency interpolating function $\delta(\lambda)$ in terms of the extrapolating functions $\delta_f(\lambda)$ and $\delta_r(\lambda)$, and to assume that it exactly satisfies eqs. 1-3, which can be rewritten in more compact form as

$$\delta(\lambda) = \delta_x(\lambda_f)\,\frac{\delta_f(\lambda)}{\delta_f(\lambda_f)} + \delta_x(\lambda_r)\left[1 - \frac{\delta_f(\lambda_r)}{\delta_r(\lambda_r)}\right]\frac{\delta_r(\lambda)}{\delta_r(\lambda_r)}, \qquad (17)$$

where $\delta_x(\lambda_f)$ and $\delta_x(\lambda_r)$ are the measured values of the internal quantum deficiency at the wavelengths λ_f and λ_r, respectively, $\delta_f(\lambda)$ and $\delta_r(\lambda)$ are defined in eqs. 4 and 5, respectively, and the constants used in these equations are defined in Table 10.2. The uncertainty associated with $\delta(\lambda)$ due to the sources of error considered in the last two sections of this paper can be obtained by summing in quadrature each of the terms on the right-hand side of the differential of eq. 17. That differential is given by

$$d\delta(\lambda) = d\delta_x(\lambda_f)\left[\frac{\delta_f(\lambda)}{\delta_f(\lambda_f)}\right] +$$

$$d\delta_x(\lambda_r)\left[\frac{\delta_r(\lambda)}{\delta_r(\lambda_r)}\right]\left[1 - \frac{\delta_f(\lambda_r)}{\delta_r(\lambda_r)}\right] +$$

$$d\delta_f(\lambda)\left[\frac{\delta_x(\lambda_f)}{\delta_f(\lambda_f)}\right] +$$

$$d\delta_r(\lambda)\left[\frac{\delta_x(\lambda_r)}{\delta_r(\lambda_r)}\right]\left[1 - \frac{\delta_f(\lambda_r)}{\delta_r(\lambda_r)}\right]. \qquad (18)$$

The differentials $d\delta_f(\lambda)$ and $d\delta_r(\lambda)$ are plotted in Figs. 10.11 and 10.12 for $\lambda_f = 440$ nm, and for $\lambda_r = 860$ nm, respectively.

EXPERIMENTAL DATA

There are not much data available against which to test eqs. 17 and 18, but there are some. For instance, Zalewski and Hoyt[5] have reported the internal quantum efficiencies at 441.6 nm and the spectral responsivities and absorptances at 633.0 nm for five multiple reflection (trap) radiometers[17,5,18,19] based on Hamamatsu 1337 photodiodes. Similarly, Fox[19] has reported the average internal quantum efficiency of ten trap radiometers also based on Hamamatsu 1337 photodiodes at six Ar^+ ion laser lines, and he has also measured the oxide-bias correction for a single Hamamatsu 1337 photodiode at four Ar^+ ion laser lines.

Zalewski and Hoyt[5] presented their data (summarized in bold face type in Table 10.3) as an intercomparison of spectral responsivity. Since the internal quantum deficiency is the quantity of interest in this

chapter, it is necessary to compute this quantity from the data reported by Zalewski and Hoyt as shown in Table 10.3. The corrections for non-linearity that Zalewski and Hoyt derived from reverse bias measurements also eliminate any effects of recombination in the rear region of the photodiodes.

Fox's[19] oxide-bias data, which is summarized in Table 10.4, was measured at 10 V, and was reported as a fractional increase in the photocurrent I given by $y_o = I(10V)/I(0) - 1$. The oxide-bias experiment reported in chapter 9 of this paper shows that the internal quantum deficiency at zero bias δ_x is given by

$$\delta_x = 1 - 1/(1 + 1.13\ y_o), \qquad (19)$$

when the maximum oxide bias-voltage is 10 V. The average internal quantum efficiencies reported by Fox are also shown in Table 10.4, and the internal quantum deficiencies calculated from them are also shown there.

Equation 17 was normalized to the results of Zalewski and Hoyt at λ_f = 441.6 nm, and the predictions of that equation are compared with the results of Zalewski and Hoyt at 633 nm in Table 10.5. Note that $\delta_x(\lambda_r) = 0$ for this data set due to the application of reverse bias. Equation 17 was also normalized to the oxide-bias results of Fox at λ_f = 468.18 nm, and the predictions of that equation are compared with the oxide-bias results in Table 10.6. Again note that $\delta_x(\lambda_r) = 0$ because oxide-bias measurements are not sensitive to recombination in the rear of the photodiode.

The uncertainty estimates for eq. 17 in Tables 10.5 and 10.6 are based

on the data in Fig. 10.11 even though those data apply to λ_f = 440 nm rather than 441.6 or 468.2 nm. This does not distort the estimated uncertainty significantly because the terms are added in quadrature, and the first term on the right-hand side of eq. 18 is larger than the second term for both data sets. Fox's data at 406.85 nm was included in Table 10.6 even though the uncertainties that are associated with extrapolating $\delta_f(\lambda)$ to wavelengths shorter than λ_f are extremely unfavorable for high-accuracy applications. The good agreement at this wavelength is fortuitous considering the uncertainty associated with the predicted value. The differences at the other wavelengths never exceeds 0.00015, and they fall within the estimated uncertainty for the differences.

Table 10.7 and Fig. 10.13 compare the internal quantum-deficiency results of Fox[19] with the predictions of eq. 17 when normalized at λ_f = 468.18 nm and at λ_r = 859.07 nm. The data in Figs. 10.11 and 10.12 that apply for λ_f = 440 nm and for λ_r = 860 nm, respectively, were used with eq. 18 to estimate the uncertainties assigned to the predictions of eq. 17. The difference at 406.85 nm is much larger than obtained with the oxide-bias data, but still falls within the uncertainty estimated for the difference.

The results shown in Tables 10.5-10.7 and Fig. 10.13 verify that the internal quantum deficiency of multiple-reflection radiometers based on Hamamatsu 1337 photodiodes can be interpolated over the 440 to 860 nm spectral region from only two measured quantum deficiencies, one at each end of the region. This greatly reduces the total number of measurements needed for high-accuracy spectral calibrations of these photodiodes and radiometers. The theoretical analysis suggests that

uncertainties as small as ± 0.0001 are possible if the errors in the calibration values at λ_f and λ_r are smaller than 0.0001. The results in Table 10.5-10.7 and Fig. 10.13 do not contradict this idea, nor do they confirm it. Higher accuracy data are needed to test this prediction. On the other hand, the experimental data do confirm that an uncertainty of ±0.0003 is obtainable.

10.4 CONCLUSIONS

This chapter has shown that Version 2 of the semiconductor-device modeling program PC-1D can be used to model the spectral shape of the internal quantum deficiency of 1337 type photodiodes with very small uncertainty over the 440 to 860 nm spectral region. The largest uncertainties are caused by uncertainties in the absorption-coefficient spectrum of silicon, diode-to-diode variations in the shape of the front region dopant distribution, and diode-to-diode variations in the position-independent rear-region minority-carrier lifetime. It was not possible to estimate the uncertainty caused by approximating the rear-region minority-carrier lifetime as being independent of position.

Simple formulae were derived that allow high-accuracy internal quantum-efficiency calibrations on 1337 type photodiodes to be interpolated from the ends of the 440- to 860-nm spectral region over the interior of that region. The uncertainties that can be obtained with these formulae are comparable to those that can be obtained with the highest-accuracy calibrations currently available.

TABLE 10.1 Recombination related parameters used with the doping distributions shown in Fig. 10.3 to model the quantum-deficiency spectra of Hamamatsu 1337 photodiodes.

CASE	Nss (cm^{-3})	S (10^5 cm/s)	τ_r (s)	$N_A(x)$
1	0	0.71264	-	dashed curve
2	$-3x10^{12}$	1.83500	-	dashed curve
3	$-1x10^{13}$	100.000	-	solid curve
4	$-4x10^{12}$	1.56000	-	solid curve

TABLE 10.2 Values of the parameters to be used in eq. 4 for extrapolating a short wavelength internal quantum-deficiency value to longer wavelengths and in eq. 5 for extrapolating a long wavelength internal quantum-deficiency value to shorter wavelengths.

parameter	equation 4	equation 5
A_0	1.38002×10^{2}	2.02157×10^{-8}
A_1	1.47530×10^{2}	3.51764×10^{3}
A_2	8.07476×10^{-5}	not used
λ_0	4.39312×10^{1} nm	7.53991×10^{1} nm
λ_2	4.27998×10^{2} nm	1.66889×10^{8} nm

TABLE 10.3 Average values of, and uncertainty estimates for the internal quantum efficiency ε_f, spectral responsivity R, one minus the reflectance $(1-\rho)$ and non-linearity correction (1-NL) reported in Ref. 5 (bold face type) at wavelength λ for five multiple-reflection radiometers based on 1337 photodiodes, and internal quantum-deficiency values $\delta_x(\lambda)$ calculated from the reported data. At 441.6 nm, $\delta_x(\lambda)$ is calculated as $1 - \varepsilon_f$; at 633.0 nm as $1 - 1.23985\ R\ (1-\rho)^{-1}\ (1-NL)^{-1}\ \lambda^{-1}$ um W/A.

λ (nm)	ε_f	R (A/W)	$(1-\rho)$	(1-NL)	$\delta_x(\lambda)$
441.6	**+0.99347** **±0.00040**				**+0.00653** **±0.00040**
633.0		**±0.50840** **±0.00009**	**±0.99704** **±0.00014**	**±0.99972** **±0.00004**	**±0.00097** **±0.00023**

TABLE 10.4 Oxide-bias data y_o reported in Ref. 19 for a single 1337 photodiode, the average internal quantum-efficiency data ε_x reported in Ref. 19 for ten multiple-reflection radiometers based on 1337 photodiodes, and the quantum deficiencies $\delta_x(\lambda)$ calculated from these sets of data.

λ (nm)	--- oxide bias ---		------ iqe ------	
	y_o	$\delta_x(\lambda)$	ε_x	$\delta_x(\lambda)$
406.85	+0.0126 ±0.00015	+0.01404 ±0.00017	+0.9867 ±0.0002	+0.0133 ±0.0002
468.18	+0.0044 ±0.00015	+0.00495 ±0.00017	+0.9934 ±0.0003	+0.0066 ±0.0003
568.35			+0.9977 ±0.00020	+0.0023 ±0.0002
647.30	+0.0007 ±0.00015	+0.00079 ±0.00017	+0.9986 ±0.0002	+0.0014 ±0.0002
799.54			+0.9989 ±0.0002	+0.0011 ±0.0002
859.07	+0.0000 ±0.00015	+0.00000 ±0.00017	+0.9987 ±0.0002	+0.0013 ±0.0002

TABLE 10.5 Comparison of predictions of eq. 17 with measured internal quantum-deficiency data $\delta_x(\lambda)$ in Table 10.3 for λ_f = 441.6 nm and $\delta_x(\lambda_r) = 0$.

λ (nm)	$\delta_x(\lambda)$ (Ref. 5)	$\delta(\lambda)$ (eq. 17)	Difference
633.0	+0.00097 ±0.00023	+0.00089 ±0.00007	-0.00008 ±0.00024

TABLE 10.6 Comparison of predictions of eq. 17 with internal quantum-deficiency data $\delta_x(\lambda)$ derived from oxide-bias data in Table 10.4 for λ_f = 468.18 nm and $\delta_x(\lambda_r)$ = 0.

λ (nm)	$\delta_x(\lambda)$ (Ref. 17)	$\delta(\lambda)$ (eq. 17)	Difference
406.85	+0.01404 ±0.00017	+0.01321 ±0.01144	-0.00083 ±0.01144
647.30	+0.00079 ±0.00017	+0.00090 ±0.00030	+0.00010 ±0.00034
859.07	+0.00000 ±0.00017	+0.00015 ±0.00005	+0.00015 ±0.00018

TABLE 10.7 Comparison of predictions of eq. 17 with measured internal quantum-deficiency data in Table 10.4 for λ_f = 468.18 nm and λ_r = 859.07 nm.

λ (nm)	$\delta_x(\lambda)$ (Ref. 17)	$\delta(\lambda)$ (eq. 17)	Difference
406.85 nm	+0.0133 ±0.00025	+0.01744 ±0.01000	+0.00414 ±0.01000
568.35 nm	+0.0023 ±0.00030	+0.00224 ±0.00007	-0.00006 ±0.00031
647.30 nm	+0.0014 ±0.00020	+0.00121 ±0.00004	-0.00019 ±0.00020
799.54 nm	+0.0011 ±0.00021	+0.00082 ±0.00009	-0.00028 ±0.00023

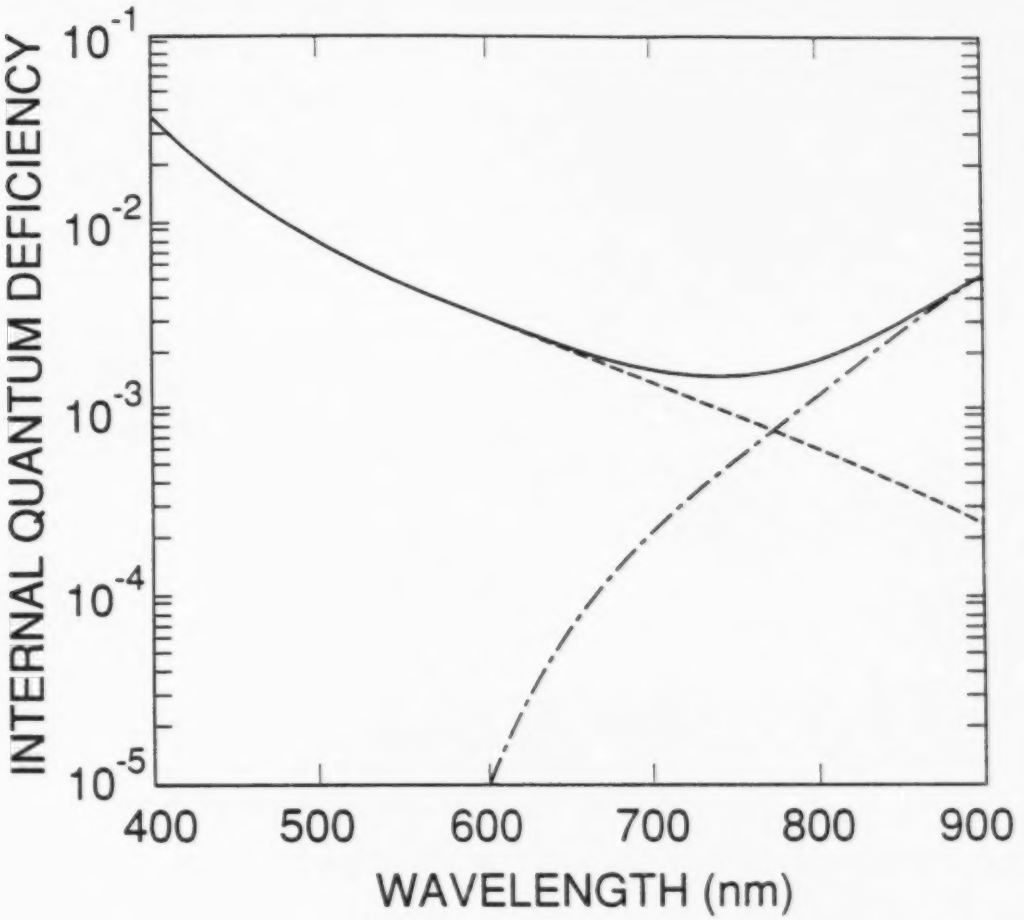

FIGURE 10.1 Internal quantum-deficiency spectra $\delta(\lambda, 0, S, -)$ for S = 71264 cm/s (dashed line) and $\delta(\lambda, 0, 0, \tau_r)$ for τ_r = 1 ms (dot-dashed line) and their sum (solid line).

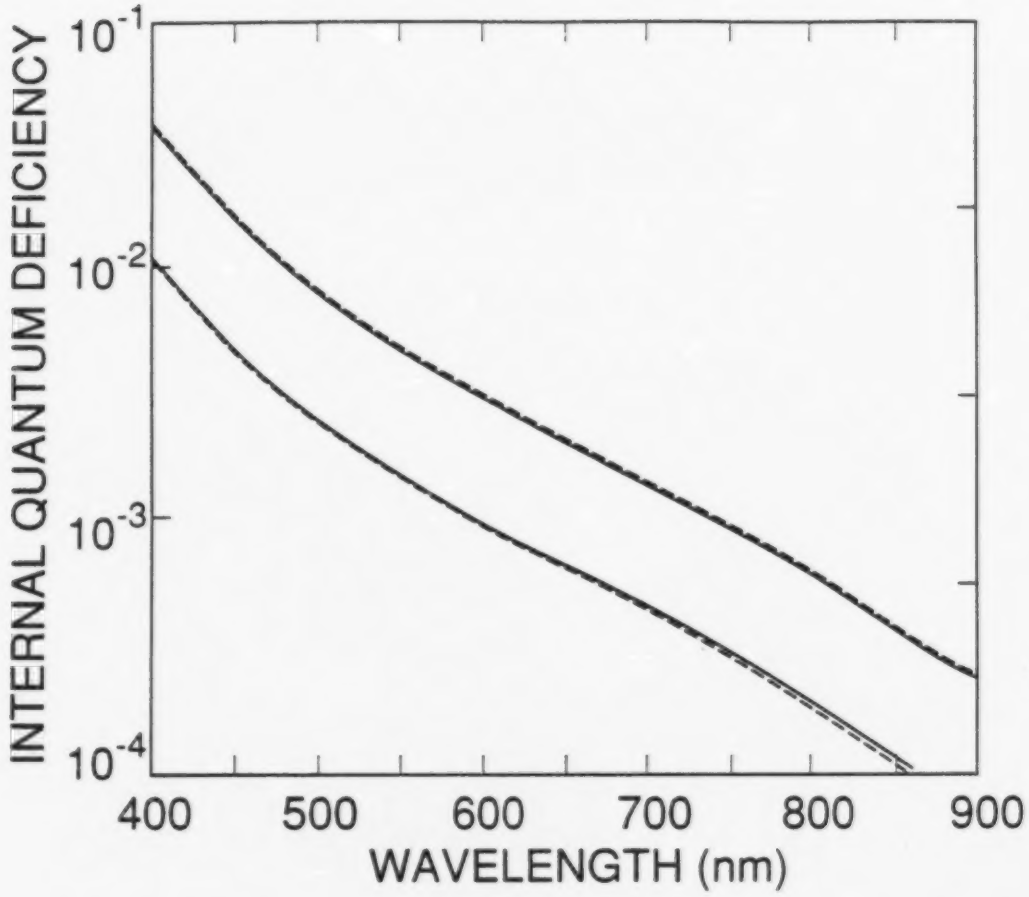

FIGURE 10.2 The quantum-deficiency spectra $\delta(\lambda, N_{ss}, S, \tau_r)$ for the conditions listed in Table 10.1. Case 1 - upper dashed line; Case 2 - lower dashed line; Case 3 - upper solid line; Case 4 - lower solid line.

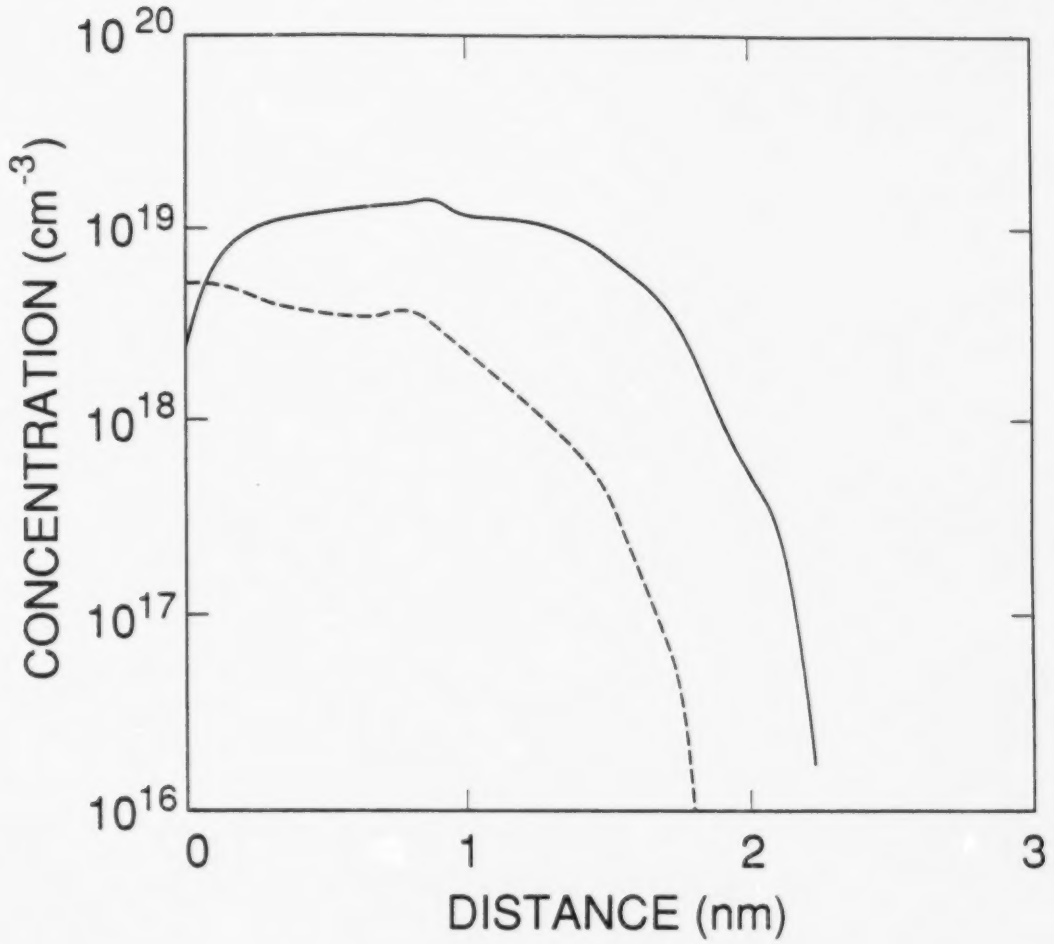

FIGURE 10.3 The front-region doping distributions $N_A(x)$ used to calculate the front-region internal quantum-deficiency curves in Fig. 10.2. These doping distributions span the range of the effect of six measured distributions on the shape of the front-region quantum deficiency.

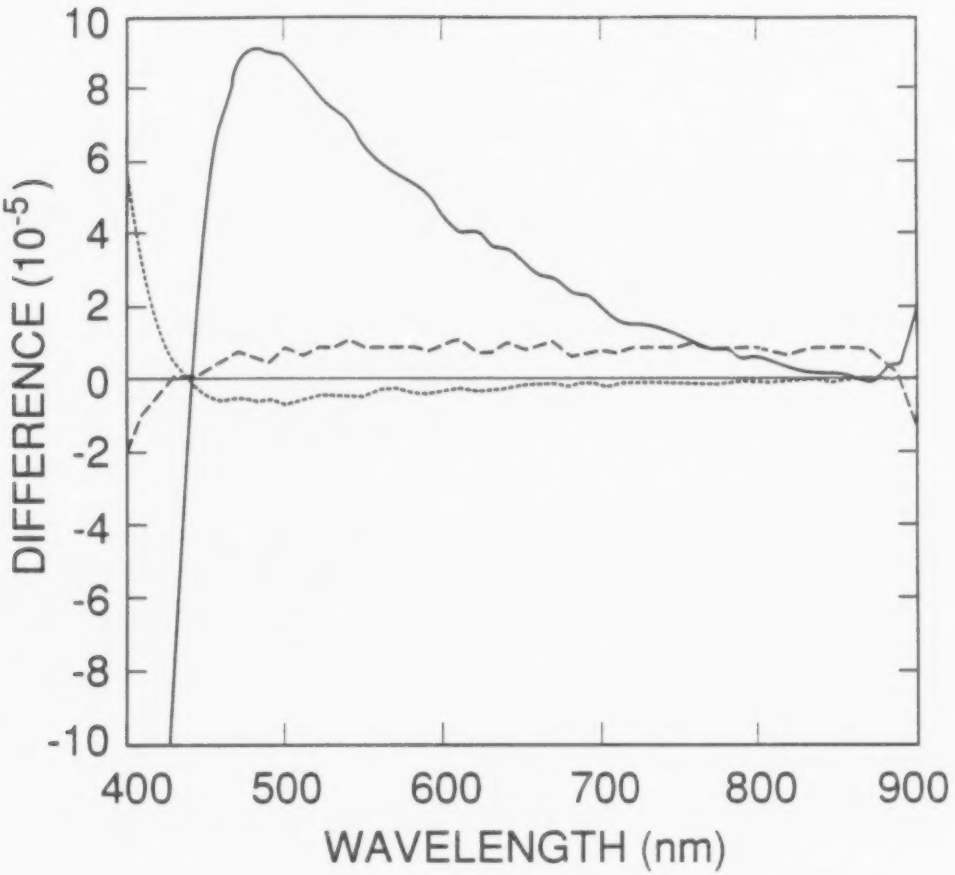

FIGURE 10.4 Differences between the internal quantum-deficiency spectra of Fig. 10.2 for Cases 1 (dashed line), 3 (dotted line), and 4 (solid line) when normalized to 0.01 at 440 nm, and that for Case 2 when normalized to 0.01 at 440 nm.

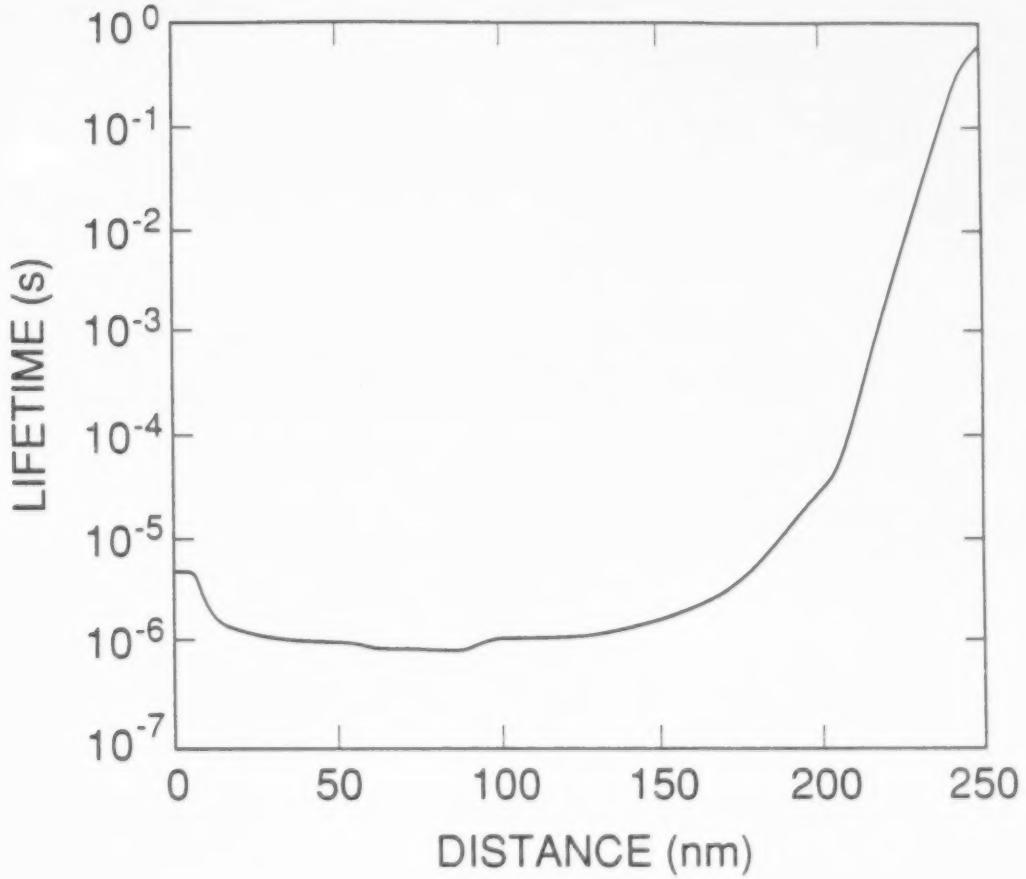

FIGURE 10.5 The default, band-to-band recombination lifetime profile calculated by PC-1D for the doping distribution shown as the solid curve in Fig. 10.3.

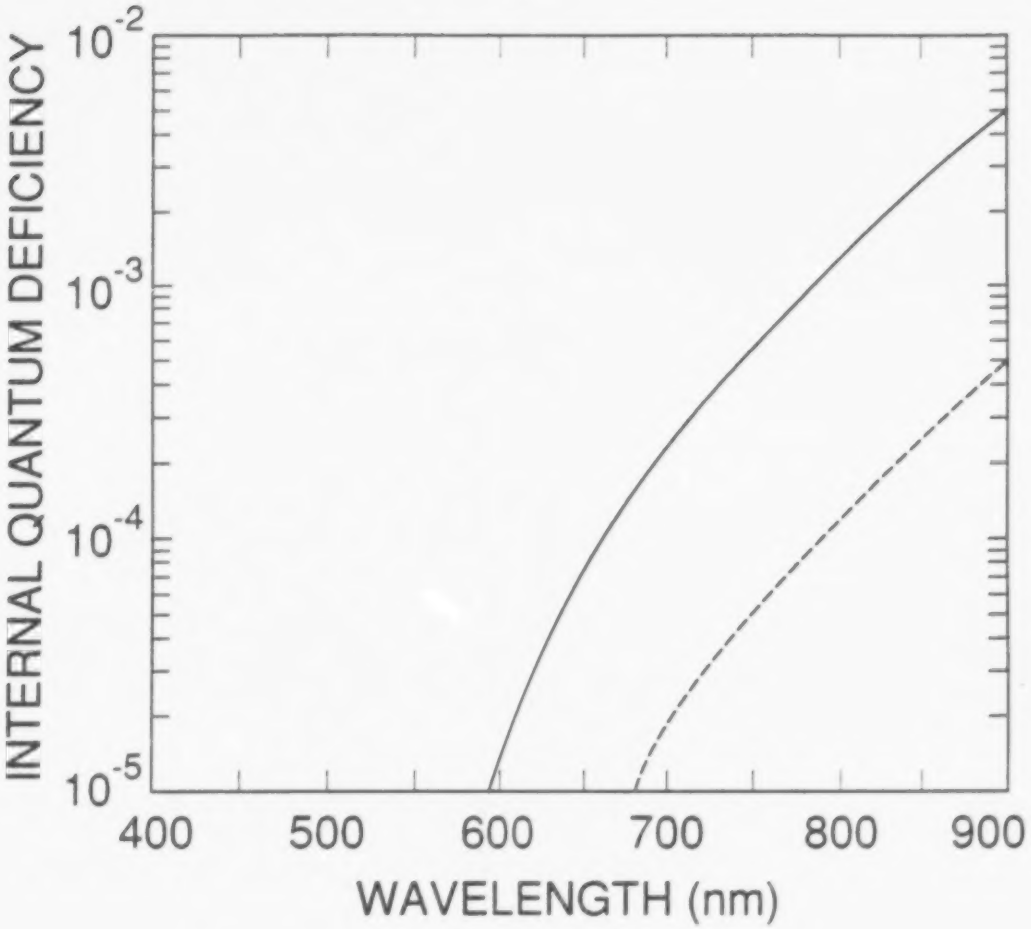

FIGURE 10.6 The internal quantum-deficiency spectra $\delta(\lambda, N_{ss}, S, \tau_r)$ for τ_r = 1 ms (solid line), and τ_r = 10 ms (dashed line) with N_{ss} = S = 0.

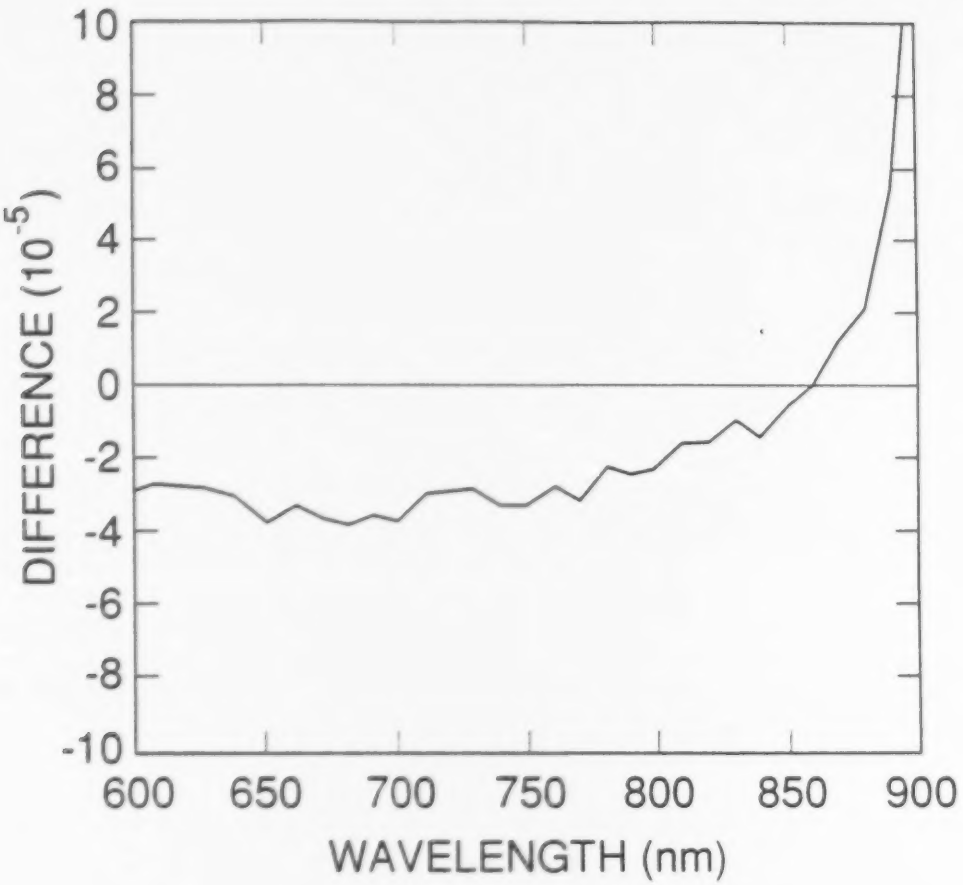

FIGURE 10.7 Differences between the internal quantum-deficiency spectra of Fig. 10.6 when normalized to 0.002 at 860 nm.

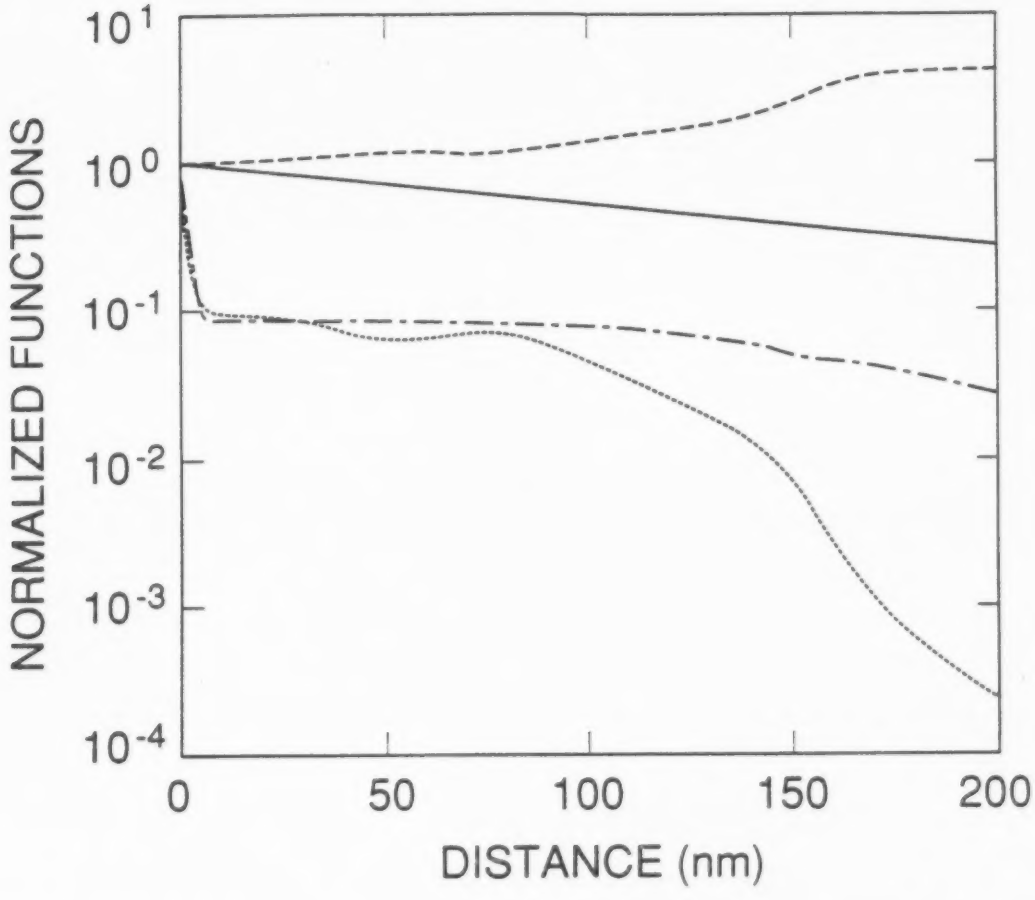

FIGURE 10.8 Comparison of $\hat{M}_0(x)$ (dotted line), $\hat{n}_{ie}(x)$ (dashed line), $\hat{\mu}_m(x)$ (dot-dashed line), and exp(-α(400 nm) x) (solid line) for a 1337 photodiode with N_{ss}, S, and τ_r set as defined in Case 2 of Table 10.1. The tildes in the preceding expressions indicate that these expressions have been normalized to unity at x = 0.

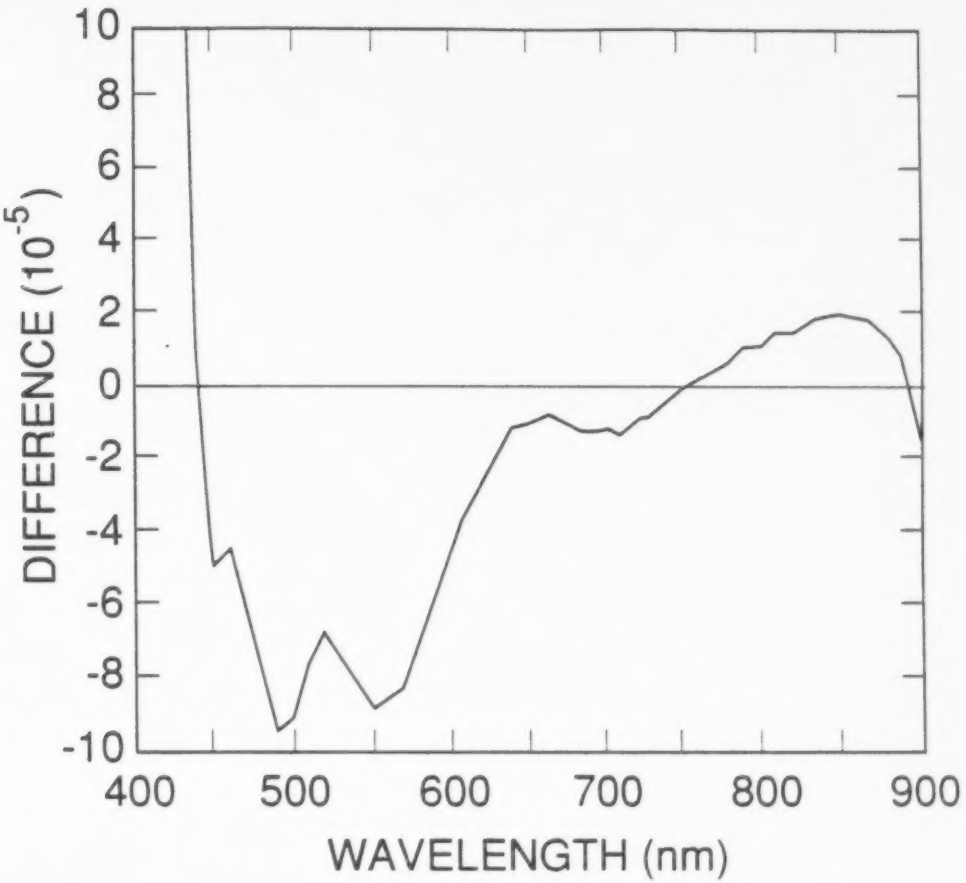

FIGURE 10.9 Differences between the internal quantum-deficiency spectrum for a 1337 photodiode described by Case 2 in Table 10.1 for the absorption-coefficient data of Ref. 16 and for the absorption-coefficient data of Ref. 14.

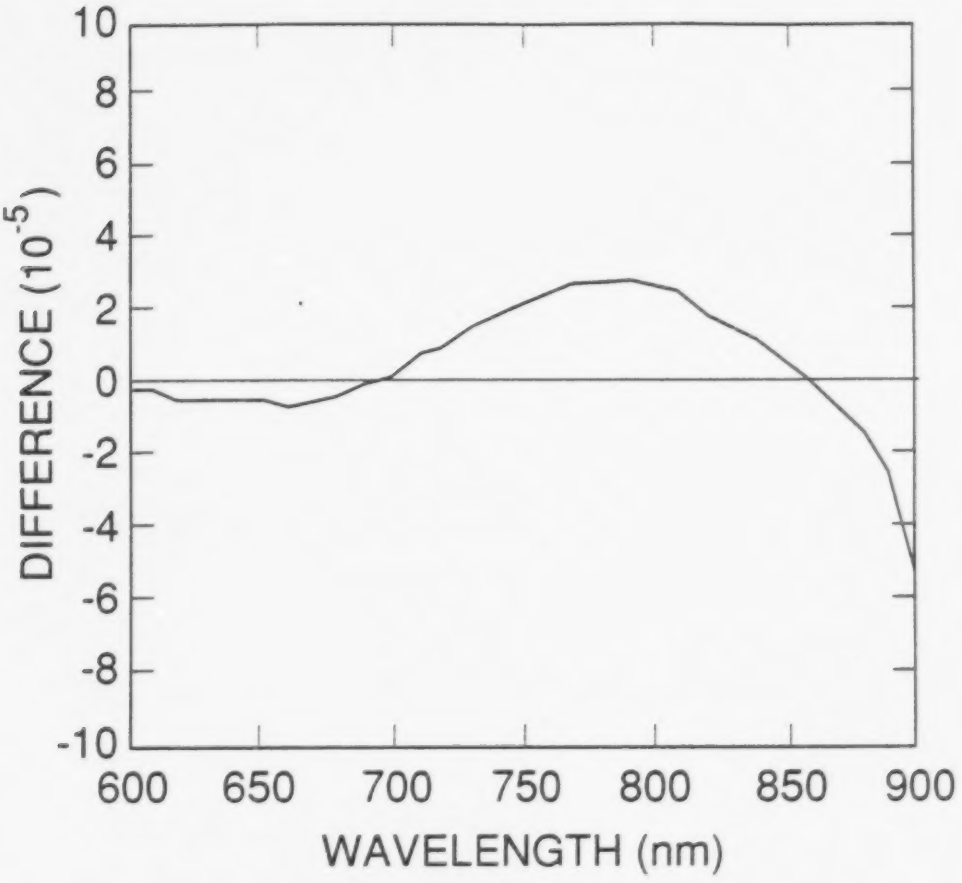

FIGURE 10.10 Differences between the internal quantum-deficiency spectra for a 1337 photodiode with S = 0 and τ_r = 1 ms for the absorption-coefficient data of Ref. 16 and for the absorption-coefficient data of Ref. 14.

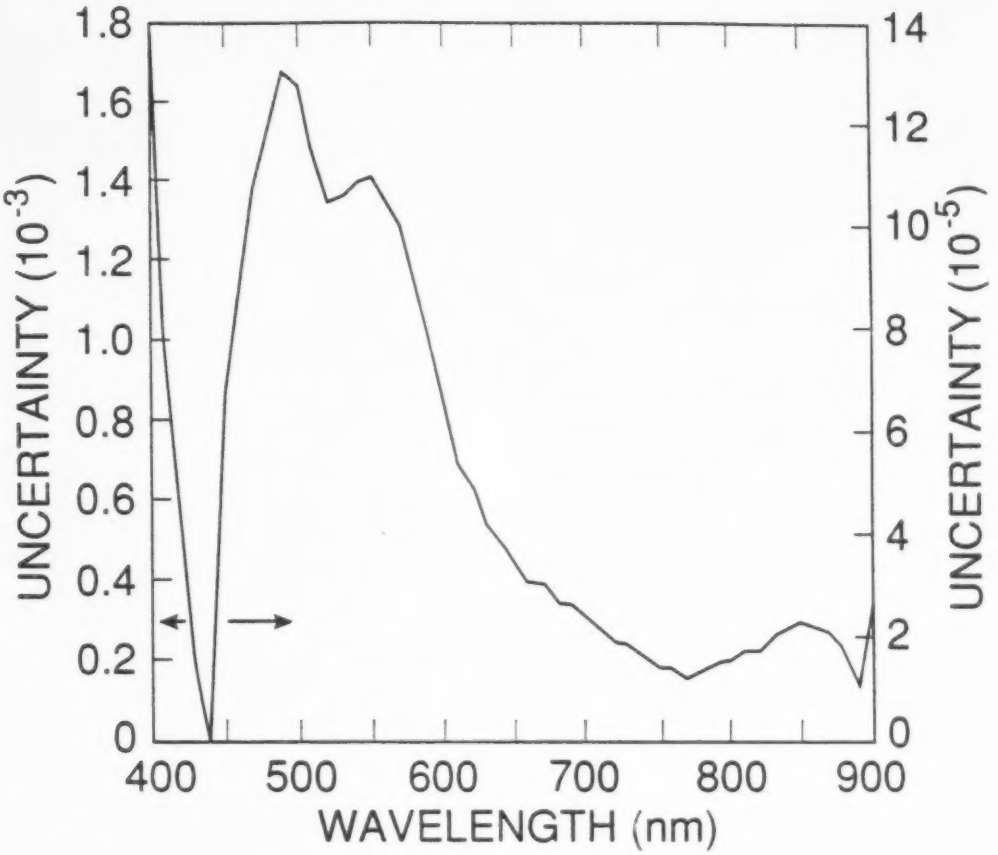

FIGURE 10.11 Sum in quadrature (root-mean-square) of the curves in Figs. 10.4 and 10.9. This curve is the nominal estimated uncertainty associated with the use of eq. 4 in eq. 17 to extrapolate an internal quantum deficiency of 0.01 at 440 nm to any other wavelength between 400 and 900 nm. Notice that the sum is plotted on different scales below and above 440 nm.

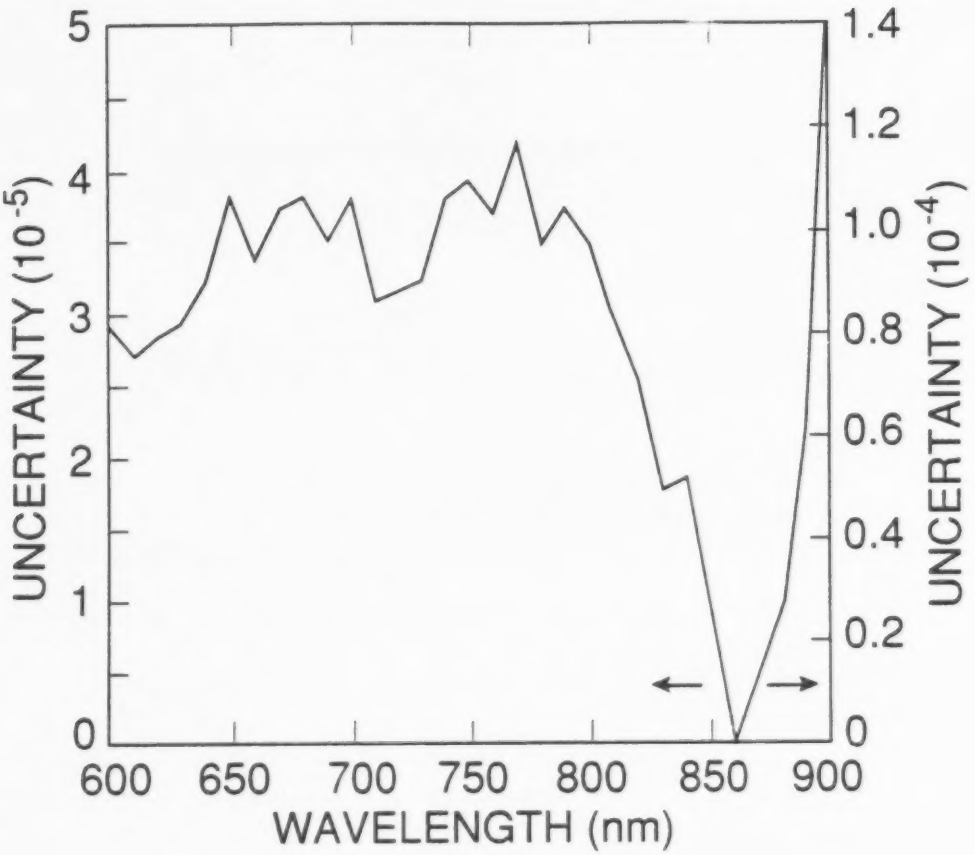

FIGURE 10.12 Sum in quadrature of the curves in Figs. 10.7 and 10.10. This curve is the nominal uncertainty associated with the use of eq. 5 in eq. 17 to extrapolate an internal quantum deficiency of 0.002 at 860 nm to other wavelengths between 400 and 900 nm. Notice that the sum is plotted on different scales below and above 860nm.

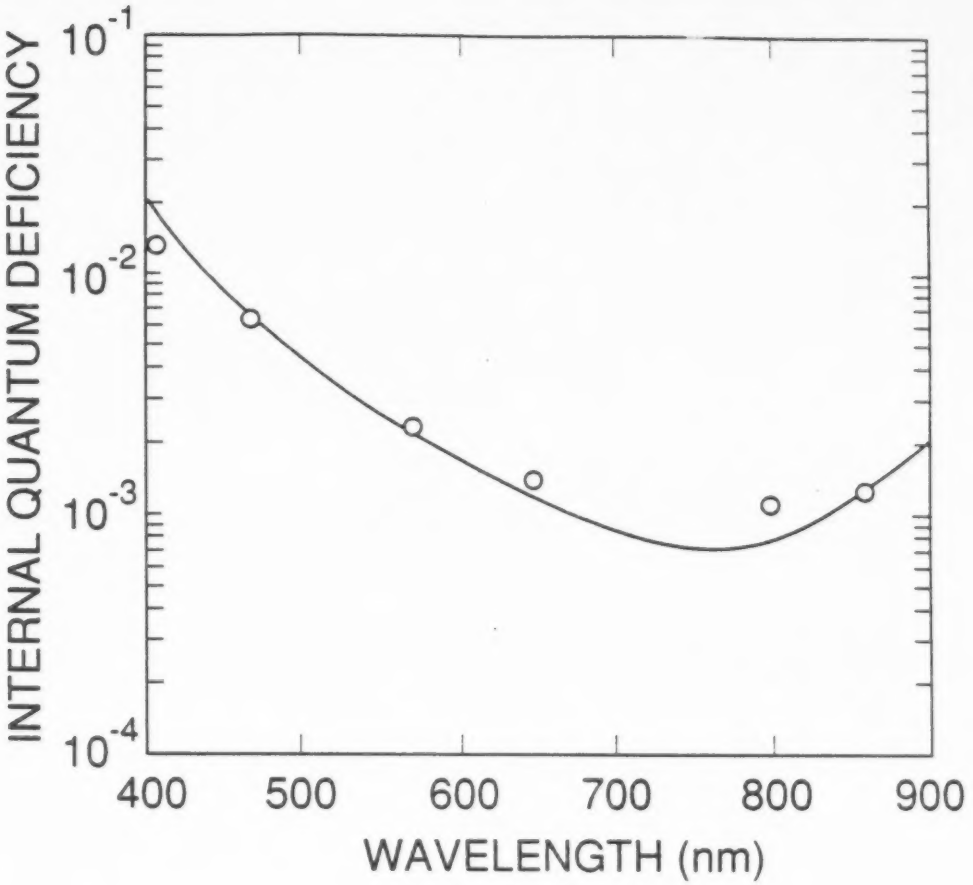

FIGURE 10.13 Comparison of measured data of Ref. 19 (open circles) with eq. 17 (solid line) normalized to pass through the measured point at 468.18 and 859.1 nm.

REFERENCES FOR CHAPTER 10

1. J. Geist, R. Koehler, R. Goebel, A. M. Robinson, and C. R. James, Numerical modeling of silicon photodiodes for high-accuracy applications. Part II: Interpreting oxide-bias experiments, J. Res. NIST **96**, 471-479 (1991).

2. J. Geist, Quantum efficiency of the p-n junction in silicon as an absolute radiometric standard, Appl. Opt. **18**, 760-762 (1979).

3. J. Geist, E. F. Zalewski, and A. R. Schaefer, Spectral response self-calibration and interpolation of silicon photodiodes, Appl. Opt. **19**, 3795-3799 (1980).

4. C. C. Hoyt, P. J. Miller, P. V. Foukal, and E. F. Zalewski, Comparison between a side-viewing cryogenic radiometer and self-calibrated silicon photodiodes, SPIE **1109**, 236-245 (1989).

5. E. F. Zalewski and C. C. Hoyt, Comparison between cryogenic radiometry and the predicted quantum efficiency of pn silicon photodiode light traps, Metrologia **28**, 203-206 (1991).

6. J. Geist, D. Chandler-Horowitz, A. M. Robinson, and C. R. James, Numerical modeling of silicon photodiodes for high-accuracy applications. Part I: Simulation programs, J. Res. NIST **96**, 463-469 (1991).

7. J. Geist and H. Baltes, High-accuracy modeling of photodiode quantum efficiency, Appl. Opt. **28**, 3929-3939 (1989).

8. J. W. Slotboom and H. C. de Graaff, Measurement of bandgap narrowing in Si bipolar transistors, Solid-State Electron. **19**, 857-862 (1976).

9. J. Geist, J. R. Lowney, C. R. James, and A. M. Robinson, Testing the accuracy of calculated equilibrium carrier concentrations in the presence of surface fields, J. Appl. Phys. **70**, 236-242 (1991).

10. Y. Ohkura, Quantum effects in Si n-MOS inversion layers at high substrate concentrations, Solid-State Electron. **33**, 1581-1585 (1990).

11. H. S. Bennett and J. R. Lowney, Physics for numerical simulation of silicon and gallium arsenide transistors, Solid-State Electron. **33**, 675-691 (1990).

12. R. B. M. Girisch, R. P. Mertens, and O. B. Verbeke, Energy-gap change in silicon n-type inversion layers at low temperature, Solid-State Electron. **33**, 85-91, (1990).

13. H. S. Bennett, Hole and electron mobilities in heavily doped silicon: comparison of theory and experiment, Solid-State Electron. **26**, 1157-1166 (1983).

14. J. Geist, A. Migdall, and H. P. Baltes, Analytic representation of the silicon absorption coefficient in the indirect transition region, Appl. Opt. **27**, 3777-3779 (1988).

15. H. A. Weakliem and D. Redfield, Temperature dependence of the optical properties of silicon, J. Appl. Phys. 50, 1491-1493 (1979), and personal communication.

16. H. R. Philipp, Influence of oxide layers on the determination of the optical properties of silicon, J. Appl. Phys. 43, 2835-2839 (1972), and personal communication.

17. E. F. Zalewski, Silicon photodiode device with 100% external quantum efficiency, Appl. Opt. 22, 2867-2873.

18. N. P. Fox, and J. E. Martin, Comparison of two cryogenic radiometers by determining the absolute spectral responsivity of silicon photodiodes with an uncertainty of 0.02%, Appl. Opt. 29, 4686-4693 (1990).

19. N. P. Fox, Trap detectors and their properties, Metrologia 28, 197-202 (1991), and personal communication.

11. CONCLUSIONS

The purpose of this chapter is to tie together the results of the preceeding chapters. Chapters 1 and 2 were intoductory in nature. Chapter 1 introduced the key ideas of the thesis: 1) photodiodes as prototypical integrated sensors, 2) accuracy as one of the measures of sensor performance, 3) silicon self-calibration as a field requiring high accuracy modeling of silicon photodiodes, and 4) the development of high accuracy models of the internal quantum efficiency of silicon photodiodes as the topic of this thesis. Chapter 2 reviewed silicon self-calibration in detail to outline the state of the art before the research in this thesis was started, and previewed the improvement in the state of the art as a result of the research reported in this thesis.

11.1 SILICON ABSORPTION COEFFICIENT

Chapters 3, 4, and 5 described investigations culminating in a formula that represents the best present knowledge of the silicon absorption coefficient spectrum from 440 nm to 1180 nm. Chapter 3 showed that the absorption coefficient of silicon is a smooth function of wavelength in the middle of the region of the indirect optical transition, just as it is near the band edge, despite published claims to the contrary. This is important; the best way to represent the absorption coefficient spectrum is in terms of a simple function based on theory, but such a representation would not be possible if the published claims were correct. The small, high resolution segment of the silicon absorption coefficient spectrum reported in Chapter 3 appears to be the most precise ever reported for a high absorption coefficient material, and the techniques described there could be used to improve the state of the art for this type of measurement in other spectral

regions.

Chapter 4 reports a very accurate measurement of the absorption coefficient of silicon at 633 nm. This value in conjunction with previously published results is used to select the most accurate of the published spectra for later fitting. This result appears to be the most accurate value ever reported for a high absorptance material, and the techniques described in this chapter can be combined with those described in Chapter 4 to give a powerful approach to simultaneously achieving high precision, high accuracy and high resolution in the measurement of large absorption coefficients.

Chapter 5 describes an eleven parameter analytic function that was fit to a carefully chosen silicon absorption coefficient spectrum from less than 0.1 cm^{-1} at 1.05 eV to greater than 10^4 cm^{-1} at 2.7 eV with a residual standard deviation of 2.5% over the entire spectral region. This function appears to be the most accurate analytic representation of the silicon absorption coefficient spectrum presently available. This level of accuracy is needed for accurate modeling of the internal quantum efficiency of silicon photodiodes as explained in Chapter 1, and verified in Chapter 10.

11.2 FORMULAE FOR UNCERTAINTY ANALYSES

Chapters 6 and 7 describe the development of techniques to assess the numerical accuracy of iterative solutions of the drift-diffusion equations for equilibrium carrier concentrations and steady-state photocurrents. These techniques are crucial to the uncertainty analyses carried out in Chapters 9 and 10 for the models of photodiodes of interest in self-calibration.

Chapter 6 describes an integral transform of the equilibrium majority carrier distribution in a photodiode. This transform is an accurate approximation to the internal quantum efficiency of the photodiode under certain conditions that are well suited for comparison with iterative solutions of the drift-diffusion equations. As a result, the integral transform can be used to test the consistency of these quantities as calculated from iterative solutions of the drift-diffusion equations. It can also be used to guide an uncertainty analysis of the calculated internal quantum efficiency. While based on an analytic expression that had been published previously, it appears to be a new result. Chapter 10 uses the integral transform to verify the numerical accuracy of, and to derive uncertainty estimates for spectra calculated in that chapter to interpolate high accuracy internal quantum efficiency calibrations.

The nature of the integral transform derived in Chapter 6 shows that the internal quantum efficiency spectrum is very sensitive to the majority carrier concentration in the front region of a silicon photodiode, which, in turn, is extremely sensitive to oxide-trapped charge. Chapter 7 shows that accurately approximating the majority carrier concentration in the presence of trapped charge is a difficult problem for iterative solutions of the drift-diffusion equations. Chapter 7 also describes an analytic function of distance from the front-surface oxide in uniformly doped material that can be used to test the accuracy with which computer programs can calculate the majority carrier concentration in uniformly doped material. This function, which is very accurate for doping concentrations of technological importance, and which is rigorous for intrinsic material, appears to

be a new result. It is used in Chapter 7 to demonstrate the accuray the equilibrium carrier distributions obtained from PC-1D.

11.3 HIGH-ACCURACY PHOTODIODE SIMULATIONS

Chapters 8, 9, and 10 are concerned with modeling silicon photodiodes in high-accuracy applications of concern to silicon self-calibration. Chapter 8 considers the suitability of Version 2 of PC-1D for high-accuracy photodiode modeling, and describes programs specifically written to support its use in this application. These programs support modeling the measurement of internal quantum efficiency spectra as well as oxide-bias self-calibration experiments. These programs also support linearity and reverse-bias self-calibration experiments, but Chapter 8 shows that PC-1D is not capable of accurately modeling the former, which suggests possible problems with the latter as well. The listings of the Turbo Pascal 5.5 source code for these programs, are provided in Appendices, and the programs are used in the modeling described in Chapters 9 and 10.

Chapter 9 describes the analysis of oxide-bias data for three different types of photodiode with the help of PC-1D and the support programs described in Chapter 8. Nominal values for the charge stored in the oxide and the surface recombination velocity at the oxide-silicon interface for two of the photodiode types are derived, and a nominal internal quantum efficiency of 0.9997 ±0.0003 from 440 nm to 460 nm for one of the photodiode types is derived. This is the first time an uncertainty has been determined for the nominal 100% internal quantum efficiency of this type of photodiode.

Chapter 10 derives two functions: one for extrapolating the internal

quantum efficiency of one type of photodiode from a wavelength greater than 440 nm to longer wavelengths, and another for extrapolating the internal quantum efficiency from a wavelength less than 860 nm to shorter wavelengths for the same type of photodiode. Chapter 10 also demonstrates by comparison with high accuracy experimental data that these functions can be used to interpolate the internal quantum efficiency of this type of photodiode over the 440 nm to 860 nm spectral region with an uncertainty of less than ± 0.0003.

11.4 SUMMARY OF CONTRIBUTION

The extrapolation formulae derived in Chapter 10, the nominal value for the internal quantum efficiency derived in Chapter 9, the absorption-coefficient formula derived in Chapter 5, and the high-accuracy absorption-coefficient value reported in Chapter 4 all meet recognized needs in the area of high-accuracy applications of silicon photodiodes. Other original results, such as the formula in Chapter 7 for the carrier concentration in uniformly doped, charge-accumulated material, the integral-transform approximation to the internal quantum efficiency in Chapter 6, the programs described in Chapter 8 to support the use of PC-1D in high-accuracy photodiode modeling, and the demonstration in Chapter 3 that the absorption coefficient spectrum of silicon is a smooth function of wavelength are of less general use, but were essential for obtaining the other more general results. With the exception of the programs, these results are also interesting in their own right as demonstrated by their publication as journal articles.

APPENDIX 1. A listing of MAKE_PRM.PAS that compiles under Turbo Pascal Version 5.5

```
PROGRAM make_temporary_prm_files_for_running_pc1d;
{RUN_PC1D.BAT runs this program when it is named MAKE_PRM.EXE.
 This program writes 2 temporary files, TEMP.PRM and TEMP.DAT.
 RUN_PC1D.BAT then runs PC-1D with input=TEMP.PRM & output=TEMP.PDF.
 RUN_PC1D.BAT then runs READ_PDF.EXE.
 READ_PDF.EXE uses TEMP.PDF and TEMP.DAT to write QE data to a file.
 RUN_PC1D.BAT runs MAKE_PRM.EXE again.
 MAKE_PRM.EXE uses TEMP.DAT to decide to either
  1) increment some parameters in TEMP.DAT and TEMP.PRM, or
  2) delete the 3 temporary files.}
{$N+}
USES CRT, DOS;

TYPE file_of_values_type = FILE OF DOUBLE;

TYPE p_index_type =
     (I_parameters, I_max_iterations,
      I_mode, I_graphs, I_size_factor, I_error_limit,
      I_clamp, I_step_size, I_final_step,
      I_solutions_step, I_eq_renode, I_ss_renode, I_tr_renode,
      I_graph_1, I_graph_2, I_graph_3, I_graph_4,

      I_area, I_area_value, I_facet_depth, I_facet_angle,
      I_temperature, I_temp_units,
      I_front_surface, I_back_surface,
      I_generation, I_front_texture, I_back_texture,
      I_int_refl_value, I_front_refl,
      I_front_refl_value, I_back_refl_value,
      I_front_n1, I_front_d1,
      I_front_n2, I_front_d2,
      I_front_n3, I_front_d3,
      I_front_barrier, I_back_barrier,
      I_front_Nss, I_back_Nss,
      I_base_location, I_emitter_location, I_collector_location,
      I_shunt_loc1, I_shunt_loc2,
      I_band_file, I_boundary_dx, I_recombine,

      I_collector, I_base, I_shunt,
      I_Vcc_shape, I_Vcc_start, I_Vcc_end,
      I_Vbb_shape, I_Vbb_start, I_Vbb_end,
      I_light_shape, I_light_start, I_light_end,
      I_spectrum, I_lambda_start, I_lambda_end,
      I_Rcc, I_Rbb, I_Rc, I_Rb,
      I_Gb, I_Gc, I_Gsh,
      I_Db, I_Dc, I_Nb, I_Nc);

     q_index_type =
     (I_w, I_material, I_material_mod,
      I_doping, I_recomb_front, I_recomb_back,
      I_taun, I_taup, I_Et,
      I_Sn_front, I_Sp_front, I_Et_front,
      I_Sn_back, I_Sp_back, I_Et_back,
      I_J0_front, I_J0_front_n, I_J0_back, I_J0_back_n,
      I_Nbk, I_Nbk_type,
      I_Nfl, I_Nfl_type, I_Nfl_shape, I_Nfl_depth, I_Nfl_peak,
```

```
        I_Nf2, I_Nf2_type, I_Nf2_shape, I_Nf2_depth, I_Nf2_peak,
        I_Nr1, I_Nr1_type, I_Nr1_shape, I_Nr1_depth, I_Nr1_peak,
        I_Nr2, I_Nr2_type, I_Nr2_shape, I_Nr2_depth, I_Nr2_peak,
        I_Eg, I_affinity, I_NcNv, I_ni0, I_eps,
        I_Cnt, I_Cpt, I_Cn, I_Cp, I_Bn, I_Bp,
        I_BGN_Phid, I_BGN_Nd, I_BGN_Phia, I_BGN_Na,
        I_n_file,
        I_n,
        I_mu_max_n,
        I_mu_min_nn, I_Nref_nn, I_alpha_nn,
        I_mu_min_np, I_Nref_np, I_alpha_np,
        I_mu_nb1, I_mu_nb2, I_mu_nb3, i_mu_nb4,
        I_mu_max_p,
        I_mu_min_pp, I_Nref_pp, I_alpha_pp,
        I_mu_min_pn, I_Nref_pn, I_alpha_pn,
        I_mu_pb1, I_mu_pb2, I_mu_pb3, i_mu_pb4,
        I_n_sat, I_p_sat,
        I_absorb_file,
        I_Egd1, I_Egd2, I_Eg_1, I_Eg2, I_Ep1, I_Ep2,
        I_Asb_Ad1, I_Abs_Ad2,
        I_Abs_A1, I_Abs_A2, I_Abs_A3, I_Abs_A4,
        I_Abs_B, I_Abs_Tg);

    variant_type = (str_16, byt_16, rea_08, int_04);

    s_type = STRING[15];
    b_type = ARRAY[0..15] OF BYTE;
    r_type = ARRAY[0..1] OF DOUBLE;
    i_type = ARRAY[0..3] OF LONGINT;

    p_type = RECORD
             CASE variant : variant_type OF
             str_16 : (s : ARRAY[p_index_type] OF s_type);
             byt_16 : (b : ARRAY[p_index_type] OF b_type);
             rea_08 : (r : ARRAY[p_index_type] OF r_type);
             int_04 : (i : ARRAY[p_index_type] OF i_type);
             END;

    q_type = RECORD
             CASE variant : variant_type OF
        str_16 : (s : ARRAY[1..3] OF ARRAY[q_index_type] OF s_type);
        byt_16 : (b : ARRAY[1..3] OF ARRAY[q_index_type] OF b_type);
        rea_08 : (r : ARRAY[1..3] OF ARRAY[q_index_type] OF r_type);
        int_04 : (i : ARRAY[1..3] OF ARRAY[q_index_type] OF i_type);
             END;

TYPE prm_data_type
    = OBJECT
      model_prm_file_path : PATHSTR;
      p : p_type;
      q : q_type;
      PROCEDURE read_prm_file;  {page }
      PROCEDURE write_prm_file; {page }
      END;

TYPE exp_data_type
    = OBJECT(prm_data_type)
      key : CHAR;
```

```
        shutter : STRING[6];
        lambda, energy, phi, Vo, Vr, depth, oxide_t, value : DOUBLE;
        index, last : LONGINT;
        QE_file_path : PATHSTR;
        FUNCTION file_exists( path : PATHSTR) : BOOLEAN;        {page }
        PROCEDURE initialize_or_update;                         {page }
          PROCEDURE initialize;                                 {page }
            PROCEDURE get_parameter_to_scan;                    {page }
            PROCEDURE get_values_from_file;                     {page }
            {OR}
            PROCEDURE get_start_stop_and_step;                  {page }
              PROCEDURE set_parameter_to_value;                 {page }
            PROCEDURE open_empty_QE_file;                       {page }
            PROCEDURE write_temp_data;                          {page }
          PROCEDURE update;                                     {page }
            PROCEDURE get_current_value;
           {set_parameter_to_value;}
           {write_temp_data;}
        PROCEDURE prepare_pq;                                   {page }
        PROCEDURE delete_temporary_files;                       {page }
        END;

VAR exp_data : exp_data_type;

FUNCTION exp_data_type.file_exists( path : PATHSTR) : BOOLEAN;
VAR f : TEXT;
BEGIN
{$I-}
ASSIGN(f, path);
RESET(f);
CLOSE(f);
{$I+}
IF (IORESULT = 0)
THEN file_exists := TRUE
ELSE file_exists := FALSE;
END;

PROCEDURE exp_data_type.initialize_or_update;
VAR f : TEXT;
BEGIN
IF NOT file_exists( 'temp.dat' )
THEN BEGIN
     CLRSCR;
     IF file_exists( 'J0.dat' )
     THEN BEGIN
          ASSIGN(f, 'J0.dat' );
          ERASE(f);
          END;
     WRITELN(
    'Parameter file (including PRM extension) defining photodiode: ');
     READLN(model_prm_file_path);
     IF NOT file_exists( model_prm_file_path )
     THEN BEGIN
      WRITELN('File: ', model_prm_file_path, ' not found.  Halting.');
          HALT;
          END;
     WRITELN('Complete path to file in which to store QE results: ');
     READLN(QE_file_path);
```

```
     initialize;
     END
ELSE BEGIN
     update;
     END;
END;

PROCEDURE exp_data_type.initialize;
VAR s : STRING[1];
BEGIN
get_parameter_to_scan;
s := ' ';
WHILE NOT ( UPCASE(s[1]) IN ['F', 'K'] )
DO BEGIN
   WRITE('Start, step, and stop values from ');
   WRITE('(K)eyboard or all values from (F)ile? ');
   READLN(s);
   s := UPCASE(s[1]);
   IF NOT ( UPCASE(s[1]) IN ['K', 'F'] )
   THEN WRITELN('Your response is unacceptable.  Try it again.');
   END;
IF s = 'F'
THEN get_values_from_file
ELSE get_start_stop_and_step;
IF NOT (key IN ['P', 'W'])
THEN BEGIN
     WRITE('Wavelength (nm): ');
     READLN(lambda);
     END;
IF key <> 'L'
THEN BEGIN
     WRITE('Incident irradiance (W per sq. cm): ');
     READLN(phi);
     END;
IF key <> 'O'
THEN BEGIN
     WRITE('Oxide bias voltage (V): ');
     READLN(Vo);
     END;
IF key <> 'R'
THEN BEGIN
     WRITE('Reverse bias voltage (V): ');
     READLN(Vr);
     END;
WRITE('Non-zero thickness of front surface oxide (nm): ');
READLN(oxide_t);
WRITE('Depth at which to get total photocurrent (um): ');
READLN(depth);
IF Vr = 0
THEN shutter := 'open'
ELSE shutter := 'closed';
open_empty_QE_file;
write_temp_data;
END;


PROCEDURE exp_data_type.get_parameter_to_scan;
TYPE letter_set_type = SET OF 'A' .. 'Z';
```

```
CONST answer_set : letter_set_type = ['O', 'R', 'W', 'P', 'L'];
VAR s : STRING[1];
BEGIN
s := ' ';
WHILE NOT ( UPCASE(s[1]) IN answer_set )
DO BEGIN
   {CLRSCR;}
   WRITELN('Type of experiment to simulate? ');
   WRITELN('(O)xide bias (Volts) scan? ');
   WRITELN('(R)everse bias (Volts) scan? ');
   WRITELN('(W)avelength (nm) scan? ');
   WRITELN('(P)hoton energy (eV) scan? ');
   WRITELN('(L)inearity (W/cm^2) scan? ');
   WRITE('Enter letter key here: '); READLN(s);
   IF NOT ( UPCASE(s[1]) IN answer_set )
   THEN WRITELN('Your response is unacceptable.  Try it again.');
   END;
key := UPCASE(s[1]);
END;

PROCEDURE exp_data_type.get_values_from_file;
VAR start, stop, step : DOUBLE;
    name : STRING[80];
    f : TEXT;
    g : file_of_values_type;
BEGIN
WRITE('Name of file with all values of scanned parameter: ');
READLN(name);
ASSIGN(f, name);
RESET(f);
ASSIGN(g, 'temp.VAL');
REWRITE(g);
READLN(f, start);
WRITE(g, start);
last := 0;
WHILE NOT EOF(f)
DO BEGIN
   READLN(f, stop);
   WRITE(g, stop);
   INC(last);
   END;
WRITE(g, stop);
INC(last);
CLOSE(f);
CLOSE(g);
index := 0;
value := start;
set_parameter_to_value;
END;

PROCEDURE exp_data_type.get_start_stop_and_step;
VAR start, stop, step : DOUBLE;
    g : file_of_values_type;
BEGIN
WRITE('First value for scanned parameter: '); READLN(start);
WRITE('Stop value for scanned parameter: '); READLN(stop);
IF key = 'L'
THEN BEGIN
```

```
  WRITE('Factor by which to increase irradiance on each iteration: ');
     READLN(step);
     IF ( (start>stop) AND (step>=1) )
     OR ( (start<stop) AND (step<=1) )
     THEN BEGIN
     WRITELN('These values would produce an endless loop.  Halting.');
          HALT;
          END;
     END
ELSE BEGIN
     WRITE('Step size for scanned parameter: ');
     READLN(step);
     IF ( (start>stop) AND (step>=0) )
     OR ( (start<stop) AND (step<=0) )
     THEN BEGIN
     WRITELN('These values would produce an endless loop.  Halting.');
          HALT;
          END;
     END;
ASSIGN(g, 'temp.VAL');
REWRITE(g);
last := 0;
IF key = 'L'
THEN BEGIN
     value := start/step;
     IF start < stop
     THEN WHILE value <= stop
          DO BEGIN
             value := value*step;
             WRITE(g, value);
             INC(last);
             END
     ELSE WHILE value >= stop
          DO BEGIN
             value := value*step;
             WRITE(g, value);
             INC(last);
             END;
     END
ELSE BEGIN
     value := start-step;
     IF start < stop
     THEN WHILE value <= stop
          DO BEGIN
             value := value+step;
             WRITE(g, value);
             INC(last);
             END
     ELSE WHILE value >= stop
          DO BEGIN
             value := value+step;
             WRITE(g, value);
             INC(last);
             END;
     END;
CLOSE(g);
DEC(last);
index := 0;
```

```
value := start;
set_parameter_to_value;
END;

PROCEDURE exp_data_type.set_parameter_to_value;
BEGIN
CASE key OF
     'O' : Vo := value;
     'R' : Vr := value;
     'W' : lambda := value;
     'P' : BEGIN
           energy := value;
           lambda := 1239.85/energy;
           END;
     'L' : phi := value;
END; {CASE}
END;

PROCEDURE exp_data_type.open_empty_QE_file;
VAR f : TEXT;
BEGIN
ASSIGN(f, QE_file_path);
REWRITE(f);
CLOSE(f);
END;

PROCEDURE exp_data_type.write_temp_data;
VAR f : TEXT;
BEGIN
ASSIGN(f, 'temp.dat');
REWRITE(f);
WRITELN(f, model_prm_file_path);
IF key <> 'P'
THEN WRITELN(f, key, ' ', lambda, ' ', phi)
ELSE WRITELN(f, key, ' ', energy, ' ', phi);
WRITELN(f, Vo, ' ', Vr, ' ', shutter);
WRITELN(f, depth, ' ', oxide_t);
WRITELN(f, QE_file_path);
WRITELN(f, index, ' ', last);
WRITELN(index, last);
CLOSE(f);
END;

PROCEDURE exp_data_type.update;
VAR dir : DIRSTR;
    name : NAMESTR;
    ext : EXTSTR;
    f : TEXT;
BEGIN
ASSIGN(f, 'temp.dat');
RESET(f);
READLN(f, model_prm_file_path);
IF key <> 'P'
THEN READLN(f, key, lambda, phi)
ELSE BEGIN
     READLN(f, key, energy, phi);
     lambda := 1239.85/energy;
     END;
```

```
READLN(f, Vo, Vr, shutter);
WHILE shutter[1] = ' '
DO DELETE(shutter, 1, 1);
READLN(f, depth, oxide_t);
READLN(f, QE_file_path);
READLN(f, index, last);
CLOSE(f);
IF shutter = 'open'
THEN BEGIN
     INC(index);
     IF key = 'R'
     THEN shutter := 'closed';
     END
ELSE shutter := 'open';
get_current_value;
set_parameter_to_value;
write_temp_data;
END;

PROCEDURE exp_data_type.get_current_value;
VAR g : file_of_values_type;
BEGIN
ASSIGN(g, 'temp.val');
RESET(g);
SEEK(g, index);
READ(g, value);
CLOSE(g);
END;

PROCEDURE exp_data_type.prepare_pq;
CONST eps_SiO2 = 3.9;
      eps_Si = 11.9;
      eps0 = 8.8541878e-14; {C/(V cm)}
      cm_per_nm = 1e-7;
      q_per_C = 1/1.60218e-19;
      {and from W. R. Thurber and J. R. Lowney, "Electrical Transport
       Properties of Silicon" Chapter 14 in the VLSI Handbook, ed. N.
       G. Einspruch (Academic Press, Orlando, 1985), page 188.}
      Ec = 30.5e4;
      c  = 0.657;
VAR Nss0, Nss, Rb0, Rb, En0, En, bot, top,
    sheet_R_ratio, concentration_ratio : DOUBLE;
BEGIN
IF shutter = 'closed'
THEN phi := 0;
p.s[I_mode] := 'Steady State';
p.s[I_graphs] := 'Specified';
p.i[I_graph_1][0] := 5;
p.s[I_front_surface] := 'Charged';
p.s[I_spectrum] := 'Fixed';
p.s[I_light_shape] := 'Fixed';
p.s[I_Vbb_shape] := 'Fixed';
p.r[I_lambda_start][0] := lambda;
p.r[I_light_start][0] := phi;
p.r[I_Vbb_start][0] := Vr;
Nss0 := p.r[I_front_Nss][0];
Nss := Nss0 + q_per_C*Vo*eps_SiO2*eps0/(oxide_t*cm_per_nm);
p.r[I_front_Nss][0] := Nss;
```

```
Rb0 := p.r[I_Rb][0];
IF ( (Nss0=0) OR (Rb0=0) )
THEN BEGIN
     Rb := Rb0;
     END
ELSE BEGIN
     IF Nss = 0
     THEN Nss := Nss + 1e7;
     concentration_ratio := Nss0/Nss;
     En0 := ABS(Nss0/(2*eps_Si*eps0));
     En := ABS(Nss/(2*eps_Si*eps0));
     top := 1 + EXP(c*LN(En/Ec));
     bot := 1 + EXP(c*LN(En0/Ec));
     sheet_R_ratio := top/bot;
     Rb := Rb0*concentration_ratio*sheet_R_ratio;
     WRITELN('conc. ratio = ', concentration_ratio);
     WRITELN('sheet R ratio = ', sheet_R_ratio);
     END;
p.r[I_Rb][0] := Rb;
END;

PROCEDURE exp_data_type.delete_temporary_files;
VAR f : FILE;
    dir : DIRSTR;
    name : NAMESTR;
    ext : EXTSTR;
    temp_file_path : PATHSTR;
BEGIN
ASSIGN(f, 'temp.dat');
ERASE(f);
FSPLIT(model_prm_file_path, dir, name, ext);
temp_file_path := dir + 'temp.val';
ASSIGN(f, temp_file_path);
ERASE(f);
temp_file_path := dir + 'temp.prm';
ASSIGN(f, temp_file_path);
ERASE(f);
temp_file_path := dir + 'temp.pdf';
ASSIGN(f, temp_file_path);
ERASE(f);
END;

PROCEDURE prm_data_type.read_prm_file;
VAR f : FILE;
    count, result : WORD;
BEGIN
ASSIGN(f, model_prm_file_path);
RESET(f, 1);
count := 16*SUCC(ORD(I_Nc));
BLOCKREAD(f, exp_data.p.s, count, result);
count := 16*3*SUCC(ORD(I_Abs_Tg));
BLOCKREAD(f, exp_data.q.s, count, result);
CLOSE(f);
END;

PROCEDURE prm_data_type.write_prm_file;
VAR f : FILE;
    dir : DIRSTR;
```

```
    name : NAMESTR;
    ext : EXTSTR;
    temp_prm_file_path : PATHSTR;
    count, result : WORD;
BEGIN
FSPLIT(model_prm_file_path, dir, name, ext);
temp_prm_file_path := dir + 'temp.prm';
ASSIGN(f, temp_prm_file_path);
REWRITE(f, 1);
count := 16*SUCC(ORD(I_Nc));
BLOCKWRITE(f, exp_data.p.s, count, result);
count := 16*3*SUCC(ORD(I_Abs_Tg));
BLOCKWRITE(f, exp_data.q.s, count, result);
CLOSE(f);
END;

PROCEDURE test_exp_data;
BEGIN
WITH exp_data
DO BEGIN
   WRITELN(model_prm_file_path);
   WRITELN(p.s[I_mode]);
   WRITELN(p.s[I_graphs]);
   WRITELN('Graph number = ', p.i[I_graph_1][0]);
   WRITELN(p.s[I_spectrum]);
   WRITELN(p.s[I_light_shape]);
   WRITELN('lambda = ', p.r[I_lambda_start][0]);
   WRITELN('phi = ', p.r[I_light_start][0]);
   WRITELN('Vo = ', Vo);
   WRITELN('Nss = ', p.r[I_front_Nss][0]);
   WRITELN('Vr = ', p.r[I_Vbb_start][0]);
   END;
END;

BEGIN {main ************************************************************}
WITH exp_data
DO BEGIN
   WRITELN('MAKE_PRM.EXE is initializing or updating as appropriate.');
   initialize_or_update;
   WRITELN('The shutter is now ', shutter);
   IF ( index >= last )
   THEN BEGIN
        WRITELN('MAKE_PRM.EXE is deleting the temporary files.');
        delete_temporary_files;
        END
   ELSE BEGIN
        WRITELN('MAKE_PRM.EXE is reading ', model_prm_file_path);
        read_prm_file;
        {test_exp_data;}
   WRITELN('MAKE_PRM.EXE is preparing the temporary parameter file.');
        prepare_pq;
        {test_exp_data;}
        WRITELN('MAKE_PRM.EXE is writing TEMP.PRM.');
        write_prm_file;
        WRITELN;
        END;
   END;
END.
```

APPENDIX 2. A listing of READ_PDF.PAS that compiles under Turbo Pascal Version 5.5.

```
PROGRAM read_total_photocurrent_from_pdf_file;

{$N+}

USES CRT, DOS;

TYPE pdf_data_type
     = OBJECT
       model_prm_file_path, QE_file_path : PATHSTR;
       key : CHAR;
       shutter : STRING[7];
       lambda, energy, phi, Vo, Vr,
       oxide_t, depth, J0, Jt, QE : DOUBLE;
       z : ARRAY[0..500] OF STRING[30];
       PROCEDURE initialize;
       PROCEDURE read_pdf_file;
         PROCEDURE write_J0_to_file;
         PROCEDURE read_J0_from_file;
       PROCEDURE append_QE_file;
       END;

VAR pdf_data : pdf_data_type;

PROCEDURE pdf_data_type.initialize;
VAR f : TEXT;
BEGIN
ASSIGN(f, 'temp.dat');
RESET(f);
READLN(f, model_prm_file_path);
READLN(f, key, lambda, phi);
IF key = 'P'
THEN BEGIN
     energy := lambda;
     lambda := 1239.85/energy;
     END;
READLN(f, Vo, Vr, shutter);
WHILE shutter[1] = ' '
DO DELETE(shutter, 1, 1);
READLN(f, depth, oxide_t);
READLN(f, QE_file_path);
CLOSE(f);
END;

PROCEDURE pdf_data_type.write_J0_to_file;
VAR f : TEXT;
BEGIN
{$I-}
ASSIGN(f, 'J0.dat');
RESET(f);
CLOSE(f);
{$I+}
ASSIGN(f, 'J0.dat');
IF ( IORESULT = 0 )
THEN APPEND(f)
ELSE REWRITE(f);
```

```
WRITELN(f, J0);
CLOSE(f);
END;

PROCEDURE pdf_data_type.read_J0_from_file;
VAR f : TEXT;
BEGIN
ASSIGN(f, 'J0.dat');
RESET(f);
WHILE NOT EOF(f)
DO READLN(f, J0);
CLOSE(f);
END;

PROCEDURE pdf_data_type.read_pdf_file;
CONST m_per_um = 1e-6;
VAR f : TEXT;
    line : STRING[80];
    n, check, how_many : INTEGER;
    x : DOUBLE;
    pdf_file_path : PATHSTR;
    dir : DIRSTR;
    name : NAMESTR;
    ext : EXTSTR;
BEGIN
FSPLIT(model_prm_file_path, dir, name, ext);
pdf_file_path := dir + 'temp.pdf';
ASSIGN(f, pdf_file_path);
RESET(f);
FOR n := 1 TO 8
DO READLN(f, line);
READLN(f, how_many);
FOR n := 1 TO how_many
DO READLN(f, line);
READLN(f, check);
FOR n := 1 TO how_many
DO READLN(f, line);
READLN(f, check);
x := -1;
WHILE x < depth*m_per_um
DO IF Vr = 0
   THEN BEGIN
        J0 := 0;
        READLN(f, x, Jt);
        END
   ELSE IF shutter = 'closed'
        THEN READLN(f, x, J0)
        ELSE READLN(f, x, Jt);
CLOSE(f);
IF Vr <> 0
THEN IF shutter = 'closed'
     THEN write_J0_to_file
     ELSE read_J0_from_file;
END;

PROCEDURE pdf_data_type.append_QE_file;
CONST lambda_0 = 1239.85;
{Lambda in nm at which 1 W gives 1 A at 100% QE.}
```

```
VAR f : TEXT;
    Jnet, J100 : DOUBLE;
BEGIN
Jnet := ABS(Jt-J0);
J100 := lambda*phi/lambda_0;
QE := Jnet/J100;
ASSIGN(f, QE_file_path);
APPEND(f);
CASE key OF
     'O' : WRITELN(f, Vo:9:6, ' ', QE:9:6);
     'R' : WRITELN(f, Vr:9:6, ' ', QE:9:6);
     'W' : WRITELN(f, lambda:9:3, ' ', QE:9:6);
     'P' : WRITELN(f, energy:9:6, ' ', QE:9:6);
     'L' : WRITELN(f, phi:12, ' ', QE:9:6);
END; {CASE}
CLOSE(f);
END;

BEGIN {main ************************************************************}

WITH pdf_data
DO BEGIN
   initialize;
   WRITELN('READ_PDF.EXE is reading TEMP.PDF.');
   read_pdf_file;
   IF shutter = 'open'
   THEN BEGIN
        WRITELN('READ_PDF.EXE is writing ', QE_file_path);
        append_QE_file;
        END;
   END;

END.
```